UNIVERSITY OF SOUTHAMPTON

OCEAN AND EARTH SCIENCE

FACULTY OF ENVIRONMENTAL AND LIFE SCIENCES

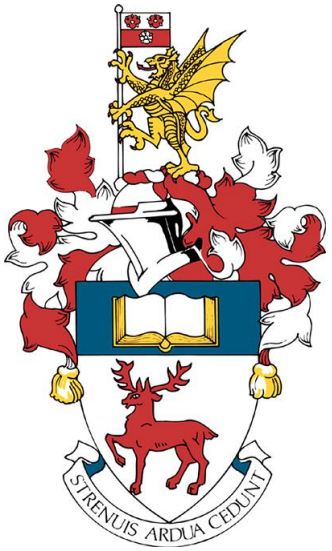

Past, present, and future variations of the Atlantic Meridional Overturning Circulation

by

Delphine Lobelle

ORCID ID: 0000-0003-1517-4815

A thesis submitted in partial fulfillment for the degree of Doctor of Philosophy

October 2019

UNIVERSITY OF SOUTHAMPTON

OCEAN AND EARTH SCIENCE

FACULTY OF ENVIRONMENTAL AND LIFE SCIENCES

Doctor of Philosophy

Past, present, and future variations of the Atlantic Meridional Overturning Circulation

by Delphine Lobelle

ABSTRACT

The Atlantic Meridional Overturning Circulation (AMOC) is a key mechanism of the global coupled ocean-atmosphere climate system, primarily via the redistribution of heat. The northward transport of warm, salty near-surface waters from the southern hemisphere is a unique feature of the Atlantic Ocean, where paleoclimate records have associated past shutdowns of the AMOC with abrupt cooling periods, potentially lasting over a millennium. According to future projections produced by the Coupled Model Intercomparison Project Phase 5 (CMIP5), an AMOC shutdown is unlikely in the next century, although a weakening is very likely, under climate change scenarios. On the other hand, studies estimating the past and current AMOC transport struggle to reach a consensus regarding whether the AMOC has recently undergone or is undergoing a transient decline, and if so, whether it is due to current anthropogenic climate change. This is due to the complexity of the relative contribution of natural and anthropogenic forcings on AMOC variability, and limited direct observational records; the longest continuous trans-basin array being RAPID, which started in 2004. Determining how many years are required to detect a statistically significant AMOC decline is therefore the starting point of this study. From simulations of an artificial AMOC timeseries, generated based on statistical properties of the RAPID and CMIP5 AMOC, an AMOC decline is detectable after 28 to 35 years (i.e., over a decade more than current observations). This reinforces the demand for improved proxy estimates, and defines the incentive behind the other analyses in this study; to investigate potential reconstructions or indicators of the AMOC's variability and trend in the past and the future. Using a multi-model approach to test the robustness, a proxy, that is presumably dynamically associated to the AMOC, is explored; sea surface height (SSH). The relationship between the AMOC and SSH is shown to be inconsistent across the CMIP5 models and therefore fails to reconstruct the AMOC's interannual variability or multi-decadal trend, using a 13-year training period. This suggests that tidal gauge data can not be used to extend the current RAPID data in the past to identify if a long-term decline has been occurring. To further characterise the potential of an AMOC slowdown, a past and future trend probability analysis is explored using the CMIP5 database. Using 250 years of historical and future scenario data reveals that forced ensemble mean AMOC trends shift the

probability of a decline outside its range of natural variability (which is estimated from the control runs), after a sustained 5-year decline or longer. This suggests that interannual AMOC events are not significantly affected by anthropogenic forcing compared to their natural variability. Furthermore, under the 'business-as-usual' scenario (RCP8.5) the probability of a 20-year decline remains high (at 86.5%), and the probability of an 'intense' decline reaches a maximum of 55.7% (vs. 13.2% in the historical scenario); in a 'stabilisation' scenario (RCP4.5) the trend probability recovers its pre-industrial values by 2100. A 20-year rogue period is identified from 1995 to 2015, marked by simultaneous unique features in the AMOC and salinity transport that are not replicated over any other 20-year period within the 250-year timeseries. These features include the maximum probability and magnitude of an 'intense' AMOC decline, and a sustained 20-year decline in subpolar salinity transport caused by internal oceanic (as opposed to atmospheric) feedbacks. This work therefore highlights the potential use of direct observations (after another decade of data), and ensemble mean numerical models to represent changes in past, present, and future natural and forced AMOC variability. Such an understanding can be used to improve future climate risk mitigation strategies and planning, with global socio-economic importance in the 21st century.

Contents

List of Figures

List of Tables

Declaration of Authorship

I, Delphine Lobelle, declare that this thesis and the work presented in it are my own and has been generated by me as the result of my own original research.

Past, present, and future variations of the
Atlantic Meridional Overturning Circulation

I confirm that:

1. This work was done mainly while in candidature for a research degree at this University;

2. Where any part of this thesis has previously been submitted for a degree or any other qualification at this University or any other institution, this has been clearly stated;

3. Where I have consulted the published work of others, this is always clearly attributed;

4. Where I have quoted from the work of others, the source is always given. With the exception of such quotations, this thesis is entirely my own work;

5. I have acknowledged all main sources of help;

6. Where the thesis is based on work done by myself jointly with others, I have made clear exactly what was done by others and what I have contributed myself;

7. This work has not been published before submission.

Delphine Lobelle

October 2019

Acknowledgements

I would firstly like to show my immense gratitude to my supervisors: Florian Sévellec, Claudie Beaulieu, Valerie Livina, and Eleanor Frajka-Williams (with a special thanks to my first supervisor, Florian). From sharing your knowledge and advice, to reading and commenting the numerous drafts, I really appreciate everything you did for me. Despite ending up in 4 (sometimes 5) different locations geographically, we created a system that worked, and I couldn't have achieved this without your support, trust, time, and patience. This was an important stepping-stone in my career, and I really enjoyed the journey. Thank you.

This PhD research would not have been possible without the joint funding from the department of Ocean and Earth Science, University of Southampton and the National Physical Laboratory - thank you for this wonderful opportunity. I would also like to thank and acknowledge the World Climate Research Programme's Working Group on Coupled Modelling, which is responsible for CMIP numerical model data that was used, and the observational data from the RAPID-MOCHA-WBTS array, where RAPID is funded by the U.K. National Environment Research Council, MOCHA is funded by the National Science Foundation, and WBTS is funded by the National Oceanic and Atmospheric Administration.

A big thanks goes to David Smeed as Principal Scientist on the RAPID JC145 cruise from Tenerife to the Bahamas in 2017, and co-supervisor of my 3-month side-project in Miami in 2018. Jointly, thanks to Bill Johns at RSMAS, University of Miami for your supervision in Miami. I learnt a lot from both of you, and thoroughly enjoyed the experience. Also, thank you to Jenny Mecking and Jeff Blundell in Southampton for your time spent helping me with LINUX and the CMIP5 data throughout my PhD.

To the ladies that shared this journey with me (the 'Superwomen'); Maria, Sophie, Aude, and Adeline. We had such an incredible time together - I'm so lucky to have met you. You really made these four years so much fun and you know how much you mean to me. Marieta, has sido un apoyo constante desde el principio hasta el final, siempre puedo contar contigo y sé que he encontrado en tí una amistad para toda la vida. Kat, you completed our crazy garden/house, I loved living with you and sharing our Californian adventures together. Dada, je suis trop contente de te connaître - ton énergie, ta joie et

ta générosité sont du jamais-vu. Rossy, thank you so much for all the coding help at the beginning and your friendship after that. To the others in Southampton: Marla, Jay, Victor, Dafydd, Nathan(uchi), Jan(cito), Elena, Conor, Giuseppe (Pepito), Hachem, Gwyn, Ale, thank you for the great times. Albert, muchas gracias por tu apoyo al principio de mi PhD- tu papel no era nada fácil y siempre te lo agredeceré mucho. For those that were unfortunate to meet me in the last 6 months of my PhD in Brest, thank you for forcing me to take breaks, once in a while! A mon papa Breton (Clément), tu as vraiment très bien pris soin de moi, et je te remercie profondément. Matías, no tengo palabras para darte las gracias por todo lo que has hecho por mí en los últimos meses - te agradezco tu paciencia y cariño. Obviously, a massive thanks also to Sus and Hannah, for the years of (best-)friendship and being my number 1 cheerleaders in everything I do.

A ma mamoush et mon papa, je ne sais pas comment vous remercier pour tout votre soutien, vos encouragements, et votre amour. Vous êtes vraiment des parents de rêves et je vous aime très fort. Ami, despite the distance and the crazy lives we lead, I know I can always count on you and you're still my rock - thank you so much for everything you've done for me, I wouldn't be who I am today without you. Phil, thanks for the support and most-importantly, the (often inappropriate) comic-relief, when it was needed. To the four of you, our family has been the one constant in our constantly-changing lives, and I am forever grateful for that.

Nomenclature

AMOC Atlantic Meridional Overturning Circulation

SSH Sea surface height

SST Sea surface temperature

SPR Subpolar region

STR Subtropical region

RAPID RAPID-Meridional Overturning Circulation and Heatflux Array-Western Boundary Time Series

IPCC Intergovernmental Panel on Climate Change

CMIP5 Coupled Model Intercomparison Project

RCP Representation Concentration Pathway

NEMO Nucleus for European Modelling of the Ocean

OLS Ordinary least squares

GLS Generalised least squares

PLS Partial least squares

MLR Multiple linear regression

AR(1) Lag-1 autocorrelation

TP Training period

PDF Probability density function

Chapter 1

Introduction

1.1 The AMOC's impact on the global climate system

Oceans form a global network of currents that act as essential regulators of the climate system by storing and redistributing heat, freshwater, and carbon. In the context of the Earth's heat budget, the incoming solar radiation is partially absorbed by surface waters in lower, tropical latitudes and released into the atmosphere at higher, subpolar latitudes (Hall and Bryden, 1982; Trenberth and Karon, 2001). The Atlantic Ocean provides the largest oceanic contribution to meridional heat transport (MHT) and thus understanding the variability and trends of its circulation is key to determining its effects on Atlantic and even global climate variability. These can be as far-reaching as hemispheric-scale surface temperature variations (Zhang et al., 2007), Atlantic hurricane activities, Sahel and Indian summer monsoons (Knight et al., 2006; Zhang and Delworth, 2006), and North American and West European drought and precipitation (Sutton and Hodson, 2005; Patricola et al., 2013).

The Atlantic Meridional Overturning Circulation (AMOC) is not a static phenomenon, and under a changing global climate, it is at risk of being destabilised. Projected increases in surface water temperatures and freshwater input from precipitation or melting of the Greenland ice sheet can decrease the density gradient required for subpolar deep water formation of the overturning circulation (Broecker et al., 1985). Changes to the thermohaline dynamics of the AMOC as well as large-scale wind patterns could therefore weaken the transport (Biastoch et al., 2008b; Lozier, 2010). Methods to disentangle effects of global warming from natural internal variability, however, are still subject to debate and current continuous records are too short (13 years) to observe decadal to multi-decadal characteristics. Hypotheses surrounding the nature of a declining AMOC trend over different timescales using observations and numerical models are therefore examined in this thesis.

Ultimately, the AMOC's variability is a key element in understanding past, present and future climate on regional and global scales and is therefore essential for developing climate predictions and future risk assessments (Keller et al., 2007b).

1.1.1 Unique features of the present day AMOC

There is an asymmetry between the northern and southern hemisphere's average surface atmospheric temperatures; the north is warmer than the south by approximately 2° C (Marshall et al., 2014). Although this is partially attributed to continental distribution (more land mass in the Northern hemisphere) (Barron et al., 1984), the AMOC's meridional ocean heat transport (OHT) also plays a role. The tropics are the only region where OHT is larger than atmospheric heat transport (AHT) (Figure 1.1). The AMOC carries around 0.4 petawatts (PW = 10^{15} W) across the equator northwards whereas the global AHT is on order 0.2 PW anomalously southwards (Wunsch, 2005; Marshall et al., 2014). Although this equatorial OHT does not appear large, the global influence is owed to water's heat capacity; approximately 2.5 m of water contain as much thermal energy as the entire atmospheric column (Visbeck et al., 2003). The subtropics experience the global peak coupled MHT, where the ocean's contribution is about 30% of total MHT; around 1.3 PW(±0.4 PW) at 26° N (Hall and Bryden, 1982; Lavin et al., 1998; Bryden et al., 2005; Johns et al., 2011).

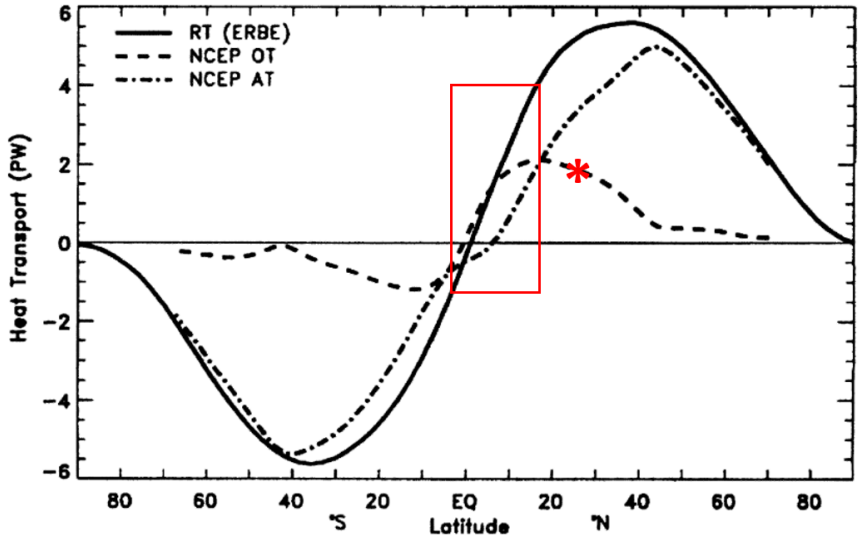

FIGURE 1.1: Global zonally-averaged annual means of meridional atmospheric heat transport (AHT) from National Centers for Environmental Prediction (NCEP) (dot-dashed line), NCEP-based oceanic heat transport (OHT) (dashed line) and the total meridional heat transport (MHT) calculated from the Earth Radiation Budget Experiment (solid line). The latitudes of OHT larger than AHT in the tropics are highlighted (red box) as is the latitude of the RAPID mooring array at 26.5° N, showing a 30% OHT contribution to total MHT (red star) (modified from Wunsch (2005)).

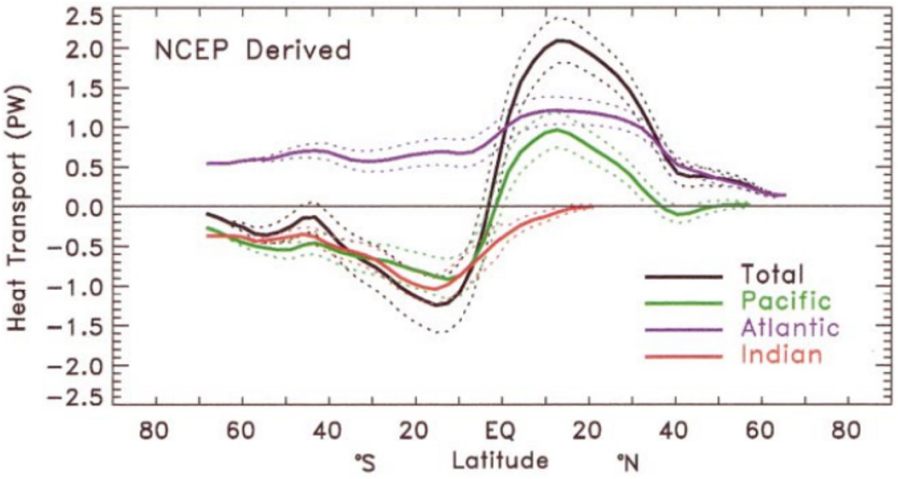

FIGURE 1.2: Oceanic contributions of zonally-averaged annual means of MHT in the Pacific (green), Indian (red) and Atlantic (purple) basins and the sum of all basins (black) with their respective errors (dashed lines) (from Trenberth and Karon (2001)).

The biggest difference between the Atlantic and the other major ocean basins is the contribution of the AMOC in transporting heat from the southern to the northern hemisphere (denoted by positive heat transport at all latitudes in Figure 1.2). The Pacific and Indian Oceans, on the other hand, show a poleward heat flux (as does the atmosphere globally, Figure 1.1) (Ganachaud and Wunsch, 2000; Trenberth and Karon, 2001). The resulting relatively higher sea surface temperature at 5° N in the North Atlantic causes a northward shift of the low pressure convergence region represented as the band of the globe's maximal zonal mean precipitation or the Intertropical Convergence Zone (ITCZ) (Zhang and Delworth, 2005; Marshall et al., 2014).

In contrast to the Atlantic, the Indo-Pacific does not produce large volumes of deep water (Ganachaud and Wunsch, 2000; Ferreira et al., 2018). The lack of deep convection can be attributed to the Indian Ocean's surface waters being too warm to sink and the Pacific Ocean's waters being too fresh (Warren, 1983). The Pacific's precipitation to evaporation ratio is higher than the Atlantic, both due to the Atlantic's narrower width encouraging evaporation and the Pacific's westerly import of atmospheric moisture from the Atlantic midlatitude (Emile-Geay et al., 2003). Thus, although both the North Atlantic and North Pacific have strong western boundary surface currents, namely the Gulf Stream and Kuroshio respectively, only the saltier Atlantic induces deep convection of surface waters (Pohlmann et al., 2006). Another hypothesis was developed based solely on dynamical principles of meridional density gradients and zonal basin extent to explain the existence of the MOC in the Atlantic and absence in the Pacific (see Sévellec and Huck (2016)).

The AMOC is central to mitigating climate change via removing and storing excess heat and carbon from the atmosphere (Kostov et al., 2014). This equilibrium adjustment

depends on the efficiency of surface absorption as well as vertical transport of the heat and carbon from surface waters into the ocean interior (Marshall et al., 2014). 25-30% of the total anthropogenic CO_2 has been taken up by the oceans since the beginning of the industrial revolution (Sabine et al., 2004; Fletcher et al., 2006). Even though the North Atlantic only occupies about 15% of the global ocean area, it is the northern hemisphere's largest ocean sink and stores 23% of the global ocean inventory of carbon (Takahashi et al., 2002; Sabine et al., 2004).

The relative impact of the Atlantic surface heat flux on regional European climate is still under ongoing debate. In simulated intensification of the AMOC and increased OHT, fewer frost days in Europe are observed and precipitation in southern (northern) Europe decreases (increases) (Pohlmann et al., 2006). The mechanism behind this process is potentially a relationship between the AMOC and low-frequency sea surface temperature (SST) variability, also known as the Atlantic Multidecadal Variability (AMV) (Knight et al., 2005; Delworth et al., 2007). Positive (negative) AMV phases correspond to warmer (colder) North Atlantic sea surface temperatures, however its periodicity is still under discussion, ranging from ∼20-30 years (Frankcombe et al., 2010; Chylek et al., 2011) to ∼40-70 years (Delworth and Dixon., 2000; Buckley and Marshall, 2016). On a global scale, the AMV is linked to decadal drought and pluvial periods in central US (Sutton and Hodson, 2005; Patricola et al., 2013), Indian and Sahel rainfall (Knight et al., 2006; Zhang and Delworth, 2006), and North Atlantic hurricane activity (Zhang and Delworth, 2006). Therefore if the AMV and AMOC are linked, indirectly the AMOC can have both regional and global impacts, therefore its understanding has prominent socio-economic benefits (Collins and Sinha, 2003).

Several studies have stated that the AMOC has recently been declining over the past decade (Smeed et al., 2014, 2018). On longer timescales and from sea-surface temperature AMOC index proxies, some report that the transport has declined by 15% since the mid-20th century (Caesar et al., 2018). Others suggest that the transport has undergone exceptional weakening relative to the past millennium since 1975 (Rahmstorf et al., 2015) or even since 1850 (Thornalley et al., 2018), whereas CMIP5 does not show such results in their historical simulations (Stocker et al., 2013). Further inferences of the past and present AMOC trend from observations and models are outlined in Sections 1.3 and 1.4.

1.1.2 Effects of an AMOC collapse on global climate

One way to understand the impacts of the AMOC on the Atlantic's neighbouring continental climate is to examine our planet without the overturning circulation. The AMOC is not a static and stable feature, but rather is sensitive to changes in temperature, salinity, and atmospheric forcings (Sévellec and Fedorov, 2011). It has been widely accepted (first shown in simple box models) that the modern climate can exist in two states:

one with North Atlantic Deep Water (NADW) formation and one without (Stommel, 1961). This bistablility has been demonstrated both in paleoclimate records and numerical simulations, causing several abrupt climate shifts, or Dansgaard-Oeschger (D-O) events, with a typical timescale of ∼1470 ±500 years (Broecker et al., 1985; Broecker and Tsung, 1987; Manabe and Stouffer, 1988; Bond et al., 1999; Boulton et al., 2014). In contrast to the relatively stable climate and AMOC of the Holocene (the current interglacial warming period over the past 10,000-year), these D-O events punctuated the last glacial interval (Dansgaard et al., 1993).

As an example, an AMOC shutdown potentially occurred approximately 11,000 years ago, according to oxygen and carbon isotope ice-core records from Greenland as well as pollen records. It onset an interglacial 800-year cooling, called the Younger Dryas Event, as seen in the paleoclimate records in continental areas surrounding the northern Atlantic (Canada, Greenland and Europe) (Broecker et al., 1985; Broecker and Tsung, 1987; Dansgaard et al., 1993). The recovery of the AMOC after this event suggests that a dramatic reduction of the AMOC is not a permanent state and oscillations between 'on' and 'off' phases have previously occurred. The AMOC is also thought to be a key player in the bipolar seesaw wherein the Arctic and Antarctic climates are out of phase climatically, and the Younger Dryas AMOC collapse potentially saw a maximum warming in Antarctica while the Arctic was cooling (Broecker, 1998). Further evidence from sediment cores of the subtropical North Atlantic (^{231}Pa/^{230}Th), shows that around 17,500 years ago during the Last Glacial Maximum, the AMOC had almost entirely shut down, potentially after a catastrophic iceberg discharge (McManus et al., 2004). Atlantic warming events consequentially appear to possibly coincide with a strengthening of the AMOC.

The mechanisms behind centennial to millennial variability of the AMOC has been thoroughly investigated in previous studies (e.g., Colin de Verdière et al. (2006); Sévellec et al. (2010); Arzel et al. (2010); Sévellec and Fedorov (2014)), where heat and freshwater flux thresholds of the North Atlantic can cause reorganisations and destabilisations of the AMOC. Simulations show that a few decades of forced intense warming (of 5 to 10° C) are followed by slow cooling over several decades (Sévellec and Fedorov, 2014). An AMOC decline can cause a positive feedback where a subarctic recirculation gyre forms, increasing the exposure that surface waters have to freshwater from precipitation and runoff, and decreasing replacement by saline warm waters from the equator. The continued dilution stops the NADW formation (Manabe and Stouffer, 1988). Furthermore, the colder sea surface and air temperature increase snow cover and albedo, which reflects the sunlight and onsets further cooling (Jacob et al., 2005). However, some model simulations suggest that after about 100 years, both the AMOC and the climatic anomalies could almost return to initial conditions after recovery (in the Holocene era) (Rahmstorf and Ganopolski, 1999; Vellinga and Wood, 2002).

Simulated temporary AMOC collapses (for example, after strong initial freshening) can result in regional impacts to sea level and atmospheric temperatures. The northern hemisphere sea level rises by 50-100 cm within a few years (Levermann et al., 2005) and within the first fifty years, atmospheric temperatures cool by 1-2° C on average (up to 8° C in regions with large changes in sea ice) (Figure 1.3). Global impacts have also been hypothesised, due to potential teleconnections. The southern hemisphere could warm slightly by 0.2° C on average (up to 1° C locally) (Vellinga and Wood, 2002) and a weakening of the Indian and Asian summer monsoons could occur (Zhang and Delworth, 2005). Paleoclimate records suggest that a southward shift in the ITCZ could occur, causing it to reside over the equator (McManus et al., 2004; Zhang and Delworth, 2005). Due to consequential changes in precipitation, global net primary productivity by land vegetation would decrease by 5% because of reduced soil moisture in the colder, drier northern hemisphere (Vellinga and Wood, 2002).

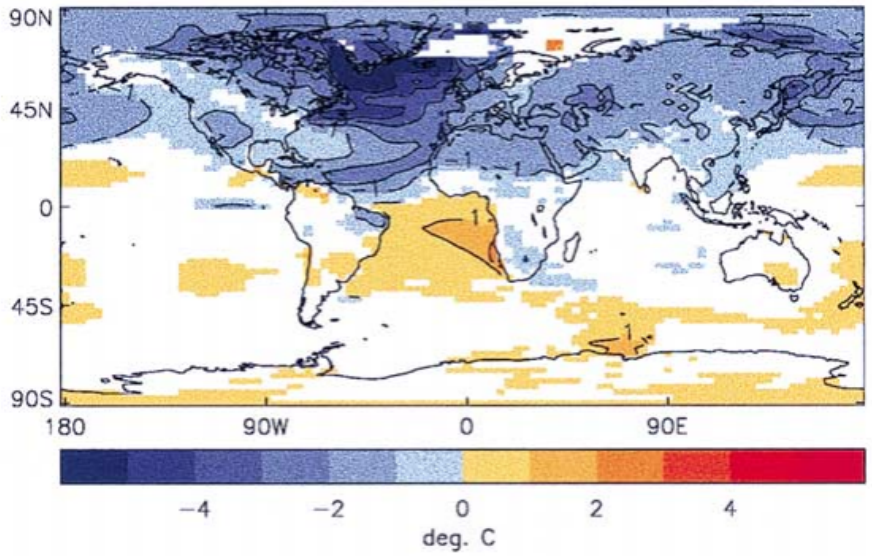

FIGURE 1.3: Predicted global air temperature changes 20-30 years after a simulated AMOC collapse from coupled numerical model HadCM3 (from Vellinga and Wood (2002)).

These past paleoclimatic events form a foundation for understanding present and future changes in the circulation. The Coupled Model Intercomparison Project Phase 5 (CMIP5) models show a decline of 10 to 50% in the 21st century, however, none of them exhibits a complete collapse (Gregory et al., 2005; Collins et al., 2013). Other studies suggest that CMIP5 models are biased towards a stable-state AMOC (Drijfhout et al., 2011). In an unstable state, the AMOC would be susceptible to large changes in response to perturbations and a total collapse could occur within 300 years of an abrupt doubling of CO_2 concentrations (Liu et al., 2017). Furthermore, if drastic changes to the hydrological cycle occur, a critical threshold or tipping point could be reached (e.g., with an increased freshwater input of ± 0.06 Sv in the North Atlantic (Rahmstorf, 1995))

causing a total collapse of the AMOC, which could take around a millennium to recover, if it ever does (Rahmstorf and Ganopolski, 1999; Alley et al., 2003; Livina and Lenton, 2007).

1.2 Physical processes linked to the AMOC

The term 'global conveyor belt' (coined by Wallace Broecker) conveys a highly simplified conceptual view of the global circulation pathway (Figure 1.4), comprising of surface and deep flows that take approximately 1,000 years to complete a loop (Broecker, 1987). The combined effects of wind and buoyancy forcing on the overturning circulation set the three-dimensional structure of the ocean. The main thermocline (approximately the upper kilometre) is largely impacted by relatively rapid changes related to surface forcing. Incoming solar radiation and cloud cover affect the temperature of the water, and precipitation and evaporation affect the salinity (Vallis, 2005).

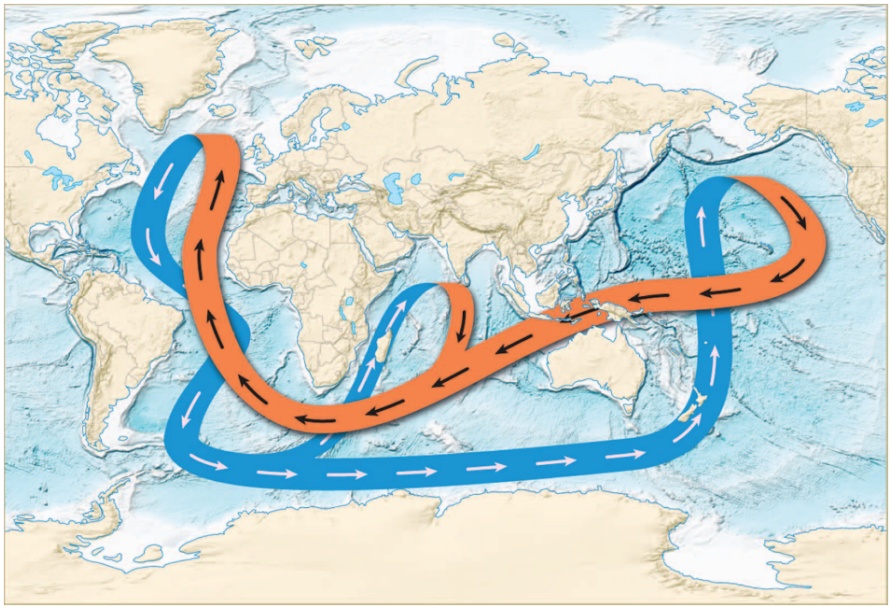

FIGURE 1.4: A highly simplified schematic of the great ocean conveyor belt showing global large-scale surface and deep currents (from Lozier (2010))

The atmosphere and ocean circulations are fuelled by different processes. The atmospheric Hadley meridional overturning circulation is driven by heating of the tropical troposphere from below and air rises due to intense convection, which is compensated by subtropical downwelling. The Atlantic Ocean's meridional overturning requires wind stress and/or tidal energy input because buoyancy is lost from the upper surface (primarily at the poles). Two cells are generated (Figure 1.6): one from the subpolar north Atlantic forming the southward-flowing 'upper cell' of NADW and a 'lower cell' from the Southern Ocean forming northward-flowing deeper abyssal Antarctic Bottom Water (AABW) (Talley et al., 2003; Buckley and Marshall, 2016).

1.2.1 The AMOC's pathway

FIGURE 1.5: Schematic of the upper cell of the AMOC showing the warmer near-surface waters (red ribbons) and cooler deep waters (blue ribbons), where arrows represent the direction of the flow. The large blue to orange arrow represent the westerly, atmospheric Jet Stream interacting with the ocean over the North Atlantic before reaching Europe. The location of the RAPID array is also displayed at 26.5°N (yellow line) (from Srokosz et al. (2012)).

The full pathway of the AMOC is as follows. For the upper cell (Figure 1.5), the South Atlantic's Agulhas leakage rings, in the form of eddies, carry warm, saline waters from the Indian Ocean (Gordon, 1986; Biastoch et al., 2008a). These eddies combine with the near-surface waters of the Benguela Current to travel northwards, some of which reach the South Atlantic western boundary via the southern equatorial current (Buckley and Marshall, 2016). Continuing northwards, the southern upper limb ends in the Gulf of Mexico via the North Brazil Current where the tropical waters undergo intense evaporation due to high incoming solar radiation (Garzoli and Matano, 2011). The warm, saline waters leave the Gulf of Mexico via the Florida Straits, becoming the Gulf Stream where it separates from the US coast at Cape Hatteras. A portion of the Gulf Stream detaches from the recirculating subtropical gyre, joining the near-surface waters of the Labrador Current and forming the North Atlantic Current (NAC). Atmospheric interactions from the westerly Jet Stream carry the waters north-eastwards, ultimately reaching the Norwegian Sea. Surface waters sink during deep convection in the Labrador Sea and the Greenland-Iceland-Norwegian Seas to form NADW (Manabe and Stouffer, 1988). The NADW flows southwards via the Deep Western Boundary Current flanking the eastern coastline of the United States (Stommel, 1958). The waters then outcrop along isopycnals back to the surface of the Southern Ocean (Marshall and Speer, 2012). Below the NADW lies the lower cell of the AMOC consisting of the abyssal AABW. The Antarctic Circumpolar Current that propagates eastwards around the Antarctic

continent due to strong westerly winds induces upwelling of the AABW as well as the NADW (Nikurashin and Vallis, 2012). The wind-driven upwelling component of the circulation is further examined below (Figure 1.6).

1.2.2 North Atlantic buoyancy-driven AMOC

Upon reaching the subpolar North Atlantic, the heat carried by the near-surface waters of the AMOC is lost to the atmosphere due to the strong ocean-atmosphere temperature gradient (that is largest during winter). The resulting buoyancy loss and presence of salt in the surface waters cause an increase in density, which induces deep-reaching convection to occur east and south-west of Greenland (Killworth, 1983). Globally, this only occurs elsewhere in the Mediterranean and occasionally in the Weddell Sea. The preconditioning phase of deep convection occurs on a cyclonic gyre-scale (100 km), where the isopycnals dome and rise to the surface, resulting in weak stratification (Marshall and Schott, 1999). Numerous intense plumes then form on horizontal scales of 1 km for the dense surface waters to sink at velocities of 5-10 $\mathrm{cm\,s^{-1}}$, after which lateral exchange and spreading occurs at depth (Region 1 in Figure 1.6) (Marshall and Schott, 1999).

1.2.3 The paradigms of the AMOC

When earlier studies only focused on the thermohaline component of the AMOC (Broecker, 1991), questions remained as to the process driving the required upwelling for the return path back to the surface (Lozier, 2010). One hypothesis proposed internal vertical diapycnal mixing (Munk and Wunsch (1998), supported by the so-called Sandström (1908) "theorum"), where mechanical energy is vital to maintain a global circulation, if heating and cooling occur at the same geopotential (i.e., surface). Vertical velocity that advects buoyancy across the flat isopycnals must be balanced by vertical diffusion since the flow into and out of the ocean interior is not equal (not purely adiabatic) (Nikurashin and Vallis, 2012)(Region 2 in Figure 1.6). Experiments using tracer-releases, however, showed that mid-depth interior mixing (away from topography) is an order of magnitude too weak to solely dictate closure of the overturning circulation (Ledwell et al., 1998, 2011). Another complementary hypothesis emerged (originally proposed by Sverdrup (1933)), wherein dense deep waters close to Antarctica reach the surface along tilted isopyncals via nearly adiabatic upwelling (Region 3 in Figure 1.6). The strength of upwelling is largely induced by westerly wind and consequent eddy adjustment around the Antarctic Circumpolar Current (Visbeck, 2007; Marshall and Speer, 2012). Therefore conceptually, the buoyancy-, mixing- and wind-driven processes are involved in closing the budget of the two-dimensional meridional circulation.

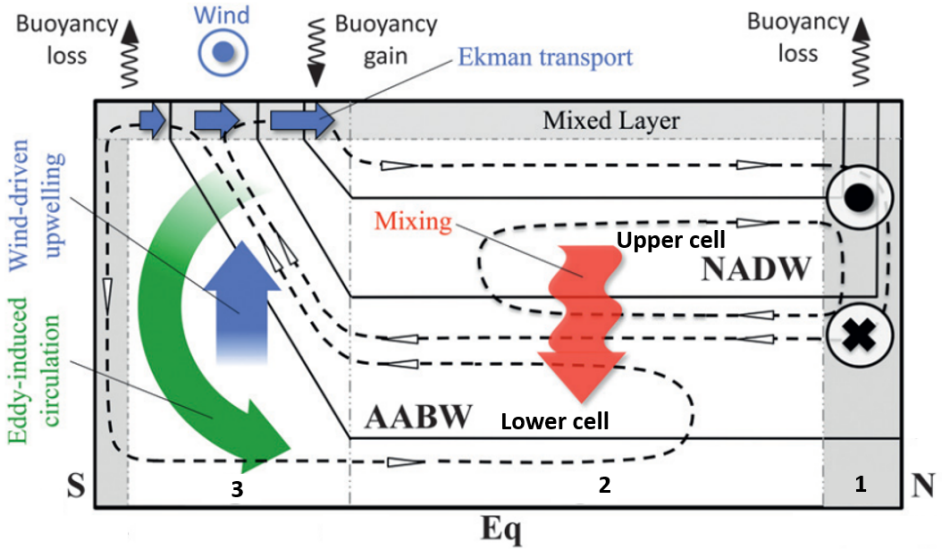

FIGURE 1.6: Schematic of the zonally-averaged Atlantic Meridional Overturning Circulation. The dashed lines with arrows depict overturning streamlines, with the upper cell (producing North Atlantic Deep Water) and lower cell (producing Antarctic Bottom Water) labelled. Shaded grey areas are the convective regions at high latitudes and surface mixed layer including Ekman transport. There are 3 regions with different driving mechanisms: (1) represents the North Atlantic buoyancy-driven region, (2) the interior ocean diapycnal mixing (red arrow) region and (3) the Southern Ocean wind-driven upwelling (blue arrow), and eddy-induced (green arrow) region (modified from Nikurashin and Vallis (2012)).

1.2.4 Geostrophic and Ekman transports

In order to illustrate the complexity of the full three-dimensional structure of the AMOC, the zonally-averaged flow explained above is somewhat oversimplified. The quantitative estimation of the large-scale, horizontal, meridional flow, is mainly characterised by two components: geostrophic and ageostrophic transports. Buoyancy anomalies on the eastern and western boundaries (zonal differences) drive the geostrophic balance and wind stress drives surface Ekman flow (Ekman, 1905). On intra-annual (seasonal) timescales, the AMOC's variability is largely reflected by wind stress whereas differences in boundary density dominate on interannual to decadal timescales (Hirschi and Marotzke, 2007). Mid-ocean geostrophic transport is generally southward due to isopycnals deepening to the west above 1000 m (Longworth et al., 2011). The geostrophic balance reads:

$$f v_g = \frac{1}{\rho_0} \partial_x p, \tag{1.1}$$

where v_g is the northward meridional velocity, x denotes the zonal direction, f is the Coriolis parameter, ρ_0 is the reference density, and p is pressure. Therefore, a balance between the effect of the earth's rotation and the zonal pressure gradient affect large-scale meridional ocean circulation.

Ekman velocity tends to affect the top ∼100 m of the sea surface and leads to the following relation:

$$v_{ek} = -\frac{\tau_x}{f\rho_0 D_{ek}}, \tag{1.2}$$

where v_{ek} is the meridional Ekman velocity, τ_x is the zonal wind stress and D_{ek} is the thickness of the Ekman layer.

If the Atlantic were a flat-bottomed, vertically-sided basin, these two components would be sufficient to estimate the full AMOC transport (Hirschi and Marotzke, 2007). Due to topography, in order to close the budget of total transport mass-balance, another physical process complements large-scale geostrophy and Ekman transport, namely the barotropic transport, which is described in Section 1.3.3. Understanding these fundamental dynamic relationships has formed the basis for setting up observational systems of the AMOC, such as hydrographic transects and mooring arrays.

1.3 AMOC variability and decline inferred from observations

1.3.1 AMOC definition

The AMOC is expressed in units of Sverdrups ($1\,\text{Sverdrup} = 10^6\,\text{m}^3\,\text{s}^{-1}$) at a particular moment in time, and as a function of latitude and depth. It represents the zonally-integrated (east-to-west), vertically-accumulated (surface-to-bottom depth) volume transport or streamfunction (ψ), estimated using:

$$\psi(y,z,t) = \int_{-H}^{z_0}\int_{x_w}^{x_e} v(x,y,z,t)dxdz, \tag{1.3}$$

where v is the meridional velocity, z is depth, y is latitude, t is time, x_w and x_e are the westward and eastward boundaries, and z_0 and $-H$ are the surface and bottom depth. Because of two-dimensional non-divergence of the zonally-integrated flow, a positive streamfunction produces a clockwise overturning in the north-south direction, with surface waters flowing northwards and deep waters flowing southwards.

In order to define the AMOC as one value per latitude and time step, the strength of the overturning is evaluated as the maximum streamfunction depth, identifying the level at which the transport of water flowing above and below this depth is balanced:

$$\text{AMOC}(y,t) = \tilde{\psi}(y,t,z_{max}), \tag{1.4}$$

where the RAPID methodology (described in Section 1.3.3 below) estimates the z_{max} at approximately 1,100 m at 26.5° N (McCarthy et al., 2015a).

1.3.2 Pre-mooring observations

Direct, continuous observations of the AMOC are very difficult to design logistically due to the zonal and meridional expanse of the Atlantic and its different dynamic components. Prior to continuous sampling techniques, estimations of the AMOC used snapshots of geostrophic transport from sporadic trans-basin hydrographic sections since the 1950s, and Ekman transport using satellite zonal wind stress since the 1990s. The narrower boundary current of the Gulf Stream within the Straits of Florida, has been monitored using continuous underwater cable measurements established in 1982 (Larsen and Sanford, 2014; Meinen et al., 2010). In the early 2000s, inverse analyses using a combination of geostrophic transport, Ekman transport and the boundary current yielded AMOC estimates of 16 ±2 Sv at 24° N (Ganachaud and Wunsch, 2000).

From the five hydrographic sections at 24.5° N between 1957 and 2004, Bryden et al. (2005) estimated a decline of 30% in the AMOC. Once seasonal and interannual variability is taken into account, however, this decline is seen as an overestimation or not statistically significant, in particular because the first and last cruises ran during months within the maximum and minimum of the seasonal cycle, respectively, that can vary by 10 Sv (Kanzow et al., 2010; Longworth et al., 2011).

A proxy of the AMOC can also be estimated using satellite data from differences in sea surface height (SSH). Zhang (2008) suggests that a slowdown of the AMOC occurred in the 1990s using altimeter data, due to a weakening of the North Atlantic subpolar gyre. Contrastingly, another method using satellite data and profiling floats shows that from 1993 to 2010, an increase by 2.6 Sv and a warming of the North Atlantic is observed. This study argues that although significant interannual and seasonal variability had been seen over those two decades, a weakening of the AMOC had not been robustly monitored (Willis, 2010). Other proxies using SSH or other properties are explored in Chapters 4 and 5.

1.3.3 Mooring observations, including the RAPID array

A few mooring arrays have been active in the past decades to estimate the AMOC. The first array started in 1997, measuring the Labrador Current at 53° N (which has suffered a few gaps over the years due to instrument loss and funding constraints) (Fischer et al., 2010; Zantopp et al., 2017). In 2000, Meridional Overturning Variability Experiment (MOVE) at 16° N was launched, which spans approximately 1,000 km of the western Atlantic basin out to the mid-Atlantic ridge to capture the NADW (Send et al., 2011). At

34.5° S, the south-west Atlantic MOC (SAM) array was deployed in 2009 using pressure sensor and current meter inverted echo sounders (Meinen et al., 2013). SAM array was paired with south-east Atlantic moorings in 2013 to form South Atlantic MOC Basin-Wide Array (SAMBA) which uses a geostrophic approximation similar to RAPID, as described in Section 1.2.4 (Ansorge et al., 2014; Morris et al., 2017). Finally, in 2014, Overturning in the Subpolar North Atlantic Program (OSNAP) deployed moorings from Scotland to Canada at 60° S (Lozier et al., 2017; Li et al., 2017). A review of all AMOC observation programs across the Atlantic is covered in Frajka-Williams et al. (2019).

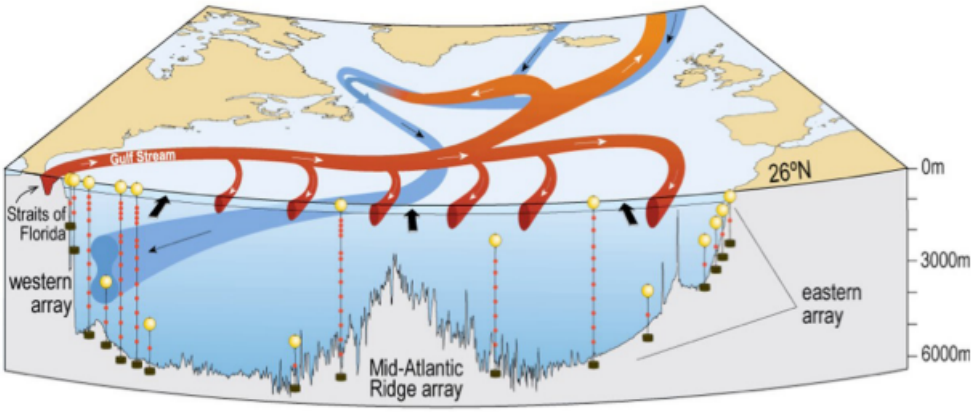

FIGURE 1.7: The AMOC north of 26.5° N. Red ribbons show the near-surface warm currents and blue the cold, deeper currents, with thin white and black arrows showing the direction of the flow. Thick black arrows show the direction of the wind-induced flow in the Ekman layer. The RAPID array moorings are also displayed (from McCarthy et al. (2017b)).

The observational data used in this thesis is currently the longest-running basin-wide estimation of the AMOC from the RAPID-MOCHA-WBTS mooring array (hereafter, RAPID) at 26.5° N since 2004 (Cunningham et al., 2007; Kanzow et al., 2010). The design of the array (Figure 1.7) is based on capturing the meridional flow through the geostrophic relationship along the zonal direction (as outlined in section 1.2.4), as well as the flow going through the Straits of Florida (i.e. the Gulf Stream), and Ekman transport (McCarthy et al., 2015a). Full-depth temperature and salinity is measured on the eastern and western boundaries as well as on either side of the Mid-Atlantic Ridge (Rayner and Kanzow, 2011) to provide the vertical shear of geostrophic velocities via the thermal wind balance.

At 26.5° N, RAPID approximates the streamfunction as a combination of the three components outlined above:

$$\tilde{\psi}_{26.5N}(t,z) = \int_{-H}^{Z_0} \{\psi_{fs}(t,z) + \psi_{ek}(t,z) + \psi_{umo}(t,z)\} dz, \tag{1.5}$$

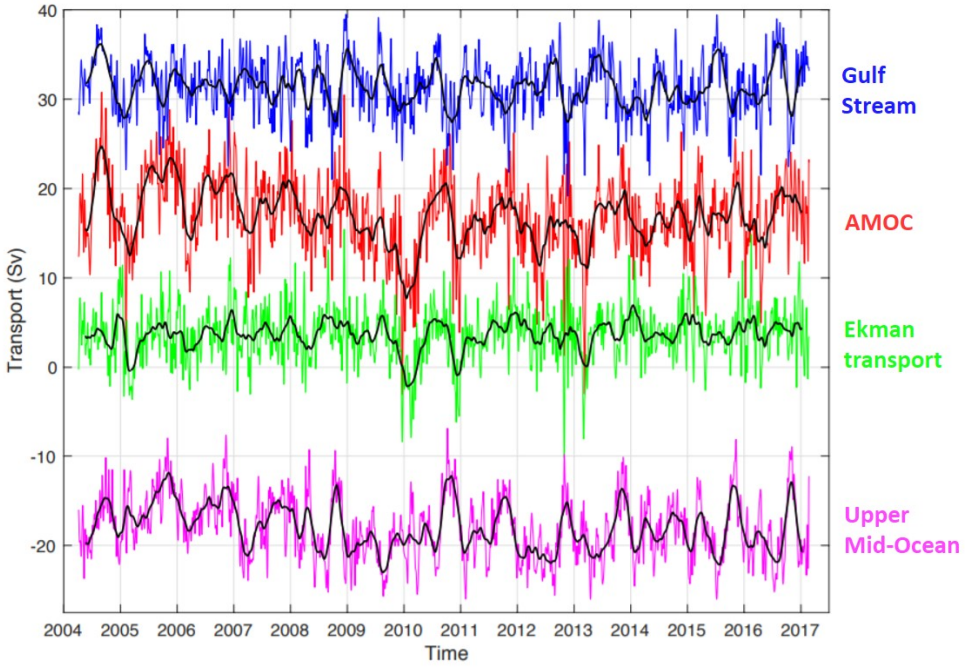

FIGURE 1.8: The components of the AMOC transport in Sverdrups measured by the RAPID array at 26.5° N. The Florida Current or Gulf Stream (blue), Ekman transport (green) and Upper Mid-Ocean (magenta). The sum of all components is the AMOC (red). The black lines show 90-day filtered data and the coloured lines 10-day filtered data (modified after Smeed et al. (2018)).

where, fs is Florida Straits, ek is Ekman transport, and umo is the Upper Mid-Ocean (UMO) (McCarthy et al., 2015a); the time series since 2004 are shown in Figure 1.8. The Florida Straits (Gulf Stream) is inferred from submarine telephone cable voltage measurements crossing the Straits of Florida (Larsen and Sanford, 2014; Shoosmith et al., 2005), and the wind-driven Ekman transport is derived from winds of the ERA-Interim reanalysis product (McCarthy et al., 2015a). The UMO is composed of the interior geostrophic transport between the Bahamas and the African coast, the western boundary wedge calculated from direct current meters on separate moorings extending out to 22 km offshore (Johns et al., 2008), and the external transport or barotropic depth-averaged flow. The latter is added uniformly at each depth and longitude as a residual mass compensation term to ensure zero net meridional flow (McCarthy et al. (2015a) provides in-depth RAPID calculation details).

Although RAPID provides direct estimates of the AMOC, one must be cautious of sampling errors and biases, outlined as three principal factors in Sinha et al. (2018). Firstly, estimating the geostrophic flow requires the knowledge of an absolute velocity for the reference level, which has been addressed by assuming a level of no motion at 4,820 m (Bryden et al., 2005; Johns et al., 2005). Choice of reference levels can lead to incoherence of transport tendencies compared to other latitudes (e.g., MOVE at 16° N, shown by Frajka-Williams et al. (2018)), and errors on the order of ±3 Sv at 26° N,

which mainly affect the variability in the upper 2,000 m. Secondly, regions not sampled by the array can affect transport below 3,000 m, and lastly the ageostrophic transport estimation mainly impacts transport above 1,000 m (but has very little variability) (Sinha et al., 2018). These factors could influence the mean AMOC (of 17.0 ±4.4 Sv from 2004 to 2017), which they suggest is underestimated using the RAPID method by ∼1.5 Sv at ∼900 m but the variability is highly accurate (Frajka-Williams et al., 2019; Sinha et al., 2018). Furthermore, mooring arrays are limited in time and space and make use of integrated estimations, therefore direct three-dimensional basin-wide records are not available, and low-frequency variability or trends are not yet fully understood from current observations.

1.3.4 The 2009-2010 'extreme' AMOC event

Focusing on one particular interannual feature of the RAPID time series, a 30% reduction in transport to 12.8 Sv from early 2009 to mid-2010 was observed (McCarthy et al., 2012; Bryden et al., 2014). Although the original cause is still under dispute, studies suggest both atmospheric forcing (an anomalous wind event), and a strengthening of the geostrophic southward flow above 1,100 m due to deepening of the western boundary thermocline (McCarthy et al., 2012; Roberts et al., 2013). Records link a change in east-west density gradient lagging Labrador Sea density decrease which can spread southward along the western boundary (Robson et al., 2014). This extreme event and heat transport anomaly brought on a −1.3°C daily mean temperature anomaly from December 2009 to February 2010 (although this did not seem extreme relative to the previous six decades of winters) (Cattiaux et al., 2010). A sea level increase of approximately 10 cm was recorded in New York within 2009-2010, probably related to the weakening of the geostrophic component (Goddard et al., 2015). Furthermore, the late 2010 SST anomaly pattern potentially shifted the atmospheric circulation into a negative NAO. Due to the shortness of the observational record and AMOC variability, it is still unclear whether such an event is just a one-off feature, or part of short-term natural fluctuations (Bryden et al., 2014; Ezer, 2015; Cattiaux et al., 2010; Roberts et al., 2014; Frajka-Williams, 2015).

1.4 AMOC variability and decline inferred from CMIP5 models

As opposed to the geographical and temporal constraints of observations mentioned above, numerical models have a strong advantage in providing a global, three-dimensional estimation of transport over longer periods of time. This study uses the CMIP5 ensemble from the Fifth Assessment Report (AR5) used in the Intergovernmental Panel on Climate Change (IPCC) Working Group I (Stocker et al., 2013). Despite the value in using numerical models, however, a caveat is the large fluctuations and uncertainty

in the AMOC mean strength, trend and variability across the CMIP5 models. Their average ensemble maximum streamfunction at 26° N is ∼19 Sv, ranging from 12.1 to 29.7 Sv (Reintges et al., 2017). This large intermodel spread could partially explain the AR5 report's statement of their 'medium' confidence in estimating the AMOC's mean strength (Flato et al., 2013).

Comparing the CMIP5 ensemble's variability with that found in RAPID, it seems to be underestimated on interannual (McCarthy et al., 2012; Roberts et al., 2014) and decadal timescales (Park et al., 2016). Multi-decadal timescales are also under-represented when compared to inferred subsurface temperature, as a proxy for a longer AMOC time series (Yan et al., 2018). Focusing on an individual model, some characteristics might be well represented, though. For example, Kim et al. (2018) show that interannual and decadal variability in CESM1-CAM5 are similar to observations, but once again, multi-decadal variability, using the NAO as a proxy, is substantially weaker. Roberts et al. (2014), however, show that the magnitude of observed interannual events (for example, the 2009-2010 annual decrease of ∼5 Sv) is not seen in the CMIP5 control simulations. From spectral analyses and examining potential links of the AMOC to the 20-year periodicity of the AMV, the CMIP5 models do seem to generally exhibit multi-decadal periodicity at 15-35 years (Zhang, 2008; Msadek et al., 2010; Muir and Fedorov, 2017).

Ongoing studies (including this thesis) aim to overcome the challenges around comparing trends of different timescales using observations (one decade) and numerical models (several centuries of simulated data). Over the same time period as RAPID, a study shows that the CMIP5 multiple model mean (regarded as an external forced response), does not show a significant AMOC declining trend between 2004 and 2015 (Yan et al., 2018). The interannual trend found from 2007 to 2015 in RAPID of 0.6 Sv yr^{-1} is an order of magnitude larger than the predictions of a decline ranging from 0 and 0.9 Sv per decade in CMIP5 under a 'business-as-usual' future scenario (Roberts et al., 2014; Smeed et al., 2018), although as they mention this is most likely due to underestimating internal variability or other limitations outlined below.

The broad range of AMOC behaviour among the models could be due to the diversity of principal driving mechanisms over different timescales (Muir and Fedorov, 2017). Failure to resolve the interannual variability could stem from overestimating wind-driven variability (Msadek et al., 2013), or lacking atmospheric variability (Roberts et al., 2014). Furthermore, ocean heat uptake is generally overestimated and SST increase underestimated due to weak stratification (Kuhlbrodt and Gregory, 2012; Kostov et al., 2014), which can affect the AMOC via buoyancy forcing. Decadal behaviour could be inconsistent among the models due to differences in autocorrelation (short-term memory) (Roberts et al., 2014) or salinity biases (Park et al., 2016). Furthermore, lack of decadal variability in wind forcing in CMIP5 (Yan et al., 2018) can lead to multi-decadal under-estimation of mid-ocean variability (Baehr et al., 2009). The CMIP5 models also largely neglect the Greenland ice sheet mass loss, which would reduce Labrador Sea

convection, thereby further weakening the AMOC (Bakker et al., 2016; Böning et al., 2016). Lastly, aerosol emissions and volcanic activity could be poorly captured by the models, which can explain up to 80% of local multi-decadal SST, AMV and therefore AMOC variability (Booth et al., 2012). However, for future projections, it is impossible to say when and where volcanic eruptions or aerosol emissions will take place.

Other challenges arise from the design of the models. The relatively coarse resolution of the CMIP5 models, of up to 2° (Taylor et al., 2012), results in features such as the Florida Straits, and smaller-scale processes governing meso-scale turbulence, such as mixing and diffusion not being resolved (Hodson and Sutton, 2012; van Sebille et al., 2018). For example, the resolution of eddies would be able to represent the Agulhas leakage, which can influence AMOC decadal variability (Biastoch et al., 2008b). Another limitation (potentially the key limitation) is the computational cost that currently makes reproducing abrupt climate events and thresholds impossible, such as past collapses and abrupt strengthening of the AMOC during the last glacial period (Alley et al., 2003; Valdes, 2011). Lastly, the CMIP5 models are biased toward a monostable regime, meaning that almost all models recover from a freshwater flux hosing experiment and a stable 'off' state of the AMOC is not sustained (Drijfhout et al., 2011), although it is still unclear if the current AMOC state is mono-stable or not.

This thesis examines whether, despite the shortcomings mentioned above, both observations and numerical model timeseries data can be used in conjunction to provide useful insight regarding the AMOC's trend and variability.

1.5 Thesis outline

The focus of this thesis is to investigate the interannual to multi-decadal trends and variability of the Atlantic Meridional Overturning Circulation from 1850 to 2100. The observations and numerical models used, as well as an outline of the linear regression methods and statistical techniques, is presented in Chapter 2. The estimation of the number of years required to detect a significant AMOC decline is then studied in Chapter 3. This chapter is adapted from a manuscript currently under revision for Geophysical Research Letters, hence there could be some overlap with introductory sections in other chapters. In Chapter 4, the relationship between sea-surface height and the AMOC is examined with the aims to reconstruct a proxy of a multi-decadal AMOC in the past. Chapter 5 displays results from a probability analysis of an AMOC decline over 250 years, which are used to identify salinity fluxes as an indicator of AMOC changes over high-probability decline periods. The final closing conclusions are outlined in Chapter 6.

Chapter 2

General Data and Methods

This research is based on a trend analysis of the North Atlantic Meridional Overturning Circulation. The timeseries data are obtained from both observations and numerical models, for a complementary study of direct, in-situ estimates from the RAPID array (from 2004 to 2017) and simulated data from the Coupled Model Intercomparison Project, CMIP5 (from 1850 to 2100). The length of the data available dictates the timescale over which the trends can be investigated, from interannual (for RAPID) to multi-decadal (for CMIP5). The relative shortness of current observations serves as motivation for using model output data in all three analyses; to determine how many years are required to detect an AMOC trend (Chapter 3), and whether sea surface height or salinity transports can be used as indicators of longer-term AMOC variability and trends (Chapters 4 and 5, respectively).

2.1 Data

2.1.1 RAPID Observations

The AMOC observations (used in Chapters 3 and 4) are acquired from the RAPID-MOCHA-WBTS mooring array (RAPID Climate Change- Meridional Overturning Circulation and Heatflux Array- Western Boundary Time Series), hereafter, RAPID. Continuous data have been collected at 26.5° N (from Tenerife to the Bahamas) every 12 hours since 2004, made publicly available (on http://www.rapid.ac.uk/rapidmoc) every 18 months, after mooring data retrieval from cruise expeditions (Cunningham et al., 2007; McCarthy et al., 2015a; Smeed et al., 2014).

The RAPID methodology estimates a depth-resolved, zonally-averaged AMOC at 26.5° N (a detailed description can be found in McCarthy et al. (2015a)). It is derived using the combination of three components: 1) the Upper Mid-Ocean geostrophic flow between

the Bahamas and Africa, via density differences using tall moorings, 2) the surface wind-driven Ekman transport, via reanalysis satellite data, and 3) the Gulf Stream flow, via submarine-cable-based measurements. The transport is then represented in units of Sverdrups ($1\,\text{Sverdrup} = 10^6\,\text{m}^3\,\text{s}^{-1}$) as the AMOC streamfunction, ψ (see Equation 1.3). For the AMOC transport timeseries at 26.5° N, the maximum streamfunction depth (z_{max}) is used (see Equation 1.4 in Section 1.3). Throughout this study, time (t) is in units of years, after computing annual averages over 13 years (from 2004 to 2017).

2.1.2 Coupled Model Intercomparison Project Phase 5 (CMIP5)

CMIP5 is the fifth phase of an international collaboration of 20 climate modelling groups that design global ocean-atmosphere general circulation models. Data from their Assessment Report (AR5) (Taylor et al., 2012), is available from the Earth System Grid-Center for Enabling Technologies; http://pcmdi9.llnl.gov/ (Williams et al., 2011).

The control simulations are time-independent and use pre-industrial atmospheric greenhouse gas (GHG) concentrations. The historical simulations run from 1850 to 2005 (inclusive), using post-industrial concentrations and the future scenarios focus on anthropogenic emissions and assume there will be no drastic changes in natural variability (such as major volcanic eruptions or secular changes in solar forcing). Future Representative Concentration Pathways (RCPs) produce a wide range of possible future GHG concentration/radiative forcing trajectories available. The two future scenarios selected for this work are RCP4.5 (a stabilisation scenario) and RCP8.5 (a 'business-as-usual') scenario. The latter is defined by emissions continuing to increase at the same rate as in 2006, i.e., the highest radiative forcing scenario available. The total radiative forcing in year 2100 relative to 1750 is $4.5\,\text{W}\,\text{m}^{-2}$ in RCP4.5, and $8.5\,\text{W}\,\text{m}^{-2}$ in RCP8.5. This equates to most CMIP5 models reaching 538 ppm (parts per million) CO_2 concentrations in RCP4.5, and 936 ppm in RCP8.5 by 2100 (Stocker et al., 2013). Several models have different ensembles, however this work uses the first ensemble member of each model, namely from the r1i1p1 series (which specifies the realisation, initial conditions, and physical parameter constants).

A total of 21 CMIP5 models are used (Table 2.1). No more than one model per institute is randomly chosen (to reduce model bias), and the selection for specific chapters' analyses depends on data availability. When extracting the AMOC data, the streamfunction at the closest latitude to 26.5° N and 1,000 m (the approximate depth of maximum streamfunction) is computed (Equation 1.4). Other output data obtained includes sea surface height for Chapter 4, and salinity and potential temperature for Chapter 5. Each institute uses a different model grid configuration, therefore, ensemble mean estimates are computed after regridding each model to the coarsest horizontal resolution, 2x2°, by finding the nearest neighbour (i.e., the closest even coordinates to the original grid).

TABLE 2.1: The CMIP5 models selected for the three chapters of analysis in this thesis. The model names, institutes (that designed the models), and the location of the institutes are shown.

Model Name	**Institute Name**	**Country**	**Used in Chapters:**
ACCESS1-0	Commonwealth Scientific and Industrial Research Organisation/Bureau of Meteorology	Australia	3, 4, 5
bcc-csm1-1	Beijing Climate Center	China	3, 4, 5
BNU-ESM	College of Global Change and Earth System Science, Beijing Normal University	China	3, 5
CanESM2	Canadian Centre for Climate Modelling and Analysis	Canada	3, 4, 5
CCSM4	National Center for Atmospheric Research	USA	3, 4, 5
CESM1-BGC	National Science Foundation-DOE-National Center for Atmospheric Research	USA	3, 4, 5
CMCC-CM	Centro Euro-Mediterraneo sui Cambiamenti Climatici	Italy	3, 4, 5
CNRM-CM5	Centre National de Recherches Météorologiques (CNRM-CERFACS)	France	3, 4, 5
CSIRO-Mk3-6-0	Commonwealth Scientific and Industrial Research Organisation	Australia	3, 4, 5
EC-EARTH	EC-EARTH Consortium published at Irish Centre for High-End Computing	Netherlands/ Ireland	3, 4, 5
FGOALS-g2	Institute of Atmospheric Physics, Chinese Academy of Sciences (LSAG-CESS)	China	4
FIO-ESM	The First Institute of Oceanography (SOA)	China	3, 4
GFDL-CM3	Geophysical Fluid Dynamics Laboratory	USA	3, 4
GISS-E2-R-CC	NASA Goddard Institute for Space Studies (NASA-GISS)	USA	3, 4, 5
HadGEM2-CC	Met Office Hadley Centre (MOHC)	UK	3, 4, 5
inmcm4	Russian Academy of Sciences, Institute of Numerical Mathematics (INM)	Russia	3, 4
IPSL-CM5A-MR	Institut Pierre Simon Laplace (IPSL)	France	3, 4, 5
MIROC-ESM	Atmosphere and Ocean Research Institute (The University of Tokyo), National Institute for Environmental Studies, and Japan Agency for Marine-Earth Science and Technology (MIROC)	Japan	3, 4
MPI-ESM-LR	Max Planck Institute for Meteorology (MPI-M)	Germany	3, 5
MRI-CGCM3	Meteorological Research Institute (MRI)	Japan	3, 4, 5
NorESM1-M	Bjerknes Centre for Climate Research, Norwegian Meteorological Institute (NCC)	Norway	3, 4, 5

2.2 Methods

2.2.1 Linear trend analysis techniques

Throughout the thesis, the term 'trend' refers to a coefficient or slope from the linear, straight line, first-order polynomial degree regression model. The equations in this section are displayed in matrix notation (in **bold**), as well as standard notation (in brackets). Different linear trend-fitting techniques are used, depending on the analyses in each chapter. Chapter 3 compares results from Ordinary Least Squares (OLS) and Generalised Least Squares (GLS), Chapter 4 uses OLS and Partial Least Squares (PLS), and Chapter 5 uses OLS only. A description of each technique, and justification for using them is outlined below.

2.2.1.1 Ordinary Least Squares (OLS)

The method of least squares dates back to 1795, with Carl Gauss (Stigler, 1981). The linear ordinary least squares model equation takes the form:

$$\mathbf{Y} = \beta\mathbf{X} + \mathbf{e}; \qquad (Y_t = \beta X_t + \epsilon_t), \tag{2.1}$$

where, $\mathbf{Y} = (Y_1, ...Y_n)'$ is the vector of the dependent variable, or observations (AMOC transport), $\mathbf{X} = (X_1, ..., X_n)$ is the vector of the independent variable (time) at $(t_1, ..., t_n)$ years, β is the magnitude of the trend, and $\mathbf{e} = (\epsilon_1, ..., \epsilon_n)'$ is the vector of residuals (here, the constant term, or intercept has been omitted).

In order to estimate the OLS linear trend of a timeseries, $\hat{\beta}$, the standard approach (which is also used in the `MATLAB` function, `polyfit` or `fitlm`, utilised in this thesis), is to find the best fit in the least squares sense (Brockwell and Davis, 2002; Sen and Srivastava, 2012). In general, a model fits the data well if the differences between the model's predicted values and the observed values are small. Those that minimise the sum of squared residuals ($\boldsymbol{\mathcal{SS}}$), therefore take the form:

$$\boldsymbol{\mathcal{SS}} = \mathbf{e'e} = (\mathbf{Y} - \mathbf{X}\hat{\beta})'(\mathbf{Y} - \mathbf{X}\hat{\beta}) \qquad \left(\mathcal{SS} = \sum_{t=1}^{n} \epsilon_t^2 = \sum_{t=1}^{n} (Y_t - \hat{\beta}X_t)^2\right). \tag{2.2}$$

After computing the partial derivative of $\mathcal{SS}$ with respect to $\hat{\beta}$ and equating it to zero, the normal equations are yielded:

$$\mathbf{X'X}\hat{\beta} = \mathbf{X'Y} \qquad \left(\hat{\beta}\sum_{t=1}^{n} x_t^2 = \sum_{t=1}^{n} X_t Y_t\right), \tag{2.3}$$

and solving for $\hat{\beta}$ if $\mathbf{X'X}$ is non-singular (or of full rank, for a square matrix) leads to:

$$\hat{\beta} = (\mathbf{X'X})^{-1}\mathbf{X'Y}; \qquad \left(\hat{\beta} = \frac{\sum_{t=1}^{n}(X_t - \bar{X})(Y_t - \bar{Y})}{\sum_{t=1}^{n}(X_t - \bar{X})^2} \right), \tag{2.4}$$

where the overbar represents the mean of the X or Y vectors.

By outlining the OLS assumptions (Brockwell and Davis, 2002), one can verify whether OLS is the appropriate least squares regression to use:

1. The errors or residuals, $\mathbf{e}$, are independent and identically distributed (iid), therefore indicative of white noise (with a mean of 0).

2. The errors are spherical, meaning they are (a) uncorrelated and (b) have a constant variance, as stated in the Gauss-Markov theorem. Under these conditions, the mean function of $\mathbf{Y}$ is expected to be: $\mathrm{E}(\mathbf{Y}) = \mathbf{X}\beta$ (Rao, 1973). The tests for these assumptions are outlined in Section 2.2.2.1 (the Durbin-Watson test for autocorrelation), and Section 2.2.2.2 (the Engle-ARCH test for heteroscedasiticty, or a non-constant variance). Upon violation of either of these assumptions (which is the case in Chapter 3), Generalised Least Squares is used (see Section 2.2.1.2).

3. $n \geq k$ when OLS is used for a multiple linear regression (MLR), where k is the number of predictor variables. For one of the analyses in Chapter 4, k is 2 (east and west SSH regressed against the AMOC) and therefore OLS is correctly used. In another analysis of Chapter 4, however, this assumption is violated when the maximum n is 94 years and k is 635 (grid points of the full North Atlantic SSH), therefore Partial Least Squares (PLS) must be used (see Section 2.2.1.4).

4. There is no collinearity between the predictors (for the MLR). PLS should be used when this assumption is violated (as is the case for Chapter 4).

This work follows the concept of parsimony, meaning that the simplest regression model is fit to a timeseries, and complexity is only increased when required. With OLS being the simplest approach for estimating a regression coefficient, it is the first technique used in Chapter 3 to detect the AMOC trend. Upon discovering short-term memory (autocorrelation) within the CMIP5 timeseries, violation of certain OLS assumptions lead to the need for a different technique, namely GLS, described below. Some of the analyses in Chapter 4 also use OLS for the regression between the AMOC and SSH, since the residual analysis does not reveal autocorrelated noise.

2.2.1.2 Generalised Least Squares (GLS)

First described by Alexander Aitken (Aitken, 1934), GLS is an adapted method of the linear regression model, OLS (Equation 2.1). This technique is used to analyse data with non-spherical errors, hence a timeseries that does not follow the OLS assumption regarding the Gauss-Markov theorem (assumption (2) in Section 2.2.1.1). Previous studies have shown the applicability of GLS to environmental data (for example, Tiao et al. (1990); Weatherhead et al. (1998); Beaulieu et al. (2013)).

Focusing first on the presence of autocorrelation, Chapter 3 presents results showing that the residuals of the 94-year CMIP5 RCP8.5 data exhibit significant lag-1 autocorrelation in over half of the models. Lag-1 autocorrelation or AR(1) is short-term memory between successive yearly data, therefore the correlation between one year and the next. The regression model for GLS is:

$$\mathbf{Y} = \beta\mathbf{X} + \mathbf{N}; \qquad (Y_t = \beta X_t + N_t), \tag{2.5}$$

where the error term in OLS (ϵ_t or $\mathbf{e}$) has been replaced by N_t or $\mathbf{N}$. These residuals now comprise of the white noise term ϵ_t plus a first-order autocorrelation term:

$$N_t = \phi N_{t-1} + \epsilon_t, \tag{2.6}$$

where ϕ is the AR(1) coefficient (note that the lag term, ϕN_{t-1}, can be used interchangeably with ϕY_{t-1}, as in Equation 2.14) (Tiao et al., 1990). In Chapter 3, the `R` package `nlme` is used to estimate the GLS trend ($\hat{\beta}_{GLS}$) and its associated AR(1) coefficient (Pinheiro and Bates, 2000).

An AR(1) process is used to characterise short-term memory in a climate system, with its autocorrelation function decaying exponentially with lags (lag in years, in this case). It should be noted that the autocorrelation function is sometimes misused and the decorrelation time is only interpretable when dealing with red noise, meaning that higher order AR is not indicative of physical processes or characteristics in the ocean (Von Storch, 1999). To explore the long-term memory in a time series, the Hurst exponent using a power law process is a more pertinent measure, which has an autocovariance that decays algebraically with lags. Vyushin et al. (2012) examine the memory or persistence in internal interannual to multi-decadal climate variability using a few decades of CMIP3 surface atmospheric temperature data to show that the climate persistence lies between the AR(1) and the power law representations. If this thesis were to examine long-term memory, the power law approach would therefore be a useful tool. Since most of the AMOC timeseries data used in this work only exhibit a significant AR(1) coefficient, as mentioned above, and periodic cycles are outside the scope of this thesis, the focus lies on the short-term memory of the AMOC, hence the AR(1) process.

GLS is also used when the variance of the errors, Cov(**e**), is not uniform through time (i.e., it exhibits heteroscedasticity). In this thesis, the AMOC data are shown to be homoscedastic, therefore this next section is simply an overview for completion (but the variance is not included as an input variable when estimating the GLS trend in Chapter 3). A detailed description can be found in Draper and Smith (1998) or Kariya and Kurata (2004).

For OLS, the expected variance-covariance matrix is symmetric and diagonal, $\text{Cov}(\mathbf{e})_{OLS} = \text{diag}(\hat{\sigma}_1^2, ..., \hat{\sigma}_n^2)$ (Orsini et al., 2006). It is simplified to a scalar multiplied by an identity matrix, as follows:

$$\text{Cov}(\mathbf{e})_{OLS} = E(\mathbf{ee'}) = \mathbf{I}\sigma^2, \tag{2.7}$$

where σ^2 is the scalar variance, since it is the same value for of each observation's error, and $\mathbf{I}$ is the identity matrix, $(\mathbf{X'X})^{-1}$. In GLS, the covariance matrix is not diagonal and is denoted by Ω:

$$\text{Cov}(\mathbf{e})_{GLS} = \Omega, \tag{2.8}$$

where the covariance matrix can either be known or unknown. If it is unknown it can be estimated, $\hat{\Omega}$, via the feasible generalised least squares.

In order to estimate the linear regression coefficients, the covariance matrix must be incorporated into the previous OLS estimation (Equation 2.4), as follows:

$$\hat{\beta}_{GLS} = \mathbf{(X'\Omega^{-1}X)^{-1}X'\Omega^{-1}Y}, \tag{2.9}$$

which can then be applied to the sum of squared residuals as in Equation 2.2 as follows:

$$(\mathbf{Y^*} - \mathbf{X^*}\hat{\beta}_{GLS})'(\mathbf{Y^*} - \mathbf{X^*}\hat{\beta}_{GLS}) = (\mathbf{Y} - \mathbf{X}\hat{\beta}_{GLS})'\Omega^{-1}(\mathbf{Y} - \mathbf{X}\hat{\beta}_{GLS}). \tag{2.10}$$

where the stars denote the linearly transformed version of the data. This is achieved by the covariance matrix having the effect of scaling the errors and hence 'decorrelating' them.

For the trend detection analysis in Chapter 3, after using standard regression approaches for data with and without autocorrelation (GLS and OLS, respectively), the analysis then considers further model complexity, i.e., whether the signal could be different to a simple linear trend. Furthermore, the analysis includes detecting whether there are points in the RAPID and CMIP5 AMOC timeseries where a sudden change occurs (a changepoint). This is motivated by the results in Smeed et al. (2018) showing that the RAPID data appears to have a changepoint in 2008-2009, with a constant mean prior and post-changepoint.

2.2.1.3 Changepoint Analysis

The detection of trends or other signals in environmental data can be hindered by internal variability, such as short- or long-term memory, in the climate system. A flexible approach for selecting the best model to fit to such a timeseries is developed by Beaulieu and Killick (2018), where combinations of a trend or constant mean superimposed to noise with or without memory are used to identify whether there are changepoints in the timeseries. A changepoint is considered as a data point that separates segments of data that have different statistical properties (Haynes et al., 2017). In Chapter 3, this technique is applied to the RAPID and CMIP5 data to verify whether the observations exhibit a changepoint and if the CMIP5 'business-as-usual' data show a steady linear trend plus AR(1) model fit.

The changepoint analysis is implemented using the `R` package, `EnvCpt`. It is developed such that a series of models are fit to the timeseries and the most appropriate model is selected according to lowest log likelihood from three information criteria, (1) the Akaike information criterion (AIC), (2) the Bayesian information criterion (BIC) and (3) the corrected AIC (AICc). The information criteria are based on the log-likelihood penalised by the number of parameters fitted. Eight changepoint models are tested on the CMIP5 data, which include:

(1) Mean: a constant mean and variance,

$$Y_t = \mu + \epsilon_t, \tag{2.11}$$

where μ (the mean), and ϵ_t are normally distributed with a mean of zero and variance σ^2;

(2) Mean + AR(1): a constant mean with AR(1) errors,

$$Y_t = \mu + \phi Y_{t-1} + \epsilon_t, \tag{2.12}$$

(3) Trend: a linear trend over time,

$$Y_t = \beta X_t + \lambda + \epsilon_t, \tag{2.13}$$

where λ is the intercept, or constant term;

(4) Trend + AR(1): a linear trend over time with AR(1) errors,

$$Y_t = \beta X_t + \lambda + \phi Y_{t-1} + \epsilon_t, \tag{2.14}$$

(5) Mean cpt: multiple changepoints in the mean

$$Y_t = \begin{cases} \mu_1 + \epsilon_t, & t \leq c_1 \\ \mu_2 + \epsilon_t, & c_1 < t \leq c_2 \\ \vdots & \vdots \\ \mu_m + \epsilon_t, & c_{m-1} < t \leq n \end{cases}, \tag{2.15}$$

where the timeseries is split into m segments with means of $\mu_1, ..., \mu_m$, and variances $\sigma_1^2, ..., \sigma_m^2$. The timing of the changepoints between each segment is $c_1, ..., c_{m-1}$;

(6) Mean cpt + AR(1): multiple changepoints in the mean with AR(1) errors,

$$Y_t = \begin{cases} \mu_1 + \phi_1 Y_{t-1} + \epsilon_t, & t \leq c_1 \\ \mu_2 + \phi_2 Y_{t-1} + \epsilon_t, & c_1 < t \leq c_2 \\ \vdots & \vdots \\ \mu_m + \phi_m Y_{t-1} + \epsilon_t, & c_{m-1} < t \leq n \end{cases}, \tag{2.16}$$

where the AR(1) coefficient in each segment is $\phi_1, ..., \phi_m$;

(7) Trend cpt: a trend with multiple changepoints in the regression parameters

$$Y_t = \begin{cases} \beta_1 X_t + \lambda_1 + \epsilon_t, & t \leq c_1 \\ \beta_2 X_t + \lambda_2 + \epsilon_t, & c_1 < t \leq c_2 \\ \vdots & \vdots \\ \beta_m X_t + \lambda_m + \epsilon_t, & c_{m-1} < t \leq n \end{cases}, \tag{2.17}$$

where $\beta_1, ..., \beta_m$ and $\lambda_1, ..., \lambda_m$ are the trend and intercept of each segment, respectively;

(8) Trend cpt + AR(1): a piecewise linear trend over time with AR(1) errors,

$$Y_t = \begin{cases} \beta_1 X_t + \lambda_1 + \phi_1 Y_{t-1} + \epsilon_t, & t \leq c_1 \\ \beta_2 X_t + \lambda_2 + \phi_2 Y_{t-1} + \epsilon_t, & c_1 < t \leq c_2 \\ \vdots & \vdots \\ \beta_m X_t + \lambda_m + \phi_m Y_{t-1} + \epsilon_t, & c_{m-1} < t \leq n \end{cases}. \tag{2.18}$$

Further details on the algorithm and information criteria can be found in Beaulieu and Killick (2018). Although the AMOC could exhibit potential nonlinearities (Buckley and Marshall, 2016), Chapter 3 demonstrates that a multi-decadal linear trend fit is suitable for almost all the CMIP5 timeseries, hence fitting a non-linear trend regression is outside the scope of this work. The final linear model used in this thesis aims to decompose the signal using explanatory variables. This is done using numerous components generated from an MLR, with SSH as a proxy in Chapter 4. The regression models outlined so

far have used independent predictors, whereas PLS now takes into account collinearity of covariables.

2.2.1.4 Partial Least Squares (PLS)

PLS, originally developed by Herman Wold (Wold, 1982), has become a standard tool in chemometrics and suitable for large datasets often found in chemistry and engineering. Modelling a response ($\mathbf{Y}$) from several predictors ($\mathbf{X}$) is done using PLS instead of an OLS MLR in the presence of correlation or collinearity between the regression input variables (Wold et al., 2001). The biased technique constructs new predictors, called components, that are linear combinations of the original predictors. This is a similar approach to the Ridge regression and principal component analysis (PCA) (hence, these methods are collectively classified as the continuum regressions (Rosipal and Krämer, 2006)). One main difference when comparing PLS to the other techniques is the generation of the components while considering the response values, which is not the case for PCA, for example (Geladi and Kowalski, 1986; de Jong, 1993). PLS can also be used to regress numerous predictors onto numerous response variables (therefore, both a multiple linear regression and multivariate regression, respectively), however in this thesis (in Chapter 4), only PLS1 is used. This means that one response variable is used ($\mathbf{Y}$), namely the AMOC transport, and numerous predictor variables ($\mathbf{X}$), namely the full North Atlantic grid of sea surface height. Since the SSH predictors are the same variable and only 2 degrees apart, they are collinear, hence the applicability of PLS.

A standard MLR model can be expressed as:

$$Y_t = \beta_1 X_{t1} + \beta_2 X_{t2} + ... + \beta_k X_{tk} + \epsilon_t, \tag{2.19}$$

or

$$\mathbf{Y} = \mathbf{bX} + \mathbf{e}; \qquad \left(Y_t = \sum_{j=1}^{k} \beta_j X_{tj} + \epsilon_t \right) \tag{2.20}$$

where k is the total number of predictor or explanatory variables, such that the set of predictors are $X_{t1}, ..., X_{tk}$ or $\mathbf{X}$. $\beta_1, ..., \beta_k$ or $\mathbf{b}$ are the linear coefficients for each of the X predictors. For example, in Chapter 4, the predictor variables are defined by 635 North Atlantic 2x2° grids ($k = 635$) of SSH ($\mathbf{X}$) with a varying total sample size (n) for the regression training period of the model, depending on the analysis.

Prior to the PLS analysis, the $\mathbf{X}$ and $\mathbf{Y}$ variables are transformed in order to be centred, via subtracting the mean of each variable separately (Wold et al., 2001). Next, the predictor data is compressed into a set of a 'few' (A in number) new orthogonal variables which are estimates of X, called X-scores (or components). The X-scores are represented

by U_a (a = 1,2,...,A), where $A \leq k$ (e.g., in Chapter 4, A = 10 components are used):

$$\mathbf{U} = \mathbf{XW}; \qquad \left(U_{ta} = \sum_{j=1}^{k} W_{ja} X_{tj} \right). \tag{2.21}$$

The components, **U**, are estimated from a linear combination of the original **X** variables and a 'weight' term, **W**. The weights correspond to the first pair of left and right singular vectors obtained from a singular vector decomposition (see de Jong (1993) for a more detailed description of SVD). The residual term, **e**, is then estimated via:

$$\mathbf{X} = \mathbf{UP'} + \mathbf{e}; \qquad \left(X_{ta} = \sum_{a=1}^{A} U_{ta} P_{aj} + e_{tj} \right), \tag{2.22}$$

where **P** is the orthogonal 'loading' term, which describes the strength of the relationship between the original X variables and the X-score (de Jong, 1993). These loadings are therefore good summaries of **X** and are defined in order for the residuals, **e**, to be as small as possible. Since in this case **Y** is univariate, then a = 1 for the Y-score component (V_1), and the weight term (Q_1):

$$\mathbf{Y} = \mathbf{VQ'} + \mathbf{G}; \qquad \left(Y_{t1} = \sum_{a=1}^{1} V_{t1} Q_1 + g_{t1} \right), \tag{2.23}$$

where, the multiplication of the Y-score (**V**) and weight (**Q**) are such that the residuals of y (**G**), are as small as possible. Note that this is a key difference between PCA and PLS (PCA does not estimate Y-scores). Going back to the X-scores, since they are good predictors of **Y**, they can now be substituted here:

$$\mathbf{Y} = \mathbf{UQ'} + \mathbf{F}; \qquad \left(Y_{t1} = \sum_{a=1}^{1} Q_1 U_{t1} + f_{t1} \right), \tag{2.24}$$

where the Y-residuals are now expressed as **F** and represent the deviations between the observed and modelled responses. The combined equations (2.21 and 2.24) can be rewritten as a multiple regression model in order to define the regression coefficients:

$$\mathbf{Y} = \mathbf{XWQ'} + \mathbf{F} = \mathbf{XB} + \mathbf{F}; \qquad \left(Y_{t1} Q_1 \sum_{j=1}^{k} W_{ja} X_{tj} + f_{t1} = \sum_{j=1}^{k} b_{1j} + X_{tj} + f_{t1} \right). \tag{2.25}$$

Hence, the PLS regression coefficients, **b**, are defined as:

$$\mathbf{b} = \mathbf{WQ'}; \qquad \left(b_j = \sum_{a=1}^{A} Q_1 W_{ja} \right). \tag{2.26}$$

For further details regarding the algorithm behind the PLS regression method, see Wold

et al. (2001) or de Jong (1993). The algorithm used in Chapter 4 (`plsregress` in MATLAB) is based on SIMPLS, which is an adaptation and simplification of the standard PLS (outlined in de Jong (1993)), however, for a univariate multiple linear regression (PLS1), as is the case here, SIMPLS and PLS1 are identical.

2.2.2 Residual analyses

Once the residuals are defined from the linear regressions described above, the following tests can determine whether the residuals are autocorrelated and if their variances are not constant through time.

2.2.2.1 The Durbin-Watson test

The Durbin-Watson (D-W) test (Durbin and Watson, 1950) is used to determine whether the residuals of a timeseries exhibit AR(1) auto-correlation (i.e. short-term memory), hence:

$$H_0 : \phi = 0, \tag{2.27}$$

$$H_a : \phi \neq 0, \tag{2.28}$$

where the null hypothesis (H_0 in Equation 2.27) is that the autocorrelation coefficient is 0 and thus the residuals are independent and only consist of white noise. The alternative hypothesis (H_a in Equation 2.28) is therefore that the autocorrelation coefficient is not 0 and the timeseries exhibits short-term memory. The Durbin-Watson test is represented by:

$$dw = \frac{\sum_{t=2}^{T} (N_t - N_{t-1})^2}{\sum_{t=1}^{T} N_t^2}, \tag{2.29}$$

where T is the number of observations. dw can be a value between 0 and 4, where the null hypothesis is accepted and the residuals are uncorrelated when $dw = 2$, whereas a value of 0 to 2 indicates positive autocorrelation and 2 to 4 indicates negative autocorrelation, and therefore the alternative hypothesis is accepted. In Chapter 3, the D-W test p-values are used to indicate whether autocorrelation is present, at a 5% significance level ($p<0.05$). As previously mentioned, over half the CMIP5 models used in Chapter 3 and the RAPID data accept the alternative hypothesis (show significant autocorrelation), and hence GLS is used. In Chapter 4, the AMOC-SSH regression accepts the null hypothesis (does not show autocorrelation), and hence OLS is used.

2.2.2.2 Engle-ARCH Test

The AutoRegressive Conditionally Heteroscedastic (ARCH) model proposed by Engle (1982) is based on a Lagrange Multiplier test by examining the significance of fitting a linear regression model to squared residuals:

$$N_t^2 = a_0 + a_1 N_{t-1}^2 + ... + a_L N_{t-L}^2 + \epsilon_t, \tag{2.30}$$

where L is the number of lags. The hypotheses have the following form:

$$H_0 : a_0 = a_1 = ... = a_L = 0, \tag{2.31}$$

$$H_a : a_0 \neq a_1 \neq ... \neq a_L \neq 0, \tag{2.32}$$

where the null hypothesis (H_0 in equation 2.31) is that the squared residuals exhibit a constant variance through time (i.e., homoscedastic) since all terms apart from the white noise are 0. The null hypothesis is rejected, and the alternative hypothesis (H_a in equation 2.32) is subsequently accepted when the variance changes through time (i.e., heteroscedastic). The majority of the CMIP5 models under RCP8.5, the RAPID data, and the SSH-AMOC regression residuals accept the null hypothesis (are homoscedastic).

2.2.3 Assessing model fit

In Chapter 4, different reconstructions of the AMOC are generated. In order to assess whether these models represent the original AMOC transport (which can either be from the observations or numerical models), a few different metrics outlined below are used to compare the timeseries.

2.2.3.1 Coefficient of determination, R^2

The R-squared, or coefficient of determination, is generally used to estimate the percentage of the variation in the response variable explained by the model, i.e., how well the model represents the data. The preamble for this method is defined in Section 2.2.1.1, namely the sum of squared residuals ($\boldsymbol{\mathcal{SS}}$, Equation 2.2). In Chapter 4, the 'model' is the AMOC's reconstruction via the AMOC* SSH proxy, hence:

$$\boldsymbol{\mathcal{SS}} = (\mathbf{Y} - \mathbf{X}\hat{\beta})'(\mathbf{Y} - \mathbf{X}\hat{\beta}) \qquad \left(\mathcal{SS} = \sum_{t=1}^{n} (Y_t - Y_t^*)^2 \right), \tag{2.33}$$

where $\mathbf{Y}$ (or Y_t) represents the AMOC transport, and the $\mathbf{X}\hat{\beta}$ (or Y_t^*) represents the AMOC*, reconstructed transport. The total sum of squares, $\boldsymbol{\mathcal{ST}}$, is then estimated via:

$$\boldsymbol{\mathcal{ST}} = (\mathbf{Y} - \overline{\mathbf{Y}})'(\mathbf{Y} - \overline{\mathbf{Y}}) \qquad \left(\mathcal{ST} = \sum_{t=1}^{n}(Y_t - \bar{Y}_t)^2\right) \tag{2.34}$$

where $\bar{Y}$ is the response variable's overall mean (i.e., the AMOC's time-mean). It is therefore the ratio of the sample variance of the fitted values to the sample variance of Y:

$$\mathbf{R}^2 = 1 - \frac{\boldsymbol{\mathcal{SS}}}{\boldsymbol{\mathcal{ST}}} \tag{2.35}$$

2.2.3.2 Relative error

The relative error is used in Chapter 4, when comparing the actual AMOC trend (either from the observations or the models) with the reconstructed trend. This is determined by finding the absolute difference between the coefficients and presenting it as a proportion relative to the true AMOC trend, as follows:

$$\mathrm{Re} = \left|\frac{(\beta - \beta^*)}{\beta}\right|. \tag{2.36}$$

Therefore, $\beta = \beta_{\mathrm{AMOC}}$ is the true value of the AMOC trend, and $\beta^* = \beta_{\mathrm{AMOC}^*}$ is the reconstructed AMOC's trend. The numerator is equivalent to the absolute error ($|\Delta\beta|$), and the relative error can be converted to a percentage error by multiplying Equation 2.36 by 100. The closer the value is to zero, the lower the error, and the better the reconstruction's trend represents the actual trend (Abramowitz and Stegun, 1972).

Other techniques that do not use standard statistical approaches outlined here, and require further explanation, are elaborated in the Methods sections of each analysis Chapter (for example, the majority of Chapter 5).

Chapter 3

Multi-decadal monitoring is required to detect an AMOC declining trend

Adapted from Geophysical Research Letters manuscript, currently under revision.

Abstract

Determining whether the Atlantic Meridional Overturning Circulation's transport of water and heat northwards from the tropics is potentially declining is crucial but challenging due to the shortness of current continuous observations. To estimate the number of years necessary to detect a decline, we conduct a simulation study with synthetic data mimicking a 100-year AMOC timeseries. The trend, variance, and autocorrelation of the AMOC strength are extracted from Coupled Model Intercomparison Project Phase 5 models under a 'business-as-usual' future scenario, and from observations to reproduce AMOC variability and short-term memory. Fitting a generalised least squares model to the simulations, statistically significant trend detection requires an average of at least 35.25 years using CMIP5 simulations (with an ensemble standard deviation of 9.7 years) and 28 years using RAPID observations. Our results suggest that continued AMOC monitoring is required in order to detect an AMOC decline.

3.1 Introduction

Coupled ocean-atmosphere numerical models generally predict a decline of the Atlantic Meridional Overturning Circulation (AMOC) in the 21st century, under the influence

of anthropogenic warming (Stocker et al., 2013). The AMOC is responsible for approximately 25% of the globe's meridional heat transport at 26° N, equivalent to 1.3 PW ($1\,\mathrm{PW} = 10^{15}\,\mathrm{W}$) (Hall and Bryden, 1982; Lavin et al., 1998; Ganachaud and Wunsch, 2003; Johns et al., 2011). Heat is absorbed in surface waters of the tropics and carried northwards to be released to the atmosphere over the north-east Atlantic. This plays a role in maintaining milder north-western European atmospheric temperatures, compared to the global average at the same latitudes (Pohlmann et al., 2006; Rhines et al., 2008).

At 26.5° N, the ongoing RAPID program has monitored the AMOC continuously since 2004 (Rayner and Kanzow, 2011). Determining whether RAPID's observed decline is secular or part of natural variability is debated by studies using up to 13 years of data (Roberts et al., 2014; Smeed et al., 2014; McCarthy et al., 2012, 2015a; Smeed et al., 2018). The Fifth Assessment Report of the Intergovernmental Panel on Climate Change states that there is no evident trend from the decade-long observations (Stocker et al., 2013). Distinguishing trends from natural variability can require several decades of high-quality data due to weak signal-to-noise ratios (Weatherhead et al., 1998; Henson et al., 2010; Beaulieu et al., 2013).

Although coupled climate numerical models can exhibit large ranges of uncertainty, they provide the best available long-term estimates of the AMOC strength. From the 50-model ensemble of the Coupled Model Intercomparison Project Phase 5, the IPCC consider a weakening of the AMOC 'likely' before 2050 and 'very likely' by an average of a 34% decline before 2100 (Stocker et al., 2013). In a study using 10 CMIP5 models under future scenario RCP8.5 forcing ('business-as-usual'), Cheng et al. (2013) estimate a decrease in AMOC transport ranging from 15 to 60% in the 21st century, relative to their historical means. These studies on future projections, however, do not estimate the significance of the trend, nor the number of years required to detect trends.

Detection of long-term linear trends can be affected by numerous factors, such as the length of data available, the magnitude of the trend to be detected, the degree of variability (e.g. variance and autocorrelation, or short-term memory), discontinuity or gaps within the timeseries, observation error, and the trend detection technique used (Santer et al., 1995; Weatherhead et al., 1998; Vellinga and Wood, 2004; Baehr et al., 2007, 2008; Keller et al., 2007a,b; Roberts and Palmer, 2012; Roberts et al., 2014; Williams et al., 2015). Using an approach that accounts for autocorrelation by generating lag-1 ARMA (autoregressive moving average) simulations, Roberts et al. (2014) compute a detection time of 40 years. Their study focuses on whether the trend from the first 8 years of RAPID can be explained by internal variability from simulations based on combined observational and model characteristics. Our study slightly modifies that approach by obtaining the noise and trend properties from the models and the now longer (13-year) observations separately to account for the different timeseries length of each (generating CMIP5 simulations using 94-year trends, for example). Furthermore, autocorrelation is

further accounted for by fitting a generalised least squares (GLS) trend instead of an ordinary least squares (OLS).

Our aim is to estimate the number of years required to detect a long-term AMOC decline using 20 future scenario RCP8.5 CMIP5 models and RAPID observations. We also manually choose over 150 combinations of trend, variance and autocorrelation values to obtain a range of detection times. This paper is structured as follows: the original observation and model data are explained in Section 3.2, the method for trend detection with autocorrelated noise and generating the AR simulations in Section 3.3, and the results and conclusions are discussed in Sections 3.4 and 3.5, respectively.

3.2 Data

We use the numerical model output from the CMIP5 RCP8.5 ('business-as-usual' future scenario) ensemble monthly means from 2006 to 2100 (94 years). The 20 models selected are: (1) FIO-ESM, (2) NorESM1-M, (3) GFDL-CM3, (4) BNU-ESM, (5) CESM1-BGC, (6) CCSM4, (7) MIROC-ESM, (8) CNRM-CM5, (9) ACCESS1-0, (10) GISS-E2-R-CC, (11) HadGEM2-CC, (12) MPI-ESM-LR, (13) EC-EARTH, (14) inmcm4, (15) CSIRO-Mk3-6-0, (16) IPSL-CM5A-MR, (17) CMCC-CM, (18) CanESM2, (19) bcc-csm1-1, (20) MRI-CGCM3 (available from the portal Earth System Grid - Center for Enabling Technologies (ESG-CET), on https://esgf-node.llnl.gov/search/cmip5/). RCP8.5 forcing is chosen as it produces the strongest decline scenarios among CMIP5. We solely focus on detecting a negative trend in this study. Furthermore, only one model per institute is selected to reduce model bias. For comparison to the observations, the zonally and vertically integrated CMIP5 AMOC streamfunction data is extracted at the closest location to 26.5° N latitude and at 1,000 m depth.

The observations from the RAPID trans-basin array at 26.5° N are available as a bi-daily timeseries from 2004 to 2017 (13 years) (described in (McCarthy et al., 2015a) and downloadable from https://www.rapid.ac.uk/rapidmoc/rapid_data/datadl.php). Both CMIP5 and RAPID data preprocessing includes annually averaging monthly means from March to February due to the first and last months of the RAPID timeseries being April (2004) and February (2017). This ensures maximal conservation of data, with RAPID's annual means only having one less month in the first year. The annually averaged CMIP5 and RAPID data can be found in Figure 3.1 and Figure 3.2a.

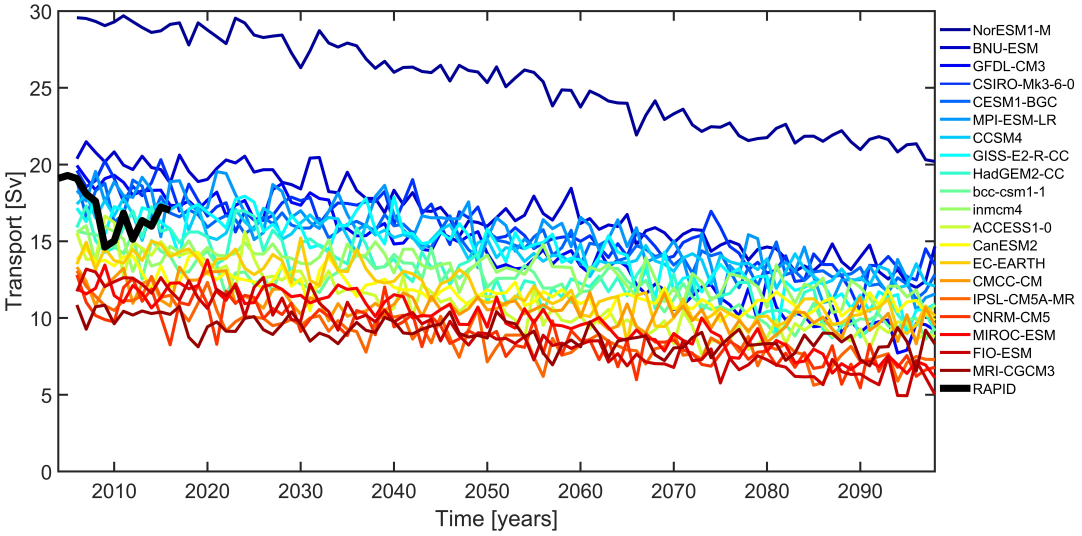

FIGURE 3.1: Time series of annual mean AMOC transport represented by observations using RAPID (black line) from 2004 to 2017 and 20 CMIP5 RCP8.5 models (coloured lines) at 26.5° N from 2006 to 2100.

3.3 Methods

3.3.1 Trend detection for autocorrelated noise

The simple linear trend model equation as a function of time is stated as:

$$Y_t = \beta x_t + \lambda + N_t, \tag{3.1}$$

where Y_t are the data (the annual means of AMOC transport [Sv]), β is the magnitude of the trend, λ is the constant term (or intercept), N_t are the residuals, and t is time. Classic linear models such as an ordinary least squares (OLS) regression assume the errors or residuals to be independent (white noise). This assumption often does not hold in climate timeseries data, where successive data points are often correlated due to memory in the system (Tiao et al., 1990; Weatherhead et al., 1998). Using OLS in the presence of autocorrelation can artificially lower the variance estimation and trends can seem statistically significant when they are not (Beaulieu et al., 2013). Conversely, a generalised least squares (GLS) regression takes autocorrelation into account.

The unexplained portion of the data, N_t, is assumed to follow a first-order autoregressive process (AR(1), or short-term memory), meaning that successive measurements (i.e., years, in our case) of the noise are autocorrelated, of the form:

$$N_t = \phi N_{t-1} + \epsilon_t, \tag{3.2}$$

where ϕ is the AR(1) coefficient determined from the GLS residuals and ϵ_t is white noise (random normally distributed error). The relationship between the total noise and the white noise is expressed through their variances, which can be stated as:

$$\sigma_\epsilon^2 = \sigma_N^2 \cdot (1 - \phi^2), \tag{3.3}$$

where σ_ϵ^2 is the white noise variance and σ_N^2 is the total variance (Brockwell and Davis, 2002).

3.3.2 Simulation experiment

We simulate the AMOC transport by generating synthetic series using parameters extracted from numerical models or observations, namely (1) the trend, (2) AR(1) coefficient, and (3) the variance. First, the trend coefficient is determined by the GLS fit of the annually averaged CMIP5 (Figure 3.1) or RAPID data (Figure 3.2a). The trend is then removed from the data to produce residuals from which the AR(1) coefficient (using Equation 3.2 above) and white noise variance (using Equation 3.3 above) are defined. This isolates the parameters without the influence of the trend. It is worth highlighting at this stage that the parameters are extracted from different lengths of data (94 years for the CMIP5 data and 13 years for the RAPID data). The results of this study should therefore not be compared directly but seen as two separate detection studies, one from a quasi-decadal trend and the other from a multi-decadal, quasi-centennial trend.

A total of 1,000 AR(1) simulations are produced (Figure 3.2b), which represent AMOC transport over 100 years based on the three parameters defined above. For each of the simulated timeseries, a GLS trend is first fit to 10 years of data, after which the sample size is increased by a one-year increment until reaching 100 years (Figure 3.2c). GLS is run on `R` using the package `nlme` (Pinheiro and Bates, 2000). At each increment, we use the GLS model to test whether the trend is significantly different from zero. Note that since model projections agree on a decreasing trend, the hypothesis tested here is a decreasing trend (i.e., one-tailed test). This determines the statistically significant declining trends ($p<0.05$) as a function of sample size. When 95% of the simulations detect a trend, the sample size is recorded as 'the number of years required to detect a trend' (hereafter, n*). This is then repeated for a range of parameters using seven trend values (from -0.02 to -0.12, with step 0.02 Sv yr^{-1}), seven AR(1) coefficients (from 0 to 0.6, with step 0.1) and three variance values (0.3, 0.8 and 1.28 Sv^2). These values are selected to encompass the range found among the CMIP5 and RAPID parameters (Table 3.1).

TABLE 3.1: The GLS trend [Sv yr^{-1}], variance [Sv^2] and AR(1) coefficients of 20 RCP8.5 CMIP5 models and their ensemble mean, as well as RAPID data (using OLS and GLS regression fits). The last column shows the number of years required to detect the statistically significant trend (n*) ($p<0.05$) at 95% detection rates from 1,000 AR simulations. The table is sorted by increasing n*.

CMIP5 models	**Institute**	**Trend [Sv yr^{-1}]**	**Variance [Sv^2]**	**AR(1) [coeff.]**	**n* [years]**
FIO-ESM	FIO (China)	−0.08 *	0.44	−0.13	21
NorESM1-M	NCC (Norway)	−0.10 *	0.34	0.30*	22
GFDL-CM3	NOAA GFDL (USA)	−0.12 *	0.56	0.30*	24
BNU-ESM	GCESS (China)	−0.09 *	0.54	0.28*	27
CESM1-BGC	NSF-DOE-NCAR (USA)	−0.06 *	0.45	−0.02	27
CCSM4	NCAR (USA)	−0.05 *	0.42	0.00	28
MIROC-ESM	MIROC (Japan)	−0.06 *	0.44	0.23*	31
CNRM-CM5	CNRM-CERFACS (France)	−0.05 *	0.78	−0.17	32
ACCESS1-0	CSIRO-BOM (Australia)	−0.07 *	0.88*	0.21*	34
GISS-E2-R-CC	NASA GISS (USA)	−0.07 *	1.03	0.14	34
HadGEM2-CC	MOHC (UK)	−0.07 *	0.94	0.15	34
MPI-ESM-LR	MPI-M (Germany)	−0.07 *	1.25	0.09	34
EC-EARTH	EC-EARTH (Europe)	−0.06 *	0.64	0.20*	37
inmcm4	INM (Russia)	−0.04 *	0.57	−0.02	37
CSIRO-Mk3-6-0	CSIRO-QCCCE (Australia)	−0.07 *	0.85	0.38*	42
IPSL-CM5A-MR	IPSL (France)	−0.05 *	0.66	0.26*	42
CMCC-CM	CMCC (Italy)	−0.03 *	0.57	0.07	45
CanESM2	CCCMA (Canada)	−0.03 *	0.43	0.29*	46
bcc-csm1-1	BCC (China)	−0.06 *	0.73	0.48*	49
MRI-CGCM3	MRI (Japan)	−0.02 *	0.48	0.23*	59
Ensemble mean					35.25 (±9.7)
RAPID OLS		−0.24 *	1.26	0.48*	25
RAPID GLS		−0.19	1.28	0.49*	28

* in 'trend' column: the trend is significantly different from zero (5% significance)
* in 'variance' column: Engle's ARCH null hypothesis rejected (5% significance): variance changes through time
* in 'AR(1) coeff.' column: Durbin-Watson null hypothesis rejected (5% significance): residuals are autocorrelated

A residual analysis has been used to test for autocorrelation and whether the variance is constant through time. The respective tests are the Durbin-Watson test (Durbin and Watson, 1950), and Engle's ARCH test (Engle, 1982), at a 5% significance level in both cases. Furthermore, following the results from Smeed et al. (2018) suggesting that a rapid change in the observed AMOC occurs in 2008, a changepoint analysis (using `R` package `EnvCpt` (Beaulieu and Killick, 2018)) is applied to the RAPID and CMIP5 data to verify whether any changes detected are trends or other characteristics of the timeseries. For further details regarding the methods behind the residual analyses or `EnvCpt` algorithm, refer to Chapter 2: General Data and Methods.

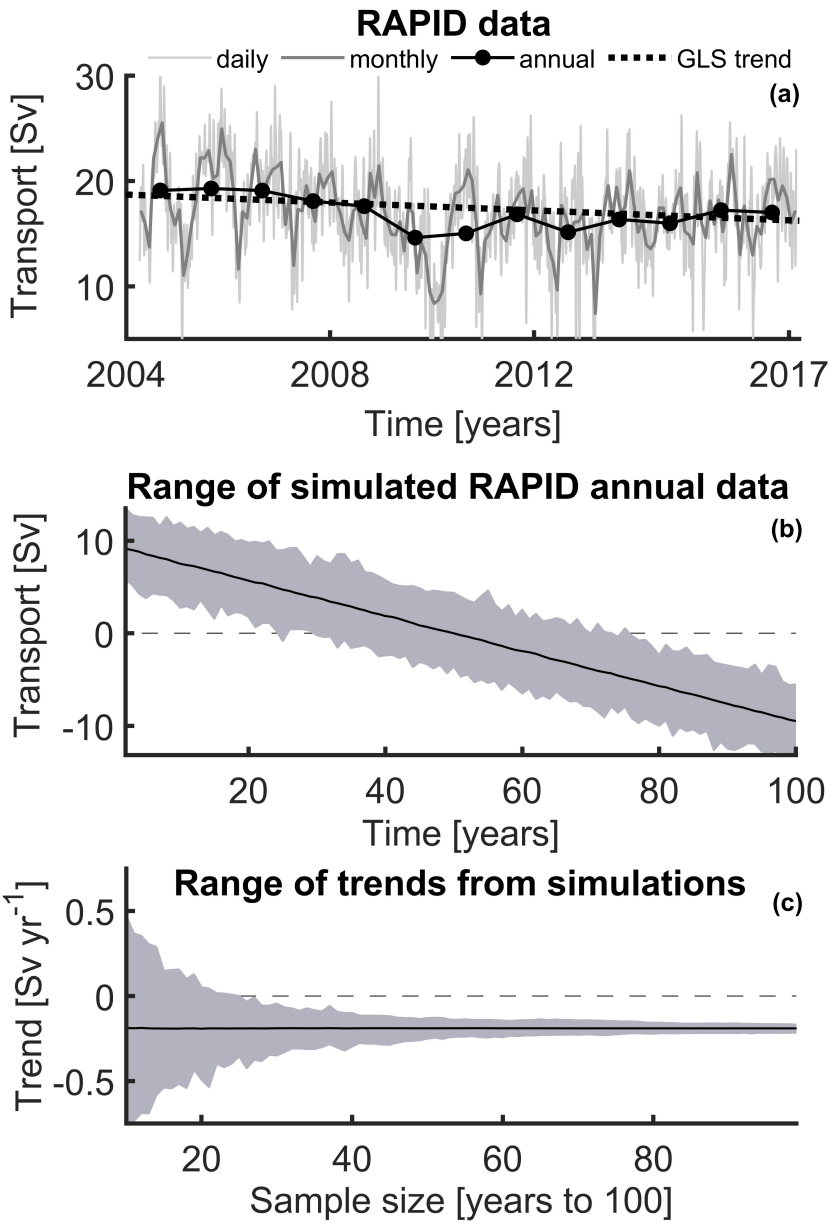

FIGURE 3.2: RAPID data and numerical experiment with simulated AMOC data. (a) Original RAPID timeseries: daily means (light grey line), monthly means (dark grey line), annual means (black solid line with filled dots), and the GLS annual trend of -0.19 Sv yr^{-1} (black dotted line). (b) Range of 1,000 AR simulations over 100 years (shaded grey) around their temporal mean (black line) to represent the anomaly of AMOC transport [Sv] with the variance, autocorrelation coefficient and trend from annually averaged RAPID data in (a) ($\sigma_\epsilon^2 = 1.28$ Sv^2, ϕ=0.49 and $\beta = -0.19$ Sv yr^{-1}). (c) Range of trends [Sv yr^{-1}] from the 1,000 simulations (shaded grey) around their temporal mean (black line) as a function of the number of years provided to the linear regression (from 10 years through to the full 100). Dashed lines at 0 have been added in (b) and (c).

3.4 Results

The RAPID data (Figure 3.2a) is first fit with an OLS regression and comparison with GLS estimates (Table 3.1) shows that the variance is slightly underestimated (1.26 Sv^2 versus 1.28 Sv^2), as is the AR(1) coefficient (0.48 versus 0.49), the trend is inflated (-0.24 Sv yr^{-1} versus -0.19 Sv yr^{-1}) and the trend falsely appears statistically significant ($p<0.05$). The GLS regression (Figure 3.2a) therefore produces a slightly better estimate of the trend and the $p>0.05$ suggests that it is not significant. CMIP5 values range from trends of -0.02 to -0.12 Sv yr^{-1}, white noise variances of 0.34 to 1.25 Sv^2, and AR(1) coefficients of -0.17 to 0.48 (see Table 3.1 for each model's values).

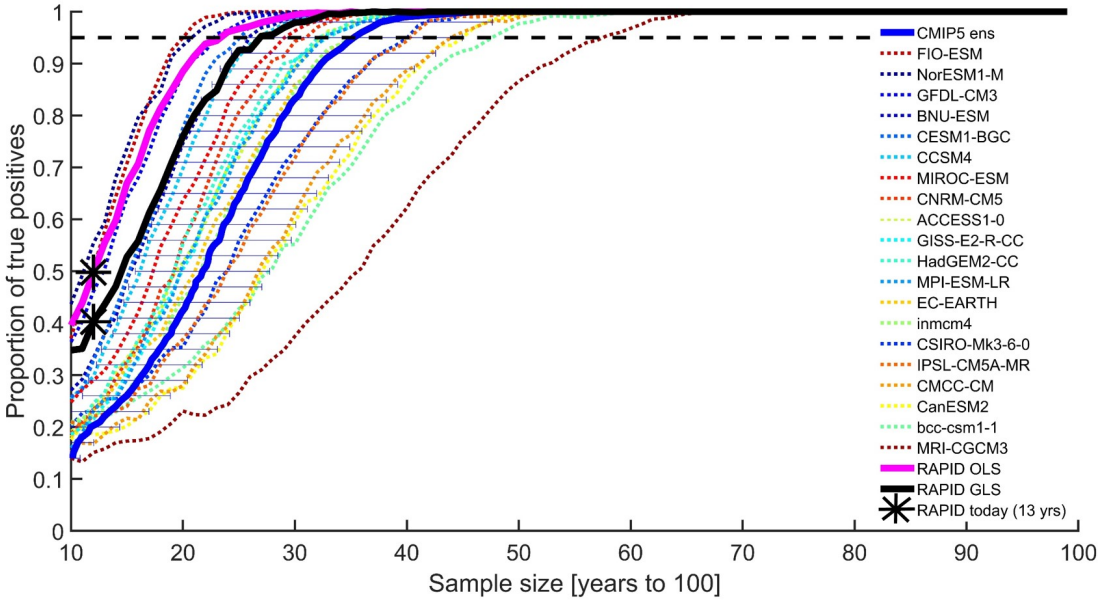

FIGURE 3.3: Detection of declining trends in simulation data of variable length. Each line represents the proportion of true positives from 1,000 simulations (i.e., true positives are defined where the trends are significant with one-sided p-values<0.05) as a function of the sample size to fit the GLS, providing 10 to 100 years of data. The proportion of true positives for simulations using 20 CMIP5 RCP8.5 model parameters are the coloured dotted lines with their ensemble mean (thick blue line) and plus-minus standard deviation errorbars (thin horizontal blue lines). The thick black line uses parameters after applying GLS to the RAPID data and the thick magenta line after applying OLS. The black stars show the proportion of true positives with only 13 years of data (the current length of RAPID data). The number of years required to detect a significant negative trend (n*) is established when each line crosses the 0.95 proportion of true positives (thick dashed horizontal black line).

The trend, variance, and AR(1) values are used within the statistical model to produce 1,000 runs of 100 years (Figure 3.2b). As the sample size increases, the range of trend values converge towards the true trend value (-0.19 Sv yr^{-1} for RAPID in Figure 3.2c). When 95% of the simulations have one-sided p-values<0.05, the sample size is recorded as n*. The n* is therefore the time when each line in Figure 3.3 crosses the dashed 0.95

threshold, which ranges from 21 years (FIO-ESM) to 59 years (MRI-CGCM3), with a CMIP5 ensemble mean of 35.25 (and a standard deviation of 9.7) years. The RAPID OLS fit of the original RAPID data produces a slightly faster detection rate than fitting a GLS (25 years versus 28 years). With a sample size of 13 years (RAPID time period), 50% of the simulations correctly detect the trend using the OLS, whereas it decreases to 40% when using the GLS (the large black stars in Figure 3.3). After 65 years, all model and observation simulations detect the trend with a 100% hit rate.

Despite RAPID's AR(1) coefficient (of 0.49) and variance (of 1.28 Sv^2) being comparable to the largest values found among the CMIP5 models, the strong trend (of -0.19 Sv yr^{-1}) reduces the n* to 28 years. However, it is worth repeating that the GLS trend on the 13-year record is not deemed significantly different from zero ($p>0.05$). Furthermore, three of the four CMIP5 models with the largest n*, from 45 to 59 years, have the weakest trends (of -0.02 to -0.03 Sv yr^{-1}; MRI-CGCM3, CanESM2, and CMCC-CM). Although the second-to-last largest n* (bcc-csm1-1) has a slightly stronger trend (of -0.06 Sv yr^{-1}), it has a high variance and the highest AR(1) coefficient (of 0.48) amongst all 50 models, increasing the n* to 49 years. Equally, the three models with the smallest n* of 21 to 24 years have the strongest trends (of -0.08 to -0.12 Sv yr^{-1}; FIO-ESM, NorESM1-M, and GFDL-CM3, respectively).

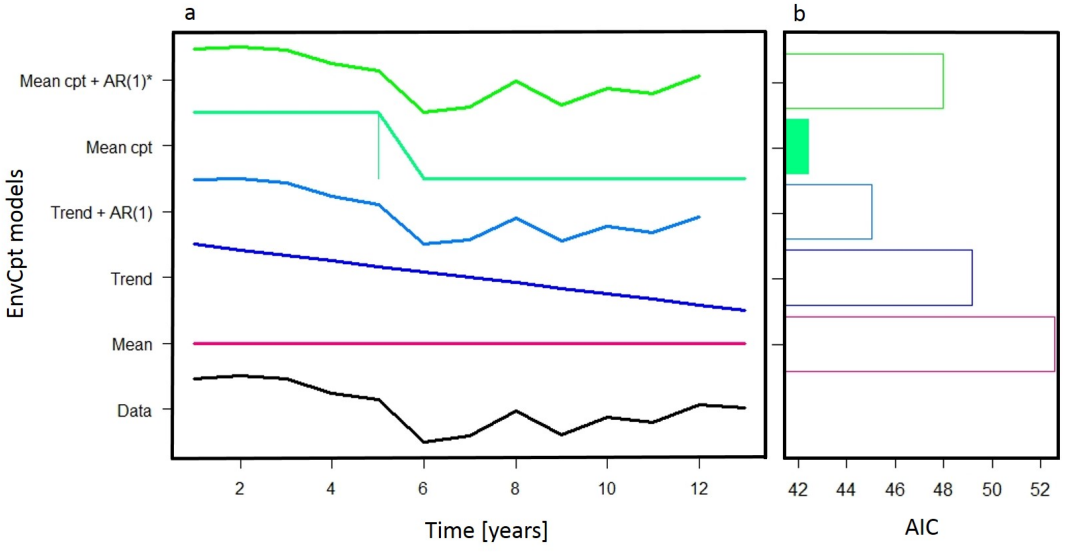

FIGURE 3.4: The changepoint analysis output. a) The models fitted to the 13 years of RAPID timeseries (black line). The star next to 'Mean cpt + AR(1)' indicates that there is no changepoint in this fit, hence why only five of the six models tested are plotted since the 'Mean + AR(1)' would be identical to 'Mean cpt + AR(1)'. b) The AIC of each model, showing that the best-performing model (with the smallest AIC value) is the Mean changepoint (filled green). The vertical line in a) represents the location of the shift in the mean between the 5th and 6th year of the timeseries, (i.e., between 2008 and 2009).

A residual analysis confirms that GLS is the appropriate regression fit, where 11 of the models and the observation data exhibit autocorrelation (the stars next to AR(1) coefficients in Table 3.1). The majority of the models show a constant white noise variance through time (the lack of stars next to 19 of the variances in Table 3.1). Furthermore, the changepoint analysis (Killick et al., 2012; Beaulieu and Killick, 2018) suggests that the best model fit for 13 of the 20 models includes just the trend or a trend + AR(1), when using AICc (Table 3.2). This justifies the use of a linear trend and autocorrelation for the multi-decadal simulated CMIP5 AMOC transport. Consistent with findings in Smeed et al. (2018), the RAPID observations show the best model selection as a change in the mean occurring between 2008 and 2009 (as shown in Figure 3.4a), with the AIC showing that 'Mean cpt' is the best model fit (Figure 3.4b and Table 3.2). This again indicates that for a decade of data (or 13 years), the best model fit does not include a trend.

TABLE 3.2: The changepoint statistical analysis model selections for the timeseries of each CMIP5 model and RAPID observations. The three columns show the best-performing model fit using three different information criteria: (1) the Akaike information criterion (AIC), (2) the Bayesian information criterion (BIC) and (3) the corrected AIC (AICc).

CMIP5 models	**AIC**	**BIC**	**AICc**
FIO-ESM	Trend AR(1)	Trend	Trend AR(1)
NorESM1-M	Trend AR(1)	Trend AR(1)	Trend AR(1)
GFDL-CM3	Mean cpt	Trend AR(1)	Trend AR(1)
BNU-ESM	Trend AR(1)	Trend AR(1)	Trend AR(1)
CESM1-BGC	Trend AR(1)	Trend	Trend AR(1)
CCSM4	Trend	Trend	Trend
MIROC-ESM	Trend cpt	Trend cpt	Trend cpt
CNRM-CM5	Trend AR(1)	Trend AR(1)	Trend AR(1)
ACCESS1-0	Trend cpt AR(1)	Trend cpt	Trend cpt AR(1)
GISS-E2-R-CC	Trend AR(1)	Trend	Trend AR(1)
HadGEM2-CC	Trend AR(1)	Trend	Trend AR(1)
MPI-ESM-LR	Trend AR(1)	Trend	Trend AR(1)
EC-EARTH	Mean cpt	Trend AR(1)	Mean cpt
inmcm4	Trend	Trend	Trend
CSIRO-Mk3-6-0	Mean cpt	Trend AR(1)	Trend AR(1)
IPSL-CM5A-MR	Trend AR(1)	Trend AR(1)	Trend AR(1)
CMCC-CM	Mean cpt	Mean cpt	Mean cpt
CanESM2	Trend AR(1)	Trend AR(1)	Trend AR(1)
bcc-csm1-1	Trend cpt AR(1)	Trend cpt AR(1)	Trend cpt AR(1)
MRI-CGCM3	Mean cpt	Mean cpt	Mean cpt
RAPID	Mean cpt (in year 2008)	Mean cpt	Trend AR(1)

3.5 Discussion and Conclusion

We have estimated the number of years of AMOC transport data required to detect a statistically significant long-term decline using simulations generated from parameters acquired in CMIP5 numerical models (ensemble mean n* = 35.25 years and standard deviation ± 9.7 years) and observations (n* = 28 years). An important application of trend detection in climate data is to determine how long a monitoring program needs to operate in order to detect a long-term trend. For the AMOC specifically, there have been several attempts in recent years to determine the decadal or multi-decadal trend, mainly to identify whether RAPID is showing a significant decline in transport or not (Bryden et al., 2005; Smeed et al., 2014; Roberts et al., 2014; Smeed et al., 2018).

There are numerous factors that can affect trend detection. Focusing on three parameters to best represent the AMOC properties, we demonstrate that the combination of a strong trend, low white noise variance and low short-term memory produces the fastest detection time (due to high signal-to-noise ratio) (Weatherhead et al., 1998). This is demonstrated when using a range of the three parameters, which suggests the applicability of this technique to other environmental data (Figure 3.5). We also show that the strength of the trend has the highest impact on detectability, with the lowest n* among the CMIP5 and RAPID simulations being the result of the strongest trends (Table 3.1), despite the comparatively high variance and AR(1) coefficient in the RAPID data, for example.

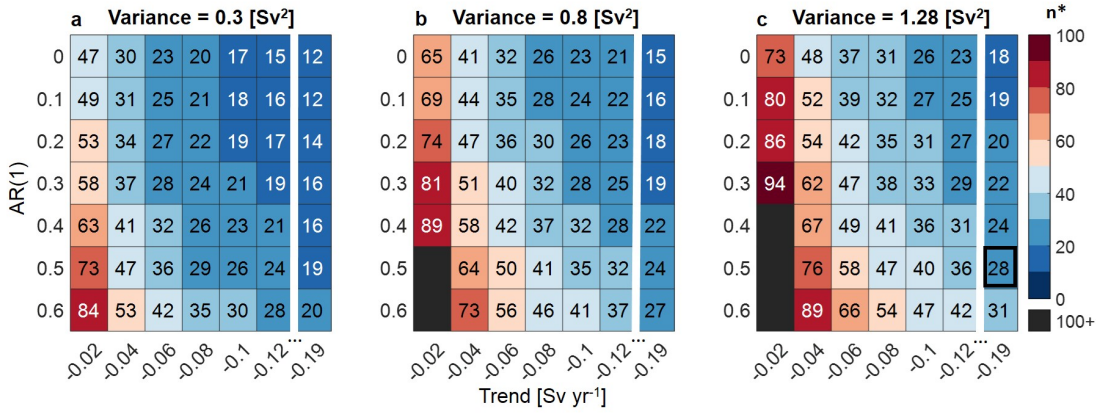

FIGURE 3.5: Numerical experiment with the number of years to detect a trend (n*) from blue to red for 0 to 100 years, respectively. Simulations are generated using a range of trend values [Sv yr^{-1}] on the x-axes, AR(1) coefficients on the y-axes, and variances of (a) 0.3, (b) 0.8, and (c) 1.28 Sv^2. The RAPID trend of −0.19 Sv yr^{-1} is added as the last column in each plot. Black filled cells represent runs that don't reach 95% detection after 100 years. The n* for the statistical model based on RAPID using GLS (28 years) is highlighted (black framed cell) in (c).

Although other studies have accounted for the AMOC's autocorrelation by using different techniques, such as generation of ARMA simulations (Roberts et al., 2014), calculation of the standard error of the trend after determining of the number of truly independent degrees of freedom (Smeed et al., 2014), and bootstrapping techniques (Baehr et al., 2007), here AR simulations and GLS is used (Santer et al., 1995; Vellinga and Wood, 2004; Baehr et al., 2008; Keller et al., 2007a,b; Roberts and Palmer, 2012). We show that the use of OLS instead of GLS can slightly underestimate RAPID's n* by 3 years (25 instead of 28 years in Table 3.1) or overestimate the proportion of true positives after 13 years (to 50% instead of 40% in Figure 3.3). This could be due to autocorrelation being confounded with trend-like segments in the data (Lennartz and Bunde, 2011; Beaulieu et al., 2013; Beaulieu and Killick, 2018). Another specification of our method is to choose only one-sided p-values, since we focus on AMOC data exhibiting a decline scenario. A two-sided test increased the n* by 2.5 years, on average. Finally, we tested the hypothesis that CMIP5 models potentially underestimate the AMOC variability (Yan et al., 2018; Roberts et al., 2014). Following the methodology in Roberts et al. (2014), simulations using the CMIP5 trend and AR(1) coefficient combined with the RAPID variance increased the n* by 10 years, on average (comparable to the n* in Roberts et al. (2014) of 40 years). However, combining a parameter from decadal observations with parameters from quasi-centennial data is speculative.

It must be noted that the present study is focused on detectability rather than an attribution analysis. Our results encourage the use of trend detection as a precursor to any attribution studies to confirm that a trend is in fact detected before investigating causes for changes. Some attribution studies estimate the timing of emergence, i.e., when an anthropogenically-forced AMOC trend falls outside the 95% confidence limits of natural variability from the control simulations. They show that the forced AMOC changes can be detected after 50 (Keller et al., 2007a) to 60 years (Baehr et al., 2008) for a sampling error of 1 Sv (the estimated error of the RAPID array (McCarthy et al., 2015a)), 80 years due to sampling gaps of 10-year intervals (Baehr et al., 2008), or 100 years due to high natural variability (Santer et al., 1995). Our results support that since a significant decline is detectable after 28 to 35 years, these studies can rightly detect the timing of emergence using model output, however RAPID still requires more observations before performing such an analysis. Therefore, although any inferences from the observations are purely speculative, our study could suggest that the variability seen in RAPID data is due to natural variations (as does Roberts et al. (2014)). This is supported by the lack of significance of the GLS trend for the RAPID 13-year record (-0.19 Sv yr^{-1}, $p>0.05$) which may result from the changepoint present in 2008, (as is also seen in Smeed et al. (2018)), showing a constant stronger and weaker transport before and after 2008, respectively.

It is important to also mention the assumptions that govern the results of this study, as well as some suggestions for future studies to overcome limitations. These include:

1. The parameters are stationary and do not change through time. For example, the CMIP5's 94-year trend, AR(1) coefficient, and variance are assumed to be the same using the full data or 35.25 years (n* of CMIP5 ensemble mean).

2. From the Durbin-Watson autocorrelation test and the changepoint analysis, we choose AR(1) as the best representation of the memory in the AMOC timeseries. Ludescher et al. (2017) show that overestimation of trend significance can occur in the presence of long-term memory (which is present in many environmental timeseries). Although RAPID is not long enough and most of the CMIP5 models do not show significant autocorrelations beyond lag-1 (annual memory), further tests including a multi-decadal cycle, for example, could be done (for example, using the two models that exhibit long-term memory (not shown): ACCESS1-0 and bcc-csm1-1).

3. We do not investigate some factors that could delay detection time (such as infrequent data collection or observation errors (Keller et al., 2007a; Baehr et al., 2008)), since we assume perfect continuous timeseries collection. A comparison study to ours could be constructed using hydrographic data to test how gaps in the data affect the n* (Beaulieu et al., 2013) or sample errors that can wrongly decrease the n* by 10 years when ignored (Roberts and Palmer, 2012).

4. Annual means of the AMOC data can vary depending on the start month (see Roberts et al. (2014), Figure S1). We assume that choosing March to February is best in order to utilise all the observations available, but the results may be sensitive to the choice of start months.

Ultimately, when looking at long-term, climate change timescale trends, 13 years of observations are not enough to robustly detect a trend, nor to assess whether the decline seen in RAPID is due to multi-decadal variability or to a secular trend. This work therefore encourages the efforts for continuous monitoring and data collection of the AMOC.

Chapter 4

Investigating the decadal to multi-decadal relationship between the AMOC and SSH in observations and numerical models

4.1 Introduction

Large-scale ocean circulations can have a major influence on regional and global climate systems. The last few decades have seen a particular interest in the evolution of the North Atlantic Meridional Overturning Circulation (AMOC) and its effect on European climate (Hall and Bryden, 1982; Johns et al., 2011; Srokosz et al., 2012; McCarthy et al., 2012; Bryden et al., 2014; Buckley and Marshall, 2016). The AMOC consists of an upper limb carrying near-surface warm waters northwards and a lower limb carrying deep cool waters southwards (Stommel, 1957). The heat is released into the atmosphere in the northern North Atlantic and is one of the factors that maintains a milder climate in Europe. This contributes to the approximately 3° C contrast between the north-western coastal Europe and the western United States and Canada (Rhines et al., 2008). Although the Intergovermental Panel on Climate Change do not predict a complete shutdown of the AMOC during this century, their 5th Assessment Report states that a decline by 2050 is 'likely' with a sustained increase in anthropogenic greenhouse gas emissions (Collins et al., 2013).

Due to the challenges in measuring the basin-wide and full-depth North Atlantic transport, historical observations were temporally sparse. This prompted the launch of the

ongoing transatlantic RAPID program at 26.5° N in 2004 (and the more recent Overturning in the Subpolar North Atlantic program in 2014 (Lozier et al., 2017)). The first eight years of RAPID's timeseries suggests that the transport reduced by approximately $-0.5\,\mathrm{Sv\ yr^{-1}}$ (Smeed et al., 2014), whereas the full 13 years suggest a step change to a reduced state of overturning since 2008 (Smeed et al., 2018). However, with the array being confined in time, it is unknown whether the decline is part of a multi-decadal feature or part of a secular trend. This outlines the need for proxies that can shed light on past or future AMOC variability across a range of timescales.

Recent efforts have aimed to establish indirect estimates of the AMOC from other ocean properties of the North Atlantic, such as bottom pressure (Elipot et al., 2014; Landerer et al., 2015), sea surface temperature (SST) (Yang, 1999; Medhaug and Furevik, 2011; Drijfhout et al., 2012; Rahmstorf et al., 2015; Sévellec et al., 2017), the geostrophic Sverdrup balance (Duchez et al., 2014), and sea surface height (SSH) (Ezer, 2015; Vinogradova et al., 2007; Hirschi et al., 2009; Ivchenko et al., 2011; Frajka-Williams, 2015). Determining such robust fingerprints would have the potential to extend the AMOC record back in time (Roberts et al., 2013), and identify if the current AMOC slow-down record is part of a longer decline or of multi-decadal natural variability. The aim of this study is therefore to test whether there is a robust 13-year relationship between the AMOC and SSH in order to extend the RAPID AMOC into the past.

4.1.1 The relationship between the AMOC and SSH

SSH and the AMOC can be linked dynamically both when changes in the sea level affect changes in the circulation and vice versa. This two-way relationship can be induced by mechanisms such as adiabatic adjustments through changes in the density structure of the basin (and wind-stress), and diabatic heating from climate change and the resulting expansion of water, for instance (Bryan, 1996; Gregory and Lowe, 2000; Levermann et al., 2005; Cromwell et al., 2007).

The Atlantic's meridional transport at 26.5° N can be estimated via the combination of the geostrophic transport, Ekman transport and Florida Straits transport (see Equation 1.5), following the RAPID calculations (which can be found in McCarthy et al. (2015a)). The geostrophic transport (or the Upper Mid-Ocean, UMO, in the RAPID terminology) can be partitioned into a barotropic flow and a baroclinic flow. The RAPID methodology estimates the barotropic flow as the residual depth-independent transport after summing the Ekman transport, Florida Straits transport and the baroclinic flow, the latter of which is based on the zonal pressure gradient force (Sime et al., 2006; Hall and Bryden, 1982). This zonal pressure (or density) gradient needed to obtain the meridional flow from the geostrophic relationship (see Equation 1.1) can be translated in terms of the dynamic height (derived from temperature and salinity profiles). SSH partly reflects the integrated buoyancy in the water below it (equivalent to the thermal content and

salinity in the water column). Indeed, model studies demonstrate that SSH mirrors dynamic height anomalies on interannual timescales, over deeper regions and at lower latitudes (Vinogradova et al., 2007), such as the subtropical North Atlantic (Piecuch and Ponte, 2011). Hence, integrating this relation from east to west one finds that changes in zonal buoyancy (or density) anomalies between the eastern and western boundaries are proportional to changes in the UMO's transport of water (Hirschi and Marotzke, 2007). It is therefore important to stress that the Ekman transport is mainly wind-driven and therefore not driven by changes in the zonal pressure gradient force, and the western boundary flow of the Florida Straits is outside the realms of this large-scale transport estimate.

Conversely, changes in the AMOC circulation can impact the regional distribution of SSH. A slowdown in the AMOC reduces the transport of mass and heat which modifies the heat content in different regions, and is consequently reflected by changes in SSH (Bryan, 1996; Häkkinen, 2001; Levermann et al., 2005; Mahajan et al., 2011; Smeed et al., 2018). Numerical models show a decrease of 1 Sv in AMOC transport corresponding to a 1.5 cm to 5 cm increase in sea level on the U.S. East coast (Levermann et al., 2005; Bingham and Hughes, 2009; Woodworth et al., 2014). Furthermore, a 30% reduction in overturning caused a 12 cm decrease over the Gulf Stream in 1995-1996 (Häkkinen, 1999). In contrast to suggested interannual to decadal fingerprints of the AMOC, some studies suggest that changes in SSH are predominantly wind-driven on these timescales, whereas the first Principal Component (PC1) of North Altantic SSH exhibits decadal to multidecadal variability that is highly correlated with the AMOC and meridional heat transport (Yin and Goddard, 2013). Hence, there is an ongoing dispute regarding the leading mechanisms affecting SSH changes on different timescales (Lorbacher et al., 2010; Yin and Goddard, 2013; Little et al., 2017).

Diagnosing the patterns of SSH anomalies that are associated with AMOC changes can also depend on temporal scales dominating in specific geographical locations (Lorbacher et al., 2010; Yin and Goddard, 2013). The eastern boundary density appears to be the most important contributor to seasonal AMOC variability (Hirschi and Marotzke, 2007; Chidichimo et al., 2010), whereas the western boundary reflects longer-term variability (Häkkinen, 2001; Bingham and Hughes, 2009; Elipot et al., 2014; Frajka-Williams, 2015). Numerical and observational studies have shown that using SSH at 41° N (across the Atlantic) (Willis, 2010), 40-50° N (along the U.S. East coast) (Bingham and Hughes, 2009) or 30° N (and 70° W) (Frajka-Williams, 2015) can recover the AMOC's interannual to decadal variability, whereas (Little et al., 2017) shows that 40-45° N in a coupled model is representative of longer multi-decadal AMOC variability.

4.1.2 Decomposing the AMOC

Another approach is to utilise correlations between the SSH and other near-surface currents or isolated components of the AMOC as indices. Altimetry and tide gauge sea level have been used to reconstruct the decadal variability of the North Atlantic Current, intergyre region or the Gulf Stream, considering the north-south geostrophic relationship on the U.S. East coast (Häkkinen, 2001; McCarthy et al., 2015b) or between Bermuda and the U.S. coast (Ezer, 2015). Away from the boundaries, the vertical density structure is almost entirely described by the first baroclinic mode which provides information about the ocean structure in the top 1,000 m, or UMO (Szuts et al., 2012; Hirschi et al., 2009; Frajka-Williams, 2015). RAPID AMOC change is also shown to primarily occur in waters above the thermocline and concurrent with changes in SSH being dominated by steric height changes above 1,000 m (Smeed et al., 2018). The western boundary's geostrophic contribution explains 74% of the total AMOC's variance for time scales longer than six months (but shorter than the seven years of data available at the time) (Elipot et al., 2014). Frajka-Williams (2015) focuses on this by determining the location of maximum correlation in the western basin between satellite altimeter data and RAPID's UMO ($r = 0.92$). The study recovers a similar 80% of the upper 1,100 m transport's interannual variability at 26.5° N but stresses that with only 10 years of observational data to validate the reconstruction (and being the same data used to train the reconstruction), further analysis is required (Frajka-Williams, 2015).

Lastly, not only the timescale but also the time period can change the relationship between the AMOC and SSH. Little et al. (2017) show that in one CMIP5 model (CESM-LE), between 25 and 45° N the AMOC can be related to 29% of the dynamic sea level variance from 1920-2010 but 89% from 2011-2100. This suggests that as the scenario impact increases, and the AMOC slow-down signal strengthens, so does the association between the AMOC and SSH (Little et al., 2017).

This study tests numerous hypotheses to identify whether there is a robust relationship between the variability and trends of AMOC and SSH data across observations and ocean-only or coupled numerical models. The tests include different regional patterns of the SSH, time periods, time scales and regression methods to generate a proxy of past and future AMOC at 26.5° N. The motivation behind using SSH is to verify whether a robust 13-year AMOC-SSH relationship can be established in order to exploit the longer tide gauge or satellite data and hence reconstruct a multi-decadal AMOC timeseries in the past. Ultimately, the aim is to investigate if RAPID's decadal decline is part of internal variability or a multi-decadal trend.

4.2 Data: *observational and numerical model AMOC and SSH*

For the observational section of the analysis, the sea level tide gauge data is used from the Permanent Service for Mean Sea Level (Holgate et al., 2013; , PSMSL) (obtainable from www.psmsl.org). An average sea level is computed from the anomalies of 16 stations on the eastern boundary and 13 stations on the western boundary between 23.5° N and 29.5° N (i.e., 26.5 ± 3° N). This range is used since the RAPID moorings are located between 23°45' N (mooring EB1) and 27°51' N (mooring EBH4) and the only eastern boundary tide gauge stations are on the Canary Islands between 27.5 and 29.5° N. Although the tide gauge data is available from 1933 for a few stations, annual means are computed from monthly data since 1958 to remain consistent with the NEMO numerical model output time available (described below). The AMOC transport data are from the RAPID transbasin array, as the maximum vertically accumulated streamfunction at 26.5° N (described in McCarthy et al. (2015a) and downloadable from https://www.rapid.ac.uk/rapidmoc/rapid_data/datadl.php). Annual averages are computed from the monthly means from January 2004 to December 2016; the first year therefore has three months of missing data (since RAPID starts in April 2004) and the first two months of 2017 available are omitted. The AMOC proxy observation reconstructions therefore have a sample size of N = 59 years (from 1958 to 2016, inclusive).

The first set of numerical model output data used is NEMO, ORCA025 (Nucleus for European Modelling of the Ocean, Oceanic Remote Chemical/Optical Analyzer), hereafter NEMO, with a Drakkar Forcing (see Barnier et al. (2006) for more details). It has a tripolar grid with a nominal horizontal resolution of 1/4 degrees and 46 vertical levels, with the 'surface' data at 6 m (Madec and the NEMO Team, 2016). Annual averages are again computed from monthly means for both AMOC and SSH data, available from 1958 to 2012. The SSH eastern and western boundaries are averages of the values closest to the coast at the same latitude range described for RAPID (23.5-29.5° N) and the AMOC streamfunction is taken at a 1,000 m depth, at the latitude closest to 26.5° N. The reconstructions based on NEMO AMOC therefore have a sample size of N = 55 years (from 1958 to 2012, inclusive).

The second set of numerical model data output is from the Coupled Model Intercomparison Project Phase 5 of the Intergovernmental Panel on Climate Change. 19 of these models have been selected: (1) ACCESS1-0, (2) bcc-csm1-1, (3) CanESM2, (4) CCSM4, (5) CESM1-BGC, (6) CMCC-CM, (7) CNRM-CM5, (8) CSIRO-Mk3-6-0, (9) EC-EARTH, (10) FGOALS-g2, (11) FIO-ESM, (12) GFDL-CM3, (13) GISS-E2-R-CC, (14) HadGEM2-CC, (15) inmcm4, (16) IPSL-CM5A-MR, (17) MIROC-ESM, (18) MRI-CGCM3, (19) NorESM1-M. Since the future scenario timeseries all run until at least 2100, a sample size for the reconstructions of N = 94 years have been selected for both the historical data (i.e., from 1912 to 2005) and for the future data (i.e., from 2006

to 2100). Two future scenarios are used, namely RCP4.5 'stabilisation' and RCP8.5 'business-as-usual' scenarios (Taylor et al., 2012). Pre-processing of the CMIP5 data requires regridding the 19 models to the coarsest resolution, 2x2°. This is done by finding the nearest even latitude and longitude (nearest neighbour) to produce a 2x2° grid cell from 20 to 60° N. For the AMOC, again the closest value to 26.5° N and 1,000 m depth is used, computed from the respective native grid.

4.3 Methods: *seven hypotheses testing the AMOC-SSH relationship*

First, the method for generating an AMOC reconstruction is outlined. To calculate the regression coefficient between the AMOC and SSH, a training period (TP) must first be defined. This establishes the number of years over which the AMOC is regressed against the SSH. Several hypotheses use a 13-year TP to test the relationship over the RAPID timeseries length and to extend the AMOC data by N years into the past. The anomalies of the annually averaged AMOC and SSH data, $\hat{Y}_t$, are computed by removing the mean from the 13-year TP (not the entire timeseries), as shown in the equation below:

$$\hat{Y}_t = Y_t - \overline{Y_t}|_{TP}, \tag{4.1}$$

where Y_t is the original annual mean of the variable (AMOC [Sv] or SSH data [m]), $\overline{Y_t}|_{TP}$ is the mean over the TP.

The AMOC is then reconstructed (AMOC*) over N years using the following equation:

$$\text{AMOC}^*{}_t = \sum_{i=1}^{k} \beta_i \hat{Y}_{ti}, \tag{4.2}$$

where k represents the number of predictors used for the regression and β is the linear regression coefficient between the AMOC and SSH over the training period, which is multiplied by the entire timeseries, Y_{ti} (i.e., the anomalies of the annually averaged SSH, for example). A residual analysis for each hypothesis tested below indicated that the noise term of the regression models do not exhibit autocorrelation nor heteroscedasticity (pval>0.05 for both the the Durbin-Watson and Engle-ARCH tests, respectively). Therefore an ordinary least squares regression model is suitable (see Chapter 2 for more information on the residual analyses).

Two statistical measures of skill for the reconstruction are used throughout this chapter: (1) the goodness of fit (R^2, between 0 and 1) which measures the proportion of AMOC variability explained by the reconstruction and (2) the percentage of relative error (Re, between 0 and 100%) between the AMOC trend and the reconstruction's trend. A skilful

reconstruction is defined here by R^2>0.5 and/or Re<50%. Note that the results depend on the statistical criteria defined in this study.

Hypotheses 1: There is a relationship between the eastern and western boundary SSH and the AMOC, using RAPID AMOC and tide gauge sea level. The observation reconstructions are generated using a multiple linear regression (using two predictor variables, $k = 2$, for the ordinary least squares fit) between the AMOC data and the eastern and western boundary SSH over the 13-year TP (2004 to 2016). Equation 4.2 therefore has two coefficients, (β_1 for the eastern SSH and β_2 for the western SSH).

Hypotheses 2: There is a relationship between the AMOC and SSH at the boundaries in NEMO, a forced ocean model. This is identical to Hypothesis 1, however the TP is from 2000 to 2012 for NEMO.

Hypothesis 3: A robust AMOC reconstruction can be generated using east and west boundary SSH in CMIP5. The same multiple linear regression, $k = 2$, is repeated from Hypotheses 1 and 2, now with the CMIP5 13-year TP from 1993 to 2005 for the historical output and from 2087 to 2099 for future scenarios. Instead of confining the test to only 23.5° N to 29.5° N for SSH and 26.5° N for AMOC as in the first 2 hypotheses, however, now a spatial robustness test is included by computing east and west regression coefficients (β_1 and β_2 in Equation 4.2) every 2 degrees from 20 to 60° N, with the AMOC in the central latitude.

Hypothesis 4: A robust AMOC reconstruction can be generated using the maximum western basin correlation of AMOC to SSH in CMIP5 (ordinary least squares). Pointwise correlation maps of the AMOC at 26.5° N against the SSH across the North Atlantic (between 20 and 60° N) are used to find the absolute maximum correlation coefficient in the western subtropical gyre between 20 and 45° N and west of 40° W (hereafter, SSH*). This single point then serves as the input for the ordinary least squares (hereafter, OLS) regression to produce one coefficient (β_1) in equation 4.2. The last 13 years of each CMIP5 scenario as in Hypothesis 3 are used for the TP.

Hypothesis 5: A robust AMOC reconstruction can be generated using the total North Atlantic basin SSH against AMOC in CMIP5 (partial least squares). SSH at each grid point across the entire North Atlantic (20 to 60° N) serves as the multiple linear regression, partial least squares, input. This regression model is used in order to avoid violating the assumption of independence of the SSH predictor variables; PLS can be used in the presence of collinearity (see Chapter 2: Data and Methods for more informaion). Again, the same CMIP5 13-year TP length is used for the reconstruction regressions.

The next analysis then aims to answer the question: *How many years are required to reconstruct the AMOC using SSH in CMIP5?* The TP is therefore extended (13<TP<94 years) and reconstructions generated using the OLS and PLS regression methodologies

described for Hypotheses 4 and 5. The number of years required to produce a reconstruction that represents the AMOC (hereafter, n*) is defined by the R^2 crossing the 0.5 threshold and remaining above it. To determine how long the sample size must be before the reconstruction's trend captures the AMOC's trend, the Re must pass and remain below the 50% threshold. The R^2 and Re over the training period and the full 94-year period are computed. The R^2 is then used to define three reconstruction classifications: (1) A true sufficient length: the n* using the R^2 over the TP (n^*_{TP}) is larger than the n* using the R^2 of the total reconstruction (n^*_{total}), i.e., the training period sample size is sufficient to reconstruct the total timeseries. (2) A false sufficient length: the n^*_{TP} is smaller than the n^*_{total}, i.e., n* is underestimated when the R^2 over the TP suggests it is sufficient to reconstruct the 94 years when it is not. (3) An insufficient length: 94 years is not sufficient to generate a reconstruction. Therefore:

$$\begin{aligned} \text{True sufficient length} &: n^*_{TP} \geq n^*_{total} \\ \text{False sufficient length} &: n^*_{TP} < n^*_{total} \\ \text{Insufficient length} &: n^*_{TP} = n^*_{total} > 94\,\text{yrs} \end{aligned} \tag{4.3}$$

Hypothesis 6: A robust AMOC reconstruction can be generated using the maximum western basin SSH correlation against the Upper Mid-Ocean instead of the total AMOC in CMIP5. This hypothesis is based on the methodology used in Frajka-Williams (2015) where the Upper Mid-Ocean (UMO) geostrophic component (top 1,100 m) of the AMOC is isolated. This eliminates any contribution of the wind (Ekman transport) and Gulf Stream on the overall transport at 26.5° N. Due to the coarse resolution of the CMIP5 models, the Florida Straits is not resolved and the Gulf Stream cannot be removed. Frajka-Williams et al. (2016), however, show that although the Gulf Stream's subannual fluctuations have a large impact on the AMOC, interannual variability is very low. Therefore, the assumption can be made that the approximation of the UMO (hereafter, UMO*) is accurate by computing the AMOC minus the Ekman transport (the net transport in near-surface waters driven by the wind). The Ekman transport is estimated from the wind stress which is available as an output from only 9 of the 19 CMIP5 models selected in this study, namely: (1) ACCESS1-0, (2) CESM1-BGC, (3) CMCC-CM, (4) CNRM-CM5, (5) CSIRO-Mk3-6-0, (6) EC-EARTH, (7) inmcm4, (8) IPSL-CM5A-MR, (9) NorESM1-M. The following equation from Sévellec and Huck (2016) is used:

$$\psi_{Ek} = -\overline{\tau_x}\left(\frac{W}{f\rho_0}\right)\left(\frac{z+H}{H}\right), \tag{4.4}$$

where ψ_{Ek} is the Ekman streamfunction (Sv) at 26.5° N, $\overline{\tau_x}$ is zonally averaged wind stress, W is the width of the basin (6500 km), f is the Coriolis parameter at 26.5° N (6.5 x 10^{-5}), ρ_0 is the average density of the ocean (1025 kg m^{-3}), z is the depth over which Ekman can affect the overturning circulation (1,000 m), and H is the average depth of the ocean (4,500 m).

Hypothesis 7: A robust AMOC reconstruction can be generated using the regression of sea surface temperature (SST) instead of SSH against the AMOC in CMIP5. The same hypotheses as 4 and 5 are tested as well as determining the n*, replacing the SSH by SST. The only difference here resides in the fact that the entire North Atlantic is used to compute the absolute maximum correlation of SST against AMOC for Hypothesis 4 (as opposed to only the western subtropical basin for SSH).

4.4 Results and Discussion

4.4.1 Hypothesis 1: There is a relationship between the eastern and western boundary SSH and the AMOC, using RAPID AMOC and tide gauge sea level

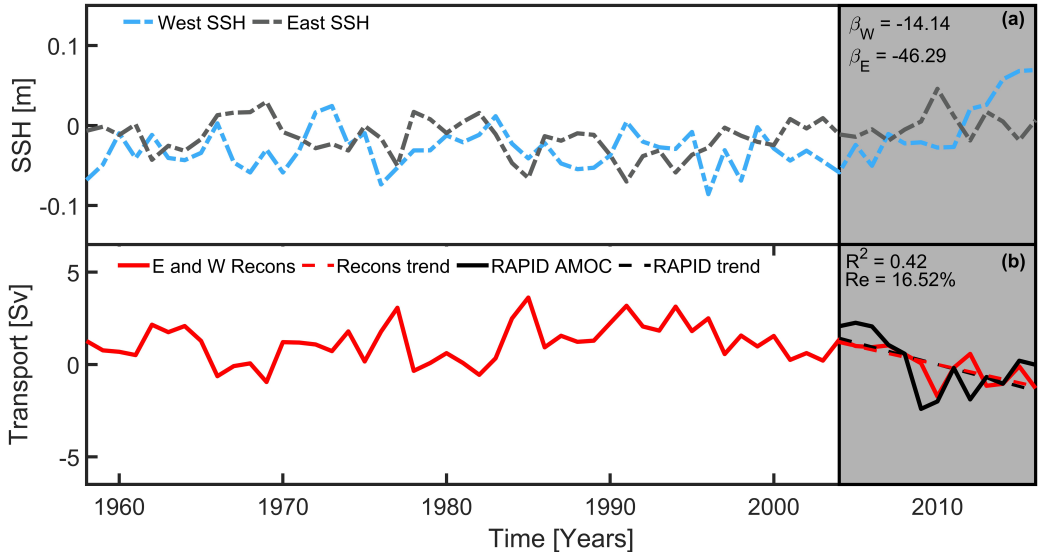

FIGURE 4.1: Reconstruction using observations. (a) Annual mean anomalies of western SSH [m] (dashed light blue line) and eastern SSH [m] (dashed grey line) from tide gauges averaged between 23.5-29.5° N from 1958 to 2016. (b) Annual mean anomalies of RAPID data [Sv] from 2004 to 2016 (black) with the reconstructed AMOC [Sv] (red) from the OLS regression between the AMOC and tide gauge eastern and western SSH over the training period (shaded grey) and their respective linear trends (dashed black and red lines). The R^2 and relative error of the trends over the TP are displayed, as well as the regression coefficients for the west and east SSH (β_W and β_E, respectively).

The first reconstruction using observations from tide gauges on the eastern and western boundaries of the North Atlantic (Figure 4.1a) against the RAPID AMOC data generates a 13-year trend of -0.2 Sv yr^{-1} between 2004 and 2016 that resembles the target RAPID trend of -0.24 Sv yr^{-1} (Figure 4.1b). The relative error between the trends is therefore low (Re = 16.52%), however the interannual variability is not well represented by the reconstruction (R^2 = 0.42). A few extra hypotheses were tested, including using a regression of the E and W SSH against the Upper Mid-Ocean component of RAPID

instead of the total AMOC (testing the Hirschi and Marotzke (2007) methodology), however the R^2 was lower (0.22) and the relative error slightly higher (25%). Results were also worse if only the W SSH was regressed against the total AMOC ($R^2 = 0.13$, Re = 44.45%) or against the UMO ($R^2 = 0.21$, Re = 30.73%), suggesting that the Frajka-Williams (2015) methodology, that uses satellite altimetry, does not work with tide gauge data. Even though all the reconstructions do represent the 13-year RAPID trend (Re<50%), they fail to reproduce the interannual variability. Regarding the relative contribution from the W and E (Figure 4.1a), although visually the strongest signature or trend appears to be coming from the western boundary (as suggested by Häkkinen (2001); Bingham and Hughes (2009); Elipot et al. (2014)), the regression coefficients (β_W of -14.14, and β_E of -46.29), show the opposite. This could be indicative of the relationship demonstrated between the AMOC and seasonally-varying wind-stress curl on the eastern boundary (Kanzow et al., 2010; Chidichimo et al., 2010), that Matei et al. (2012) speculate could repeatedly imprint onto eastern boundary density and reflects forcing over a longer period in the past. This implies that the eastern boundary could be dominant on interannual timescales, which might explain why the 2009-2010 extreme event with a 30% decline in RAPID transport is also somewhat represented by the reconstruction (Figure 4.1b). With the RAPID data being available from 2004, however, the rest of the reconstruction (from 1958 to 2004) cannot be compared to target data for validation. This therefore introduces the need for and motivation behind using numerical model output for the next reconstructions in order to test and compare them to multi-decadal AMOC trends and interannual variability.

4.4.2 Hypothesis 2: There is a relationship between the eastern and western boundary SSH and the AMOC, using NEMO, a forced ocean model

The western and eastern boundary SSH output from the forced ocean numerical model, NEMO, both display a multi-decadal increase from 1958 to 2012 (Figure 4.2a), while the AMOC shows a multi-decadal decrease (Figure 4.2b). Over the TP, the western SSH variability is larger than the east, however the regression coefficients (similarly to the observations), once again support the dominance of the eastern boundary SSH (β_W of -1.91, and β_E of -47.30). The reconstruction also shows an improvement over the TP compared to RAPID's reconstruction, where the relative error is 13.47% and R^2 is 0.57. The advantage here is being able to compare the reconstruction to the NEMO AMOC timeseries from 1958 to 2012. There is a low relative error between the multi-decadal trend of the AMOC and the reconstruction's trend (16.03%) and almost 60% of the interannual variability is represented by the reconstruction. The NEMO reconstruction represents the 2009-2010 event almost identically to the model AMOC data.

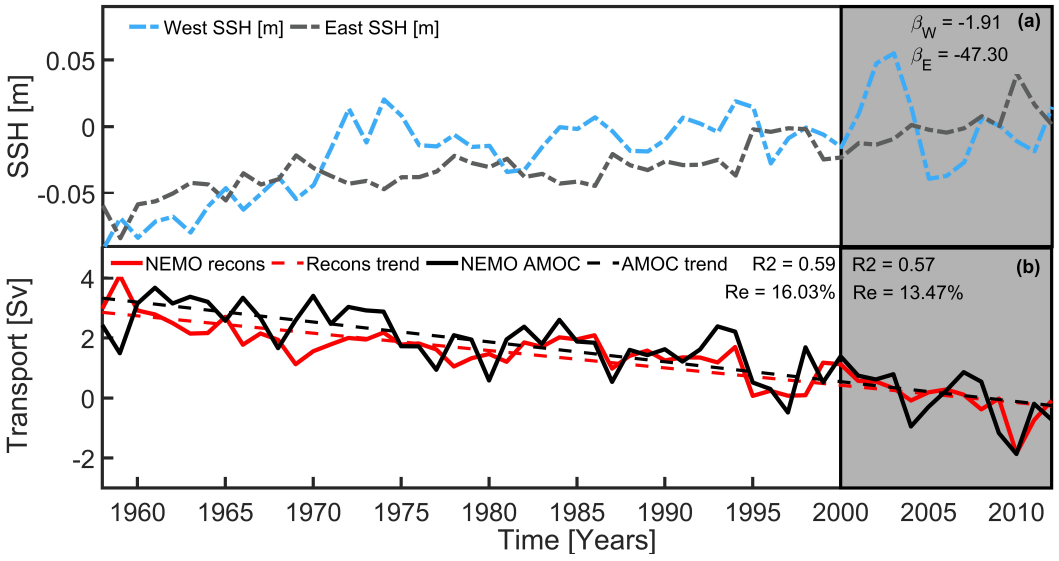

FIGURE 4.2: Reconstruction using the ocean-only NEMO numerical model. (a) Annual mean anomalies of NEMO western SSH [m] (dashed light blue line) and NEMO eastern SSH [m] (dashed grey line) averaged between 23.5 and 29.5° N from 1958 to 2012. (b) Annual mean anomalies of NEMO AMOC data (black) with the reconstructed AMOC (red) from the OLS regression between the AMOC and eastern and western SSH over the training period (shaded grey) with their respective linear trends (dashed red and black lines). The R^2 and relative error of the trends over the total period and TP are displayed, as well as the regression coefficients for the west and east SSH (β_W and β_E, respectively).

Testing for temporal robustness of this relationship over the 55 years of NEMO data, however, the E and W linear regression coefficients over different 13-year TPs show a large variability (Figure 4.3a). The trends of the reconstructions resulting from different TPs are also inconsistent through time (Figure 4.3b), ranging from -0.1 Sv yr^{-1} to 0.004 Sv yr^{-1} (with an average value of -0.05 Sv yr^{-1}). Although the trend values are mostly negative, the majority of the reconstructions underestimate the actual multi-decadal NEMO trend of -0.06 Sv yr^{-1}. This shows that extending a timeseries using 13 years of SSH as a proxy depends on the assumption that the relationship between SSH at the boundaries and the AMOC remains constant over any 13-year period, or that 13 years is enough to capture the secular relationship, and both such assumptions are not valid.

Since the relationship could be influenced by the forcing of ocean-only NEMO model, the next hypothesis checks both temporal and spatial robustness of the AMOC-SSH relationship in an ensemble of coupled ocean-atmosphere models from CMIP5.

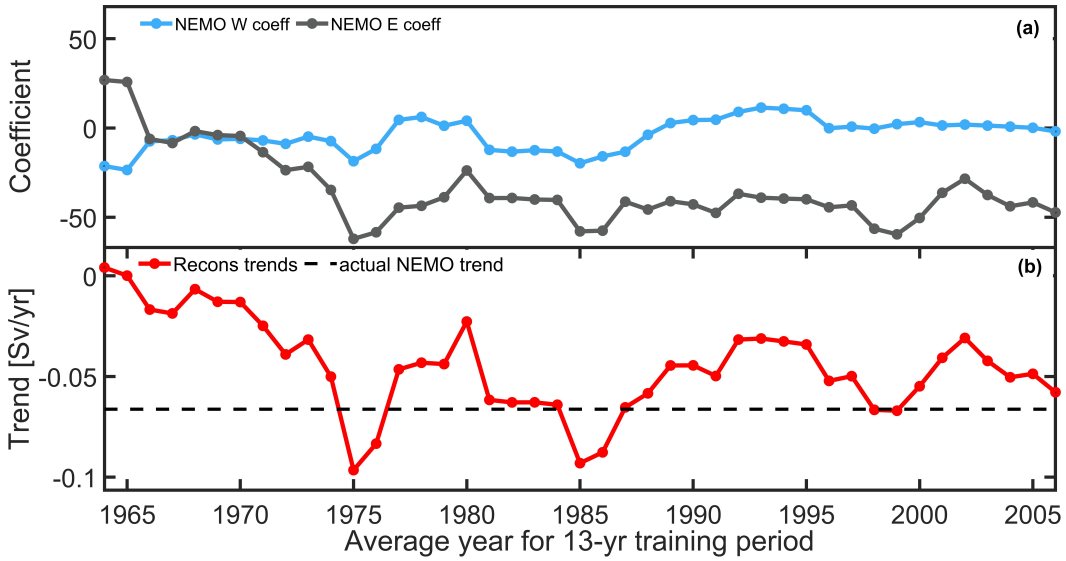

FIGURE 4.3: (a) The NEMO reconstruction coefficients as a function of sliding window 13-year training periods for W SSH coefficients (light blue dots and line) and E SSH coefficients (grey dots and line) averaged between 23.5 and 29.5° N from 1958-1960 to 2000-2012. The x-axis shows the midpoint of the 13-year training period and the sliding window moves by increments of 1 year. (b) same as (a) but for the reconstruction secular (1958-2012) trends (red dots and line) and the actual NEMO trend (dashed black line).

4.4.3 Hypothesis 3: A robust AMOC reconstruction can be generated using east and west boundary SSH in CMIP5

For comparison with the observations and NEMO, the first CMIP5 reconstructions are generated from the multiple linear OLS regression between the AMOC at 26.5° N and SSH on the eastern and western averaged between 23.5 and 29.5° N. Results from the three CMIP5 experiments used, (1) historical, (2) RCP4.5, and (3) RCP8.5 show poor skill in reconstructing the AMOC (Tables 4.1, 4.2, and 4.3). Fewer than half of the 19 models produce R^2>0.5 and relative error<50%, regardless of computing the values over the full timeseries (94 years) or the TP (13 years) and regardless of the experiment. For example, none of the historical reconstructions reproduce the interannual variability over the full time frame or TP. These results show that 13 years are not enough to reconstruct the AMOC in CMIP5.

The inconsistency of the results from the E and W reconstructions is highlighted by the large variability of E and W regression coefficients across the models at different latitudes from 20 to 60° N (Figure 4.4). Although one could have expected the eastern boundary coefficients to dictate the reconstructions, as is the case in both the observation and NEMO reconstructions, it is not the case for CMIP5. The 19 models show a large intermodel spread (standard deviation in Figure 4.4) across positive and negative coefficient values in all experiments for both E and W coefficients. The ensemble mean in RCP4.5 and RCP8.5 suggests that there could be an anti-correlation between western boundary SSH and AMOC at all latitudes (Figure 4.4c and Figure 4.4e), which could

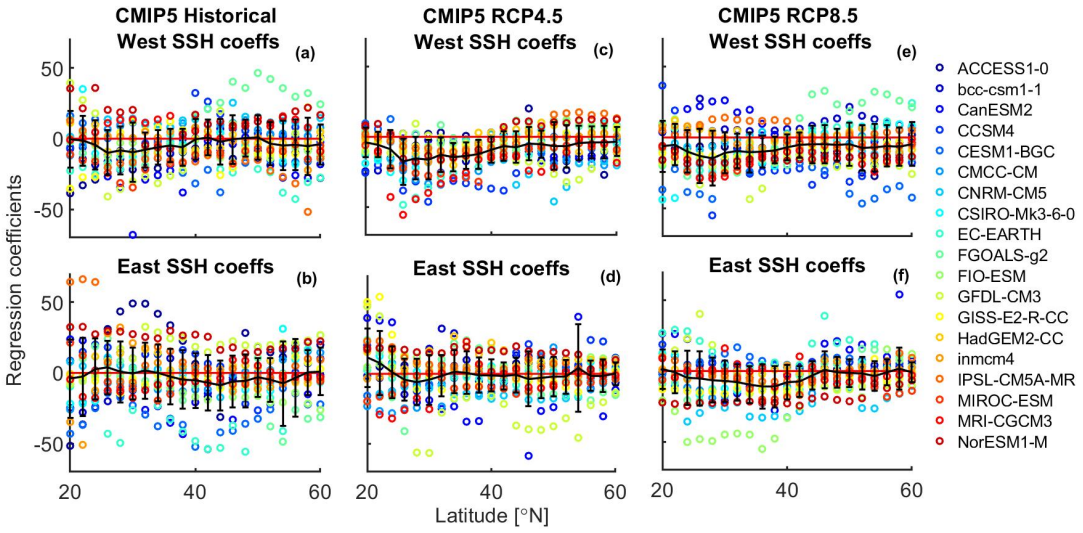

FIGURE 4.4: The CMIP5 regression coefficients between the AMOC at 26.5° N and SSH every 2° from 20 to 60° N on the western boundary (a) and eastern boundary (b) from the last 13 years (TP) of the historical experiment. (b) and (c) are the same but for future scenario RCP4.5 and (d) and (e) for future scenario RCP8.5. Each of the 19 CMIP5 models is represented by a different coloured circle and the ensemble mean is represented by a solid black line with errorbars of 1 standard deviation.

support the results seen in Frajka-Williams (2015). Without ignoring that the upper limit of standard deviation crosses into the positive values almost everywhere (suggesting that this anticorrelation is not a robust relationship, once again), this finding serves as an incentive for the next hypothesis (Hypothesis 4, Section 4.4.4) to use only the maximum correlation location, which on average seems to appear around 30° N in both RCP4.5 and RCP8.5 (Figure 4.4(c) and (e)), as is also found in Frajka-Williams (2015).

4.4.4 Hypothesis 4: A robust AMOC reconstruction can be generated using the maximum western basin correlation of AMOC to SSH in CMIP5 (ordinary least squares)

Since the combined western and eastern coastal SSH does not produce a robust fingerprint of the AMOC, a univariate regression is now tested using the maximum western subtropical basin's SSH, following suggestions from previous studies indicating that the western basin represents the variability of the AMOC (Häkkinen, 2001; Bingham and Hughes, 2009; Willis, 2010; Elipot et al., 2014; Frajka-Williams, 2015). The location of maximum absolute correlation between the AMOC at 26.5° N and SSH from 20 to 45° N and east of 40° W (hereafter SSH*) is determined from the correlation maps for each CMIP5 experiment (Figure 4.5 for historical, Figure 4.6 for RCP4.5, and Figure 4.7 for RCP8.5). These maps once again indicate that there is no consistent intermodel relationship since the location of the SSH* is different across the 19 models within an experiment, as well as for the same model across the three experiments. Furthermore,

TABLE 4.1: Reconstruction results for each of the 19 CMIP5 models under the historical scenario using three reconstruction methodologies and SSH locations (1) eastern and western boundary SSH, (2) maximum western basin correlation location (ordinary least squares regression), (3) Total North Atlantic SSH (partial least squares regression). Statistical values include the R^2 over the training period (1992 to 2005), R^2 over the total timeseries (1912 to 2005) and relative error over the total period. The number of models that have a good AMOC* reconstruction (an R^2>0.5 or Re<50%) is shown in the last row, as well as represented in bold.

	East and West SSH			Max W SSH: OLS			Total NA SSH: PLS		
CMIP5 Model names	TP R^2	Total R^2	Total Re	TP R^2	Total R^2	Total Re	TP R^2	Total R^2	Total Re
ACCESS1-0	0.39	0.05	**20.59**	**0.78**	0.00	**33.78**	**0.88**	0.05	**8.49**
bcc-csm1-1	0.18	0.14	**18.49**	0.26	0.00	192.73	0.24	0.00	186.97
CanESM2	0.15	0.00	52.17	0.48	0.00	**44.63**	0.43	0.00	133.92
CCSM4	0.01	0.00	97.48	0.44	0.00	163.30	**0.75**	0.00	239.81
CESM1-BGC	0.03	0.00	88.86	**0.54**	0.00	196.79	**0.89**	0.00	100.21
CMCC-CM	0.05	0.01	**30.98**	0.45	0.00	272.20	**0.89**	0.00	241.52
CNRM-CM5	0.18	0.00	626.18	0.33	0.00	821.12	**0.83**	0.00	1343.22
CSIRO-Mk3-6-0	0.07	0.03	**18.68**	**0.55**	0.06	**10.27**	**0.91**	0.29	**4.79**
EC-EARTH	0.18	0.00	227.99	**0.60**	0.00	170.09	**0.83**	0.00	**11.38**
FGOALS-g2	0.08	0.00	95.97	0.41	0.00	148.07	**0.91**	0.00	**15.69**
FIO-ESM	0.01	0.00	95.74	0.25	**0.53**	**1.49**	**0.74**	0.00	**38.40**
GFDL-CM3	0.21	0.36	**4.94**	**0.74**	0.42	**41.39**	**0.87**	0.48	**39.82**
GISS-E2-R-CC	0.29	0.00	395.26	**0.57**	0.00	2751.60	**0.80**	0.00	280.14
HadGEM2-CC	0.13	0.00	67.95	0.40	0.00	199.45	**0.88**	0.00	164.37
inmcm4	0.03	0.00	122.94	0.27	0.00	124.08	**0.92**	0.00	107.03
IPSL-CM5A-MR	0.16	0.00	166.95	**0.58**	0.00	**24.34**	**0.73**	0.00	289.93
MIROC-ESM	0.14	0.04	93.20	0.33	0.00	**48.39**	**0.88**	0.00	315.03
MRI-CGCM3	0.26	0.02	**47.23**	**0.59**	0.00	129.38	**0.94**	0.13	124.46
NorESM1-M	0.42	0.00	951.80	**0.54**	0.00	651.54	**0.92**	0.00	1856.21
Num of good AMOC*	0	0	6	9	1	7	17	0	6

the timeseries of the SSH* anomalies and the values of absolute maximum correlation over the 13-year training period vary greatly in each scenario and each model (Figures 4.8, 4.9, 4.10). This leads to the reconstructions also not capturing the interannual variability nor the long-term trend of the AMOC timeseries in the three experiments (Figures 4.11, 4.12, 4.13). Although the results are slightly better than the E and W reconstructions, there are still fewer than half of the models with an R^2>0.5 and an Re<50% over the TP and the total timeseries, regardless of the scenario (Tables 4.1, 4.2 and 4.3). The other prominent feature is that the patterns of correlations (patches of positive and negative correlations in Figures 4.5, 4.6, and 4.7) are completely different across all models.

TABLE 4.2: As Table 4.1 but for RCP4.5.

	East and West SSH			Max W SSH: OLS			Total NA SSH: PLS		
CMIP5 Model names	TP R^2	Total R^2	Total Re	TP R^2	Total R^2	Total Re	TP R^2	Total R^2	Total Re
ACCESS1-0	0.01	0.00	114.89	0.32	0.00	88.18	**0.71**	0.00	176.86
bcc-csm1-1	0.04	0.02	66.28	0.24	0.00	103.61	**0.75**	0.00	81.95
CanESM2	0.05	0.00	63.61	0.39	0.00	160.85	**0.86**	0.00	**34.63**
CCSM4	0.14	0.00	157.33	**0.52**	0.00	385.52	**0.75**	0.00	180.27
CESM1-BGC	0.03	0.00	92.25	0.49	0.00	85.85	**0.62**	0.00	58.39
CMCC-CM	**0.54**	0.00	1776.17	**0.64**	0.00	795.66	**0.74**	0.00	911.60
CNRM-CM5	0.26	0.00	125.74	0.41	0.00	122.30	**0.89**	0.00	131.04
CSIRO-Mk3-6-0	0.11	0.00	131.11	**0.51**	0.00	145.38	**0.53**	0.00	111.88
EC-EARTH	**0.54**	0.43	69.87	**0.65**	0.00	112.95	**0.78**	0.04	82.99
FGOALS-g2	0.01	0.00	106.87	0.41	0.00	116.65	0.50	0.00	115.80
FIO-ESM	0.15	0.00	92.17	0.32	0.00	92.93	**0.83**	0.00	158.30
GFDL-CM3	0.04	0.00	110.81	0.27	0.00	119.49	**0.92**	0.00	183.64
GISS-E2-R-CC	0.20	0.00	281.16	0.35	0.00	239.94	**0.83**	0.48	**42.49**
HadGEM2-CC	0.03	0.24	51.34	**0.52**	**0.74**	**4.99**	**0.91**	0.28	68.32
inmcm4	0.02	0.00	65.17	**0.53**	0.05	**27.47**	**0.71**	0.00	99.86
IPSL-CM5A-MR	0.08	0.00	132.76	0.38	0.00	184.66	**0.83**	0.00	81.25
MIROC-ESM	0.45	**0.65**	**28.62**	**0.58**	0.00	74.28	**0.95**	**0.67**	**26.77**
MRI-CGCM3	**0.72**	0.00	326.44	**0.63**	0.00	207.25	**0.93**	0.00	**9.26**
NorESM1-M	0.08	**0.74**	**1.98**	0.33	**0.56**	**11.46**	**0.79**	0.00	140.61
Num of good AMOC*	3	2	2	8	2	3	18	1	4

4.4.5 Hypothesis 5: A robust AMOC reconstruction can be generated using the total North Atlantic basin SSH against AMOC in CMIP5 (partial least squares)

Although there seem to be no consistent spatial patterns of correlation between SSH and the AMOC across the 19 models, a more flexible approach is now examined, using the basin-wide SSH, where any dominant signatures of the AMOC would be highlighted and selected for the reconstruction. This multiple linear regression requires a partial least squares (PLS) regression method to account for collinearity between each SSH value (the regression predictors). Such an analysis is beneficial for testing numerous previous studies that have suggested that the AMOC's variability can be estimated using the SSH from different locations, for example using the leading SSH EOF of a dipole relationship between the Gulf Stream and subpolar gyre (e.g., Häkkinen (2001) or a North-South relationship along the US east coast (e.g., McCarthy et al. (2015b)). Similarly to using the SSH*, however, the reconstructions also poorly represent the AMOC (Figures 4.11, 4.12, and 4.13). The only difference is that the majority of the models (17 out of 19 for historical and 18 out of 19 models for RCP4.5 and RCP8.5) can reproduce the TP interannual variability (R^2>0.5). For the full timeseries, however, fewer than half of

TABLE 4.3: As Table 4.1 but for RCP8.5.

	East and West SSH			Max W SSH: OLS			Total NA SSH: PLS		
CMIP5 Model names	TP R^2	Total R^2	Total Re	TP R^2	Total R^2	Total Re	TP R^2	Total R^2	Total Re
ACCESS1-0	0.04	0.00	105.25	0.41	0.00	145.49	**0.82**	0.00	92.30
bcc-csm1-1	0.01	0.00	102.67	0.27	0.00	114.94	**0.77**	0.00	107.28
CanESM2	**0.52**	0.39	**33.51**	0.46	0.37	**41.21**	**0.95**	0.48	**7.77**
CCSM4	0.06	0.00	113.57	**0.61**	0.00	71.87	**0.87**	0.00	92.21
CESM1-BGC	**0.64**	0.00	103.38	**0.58**	0.00	78.42	**0.84**	0.00	130.44
CMCC-CM	0.32	0.40	51.55	0.36	**0.53**	**27.17**	**0.69**	0.00	95.93
CNRM-CM5	**0.56**	**0.66**	**4.82**	**0.62**	0.00	102.11	**0.82**	0.00	112.28
CSIRO-Mk3-6-0	0.46	0.00	63.46	**0.57**	0.00	133.15	**0.80**	0.36	**35.09**
EC-EARTH	0.34	0.00	125.63	0.34	0.00	117.00	**0.85**	0.00	76.12
FGOALS-g2	0.21	0.28	60.78	**0.72**	0.00	386.28	**0.60**	0.00	61.40
FIO-ESM	0.46	0.00	82.44	0.41	0.00	120.73	**0.92**	0.00	62.25
GFDL-CM3	0.26	0.08	54.35	0.45	0.00	100.39	**0.93**	0.00	80.90
GISS-E2-R-CC	0.14	0.00	84.99	0.41	0.00	115.19	**0.88**	**0.85**	**8.55**
HadGEM2-CC	0.04	0.00	118.62	**0.66**	0.30	**33.05**	**0.96**	0.00	65.22
inmcm4	0.12	0.00	106.04	0.41	0.00	104.88	**0.88**	0.00	**45.01**
IPSL-CM5A-MR	0.22	0.00	68.29	**0.72**	0.00	**48.13**	**0.90**	0.00	78.37
MIROC-ESM	0.27	0.33	**37.08**	0.34	**0.85**	**8.27**	0.46	0.37	**37.53**
MRI-CGCM3	0.22	0.00	160.00	0.32	0.00	142.72	**0.83**	0.00	87.46
NorESM1-M	**0.60**	**0.62**	**31.07**	**0.71**	**0.74**	**23.60**	**0.80**	**0.59**	**32.05**
Num of good AMOC*	4	2	4	8	3	6	18	2	6

the models generate a reconstruction that expresses the AMOC trend or variability of the models for all scenarios (Tables 4.1, 4.2 and 4.3). The measure of fit defined in this study using the TP suggests that 13 years of data are enough to reconstruct the same 13 years of the AMOC, however the extended AMOC* does not reproduce the multi-decadal interannual variability or trend of the AMOC.

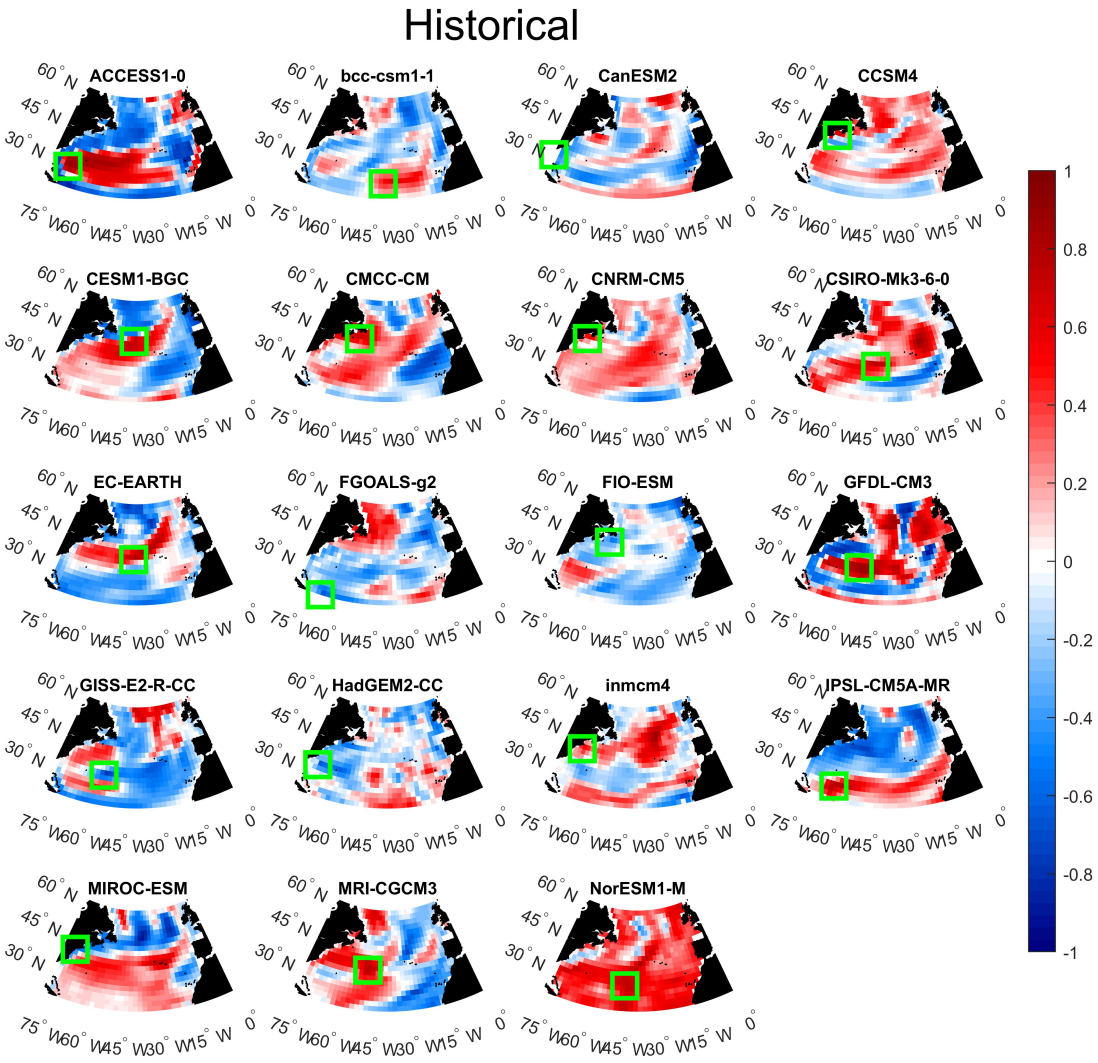

FIGURE 4.5: CMIP5 pointwise correlation maps between anomalies of annually averaged SSH [m] in the North Atlantic and the AMOC transport anomaly [Sv] at 26.5° N over the historical 13-year TP (1993 to 2005) in 19 CMIP5 models. The green boxes show the maximum absolute correlation coefficient location in the western sub-tropical gyre (between 20 and 45° N and west of 40° W).

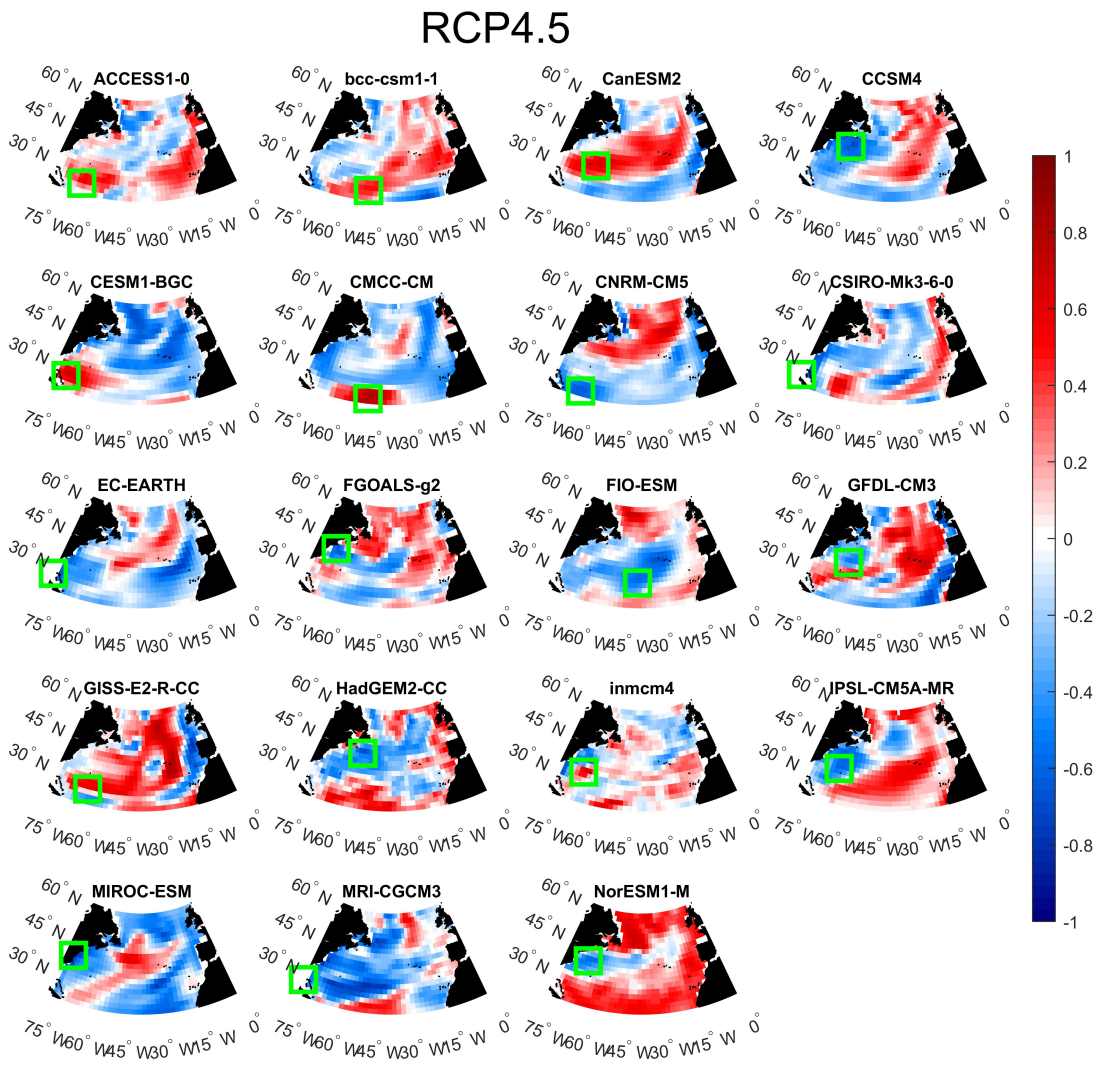

FIGURE 4.6: As Figure 4.5 but for RCP4.5 (therefore with the TP from 2087 to 2099).

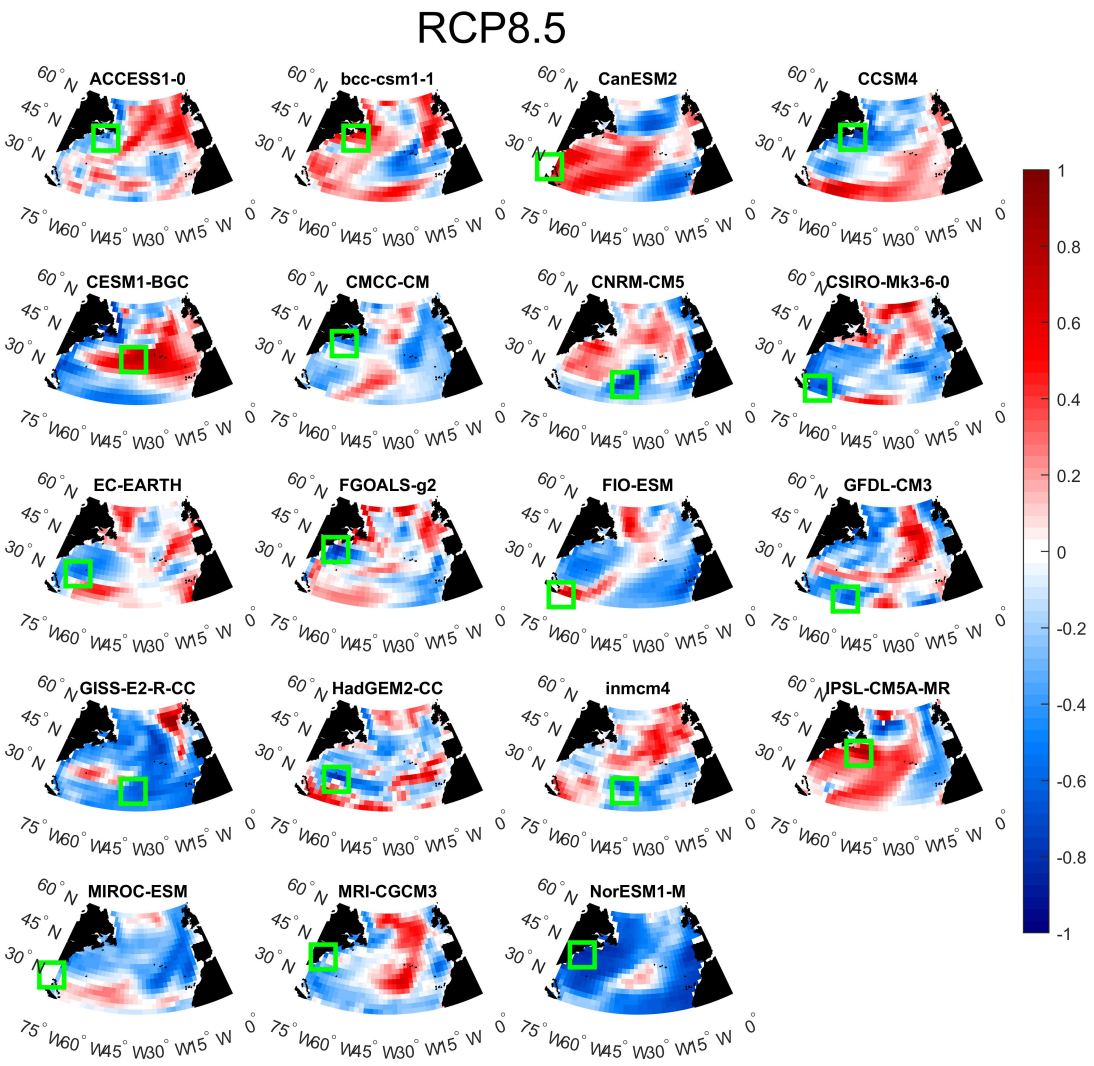

FIGURE 4.7: As Figure 4.5 but for RCP8.5 (therefore with the TP from 2087 to 2099).

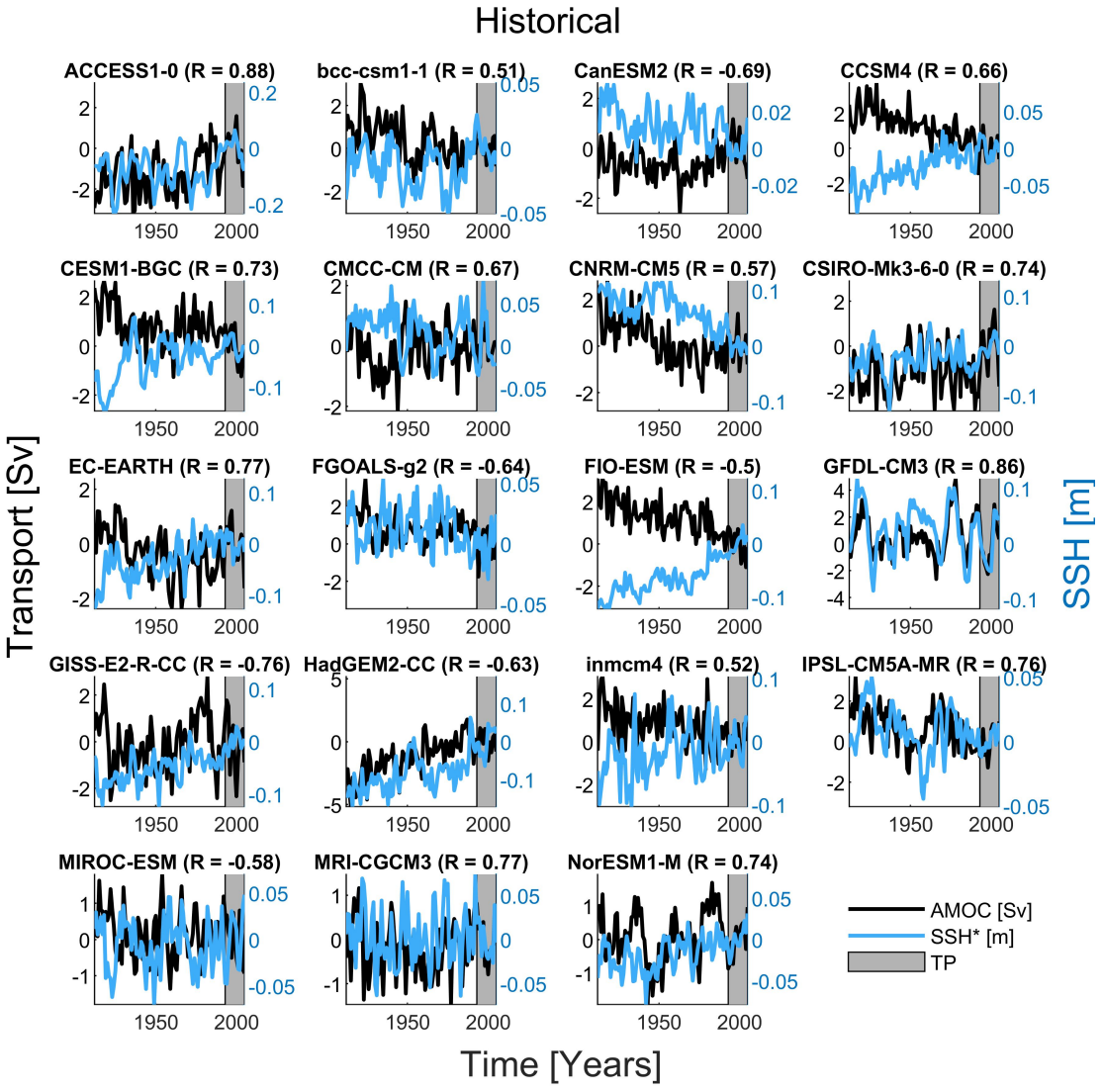

FIGURE 4.8: CMIP5 historical AMOC transport [Sv] anomalies (black lines) and the SSH anomalies [m] at the location of absolute maximum western boundary SSH correlation with AMOC (i.e., SSH*) for the 19 models (light blue line). The location of the SSH* timeseries is shown as green boxes in Figure 4.17. The value of this maximum correlation (R) over the training period (grey shaded region) is shown in the title of each subplot.

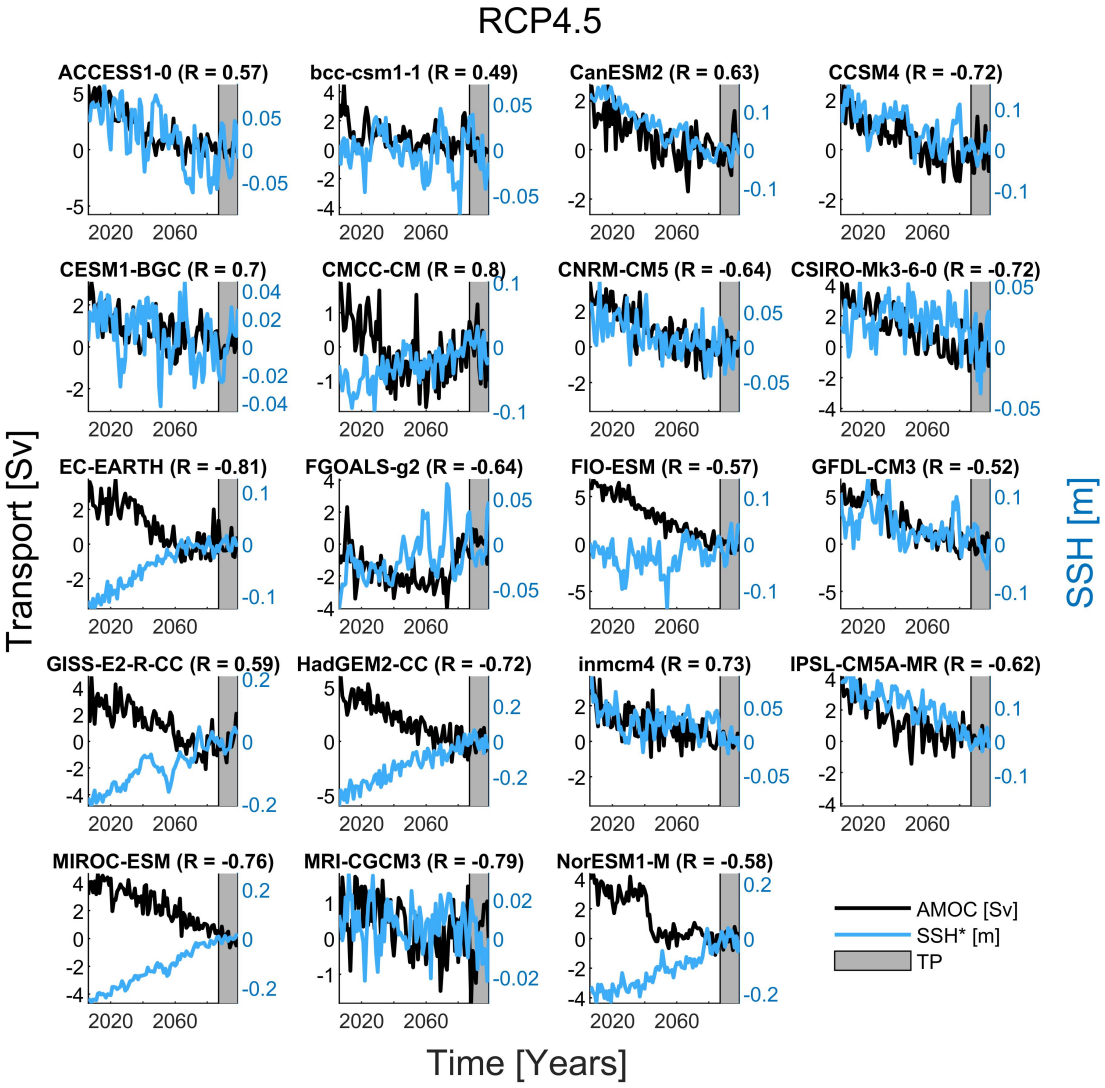

FIGURE 4.9: As Figure 4.8 but for RCP4.5 (with a TP from 2087 to 2099)

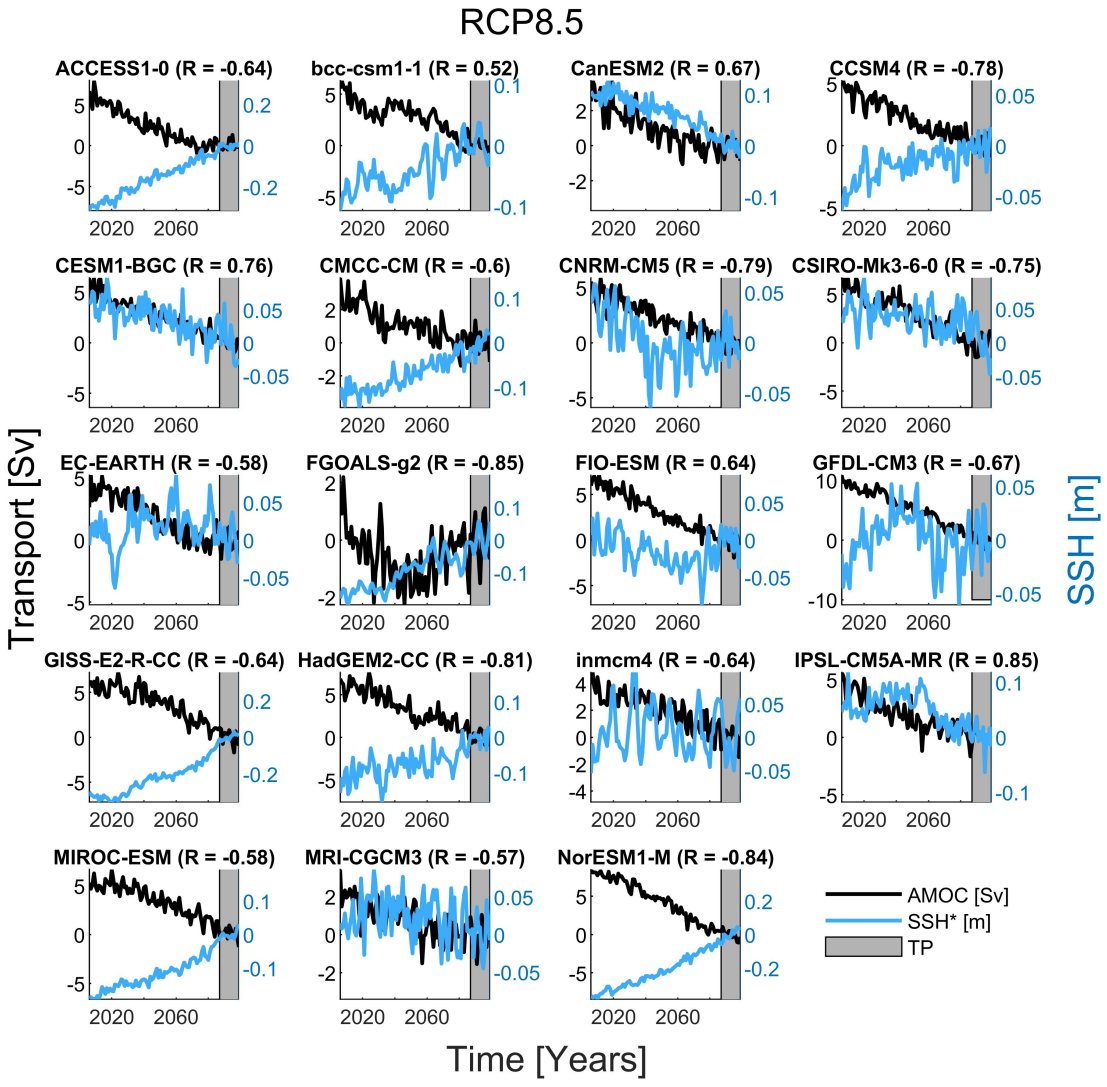

FIGURE 4.10: As Figure 4.8 but for RCP8.5 (with a TP from 2087 to 2099)

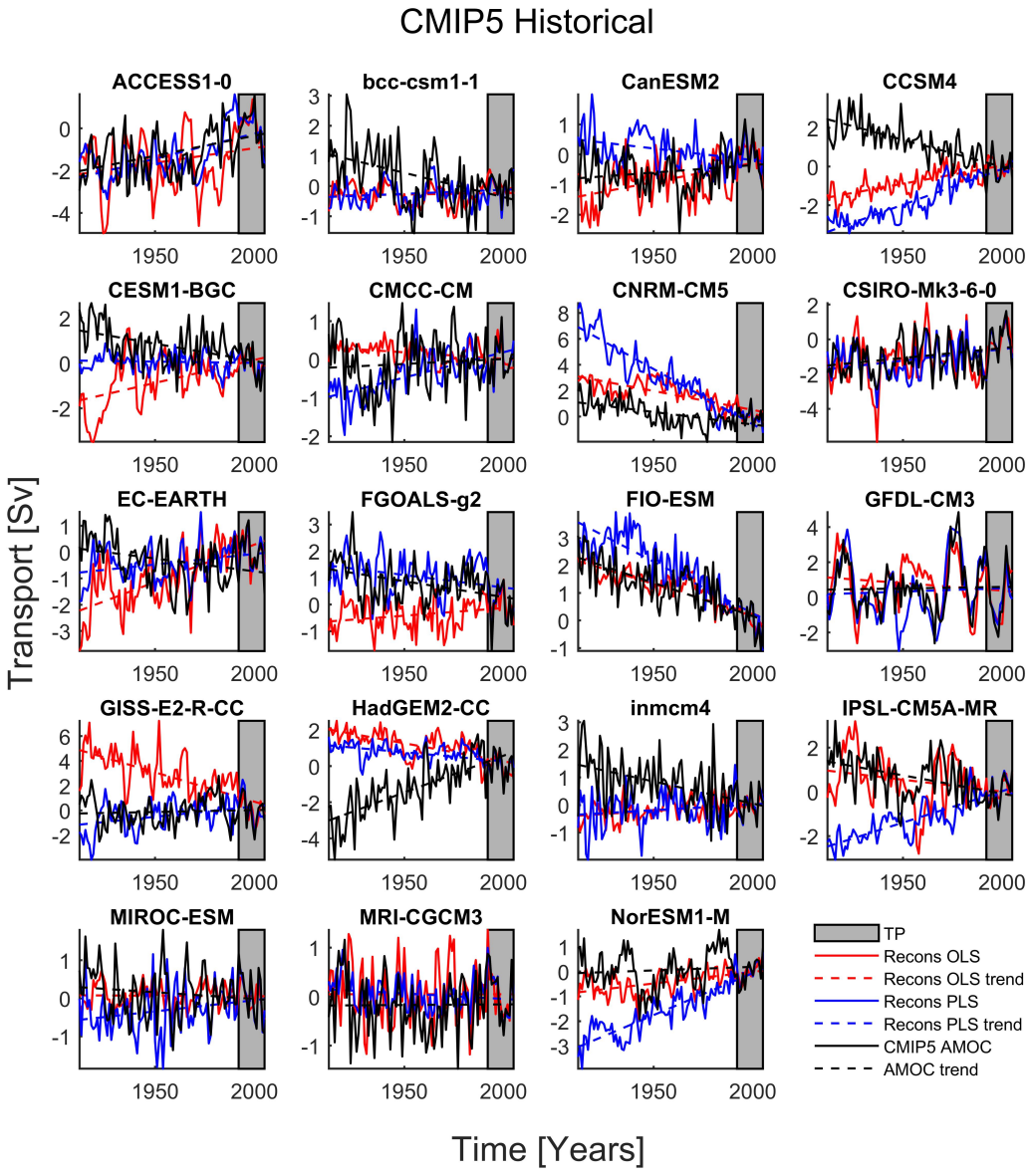

FIGURE 4.11: CMIP5 historical reconstructions for each of the 19 models using two regression methods with different SSH locations. Method 1: The ordinary least squares (OLS) regression using the location of maximum western boundary SSH correlation with AMOC (i.e., SSH*) (red lines). The SSH* locations are determined by the absolute maximum correlation of the SSH between 20 and 45° N and west of 40° W and the AMOC at 26.5° N over the TP from 1993 to 2005 (green boxes in Figure 4.5). Method 2: The partial least squares (PLS) regression using the total North Atlantic SSH (blue lines). Both regression methods are fit against the AMOC at 26.5° N (black lines) between the 13-year (1993 to 2005) training period (grey shaded region). The linear trends of the AMOC, OLS and PLS reconstructions are also displayed (dashed black, red and blue lines, respectively).

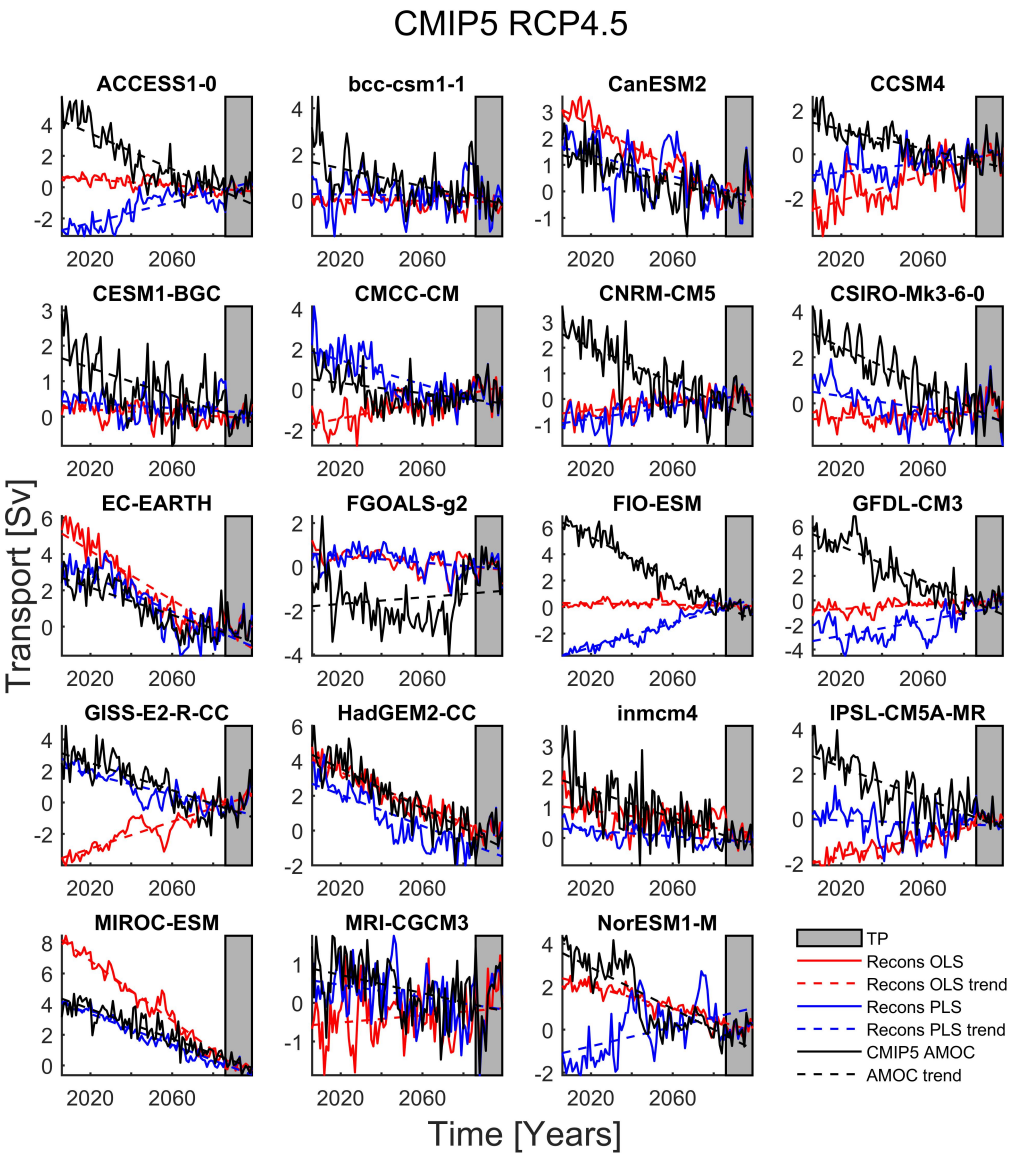

FIGURE 4.12: As Figure 4.11 but for RCP4.5 (with a TP from 2087 to 2099)

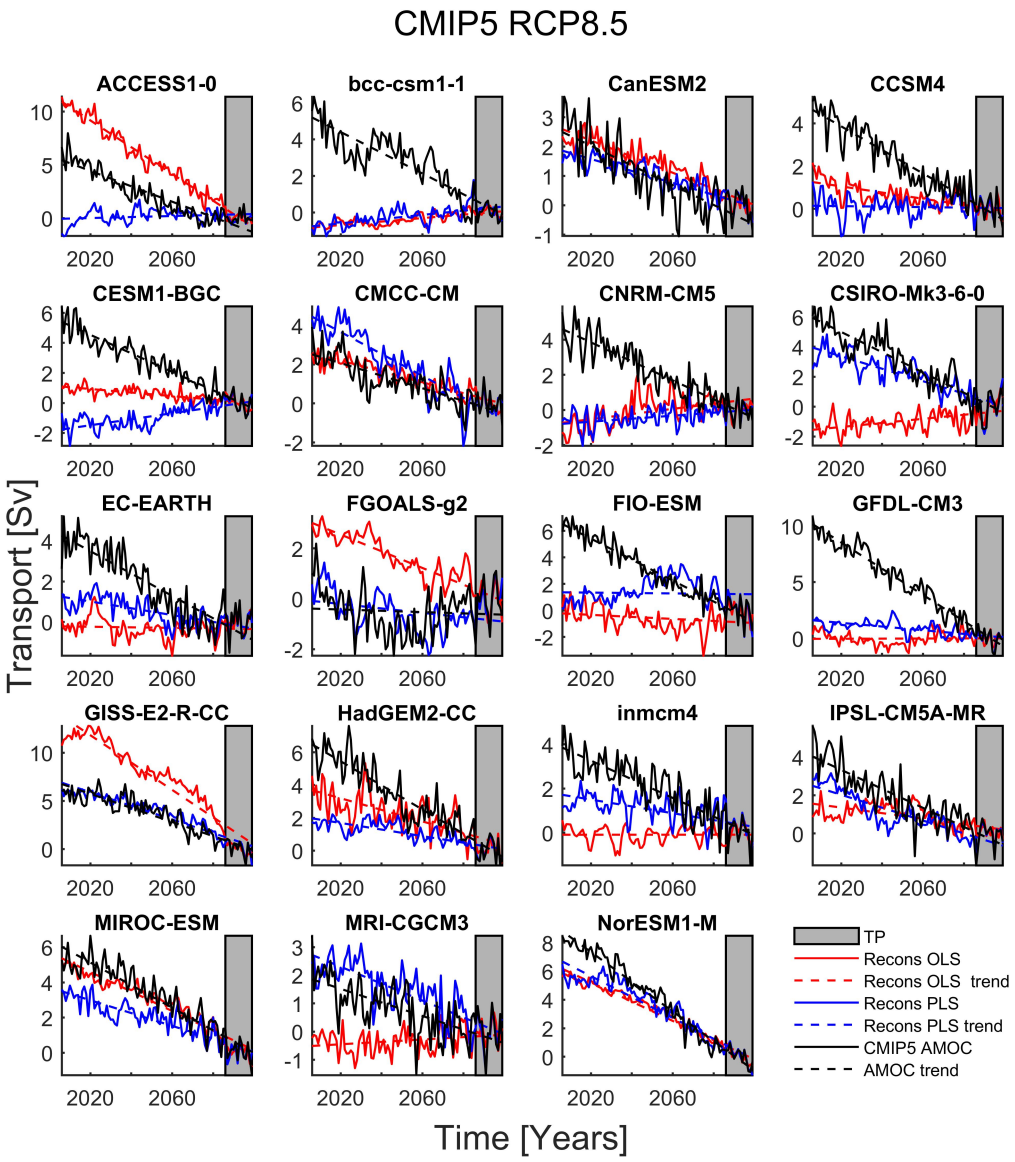

FIGURE 4.13: As Figure 4.11 but for RCP8.5 (with a TP from 2087 to 2099)

Now that the RAPID length of data has been tested for the training period, and shows that 13 years is not enough for a spatially and temporally robust relationship between SSH and AMOC, the training period is extended to estimate the number of years needed to see a relationship.

4.4.6 How many years are required to reconstruct the AMOC using SSH in CMIP5?

After rejecting the CMIP5 hypotheses that test the 13-year TP (the RAPID sample size) using different temporal periods and spatial relationships between the SSH and AMOC, this next section estimates n*. This represents the number of years of observations required for the SSH proxy to robustly represent the AMOC transport variability and trend across the CMIP5 models. Extending the training period from 13 years to the total of 94 years, the reconstruction is considered representative of the variability once the R^2 crosses and remains above the 0.5 threshold as the TP sample size increases, and representative of the trend once the relative error crosses and remains below 50%. The n* of each model's reconstruction is sorted into three classifications using the R^2; a true sufficient length ($n^*_{TP} \geq n^*_{total}$), a false sufficient length ($n^*_{TP} < n^*_{total}$) and an insufficient length ($n^*_{TP} = n^*_{TP}$ >94 years), shown by model examples in Figure 4.14. A false sufficient length can reveal the risk of assuming that the goodness of fit between the AMOC and the reconstruction is sustained through time (or at least remains beyond the TP). For example, if one were to base the n* solely on the R^2 of a short TP, although a strong interannual relationship could appear robust, a longer relationship might not be accurately estimated from this short TP (i.e., false sufficient length in Figure 4.14b).

Fewer than half the models have a true sufficient length n* (Figure 4.15), regardless of the regression method (OLS or PLS) and of the CMIP5 scenario (historical, RCP4.5 or RCP8.5). The n* ensemble means should therefore be seen as estimations but their lack of significance should be noted. The overall tendency, however, is that the average TP required to reconstruct the 94 years decreases as the climate change/AMOC slowdown signal becomes stronger (from historical: 77 years to RCP4.5: 61 years to RCP8.5: 48 years for PLS R^2 in Figure 4.15a, b and c). The relative error, that measures the inability to recover the trend, remains high throughout all models and CMIP5 scenarios, with an n* of 80 years for RCP8.5 using both OLS and PLS (Figure 4.15f). The OLS method shows more models producing true sufficient lengths throughout and the n* is lower than the PLS. This suggests that using one SSH value in the western subtropical basin produces better reconstructions than using the entire North Atlantic SSH. It is worth noting that if 80 years of TP are required it means that it only extends the reconstruction by 14 years. Hence, the extension is relatively modest, and will not provide significant new insight in the trend or variability of the AMOC.

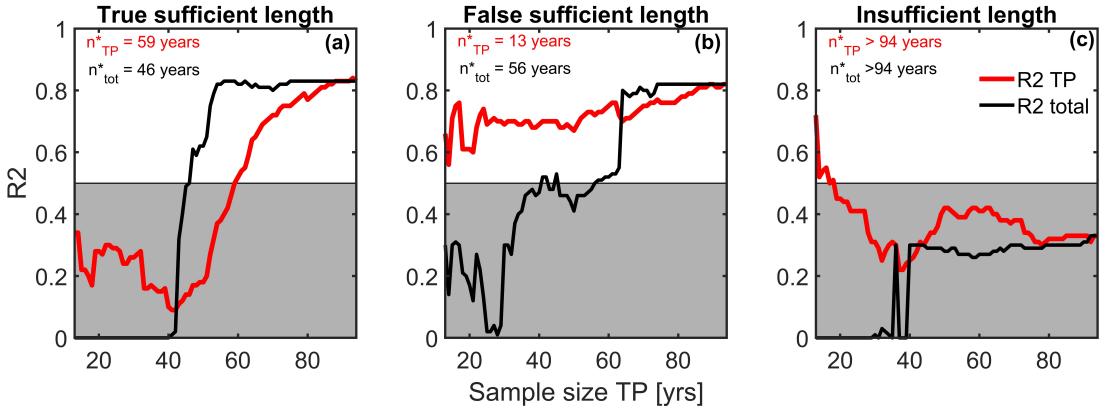

FIGURE 4.14: Examples of (a) a true sufficient length (using EC-EARTH), where the R^2 over the training period (red line) crosses into the white region (R^2>0.5) after the R^2 of the total reconstruction (black line), i.e., $n^*_{TP} \geq n^*_{total}$ (b) a false sufficient length (using HadGEM2-CC), where the R^2 over the training period crosses the threshold before the R^2 of the total reconstruction, i.e., $n^*_{TP} < n^*_{total}$ (c) an insufficient length (using FGOALS-g2), where 94 years is not enough to reconstruct the AMOC using SSH (neither the R^2 from TP of the total reconstruction cross into the white region) i.e., $n^*_{TP} = n^*_{TP} > 94$ yrs. All models used are for the OLS regression method (maximum western basin correlation) under RCP8.5 future scenario.

4.4.7 Hypothesis 6: A robust AMOC reconstruction can be generated using the maximum western basin SSH correlation against the Upper Mid-Ocean instead of the total AMOC in CMIP5

Basing this sixth hypothesis on the Frajka-Williams (2015) methodology, Hypothesis 4 is recreated but the full AMOC is replaced by the Upper Mid-Ocean transport, (UMO*, estimated here as the AMOC minus the Ekman streamfunction). When comparing the n* for the AMOC* vs. UMO*, the R^2 over the 94-year period ('Total R^2' in Figure 4.16b) do not differ greatly, apart from CESM1-BGC with a larger UMO* n* and EC-EARTH with a larger AMOC* n*. The prominent difference between the AMOC* and UMO* reconstructions results from the majority of the models producing false sufficient lengths when using UMO*. For almost all models, the n^*_{TP} is 13 years, suggesting a short TP is sufficient to reconstruct the AMOC using UMO* (R^2>0.5 in Figure 4.16a). However, from the R^2 and relative error of the total period (Figures 4.16b and c), it becomes evident that none of the models reconstruct the 94 years skilfully using 13 years (the average n^*_{total} is 52 years using the 9 models). This could explain the fact that Frajka-Williams (2015) reconstructs 90% of the variability using a 10-year training period from altimetry data, since the R^2 between the RAPID AMOC and their reconstructed AMOC over these 10 years is high (similarly to the results here). Reconstructions using the full AMOC, on the other hand, appear to have comparatively fewer false sufficient lengths. Therefore, one must be particularly careful, if using UMO, to specify the length of time that the reconstruction can recover the interannual variability so as to not falsely assume that this interannual link is constant from decadal to multi-decadal timescales.

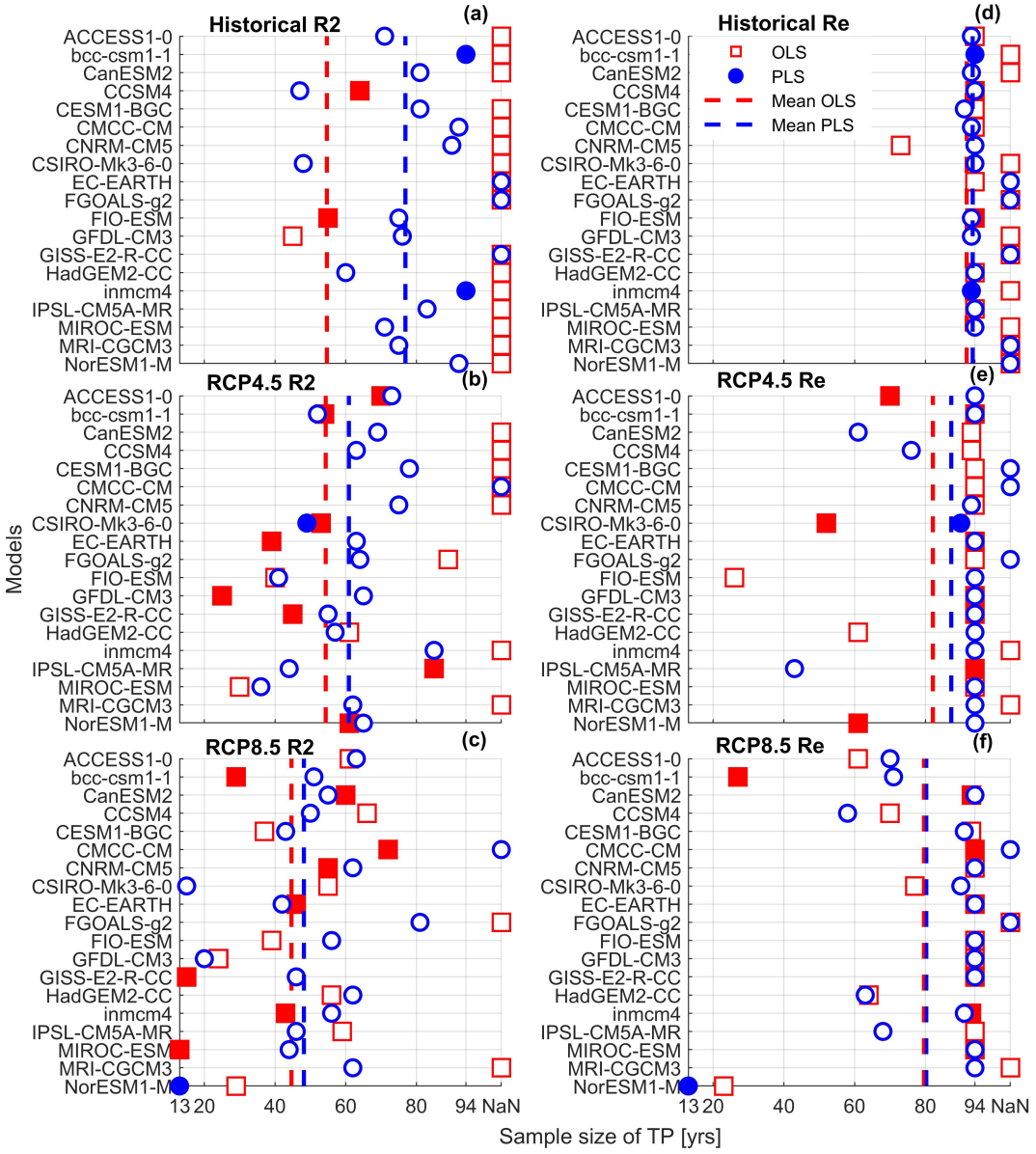

FIGURE 4.15: The n* or minimum TP sample size required to accurately extend the reconstruction of the AMOC using SSH for the 19 CMIP5 models in the 3 scenarios (historical, RCP4.5 and RCP8.5) using the R^2 (a), (b), and (c) and the relative error in (d), (e), and (f), respectively. The n* is determined by the number of years after which the R^2 or Re cross the 0.5 or 50% threshold, respectively (see Figure 4.14, for example). The two regression methods are represented: OLS (red boxes) using the maximum western basin correlation, SSH*, and PLS (blue circles) using the entire North Atlantic SSH. Sufficient lengths (see Figure 4.14 for description) are represented by filled boxes or circles and false sufficient lengths by empty boxes or circles. The mean numbers of years (vertical lines) are dashed to indicate that the mean is calculated but fewer than half of the 19 models show a true sufficient lengths. The last column on the x-axis ('NaN') serves to indicate an insufficient length, where 94 years is not sufficient to reconstruct the AMOC.

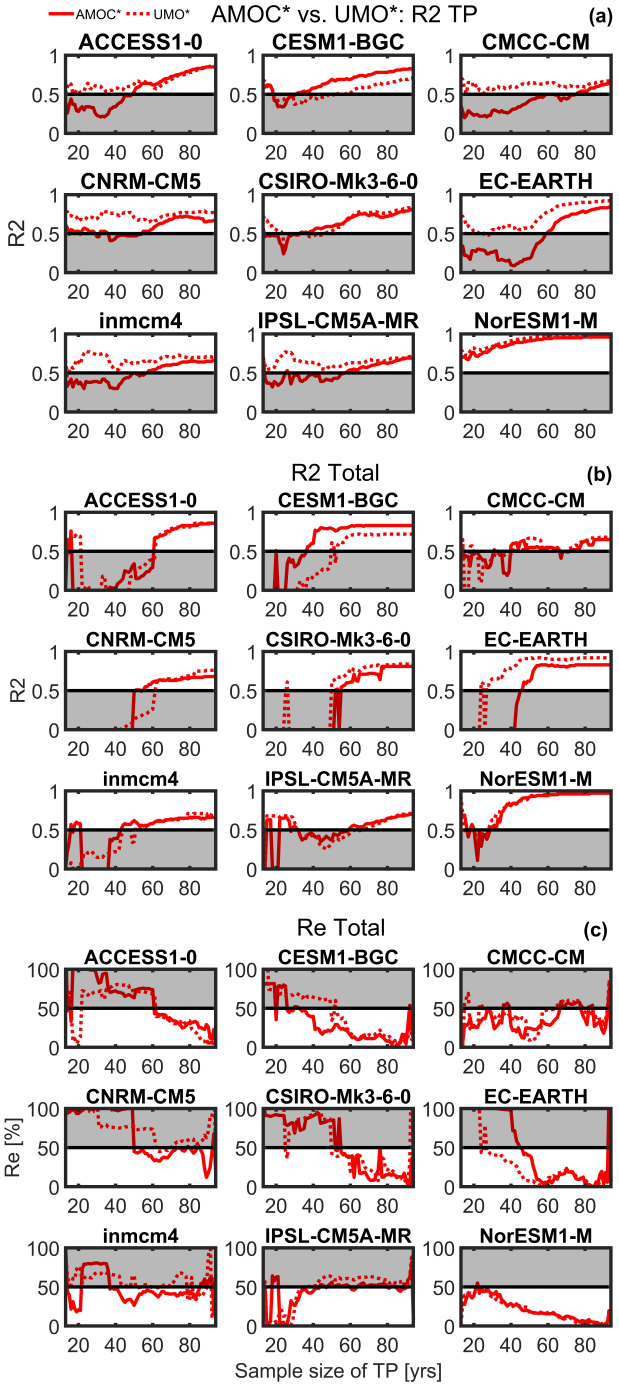

FIGURE 4.16: Comparing the AMOC* (solid red lines) vs. UMO* (dotted red lines) reconstructions in 9 RCP8.5 CMIP5 models against the absolute maximum correlation location of SSH as a function of the TP's sample size. (a) The R^2 over the TP, (b) the R^2 over the total 94-year period, and (c) Re over the total 94-year period. The grey shaded region shows an R^2<0.5 or Re>50%. As before, the n* can be computed as the TP sample size when the R^2 or Re value crosses and remains in the white zone.

4.4.8 Hypothesis 7: A robust AMOC reconstruction can be generated using the regression of sea surface temperature (SST) instead of SSH against the AMOC in CMIP5

The final hypothesis tests whether the SST has a more consistent and robust relationship with the AMOC in the CMIP5 models than SSH. From the correlation maps (Figures 4.17, 4.18, and 4.19), however, the spatial distribution of correlated patches between SST and the AMOC over the 13-year TP vary substantially across and within models in all three scenarios. Furthermore, now the absolute maximum correlation is not confined to the western subtropical gyre and allow it to be located anywhere in the North Atlantic, and once again, these locations differ between the models (green boxes in Figures 4.17, 4.18, and 4.19). The "Warming Hole" that has previously been shown to be linked to a decline of the AMOC under a warming climate (e.g., Drijfhout et al. (2012); Rahmstorf et al. (2015); Sévellec et al. (2017)) does not seem to be noticeable in these maps. This suggests that there is no robust relationship between the AMOC at 26.5° N and the subpolar North Atlantic in these models, although it should not be ruled out that repeating this test using the AMOC at 40° N (or another latitude further north), longer timeseries or using a lagged correlation analysis could show otherwise.

The n* from proxies using SST is similar to that from proxies using SSH (Figure 4.20 vs. 4.15). The majority of the experiments once again show false sufficient lengths, where the n* based on the R^2 over the TP is shorter than that based on the total reconstruction. Only RCP4.5 using OLS produces a significant ensemble mean (Figure 4.20b and e) where 10 models have a true sufficient length n*, hinting that OLS is again a slightly more efficient method than PLS. Conversely, the historical OLS results show that all TPs are insufficient lengths, where 94 years are not enough to recover the AMOC interannual variability (Figure 4.20a), although some can reconstruct the trend (Figure 4.20d). As with the SSH, the tendency of a decrease in the average required TP sample size occurs as the climate forcing trend becomes stronger and more defined in RCP8.5 (historical, n* = 69 years; RCP4.5, n* = 67 years; RCP8.5, n* = 51 years for PLS R^2 in Figure 4.20a, b and c).

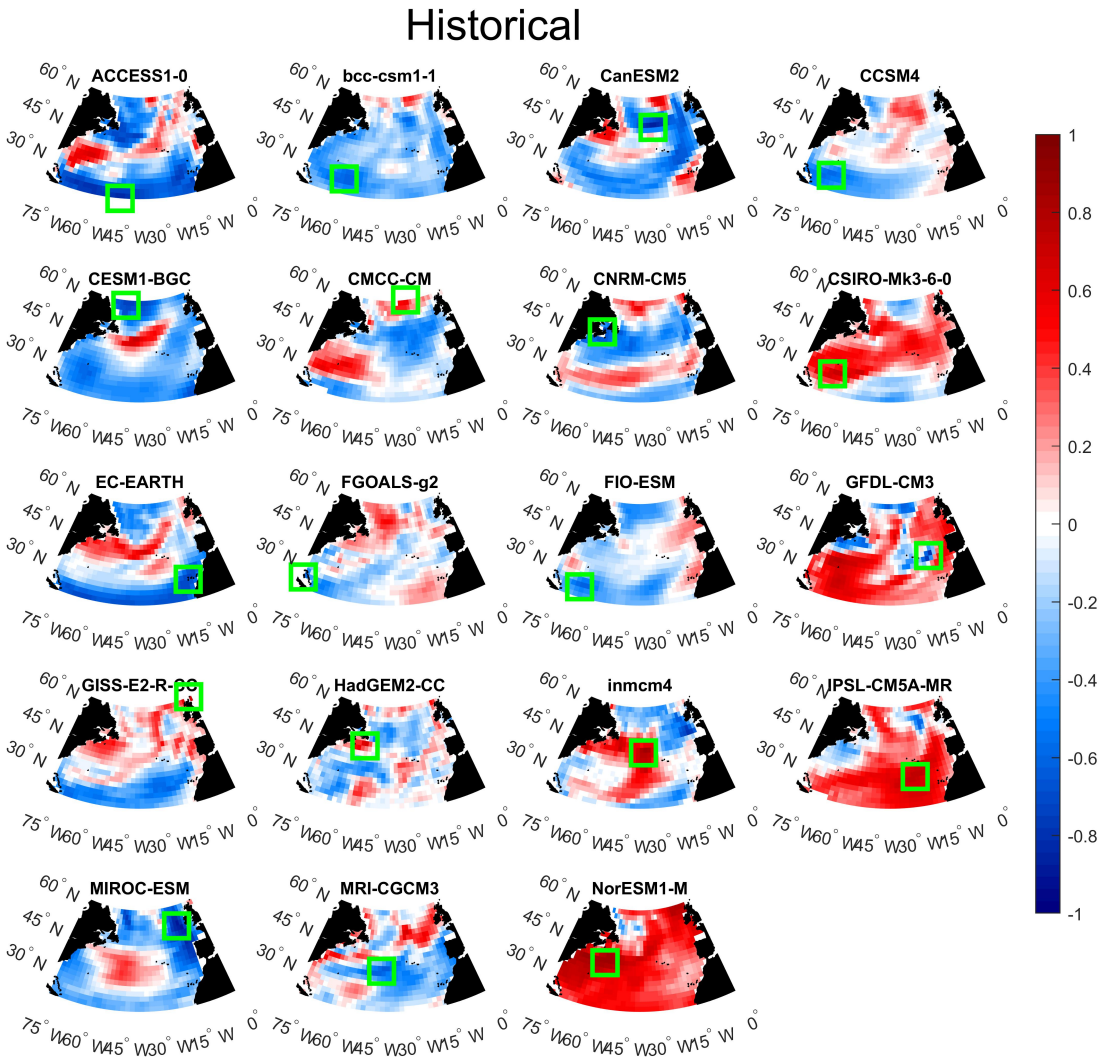

FIGURE 4.17: CMIP5 pointwise correlation maps between anomalies of annually averaged SST [m] in the North Atlantic against the AMOC transport anomaly [Sv] at 26.5° N over the historical TP (1993 to 2005) in 19 CMIP5 models. The green boxes show the maximum absolute correlation coefficient location in the entire North Atlantic basin.

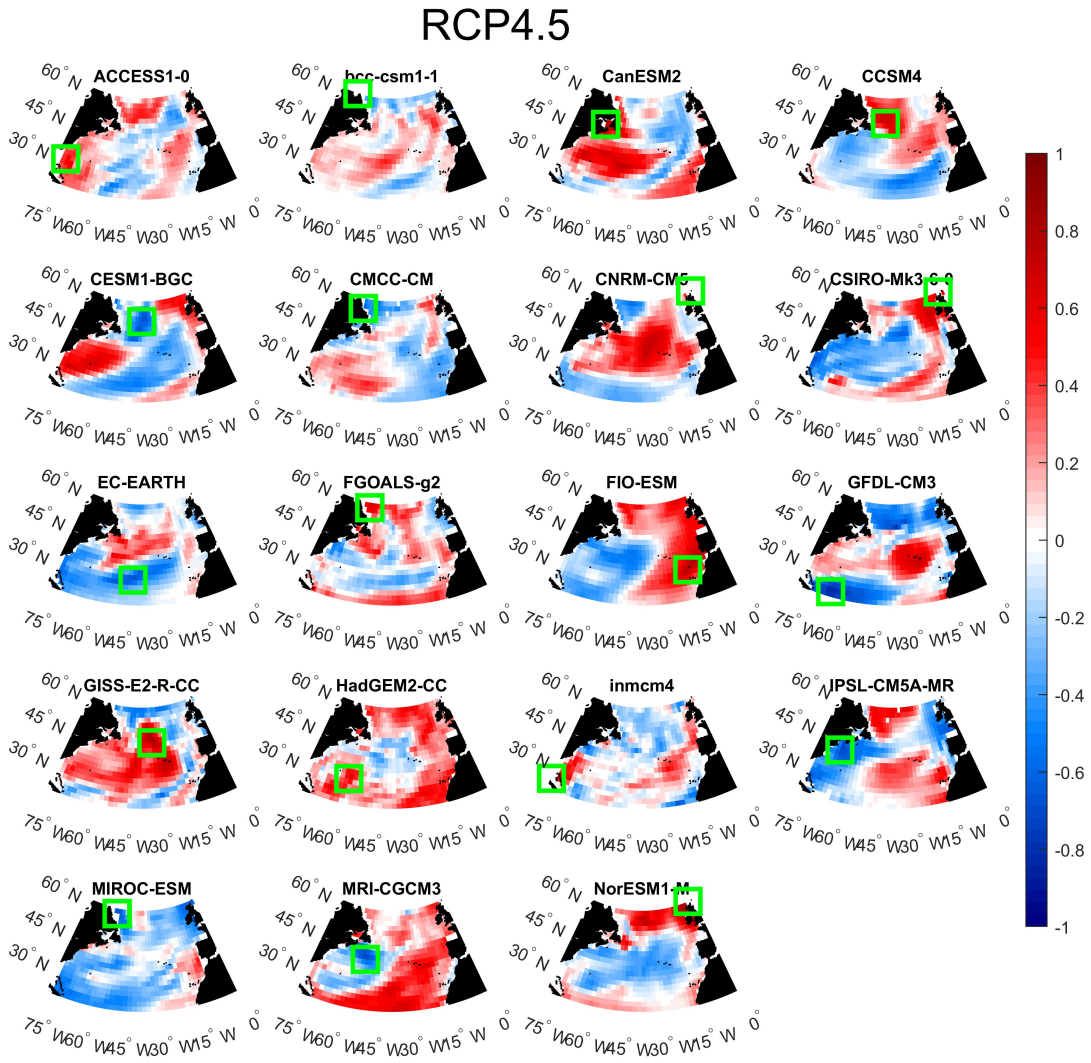

FIGURE 4.18: As Figure 4.17 but for RCP4.5 (therefore with the TP from 2087 to 2099).

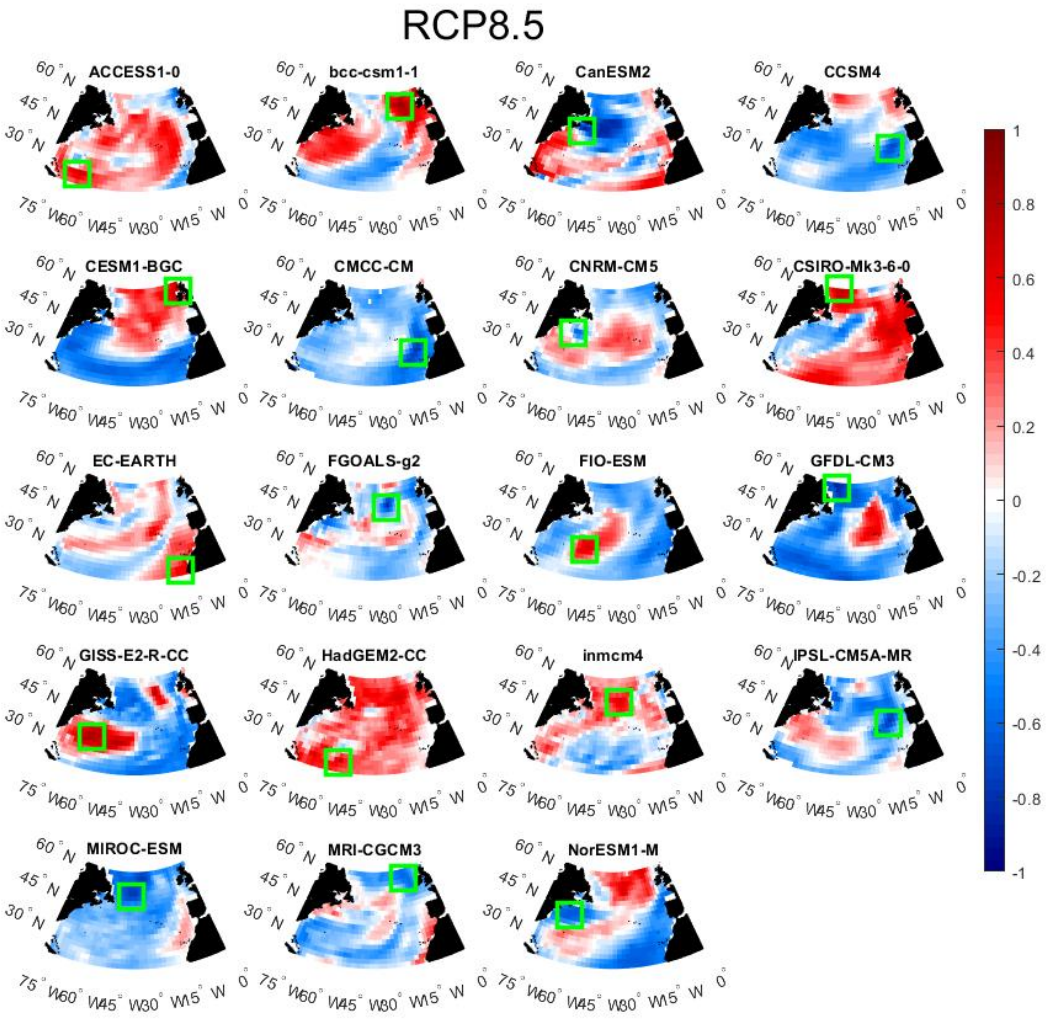

FIGURE 4.19: As Figure 4.17 but for RCP8.5 (therefore with the TP from 2087 to 2099).

4.5 Conclusion

In the interests of extending the AMOC timeseries beyond the 13 years of continuous RAPID mooring observations, this study aims to investigate whether there is a robust temporal and spatial relationship between the AMOC and SSH in the North Atlantic. Reconstructing a proxy of the AMOC over the tidal gauge or satellite eras would allow

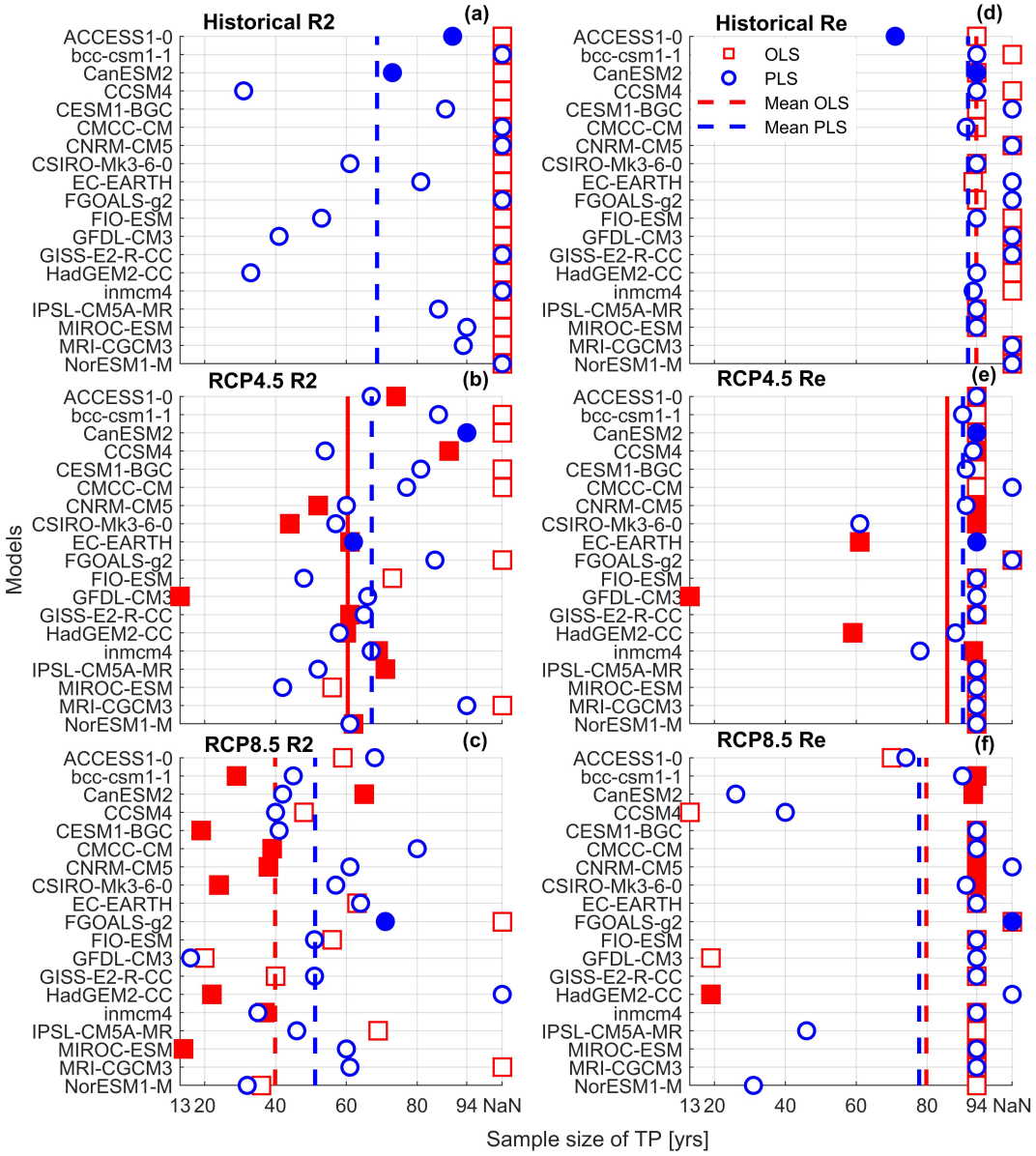

FIGURE 4.20: As Figure 4.15 but for SST

us to understand its variability and trend over longer timescales, and ultimately explore whether the RAPID decline is a transient phenomenon forced by climate change or part of internal variability. The results show that 13 years is not long enough for SSH to exhibit a fingerprint of the AMOC at 26.5° N across observations, ocean-only and coupled numerical models. Hypotheses have been tested to determine whether reconstructions work using different locations of the SSH (eastern and western boundaries, maximum western basin correlation or total Atlantic), different components of the AMOC (total AMOC or UMO) or even SST instead of SSH, but neither produced the long-term variability nor the trend of the AMOC. By extending the training period of the reconstruction, however, the results show that the AMOC and SSH are possibly robustly linked on multi-decadal timescales, which is consistent with previous studies discussed

below.

The first two hypotheses test the eastern and western boundary SSH relationship with the AMOC using observations and NEMO output. A skilful reconstruction is revealed both for the 13-year RAPID trend (Re = 16.52%) and NEMO's interannual variability (almost 60%) and trend (Re=16.03%). By comparing the coefficients from these two SSH regression predictors, the dominant component appears to be the eastern boundary SSH in both reconstructions ($\beta_E > \beta_W$). In order to verify this relationship as robust across different models, the CMIP5 data are used, however, the hypothesis is refuted, demonstrating that the CMIP5 East coefficients are highly variable across all models, latitudes and scenarios. Instead, a small potential relationship between the AMOC and the western boundary in the future scenarios appears in the coefficient analysis, and since previous work supports this relationship (Frajka-Williams, 2015; Bingham and Hughes, 2009; Ezer, 2015), another hypothesis tests whether the western boundary can dominate the AMOC interannual variability, however this hypothesis is also refuted.

It is important, however, to recognise that the presence or lack of the tested relationship is completely reliant on the statistical estimators defined in this study. In other words, the 50% threshold for defining a 'good' reconstruction is chosen arbitrarily and other thresholds could be used, hence changing the classification of whether a reconstruction shows skill or not (as well as estimating a 'true sufficient length', 'false sufficient length' or 'insufficient length' to reconstruct the AMOC). One could argue, however, that the criteria defined is already rather relaxed (a threshold of Re<10% could have been used, for example). Furthermore, there are ongoing discussions regarding whether the R^2 is the best estimator to assess the goodness of fit between a model and actual data. Some reasons for this include that the R^2 can be arbitrarily low when the model is correct, and vice versa, it can also not be compared across different data sets (i.e., previous proxy studies using R^2, against this study), and it does not measure how one variable inherently explains another (Kvålseth, 1985). It has been used here to simply establish if a time-varying point by point linear relationship is present, however, future work could therefore compare these results to other estimators, such as the root mean square error. Furthermore, AIC and BIC could be used in order to compare the models and therefore choose the best one for this analysis.

There are several other potential reasons why, under the criteria used in this study, the quasi-decadal AMOC-to-SSH correlation produces an unsuccessful proxy of the AMOC at 26.5° N. These include: the dynamical relationship between the AMOC and SSH, the data used, the location of the AMOC, or the fact that as the results show, there is solely a multi-decadal relationship.

Revisiting the eastern and western boundary SSH as regression inputs for the first three hypotheses in this work, surface dynamic height adjustment of circulation features at the boundaries might not be indicative of the full-depth basin changes. This could be

due to higher-order vertical modes dominating at the boundaries (Szuts et al., 2012), the importance of the deep density gradient between the boundaries (Cromwell et al., 2007; McCarthy et al., 2017a) or influences of the seasonal thermocline (upper 200 m) which do not affect the total transport (Ivchenko et al., 2011). However, other in-situ full-depth observational profiles or SSH estimates can have other challenges. For example, Argo has difficulty collecting data in continental slopes shallower than 2,000 m (Willis, 2010) and satellite resolution does not capture rapid decrease of SSH near the western boundary (Szuts et al., 2012). More importantly, neither of their records date back far enough to be able to test the hypothesis for building a multi-decadal AMOC timeseries.

The optimal geographic location is then tested for the SSH-AMOC relationship, without restricting it to the boundaries in coupled climate models (either using the western basin in Hypothesis 4 or the entire North Atlantic in Hypothesis 5). The presence of systematic biases in numerical models (Hofmann and Rahmstorf, 2009) could be the leading cause of large-scale SSH pattern discrepancies and the lack of a consistent region of highest correlation under an AMOC decline scenario (Figures 4.5, 4.6, 4.7), as shown in other studies. MPI-OM used in Landerer et al. (2007) manifests a tripole SSH pattern across the subpolar and subtropical gyre front but other coupled climate models (Levermann et al., 2005) and ocean-ice models (Lorbacher et al., 2010) show a basin-scale, broader SSH increase over the North Atlantic under climate forcing. Results in this study are consistent with the incongruence they find and show that neither pattern is dominant across the models.

With regards to the use of the UMO instead of the AMOC in Hypothesis 6, the reconstructions could have failed due to results found in Hirschi et al. (2009). They use a general circulation model to show that significant correlations (0.3-0.9) occur between the zonal differences of SSH and the top 1,100 m of the eastern and western branches of the horizontal gyre circulation only if they are considered separately. Low correlations are computed, however, for the basin-wide meridional transport (the sum of top 1,100 m of the eastern and western branches). They attribute this to the errors of each branch being relatively large compared to the AMOC's variability at certain depths (Hirschi et al., 2009).

The final test using SST in Hypothesis 7 examines the potential correlation between the AMOC and the subpolar gyre's "Warming Hole" (Medhaug and Furevik, 2011; Drijfhout et al., 2012; Rahmstorf et al., 2015; Sévellec et al., 2017). Wang et al. (2015) also show that the AMOC at 32°N is not correlated to SSH variations but has moderate correlations to the second Principle Component (PC2) of surface heat flux. A reason for this weak SSH correlation, however, could be the weak surface AMOC signal to background noise ratio that is considerably influenced by the atmosphere and radiative forcings (Mahajan et al., 2011). Subsurface temperature (at 400 m, for example) is therefore once again a potentially optimal candidate for the AMOC signature which has been seen to be highly correlated with altimetry data from 1993-2003 (Zhang, 2008;

Mahajan et al., 2011). However, the caveat is that this relationship is present only in one model and would probably not be robust across all climate models (Stouffer et al., 2006). Furthermore, as with SSH, the overall aim of building a multi-decadal proxy would also not be attainable since there are no subsurface observation data that are long enough.

Since this study focuses on RAPID AMOC data, the analysis purposefully uses only the AMOC latitude in numerical models (26.5° N). However the strongest surface signals could be found in the northern part of the Gulf Stream and the North Atlantic Current and weaker changes could occur in the subtropical region (Lorbacher et al., 2010). Furthermore, there are potentially lagged correlations between the AMOC at 26.5° N and the subpolar gyre SSH of up to 8 years, (Jackson et al., 2016; van Sebille et al., 2011). The multi-decadal memory (exceeding 15 years) of the 26.5° N AMOC are also shown to be dominated by subpolar thermal forcing that shows a signature in the SSH (Pillar et al., 2016). Investigation of factors such as lags or memory is outside the scope of this study, however.

From the analysis using NEMO, the results show that a 13-year period that produces a good reconstruction could simply be by chance since every 13-year sliding window segment produces different regression coefficients and trends (Figure 4.3). The lack of a consistent relationship through time mirrors the results found in Little et al. (2017), where an increase from 30 to 90% of the variance is explained using the future scenario versus historical CMIP5 data. This also highlights another important factor, namely the signal-to-noise ratio which the results also show; the training period required to represent the AMOC's secular trend decreases from 80 years (using the total North Atlantic in the historical scenario) to 50 years in the RCP8.5 scenario (Figure 4.15), where the AMOC decline is stronger.

Lastly, the most probable explanation for the poor reconstructions is the SSH-to-transport relationship's dependence on timescales, which has already been challenged in recent years (Frajka-Williams, 2015; Lorbacher et al., 2010; Little et al., 2017). Little et al. (2017) and Woodworth et al. (2014) show that SSH variability is driven by internal wind-driven processes interannually to decadally but is dominated by an externally-forced AMOC on multi-decadal timescales. Furthermore, Kanzow et al. (2010) and Chidichimo et al. (2010) demonstrate the effects of wind as a primary driver of AMOC variability on shorter timescales, and Matei et al. (2012) extends this, suggesting that the short term variability could imprint on density gradients on a longer (multi-annual) timescale. Cromwell et al. (2007) suggest a 10-year training period is necessary in their statistical model, and Lorbacher et al. (2010) suggest 20-30 years for a detectable imprint in subpolar gyre or eastern north Atlantic SSH with an AMOC decline of 0.1 Sv yr^{-1}. Since this analysis uses annual data, large interannual swings in the wind-driven variations of the SSH and AMOC could be hindering the detection of any potential relationship between the AMOC and SSH, as well as dictating the varying location

of highest correlation. Although some initial tests using decadally or multi-decadally smoothed AMOC and SSH data showed equally poor reconstructions, a more rigorous analysis could be considered for future work. In other studies that use longer observational timeseries (such as tide gauge data since the 1920s in McCarthy et al. (2015b)), a 7-year smoothing is used to rebuild the intergyre transport, so this could be tested for the AMOC at 26° N. Possibly the combination of smoothing the data prior to the regression, as well as extending the training period could produce a better reconstruction.

Regarding the tide gauge data, a 60-year signal has been identified (linked to the Atlantic Multi-decadal Oscillation), which Chambers et al. (2012) and Kopp (2013) use to suggest that there is not enough data to detect whether the sea level rise since 1975 in the mid-Atlantic U.S. East coast is outside the natural variability of the 20th century. One can argue that if this duration is required to detect the SSH trend alone, it supports findings here from the CMIP5 ensemble mean of approximately 80 years of records necessary to capture the trend relationship between the SSH and AMOC under a future RCP4.5 or RCP8.5 scenario.

Ultimately, the results show that although using SSH as a proxy initially appears to indicate AMOC changes, with 13 years of data of RAPID and tide gauge data, any reconstruction of the AMOC variability seems to be random. Therefore, there are currently insufficient observational data to reconstruct the past AMOC's variability and trend over multi-decadal timescales. Furthermore, multi-model results show a lack of robustness in the link between SSH and the AMOC through temporal or spatial patterns in the North Atlantic. One key result underlined here is the need for multi-decadal observations to build a robust relationship between SSH and the AMOC, which means that 50-60 years of observations are required before being able to build an AMOC hindcast using SSH.

Chapter 5

Probability of interannual to multi-decadal AMOC trends from 1850 to the end of the 21st century

5.1 Introduction

Due to the rising concern regarding impacts of climate change, interest in the Atlantic Meridional Overturning Circulation (AMOC) has substantially grown, following its pertinence in redistributing heat, salt, and carbon in the ocean (Ganachaud and Wunsch, 2003). In the near-surface layer, warm and salty northward flowing waters transfer heat to the atmosphere in the north-east North Atlantic (Hall and Bryden, 1982). This feature is particularly important when understanding how changes in the AMOC can impact both European and global climate (Pohlmann et al., 2006). Furthermore, this release of heat in the subpolar North Atlantic and sustained northward flux of salinity contributes in maintaining dense water for deep convection within the thermohaline component of the AMOC (Manabe and Stouffer, 1988). There is a certain co-dependence between the AMOC and the distribution of temperature and salinity in the North Atlantic, which highlights their reciprocal active roles within feedback loops (Marotzke, 1996). This study therefore aims to (1) determine whether there are any periods of a higher probability of a decline in the AMOC transport from 1850 to 2100, and (2) identify whether salinity transports from atmospheric and ocean feedbacks can indicate or explain this probability.

5.1.1 Recent past and future AMOC decline probability

From AMOC observations using the first 8.5 years of the RAPID array data, Smeed et al. (2014) suggest a potential decline of approximately 0.5 Sv yr^{-1} occurred, although they mention that the data are not long enough to separate long-term change forced by anthropogenic warming from decadal-scale internal variability. A longer-term (centennial) forced signal can potentially exhibit shorter (decadal) periods of natural variability, with an opposite (or lack of) trend (Easterling and Wehner, 2009). This is seen, for example, among the multi-decadal increasing trend of atmospheric temperature data, as a hiatus or stabilisation period (Sévellec et al., 2016). Hence, the aim is to verify whether the decadal decline reported from the RAPID AMOC observations is also a consequence of natural variability or is part of a longer-term trend driven by climate change.

Since the observational time window does not permit the separation of a longer term trend from short term variability, other studies have turned to proxies to assess the multi-decadal past characteristics of the AMOC. Most conclude that over the last 50-100 years, the AMOC has probably not experienced an anthropogenically-driven decline, and trends from natural variability have been weak (Buckley and Marshall, 2016). Parker and Ollier (2016) imply that trends in their combined observational proxy since 1860 fall within the interannual to multi-decadal variability of the AMOC. Hindcast numerical simulations also support that the increase seen from the 1980s to mid-1990s, and a decline thereafter, are indicative of the quasi-decadal (to quasi 30-year) AMOC internal variability (Huang et al., 2012a,b; Robson et al., 2014). On the other hand, Rahmstorf et al. (2015) uses another proxy to show that a 20-year weakening from 1975 to 1995 was unprecedented and had a <0.005 probability of occurrence just by natural variability. Such inconsistencies regarding the intrinsic or extrinsic forces of AMOC changes are explored in a coupled model-mean probability analysis here.

Future projections from the IPCC Fifth Assessment Report and follow-up studies have focused on the likelihood of a centennial decline by 2099 (Stocker et al., 2013; Schleussner et al., 2014). A reduction in AMOC strength is likely (within the 66%-percentile) by the end of the 21st century, although studies show a wide model spread of 12-30% likelihood in a climate stabilisation scenario (RCP4.5) and 25-56% likelihood in the 'business-as-usual' (RCP8.5) scenario (Weaver et al., 2012; Schleussner et al., 2014). Declining trend intensities also have a broad range, from 0 to 0.9 Sv per decade under the RCP8.5 scenario (Roberts et al., 2014; Smeed et al., 2018). The probability of seeing declines on different timescales is still under discussion, however, hence the current study's focus.

5.1.2 Dynamics of an AMOC decline

Understanding of North Atlantic transport dynamics, namely distinguishing overturning and horizontal gyre transport of temperature and salt, can shed light on understanding changes in the probability of an AMOC decline. A positive feedback in ocean salinity transport, first described by Stommel (1961), occurs when a reduction in the AMOC, results in less salt reaching the North Atlantic, reducing the density of northern waters, and further weakening the AMOC (Marotzke, 1996). Interest in the mechanisms behind this feedback emerged upon discovery of the AMOC's sensitivity to freshening thresholds (or bifurcation points) that can force the AMOC into a stable reduced or collapsed state (Stommel, 1961; Manabe and Stouffer, 1988; Rahmstorf, 2000; Dijkstra, 2007; Sévellec and Fedorov, 2011). Some evidence of a possible bi-stability of the AMOC has been seen in the geological record, suggesting that past deep water formation can 'switch off' during abrupt climate shifts. One of the hypotheses believed to have initiated such events is moderate freshwater discharge in the northern North Atlantic (Broecker et al., 1985; Dansgaard et al., 1993; Broecker, 1998; Bond et al., 1999). Since then, some studies have used global numerical models to understand this potential AMOC shutdown threshold, and its early warning signs, by simulating an increase in atmospheric carbon dioxide (and hence surface temperature), or anomalous freshwater input in the subpolar North Atlantic, also called "hosing" experiments (Manabe and Stouffer, 1994; Rahmstorf, 1995; Wood et al., 1999; Zhang and Delworth, 2005; Stouffer et al., 2006; Boulton et al., 2014). From the CMIP5 ensemble, however, none show a likelihood of a total collapse within the 21st century as a consequence of global warming (Gregory et al., 2005; Weaver et al., 2012).

Other numerical model studies have focused on simulating potential North Atlantic temperature and salinity changes in the nearer future and examining the AMOC's response. An example includes the effects of anthropogenic warming on subpolar freshwater from Greenland ice sheet melting (Bakker et al., 2016) and Arctic ice retreat (Sévellec et al., 2017), both of which are not well represented in CMIP5 models (Stocker et al., 2013). Thorpe et al. (2001) show that with a 2% increase in CO_2 per year over 70 years, a 20% weakening of the AMOC occurs, of which 60% is attributed to an increase in temperature at high latitudes and 40% to salinity decreasing at high latitudes and increasing at lower latitudes. Similarly, Hu et al. (2009) show that a 1% per year increase of Greenland freshwater melt flux induces a 26% AMOC reduction in the last 20 years of the 21st century relative to the 20th century. Other opposing results, however, do not simulate a weakening AMOC with a forced increase in CO_2 (Latif et al., 2000) or that freshwater anomalies have not yet impacted the AMOC (Böning et al., 2016), therefore demonstrating the wide spread in AMOC behaviour in different models (Schmittner et al., 2005; Manabe and Stouffer, 1999). This leads to large uncertainty in the response to forcing when using one model, refining our focus to the multi-model ensemble in this study.

To explore the recent past changes, observations using hydrographic data from the Labrador Sea and six cruises across 24.5° N have shown that since the 1960s a sustained freshening of the North Atlantic has occurred (Dickson et al., 2002; Hall and Bryden, 1982; McDonagh et al., 2015), having an important role in producing record low densities by 2015 (Robson et al., 2016). Though the cause is still under discussion, one possibility is a recent increase in precipitation, therefore atmospheric forcing, over the subpolar gyre (Josey and Marsh, 2005). McDonagh et al. (2015) on the other hand, focuses on the respective contribution of the overturning or gyre transports in freshwater divergence between the Bering Strait and 26.5° N. They show that the positive freshwater flux (of 0.37 Sv) is dominated by the AMOC, which explains 91% of the variance versus the horizontal component that has a much smaller impact. This methodology in separating the circulation components can help to further understand drivers of a flux, and is therefore used in this study.

The work has been separated into two parts. Part I (in Section 5.2) looks at the probability and intensity of a past or future decline in the AMOC using over two centuries of data in coupled numerical models. This provides a robust analysis for trends of different lengths and hence aid in understanding the AMOC's interannual to multi-decadal properties through time. Part II is motivated by the results in Part I, showing an increase in future probability and intensity of a decline over decadal to multi-decadal timescales as well as the appearance of a rogue period, high probability of a transient AMOC slowdown at the turn of the 21st century. Both being linked to the forced AMOC trend, salinity budgets in the subtropical and subpolar gyres are generated to examine the changes in gradients and fluxes between these regions from 1850 to 2099. Ultimately, the two parts of this chapter are linked by investigating the cause of the long-term change and the rogue period in the AMOC decline probability.

5.2 Part I: Probability of an AMOC decline

5.2.1 Data: *CMIP5 AMOC control, historical, RCP4.5 and RCP8.5*

Due to the lack of control runs for some CMIP5 models, this study uses a selection of 16 models, namely: (1) ACCESS1-0, (2) bcc-csm1-1, (3) BNU-ESM, (4) CanESM2, (5) CCSM4, (6) CESM1-BGC, (7) CMCC-CM, (8) CNRM-CM5, (9) CSIRO-Mk3-6-0, (10) EC-EARTH, (11) GISS-E2-R-CC, (12) HadGEM2-CC, (13) IPSL-CM5A-MR, (14) MPI-ESM-LR, (15) MRI-CGCM3, (16) NorESM1-M. Four datasets are used: (1) control simulations, which are based on pre-industrial atmospheric greenhouse gas emissions, (2) historical simulations, which are based on post-industrial forcing from 1850 to 2005, (3) the RCP4.5 future 'stabilisation' of emissions scenario, and (4) RCP8.5 future 'business-as-usual' scenario; the latter two running from 2006 to 2099. The vertically- and zonally-integrated AMOC transport streamfunction is taken at 48° N and at a depth of 1,000 m.

This latitude is chosen for a direct comparison with the study in Part II, since the salinity transports (in the subpolar and subtropical regions) show a different behaviour north and south of 48° N. The original data are monthly (in order have at least 12 data points to estimate one-year trends). Annual means are computed after removing the seasonal cycle of the monthly means by subtracting each month's overall mean. This is done separately for each dataset (i.e., four seasonal components are estimated for the control, historical, RCP4.5 and RCP8.5).

5.2.2 Methods: *probability analysis*

The CMIP5 pre-industrial control simulations are used to represent what will hereafter be referred to as 'natural variability' of the AMOC, i.e., variability existing in the absence of anthropogenic greenhouse emissions. Moving linear regression trends are fit to each of the 16 models' control timeseries using windows of different trend durations (2, 10, 20, and 40 years) and moving in increments of 12 months. The total range of trends computed over the full timeseries of the 16 models is placed into 50 equally-spaced bins. Then, the frequency of each bin is estimated using the full timeseries to build a probability density function for each model. These 16 PDFs are averaged in order to generate the multi-model ensemble mean reference PDF that defines the natural variability of the AMOC in this study. The ensemble mean PDF is therefore approximately centred around zero, where positive values indicate in increasing AMOC trend and negative values a decreasing trend. One of the key assumptions in this methodology is that the natural variability does not change through time. This is supported by an assumption stated in the design of the IPCC's future scenarios; that no drastic changes in natural variability occur, such as volcanic eruptions or secular changes in solar forcing (Stocker et al., 2013).

Next, the AMOC's response to different anthropogenic forcing emission pathways is assessed. The forcing is estimated here by the ensemble mean trends from the CMIP5 historical and future (RCP4.5 and RCP8.5) scenarios. Hence, the term hereafter referred to as the 'forced component' is defined as the common component within the ensemble of simulations. To identify the probability distribution that includes both natural variability plus anthropogenic forced variability, the smoothed forced trends of the ensemble mean (using the same four trend duration windows as above) are added to the reference (control) PDF. This forced trend can either be time-averaged per scenario (and therefore generate one PDF per scenario), or time-varying (which produces the PDF as a function of time per scenario). A hypothetical illustration of a reference PDF (Figure 5.1a) that experiences a time-averaged forced increase in AMOC strength would shift the entire PDF to the right (Figure 5.1b) leading to a higher probability of an AMOC increase, and a time-averaged forced decline in AMOC strength would shift the entire PDF to the left (Figure 5.1c), leading to a higher probability of an AMOC decrease.

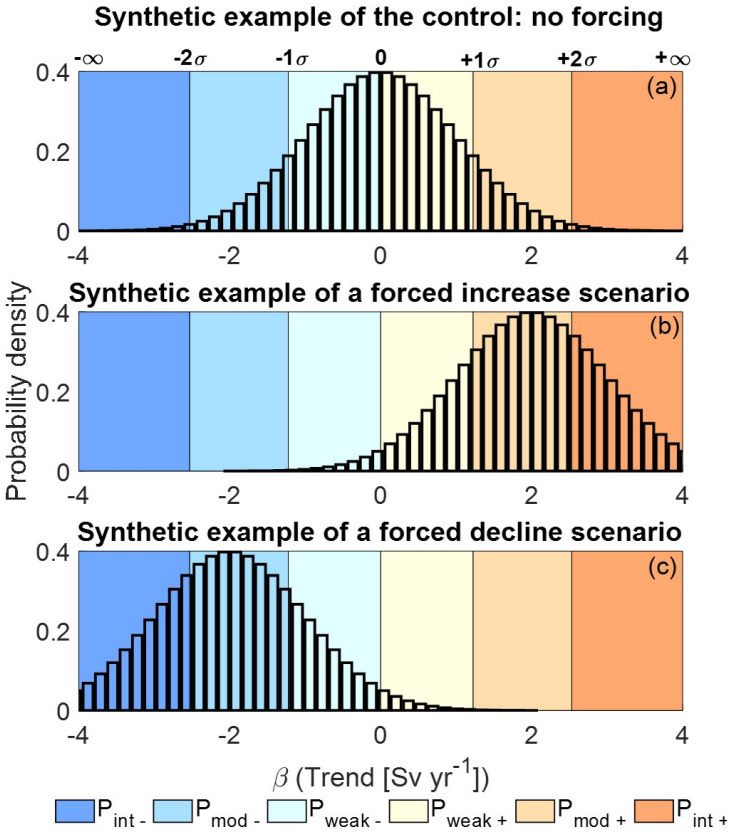

FIGURE 5.1: The effects of anthropogenically-forced AMOC trends on its probability density function of natural variability. Illustration of a normalised probability density function with synthetic data that represents: (a) natural variability (from the control simulations in this study), without anthropogenic forcing, (b) a 'forced' time-averaged increasing AMOC trend of $+2\,\mathrm{Sv\,yr^{-1}}$, and (c) a 'forced' time-averaged declining AMOC trend of $-2\,\mathrm{Sv\,yr^{-1}}$. The colours represent the six categories of trend probabilities: intense decrease (P_{int-}) and intense increase (P_{int+}), for the area >2 standard deviations in dark blue and dark orange, respectively, moderate decrease (P_{mod-}) and moderate increase (P_{mod+}), for the area between 1 and 2 standard deviations in light blue and light orange, respectively, and weak decrease (P_{weak-}) and weak increase (P_{weak+}), for the area between 0 and 1 standard deviations in pale blue and yellow, respectively.

Elaborating on the method in Sévellec et al. (2016), the full range of trends found in the control is split into six probability categories (see Figure 5.1 and Equation 5.1): intense decrease (P_{int-} in Equation 5.1a), moderate decrease (P_{mod-} in Equation 5.1b), weak decrease (P_{weak-} in Equation 5.1c), weak increase (P_{weak+} in Equation 5.1d), moderate increase (P_{mod+} in Equation 5.1e), and intense increase ($P_{int.+}$ in Equation 5.1f). These categories are based on the probability of trends in the multi-model control PDF falling between 0 and 1 standard deviation ('weak'), from 1 to 2 standard deviations ('moderate'), and above 2 standard deviations ('intense'). These probability categories read:

$$\mathrm{P_{int-}} = \mathrm{P}(\beta \leq -2\sigma) = \int_{-\infty}^{-2\sigma} \mathrm{p}(\beta)\,\mathrm{d}\beta, \tag{5.1a}$$

$$\mathrm{P_{mod-}} = \mathrm{P}(-2\sigma < \beta \leq -\sigma) = \int_{-2\sigma}^{-\sigma} \mathrm{p}(\beta)\,\mathrm{d}\beta, \tag{5.1b}$$

$$\mathrm{P_{weak-}} = \mathrm{P}(-\sigma < \beta \leq 0) = \int_{-\sigma}^{0} \mathrm{p}(\beta)\,\mathrm{d}\beta, \tag{5.1c}$$

$$\mathrm{P_{weak+}} = \mathrm{P}(0 < \beta \leq +\sigma) = \int_{0}^{+\sigma} \mathrm{p}(\beta)\,\mathrm{d}\beta, \tag{5.1d}$$

$$\mathrm{P_{mod+}} = \mathrm{P}(+\sigma < \beta \leq +2\sigma) = \int_{+\sigma}^{+2\sigma} \mathrm{p}(\beta)\,\mathrm{d}\beta, \tag{5.1e}$$

$$\mathrm{P_{int+}} = \mathrm{P}(+2\sigma < \beta) = \int_{+2\sigma}^{+\infty} \mathrm{p}(\beta)\,\mathrm{d}\beta, \tag{5.1f}$$

where σ is the standard deviation of the natural variability (i.e., from the multimodel mean of the control PDF), β is the forced trend (i.e., from the historical or future scenario data), and p is the probability density function. The $\mathrm{p}(\beta)$ here can either be the probability density function of the time-averaged trends, or the time-varying trends. The six computations, in Equation 5.1, are repeated for each of the moving-window trend filters (2, 10, 20, and 40 years), and for each forced scenario (historical, RCP4.5 and RCP8.5). This determines the probability of the six categories for interannual to multi-decadal trends in each scenario.

Lastly, the expected intensity of both an increasing and decreasing trend is computed. As opposed to the six probability categories above (in Equation 5.1), there are now only two categories, the expected decrease ($\mathrm{E_-}$), and the expected increase ($\mathrm{E_+}$), which are

estimated as follows:

$$\mathrm{E}_{-} = \frac{\int_{-\infty}^{0} \mathrm{p}(\beta)\,\beta \mathrm{d}\beta}{\int_{-\infty}^{0} \mathrm{p}(\beta)\,\mathrm{d}\beta}, \tag{5.2a}$$

$$\mathrm{E}_{+} = \frac{\int_{0}^{+\infty} \mathrm{p}(\beta)\,\beta \mathrm{d}\beta}{\int_{0}^{+\infty} \mathrm{p}(\beta)\,\mathrm{d}\beta}, \tag{5.2b}$$

where the probability density function, $\mathrm{p}(\beta)$, is only computed for the time-varying trends, and not time-averaged. Therefore, the E_{-} and E_{+} are time-varying expected intensities of an AMOC negative trend and positive trend, respectively. It is important to note that though this analysis uses the AMOC at 48° N, it was also performed for 20 to 60° N (not shown), and produced similar results. Therefore, comparisons with previous work using other latitudes (for example, 26.5° N) are valid.

5.2.3 Results and discussion

This study uses the control ensemble PDFs as a reference, representing the AMOC's natural variability, where trend values range from -3 to 3 $\mathrm{Sv\,yr^{-1}}$ across the 16 models for the 2-year trends (Figure 5.2a) and -0.1 to 0.1 $\mathrm{Sv\,yr^{-1}}$ for the 40-year trends (Figure 5.2d). These PDFs show an almost symmetrical probability (also known as zero skewness) of an increase or a decrease in the AMOC transport, regardless of the trend length (Figure 5.2a, b, c, and d). The interannual, decadal and multi-decadal forced trends in historical and 21st century (RCP4.5 and RCP8.5) scenarios are now considered (Figures 5.4 and 5.5), both as time-mean and time-varying forcing, in order to discuss the total (natural plus forced) variability from 1850 to 2099. The timing of a shift in probabilities is revealed when considering these PDFs as a function of time, among the combined ensemble historical and future scenario data (Figure 5.6 and 5.7).

5.2.3.1 Historical interannual to multi-decadal trends

The historical ensemble PDFs are almost identical to the controls', meaning that the average interannual to multi-decadal forced trends of the AMOC from 1850 to 2005 are equivalent to natural variability (Figure 5.2a, b, c, and d). The forcing, on average, is therefore negligible over the historical period. The time-varying trends, however, show that there are large oscillations around zero (Figures 5.4 and 5.5), which produce

time-evolving shifts in the probability of a weak increase (P_{weak+}) or a weak decrease (P_{weak-}) in the AMOC (Figures 5.6 and 5.7). This demonstrates that the effects of forcing on probabilities of strengthening and weakening are time-dependent, although the relative contributions of natural and forced signals on the trends cannot be distinguished. This is a point that is still under discussion among the scientific community. A study using one iteration of an AMOC timeseries (an observational proxy) recovers a stable AMOC since 1860, without finding any trends that fall outside the range of interannual to multidecadal natural variability (Parker and Ollier, 2016). On the other hand, Rahmstorf et al. (2015) suggest that the 20-year decline from 1975 to 1995 had almost a 100% probability of being anthropogenically-caused. Here, the results indicate that when using a timeseries constructed from an ensemble mean of forced historical AMOC trends from 1850 to 2005, the time-average is dominated by natural variability.

5.2.3.2 Interannual (one- to two-year) trends in the 21st century

The future scenario interannual PDFs (1-year and 2-year time-mean trends in Figure 5.2a and Figure 5.3) mirror the control and historical PDFs. The time-varying trends and probabilities (Figures 5.4a and 5.5a, and Figures 5.6a and 5.7a) also represent a similar behaviour to the historical period. This illustrates that even though the AMOC is under two climate change scenarios, on higher-frequency timescales, the time-mean and time-varying natural variability is larger than anthropogenically-forced changes (the signal-to-noise ratio is weak). An example of the implications of these findings is that the probability of an event such as the potential decline in strength of 30%, observed over 14 months between 2009-2010 (McCarthy et al., 2012; Srokosz et al., 2012; Bryden et al., 2014), falls within the range of natural variability. Ezer (2015) suggests that this so-called 'extreme event' is simply the last part of a longer, decadal trend, that started before RAPID (according to three observational datasets from 2000). Although McCarthy et al. (2012) and Roberts et al. (2014) infer that the CMIP5 ensemble underestimates the observed interannual variability and trends (of the 2009-2010 magnitude, 4.7 Sv, for example), the ratio between the trends and the variability could still be accurate, therefore not affecting the results.

5.2.3.3 Semi-decadal and decadal trends in the 21st century

Upon examining 5-year and 10-year trends in the 21st century, the average probability of seeing a decline in the future scenarios increases slightly, shown by a small shift in the PDFs towards negative values (Figure 5.2b). The average probability of a weak decline from 2006-2099 for 10-year trends is 61.3% and 67.1% under an RCP4.5 and RCP8.5 scenario, respectively (Figure 5.2b, and Figure 5.3). The time-varying trend intensities are generally negative throughout the 21st century in both scenarios (Figures 5.4b and 5.5b), although the last few decades under RCP4.5 show a recovery of the

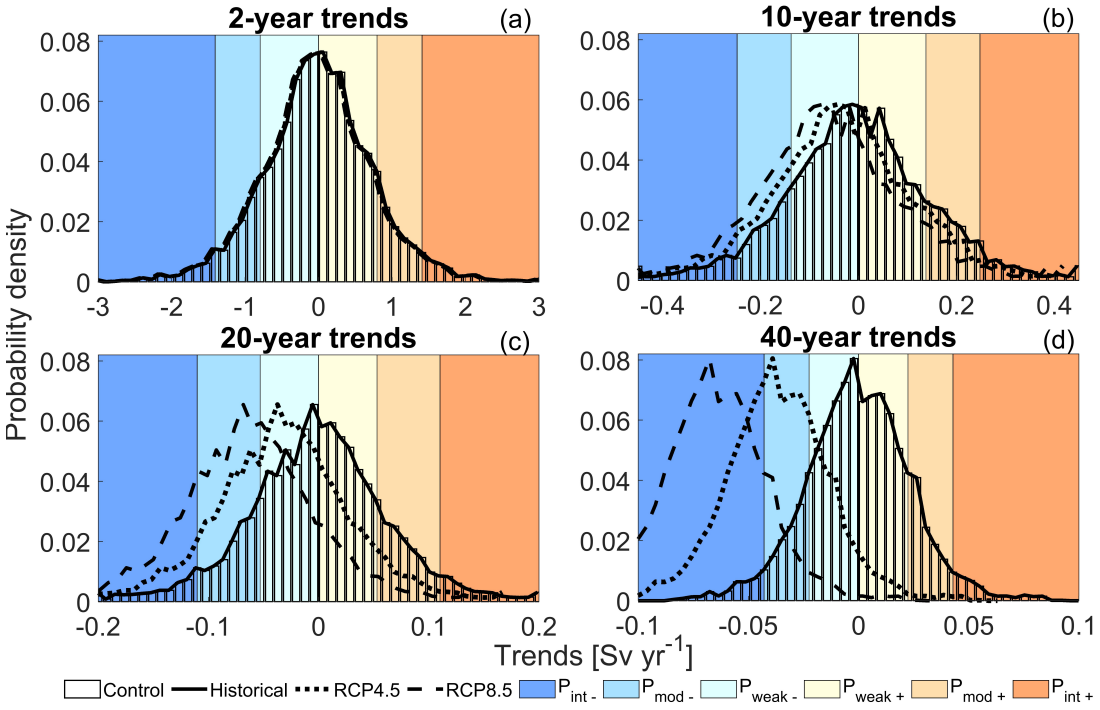

FIGURE 5.2: Probability density functions of the 48° N AMOC's natural variability, from the control simulations (vertical bar-plots), natural variability plus historical time-mean forcing (solid lines), natural variability plus RCP4.5 time-mean forcing (dotted lines), natural variability plus RCP8.5 time-mean forcing (dashed lines) using different time-mean forced trend durations: (a) 2 years, (b) 10 years, (c) 20 years, and (d) 40 years. The six colours display the six probability categories defined in Equation 5.1 and Figure 5.1.

trends oscillating around zero. The time-varying P_{weak-} remains above 50%, with one moderate P_{mod-} peak at the turn of the century in both RCP4.5 and RCP8.5 (Figures 5.6b and 5.7b), and RCP4.5 again returns to probabilities oscillating between a P_{weak+} and P_{weak-} by 2099. Contrary to the interannual results, since a forced decadal decline is probable at the turn of the century (of 79% in 2010 for 'business-as-usual'), the observed decadal trend from RAPID of -0.41 ($\pm$ 0.18) Sv yr^{-1} between 2004 and 2014 (Jackson et al., 2016) was likely to occur, according to the RCP4.5 and RCP8.5 ensemble mean forcing here. These results suggest that the AMOC therefore starts being sensitive to ensemble mean climate forcings of trend durations longer 5 years.

5.2.3.4 Multi-decadal (20-year) trends in the 21st century

The 20-year ensemble time-mean trends in the 21st century generate a distinctively augmented AMOC slowdown probability. The average probabilities of a 20-year decline from 2006-2099 under an RCP4.5 and RCP8.5 scenario, are 72.2% and 86.5%, respectively (Figures 5.2c and 5.3). Although also clearly seen in the 10-year trends, here the most prominent feature is a rapid jump in both 20-year decline intensity (Figures 5.4c

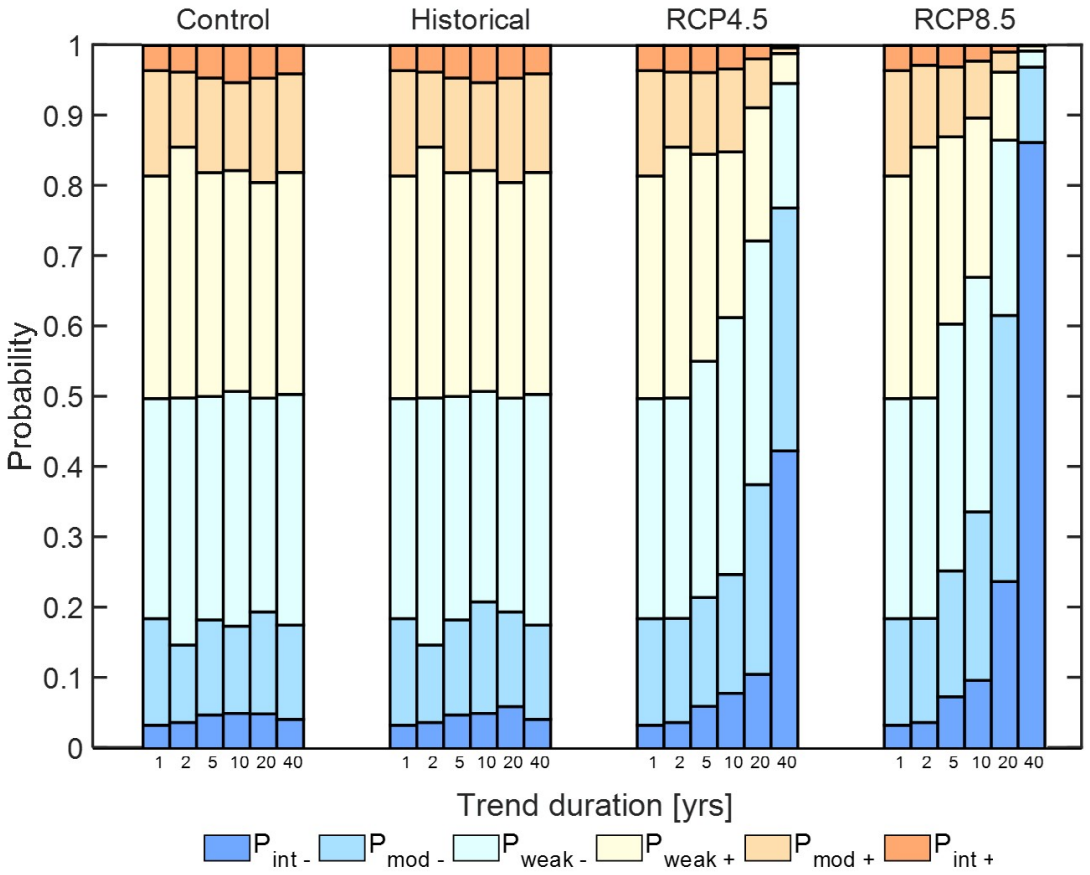

FIGURE 5.3: Probabilities of the natural variability or natural variability plus time-mean forcing trends for the six probability categories defined in Equation 5.1. Here, some additional trend durations are also included (1, 2, 5, 10, 20 and 40 years). The different scenarios are grouped together and labelled above: control (pre-industrial simulations), historical (from 1850 to 2005), RCP4.5 and RCP8.5 (both from 2006 to 2099).

and 5.5c) and probability (Figures 5.6c and 5.7c) at the beginning of the 21st century. This 20-year period, from 1995 to 2015 is therefore hereafter defined as the 'rogue period', characterised by the maximum negative trend intensity and decline probability over 250 years. The maximum trend magnitude is -0.11 Sv yr^{-1} in both future scenarios (Figures 5.4c for RCP4.5, and 5.5c for RCP8.5). Pre-1995, the trends oscillate around zero and post-2015, the negative trends relax partially, under RCP8.5, and fully (back to zero), under RCP4.5. Furthermore, due to the PDF shifting almost entirely to negative values during the rogue period, the ensemble AMOC trends mirror the expected declining trend intensities (E_-). The time-varying probability of an intense 20-year decline (P_{int-}) reinforces the uniqueness of the rogue period; it shows a maximum intense decline probability of 49.9% under RCP4.5, and 55.7% under RCP8.5, compared to their pre-1995 maximum of 13.2% and post-2015 maximums of 23.8% and 37.6%, respectively (Figures 5.6c and 5.7c).

The timing of this 20-year rogue period, which suggests an overall probability of decline

of 95.4% over 1995-2015, is interestingly consistent with observational findings showing that the AMOC has indeed sustained a decline since the mid-1990s (Smeed et al., 2013; Robson et al., 2014). Robson et al. (2016) associate the decline to a simultaneous dramatic decrease in the Labrador Sea density index, stimulated by a deep ocean warming and long-term freshening of the subpolar gyre waters. They mention that the magnitude of the anthropogenic and ocean circulation contributions to this change in temperature and salinity remains an open question, (and is therefore the focus of one of the aims in Part II of this study). The results from this analysis suggest that 1995-2015 is a rogue period where the AMOC is forced to decline, regardless of natural variability.

5.2.3.5 Multi-decadal (40-year) trends in the 21st century

The 40-year time-mean ensemble trends produce the highest probabilities of an AMOC decline relative to the other trend durations (94.6% under RCP4.5, and 99.2% under RCP8.5 in Figures 5.2d and 5.3). The striking feature under the 'business-as-usual' scenario is the time-average probability of an intense decline (P_{int-}) at 86.2%, whereas none of the other trend durations or scenarios exceed a P_{int-} of 50%. This is also seen in the time-varying RCP8.5 probabilities (Figure 5.7d), where there is a sustained high P_{int-} throughout the 21st century. This contrasts to the 20-year probabilities that oscillate between a P_{weak-} and P_{mod-} in the 21st century (Figure 5.7c). The time-varying intensity of the trends is also identical to the expected decline in RCP8.5 (Figure 5.5d). Although the RCP4.5 probabilities also sustain a high P_{int-}, after 2060, once again, the stabilisation of an equal probability of increase and decrease occurs by 2099 (Figure 5.6d), and trend intensity is no longer identical to (E_-) (Figure 5.4d). Further smoothing of the trends (above 40 years) would mechanically increase the contribution of the forced trend over the natural one, simply increasing the probability of a decline. Therefore, these results find that not only a multi-decadal but also a quasi-centennial sustained decline is highly probable throughout the 21st century (consistent with the IPCC report's conclusion in Weaver et al. (2012); Flato et al. (2013)).

In summary, Part I's results suggest that the AMOC's interannual natural variability is stronger than the forced signal over 250 years, regardless of the forcing applied (future 'business-as-usual' or 'stabilisation'). The longer-term forced trends (more than 5-years in duration) under future scenario anthropogenic forcing skew the probability to a decline. Both a 20-year rogue period (from 1995 to 2015) and a sustained 21st century intense decline probability in RCP8.5 set the stage for Part II. The next analysis therefore investigates the cause of these probability changes, where the dynamical relationship between the AMOC and salinity fluxes can direct whether the changes originate from internal forcing (oceanic processes), or external forcing (atmospheric processes).

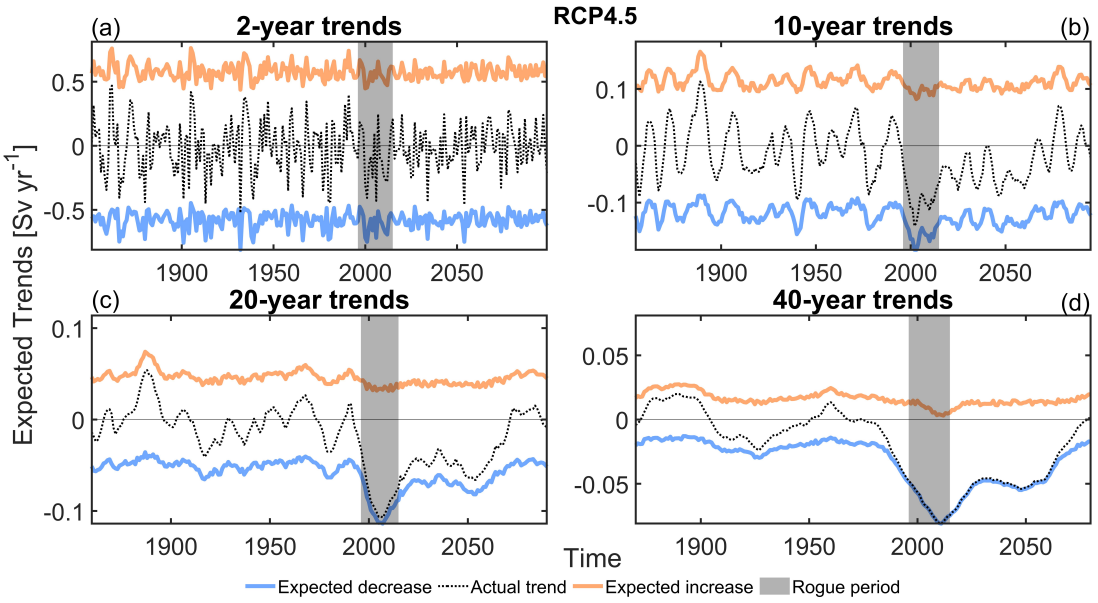

FIGURE 5.4: Actual and expected trends over the historical and future RCP4.5 periods. The time-varying actual (black dotted lines) and expected forced ensemble-mean trend increase (orange lines) and decrease (blue lines) intensities [Sv yr^{-1}] of the AMOC at 48° N from 1850 to 2099 are displayed. The forced trends are filtered over different trend durations: (a) 2 years, (b) 10 years, (c) 20 years, and (d) 40 years. The 20-year rogue period from 1995 to 2015 is centred around the 20-year maximum AMOC decline (from subplot c), and shown in grey on all plots.

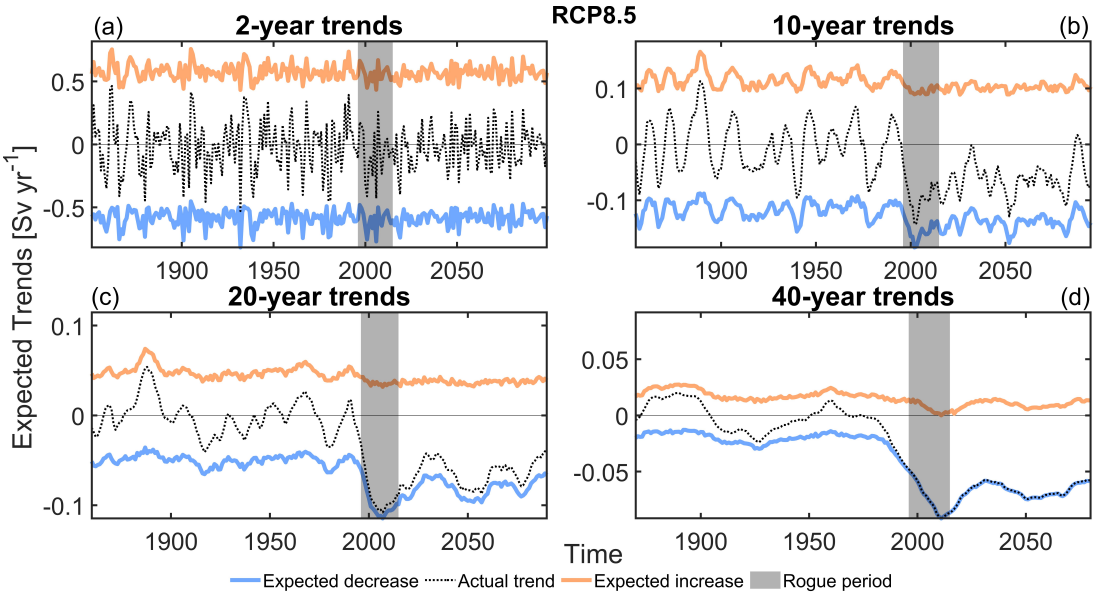

FIGURE 5.5: As Figure 5.4 but for RCP8.5

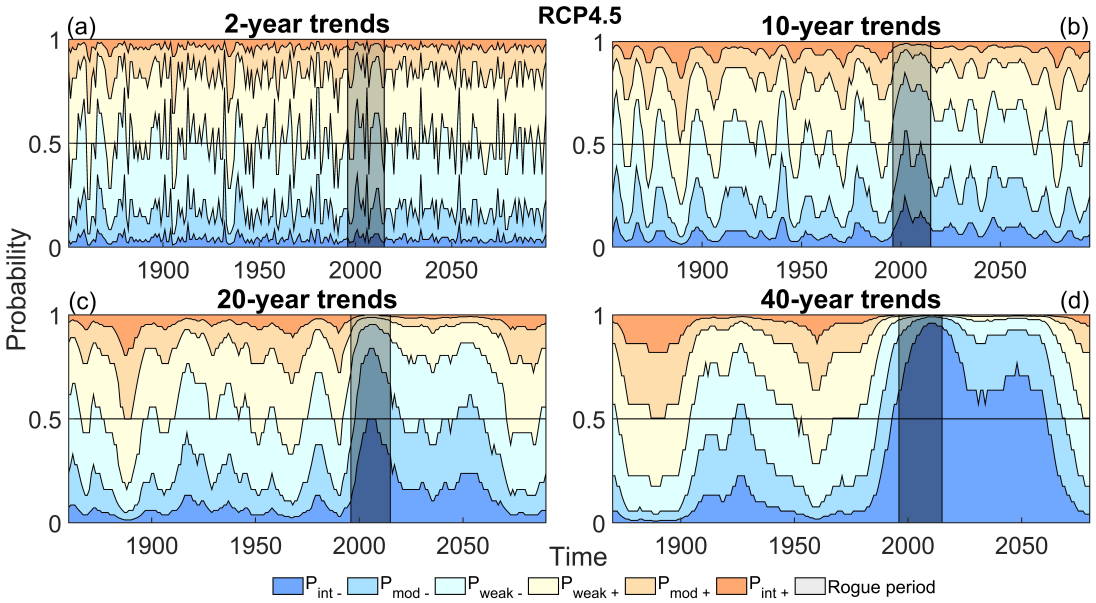

FIGURE 5.6: Probability of events over the historical and future RCP4.5 periods. The time-varying ensemble mean probabilities of the natural variability plus forcing over the historical and future scenario of the AMOC at 48°N, from 1850 to 2099. The forced trends are filtered over different trend durations: (a) 2 years, (b) 10 years, (c) 20 years, and (d) 40 years. The rogue period from 1995 to 2015 representing the maximum 20-year AMOC decline probability is shaded in grey. The six colours display the six probability categories defined in Equation 5.1 and Figure 5.1.

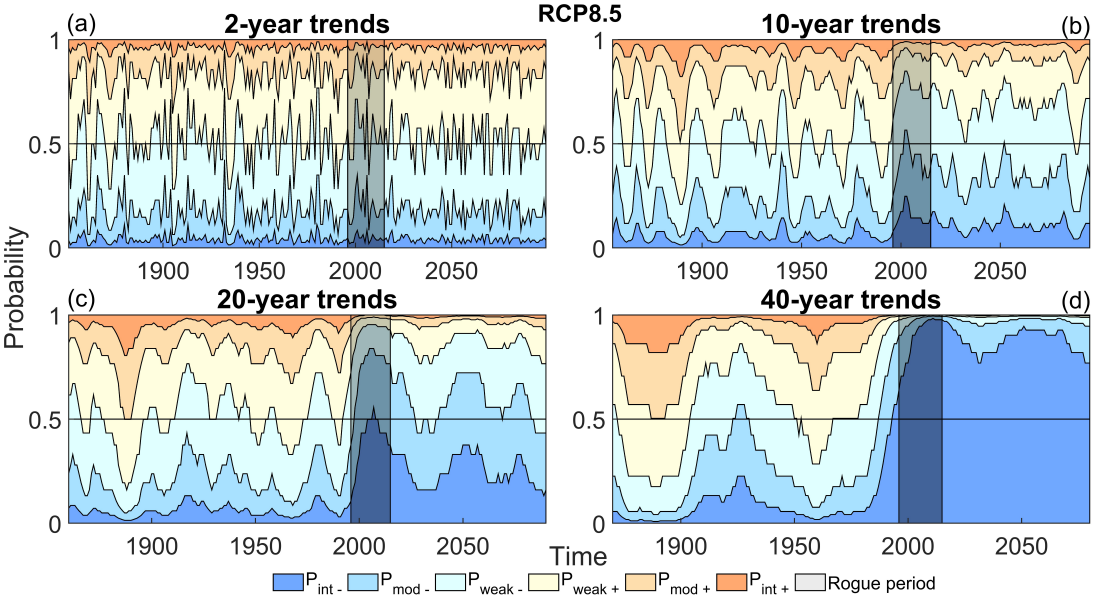

FIGURE 5.7: As Figure 5.6 but for RCP8.5.

5.3 Part II: Drivers of the forced AMOC slowdown

5.3.1 Data: *CMIP5 RCP8.5 salinity and temperature in three dimensions*

The same CMIP5 models are used as in subsection 5.2.1, however here, only historical and RCP8.5 scenarios are used. The full four-dimensional output data are also obtained (three dimensions in the spatial field and as a function of time) for the salinity and absolute potential temperature profile data. Among the 16 models used, the number of vertical levels vary from 31 to 70, with a resolution of 4.5 m to 15 m at the surface, and 206 m to 550 m at the bottom. The North Atlantic data are extracted between 96° W and 2° W (from the Gulf of Mexico, inclusive, to the eastern African coast) and 20°N to 60°N. Since each CMIP5 model grid has a different horizontal resolution, to acquire the ensemble mean as a function of latitude, the models are first re-gridded to a 2x2° resolution by finding the nearest neighbour even longitude and latitude values. The North Atlantic is then split into two regions, the subtropical region (STR) and the subpolar region (SPR). The boundary between these regions is determined robustly from the Hovmöller plots of the ensemble mean of zonally, and full-depth averaged salinity as a function of latitude (Figures 5.10h and 5.11h). North and south of 48°N, there is a clear distinction between the decrease in salinity (freshening) in the SPR and an increase in salinity in the STR.

5.3.2 Methods: *estimating the salinity budget*

The mathematical framework outlined below has been used in several studies focusing on meridional temperature or salinity fluxes, and their respective temperature or salinity budget in the Atlantic (Bryden et al., 2011; Drijfhout et al., 2011; Weaver et al., 2012; McDonagh et al., 2015; Mecking et al., 2016, 2017). It was formulated by Rahmstorf (1996) and de Vries and Weber (2005), a rigorous derivation can be found in Mecking et al. (2016), and it is derived in further detail below.

5.3.2.1 Mathematical framework of the salinity budget

To estimate the salinity budget within the subtropical or subpolar boxes defined in this study, first the advective equation is simplified given the incompressibility or non-divergence in the three spatial dimensions (x for zonal, y for meridional and z for vertical):

$$Adv = u\partial_x S + v\partial_y S + w\partial_z S, \tag{5.3}$$

where u is the zonal velocity, v is the meridional velocity, w is the vertical velocity and S is salinity. Therefore, due to non-divergence:

$$\partial_x u + \partial_y v + \partial_z w = 0, \tag{5.4}$$

and (5.3) can be transformed to:

$$Adv = \partial_x(uS) + \partial_y(vS) + \partial_z(wS). \tag{5.5}$$

The advection-diffusion equation reads:

$$D_t S = \underbrace{\partial_t S}_{\substack{\text{Time} \\ \text{deriva-} \\ \text{tive}}} + \underbrace{\partial_x(uS) + \partial_y(vS) + \partial_z(wS)}_{\text{Advection}} = \underbrace{\partial_x(\kappa_x \partial_x S) + \partial_y(\kappa_y \partial_y S) + \partial_z(\kappa_z \partial_z S)}_{\text{Diffusion}}, \tag{5.6}$$

where t is time, D_t is the material derivative, and κ_x, κ_y, and κ_z are the zonal, meridional and vertical diffusivity coefficients.

Before undergoing the zonal, meridional, and vertical integrations of salinity in a region, the boundary conditions are defined. The northern and southern boundaries have free flow into and out of the box via advection and diffusion. The eastern and western edges, and the bottom (the seafloor) neither exchange salinity via advection nor diffusion (although the inflow from the Mediterranean and other river run-offs are added to the residual term). In the vertical, at the atmosphere-sea surface interface, atmospheric forcing can change the salinity via freshwater fluxes (evaporation and precipitation). The terms that therefore remain as an end-product are the meridional advective fluxes at the northern and southern boundaries and a residual term including primarily vertical flux from the atmospheric forcing (plus a few other residual terms shown in Equations 5.10 and 5.28). The notation for the integrals in the three directions are simplified to: $\int_X dx = \int_{X_w}^{X_e} dx$ for the zonal integral from 2° W (X_e) to 96° W (X_w), then $\int_Z dz = \int_{-H}^{z_0} dz$ in the vertical direction from the surface (z_0) to the sea floor ($-H$), and $\int_Y dy = \int_{Y_s}^{Y_n} dy$ for the meridional direction from 60° N (Y_n) to 48° N (Y_s) for the subpolar box (or 48° N to 20° N for the subtropical box). The first integration is zonal:

$$\begin{aligned} &\int_X \partial_t S \; dx + [(uS)|_{X_e} - (uS)|_{X_w}] + \partial_y \left(\int_X vS \; dx \right) + \partial_z \left(\int_X wS \; dx \right) \\ &= [(\kappa_x \partial_x S)|_{X_e} - (\kappa_x \partial_x S)|_{X_w}] + \partial_y \left(\int_X \kappa_y \partial_y S \; dx \right) + \partial_z \left(\int_X \kappa_z \partial_z S \; dx \right), \end{aligned} \tag{5.7}$$

where, due to the east and west solid zonal walls, $\partial_x S|_{X_e} = \partial_x S|_{X_w} = 0$. There could be residual zonal (advective and diffusive) inflow from the Mediterranean Sea (but not from the Gulf of Mexico since it is included in the box), therefore, $u|_{X_e} \neq 0$, which will

later be defined as a residual term in the zonal direction. The next integration is in the vertical:

$$\int_X \int_Z \partial_t S \; dxdz + \int_Z (uS)|_{X_e} dz + \partial_y \left(\int_X \int_Z \; vS \; dxdz \right) + \left[\int_X (wS)|_{z_0} \; dx - \int_X (wS)|_{-H} \; dx \right]$$
$$= \int_Z (\kappa_x \partial_x S)|_{X_e} dz + \partial_y \left(\int_X \int_Z \kappa_y \partial_y S \; dxdz \right) + \left[\int_X (\kappa_z \partial_z S)|_{z_0} \; dx - \int_X (\kappa_z \partial_z S)|_{-H} \; dx \right], \tag{5.8}$$

where, due to the lack of mass and salinity transfer across the ocean floor and lack of mass transfer across the sea surface, the residual term in the vertical dimension is as a result of salinity flux across the surface (due to precipitation and evaporation) which will later be defined as a 'forcing' residual. The final integration is meridional:

$$\begin{aligned}
&\int_X \int_Y \int_Z \partial_t S \; dxdydz = - \int_Y \int_Z (uS)|_{X_e} dydz \\
&- \left[\int_X \int_Z (vS)|_{Y\,60N} \; dxdz - \int_X \int_Z (vS)|_{Y\,48N} \; dxdz \right] \\
&+ \int_Y \int_Z (\kappa_x \partial_x S)|_{X_e} dydz + \left[\int_X \int_Z (\kappa_y \partial_y S)|_{Y\,60N} \; dxdz - \int_X \int_Z (\kappa_y \partial_y S)|_{Y\,48N} \; dxdz \right] \\
&+ \int_X \int_Y (\kappa_z \partial_z S)|_{z_0} \; dxdy,
\end{aligned} \tag{5.9}$$

where, though the assumption is that advection is a lot larger than diffusion in large-scale processes, the salinity transfer due to meridional diffusion term will also be added to the residual term. Therefore the residual terms so far are combined into one term, $\mathcal{R}$:

$$\begin{aligned}
\mathcal{R} = &\int_Y \int_Z (\kappa_x \partial_x S)|_{X_e} dydz + \left[\int_X \int_Z (\kappa_y \partial_y S)|_{Y\,60N} \; dxdz - \int_X \int_Z (\kappa_y \partial_y S)|_{Y\,48N} \; dxdz \right] \\
&- \int_Y \int_Z (uS)|_{X_e} dydz + \int_X \int_Y (\kappa_z \partial_z S)|_{z_0} \; dxdy.
\end{aligned} \tag{5.10}$$

The time derivative of salinity transport in the subpolar box condenses to the divergence of the meridional transport of salinity, which is the difference between the southern boundary and northern boundary meridional transport, plus the residual term:

$$\int_X \int_Y \int_Z \partial_t S \; dxdydz = \int_X \int_Z (vS)|_{Y\,48N} \; dxdz - \int_X \int_Z (vS)|_{Y\,60N} \; dxdz + \mathcal{R}. \tag{5.11}$$

Now, from the first term in the right hand side of Equation 5.11, both the meridional velocity (v) and salinity (S) can be split into their respective zonal means and anomalies:

$$\mathcal{S} = \int_X \int_Z vS \; dxdz = \int_X \int_Z (\overline{v} + v')(\overline{S} + S') \; dxdz, \tag{5.12}$$

where $\mathcal{S}$ is the transport of salinity at a chosen latitude, the overbar indicates a zonal average and the prime refers to the anomaly. A zonal average for a given variable (f) at a specific latitude and as a function of depth is therefore:

$$\overline{f}(z) = \frac{\int_X f \; dx}{\int_X \; dx} = \frac{\int_X f \; dx}{\mathcal{W}_x}, \tag{5.13}$$

where f represents either v or S, and the width of the basin ($\int_X \; dx$) is denoted as $\mathcal{W}_x$ from now on. The average terms ($\overline{v}$ and $\overline{S}$) are then separated into two terms: (1) the zonally and vertically averaged net term (or 'net', a constant), and (2) the overturning component (or 'ov', that varies vertically). The anomaly remains one term which is azonal (or 'az', that varies zonally and vertically). These new definitions therefore expand Equation 5.12 as follows:

$$\mathcal{S} = \int_X \int_Z (v_{\text{net}} + v_{\text{ov}} + v_{\text{az}})(S_{\text{net}} + S_{\text{ov}} + S_{\text{az}}) \; dxdz. \tag{5.14}$$

The first term ('net') on the RHS of Equation 5.14 for a given variable (f) at a specific latitude is therefore:

$$f_{\text{net}} = \frac{\int_X \int_Z f \; dxdz}{\int_X \int_Z \; dxdz} = \frac{\int_X \int_Z f \; dxdz}{\mathcal{A}_{xz}}, \tag{5.15}$$

where the zonal and vertical area ($\int_X \int_Z \; dxdz$) is denoted as $\mathcal{A}_{xz}$ from now on. The net term becomes a constant from integrating and averaging zonally and vertically. The second term ('ov') on the RHS of Equation 5.14 is:

$$f_{\text{ov}}(z) = \frac{\int_X f \; dx}{\mathcal{W}_x} - \frac{\int_X \int_Z f \; dxdz}{\mathcal{A}_{xz}} = \overline{f}(z) - f_{\text{net}}, \tag{5.16}$$

where the overturning term is the zonal average (Equation 5.13) minus the net term (Equation 5.15). And finally, the third term ('az') on the RHS of Equation 5.14 is the azonal term, or the total function's deviation from the zonal mean:

$$f_{\text{az}}(x, z) = \frac{\int_X f \; dx}{\mathcal{W}_x} - f(x, z) = \overline{f}(z) - f(x, z). \tag{5.17}$$

Now, solving for Equation 5.14 takes the form:

$$\mathcal{S} = \int_X \int_Z (\underbrace{v_{\text{net}} S_{\text{net}}}_{\text{A}} + \underbrace{v_{\text{ov}} S_{\text{net}}}_{\text{B}} + \underbrace{v_{\text{az}} S_{\text{net}}}_{\text{C}} + \underbrace{v_{\text{net}} S_{\text{ov}}}_{\text{D}} + \underbrace{v_{\text{ov}} S_{\text{ov}}}_{\text{E}} + \underbrace{v_{\text{az}} S_{\text{ov}}}_{\text{F}} + \underbrace{v_{\text{net}} S_{\text{az}}}_{\text{G}} + \underbrace{v_{\text{ov}} S_{\text{az}}}_{\text{H}} + \underbrace{v_{\text{az}} S_{\text{az}}}_{\text{I}}) \, dxdz, \tag{5.18}$$

where each term in Equation 5.18 has been labelled in order to solve for them separately to see which terms can be removed. Firstly:

$$A = \int_X \int_Z v_{\text{net}} S_{\text{net}} \, dxdz = v_{\text{net}} S_{\text{net}} \mathcal{A}_{xz}, \tag{5.19}$$

where A is a constant and will be added as a residual 'net' term (that is not important for the core of the study, since the focus is on change from a reference state). The following terms can be removed from Equation 5.18:

$$\begin{aligned} B &= \int_X \int_Z v_{\text{ov}} S_{\text{net}} \, dxdz = S_{\text{net}} \left(\int_X \int_Z v_{\text{ov}} dxdz \right) = 0, \\ C &= \int_X \int_Z v_{\text{az}} S_{\text{net}} \, dxdz = S_{\text{net}} \left(\int_X \int_Z v_{\text{az}} dxdz \right) = 0, \\ D &= \int_X \int_Z v_{\text{net}} S_{\text{ov}} \, dxdz = v_{\text{net}} \left(\int_X \int_Z S_{\text{ov}} dxdz \right) = 0, \end{aligned} \tag{5.20}$$

and E remains in the final equation, as a vertical integration of the two 'ov' terms:

$$E = \int_X \int_Z v_{\text{ov}} S_{\text{ov}} \, dxdz = \int_Z \mathcal{W}_x \, v_{\text{ov}} S_{\text{ov}} \, dz. \tag{5.21}$$

The next 3 terms can also be removed:

$$\begin{aligned} F &= \int_X \int_Z v_{\text{az}} S_{\text{ov}} \, dxdz = 0, \\ G &= \int_X \int_Z v_{\text{net}} S_{\text{az}} \, dxdz = v_{\text{net}} \left(\int_X \int_Z S_{\text{az}} dxdz \right) = 0, \\ H &= \int_X \int_Z v_{\text{ov}} S_{\text{az}} \, dxdz = 0, \end{aligned} \tag{5.22}$$

which leaves the last term, the vertically and zonally varying 'az' terms, which are not simplified further:

$$I = \int_X \int_Z v_{\text{az}} S_{\text{az}} \, dxdz. \tag{5.23}$$

Therefore, from Equations 5.19 to 5.23, terms B, C, D, F, G, and H are formally equal to zero by construction, and the terms that remain from Equation 5.18 are the simplified A, E and I terms:

$$\mathcal{S} = v_{\text{net}} S_{\text{net}} \mathcal{A}_{xz} + \int_Z \mathcal{W}_x \, v_{\text{ov}} S_{\text{ov}} \, dz + \int_X \int_Z v_{\text{az}} S_{\text{az}} \, dxdz, \tag{5.24}$$

where the transport of salinity (in units of Sv psu) at a given latitude, via the overturning and azonal components, are defined as:

$$\mathcal{S}_{\text{ov}} = \int_Z \mathcal{W}_x \, v_{\text{ov}} S_{\text{ov}} \, dz, \tag{5.25}$$

and

$$\mathcal{S}_{\text{az}} = \int_X \int_Z v_{\text{az}} S_{\text{az}} \, dxdz. \tag{5.26}$$

These two equations are used to compute the $\mathcal{S}_{\text{ov}}$ and $\mathcal{S}_{\text{az}}$ at the three latitudes (20° N, 48° N and 60° N) to estimate the salinity transport across the northern and southern boundaries of the subpolar and subtropical boxes. To close the budget, the time derivative of integrated salinity in the each box becomes the sum of three components: the difference between the $\mathcal{S}_{\text{ov}}$ at the northern and southern boundaries of the box plus the difference between the $\mathcal{S}_{\text{az}}$ at the same latitudes, plus the total residual term. Using the subpolar box (SP) as an example:

$$\int_X \int_Y \int_Z \partial_t S|_{\text{SP}} \, dxdydz$$

$$= (\mathcal{S}_{\text{ov}}|_{48N} - \mathcal{S}_{\text{ov}}|_{60N}) + (\mathcal{S}_{\text{az}}|_{48N} - \mathcal{S}_{\text{az}}|_{60N}) + \mathcal{R}_{\text{total}} = \mathcal{S}_{\text{ov}}|_{\text{SP}} + \mathcal{S}_{\text{az}}|_{\text{SP}} + \mathcal{R}_{\text{total}}|_{\text{SP}}, \tag{5.27}$$

where the residual term, $\mathcal{R}_{\text{total}}$, is now the combination of the terms in Equation 5.10 and the net velocity and salinity terms:

$$\mathcal{R}_{\text{total}} = \mathcal{R} + v_{\text{net}} S_{\text{net}} \mathcal{A}_{xz}. \tag{5.28}$$

One of the caveats in our methodology is the grouping of these terms, meaning the separate contribution of each term towards the $\mathcal{R}_{\text{total}}$ cannot be attained. Following results from Mecking et al. (2016), however, the residual term that dominates both in the subtropical and subpolar gyre is the evaporation-precipitation+runoff, which is almost an order of magnitude larger than the other mixing or eddy terms. Here, the assumption is therefore that $\mathcal{R}_{\text{total}}$ is dominated by the surface boundary flux, forcing term, and therefore hereafter will be defined as $\mathcal{F}$.

To compare the anomalies of each component, a reference year is chosen according to when the accumulated Sv psu is approximately zero (t_{ref} =1975). By removing the mean over the beginning of the timeseries to t_{ref} (from 1851 to 1975), this allows all fluctuations in the timeseries until 1975 to oscillate around zero, after which the future accumulated anomalies are more easily distinguishable (over 1975 to 2099). Using one of the components, $\mathcal{S}_{\text{ov}}$, at any latitude as an example, the anomaly of $\mathcal{S}_{\text{ov}}$ is:

$$\mathcal{S}_{\text{ov}}|_{anom}(t) = \mathcal{S}_{\text{ov}}(t) - \frac{1}{t_{\text{ref}}} \int_{t_0}^{t_{\text{ref}}} \mathcal{S}_{\text{ov}}(t')dt', \tag{5.29}$$

with dt being the seconds in a year. The accumulated anomaly transport of the overturning component (which therefore recovers a measure of salinity content) then reads:

$$\mathbf{\Sigma}_{\mathrm{ov}}(t) = \int_{t_0}^{t} \mathcal{S}_{\mathrm{ov}}|_{anom}(t')dt', \tag{5.30}$$

where $\mathbf{\Sigma}$ is the accumulated anomaly of any transport and expressed as Sv psu yr or 10^{15} m^3 psu, equivalent to petametres^3 psu (Pm^3 psu), and $\mathbf{\Sigma}(t_{ref}) = 0$ by definition. Smoothing of the accumulated data is then performed using a 10-year moving-average.

Finally, a direct comparison with Part I and the 20-year forced moving trends of the AMOC transport, linear regressions of 20-year sliding windows for each salinity transport component from 1851 to 2099 are computed and represented as $\Theta\mathcal{S}$. Similarly to Part I, the 20-year window slides in increments of one year, to produce a timeseries as a function of the midpoint of this window.

5.3.2.2 The salinity feedback in the North Atlantic

The mathematical derivations of the salinity budget above have been performed in order to have a clearer understanding of the components driving the salinity feedback loop associated with the AMOC. Under certain conditions (such as anthropogenic forcing), the AMOC could respond to thresholds due to positive feedbacks (Stommel, 1961). A key driver of the positive oceanic feedback that destabilises the AMOC is anomalous freshwater input in the subpolar North Atlantic (Stommel, 1961; Baumgartner and Reichel, 1975). If the AMOC weakens (regardless of the original cause), the near-surface waters that carry heat and salt to the deepwater formation sites also slow down. At high latitudes, since it is a region of net freshwater input from the atmosphere, transit time of AMOC surface waters passing through is increased, therefore further decreasing the rate of poleward salt transport. This reduces the salinity of the water and hence the density, which further weakens the overturning via this positive feedback (Urban and Keller, 2010; Marotzke, 1996).

In this study, oceanic salinity transports are expressed in Sv psu as an overturning component ($\mathcal{S}_{\mathrm{ov}}$) and an azonal component, from the gyre recirculation ($\mathcal{S}_{\mathrm{az}}$). As mentioned above (and following results from Mecking et al. (2016)), the atmospheric forcing salinity flux (via precipitation and evaporation with the addition of the runoff) is assumed to dominate the residual term ($\mathcal{F}$), so the distinction between internal oceanic ($\mathcal{S}_{\mathrm{ov}}$ plus $\mathcal{S}_{\mathrm{az}}$) and external atmospheric ($\mathcal{F}$) transport can be made. The sum of the divergence of $\mathcal{S}_{\mathrm{ov}}$ and $\mathcal{S}_{\mathrm{az}}$, plus the residual, estimates the time derivative of total net salinity transport in a region. Changes to these individual components, as well as the overall salinity transport in the STR and SPR, are used to identify whether the AMOC slowdown is primarily driven by the external atmospheric processes or internal ocean processes.

5.3.3 Results and discussion

5.3.3.1 Salinity budget at equilibrium of the forced component

The 250-year timeseries of the various salinity transports (from 1851 to 2099) has been split into a reference period over the first 125 years (from 1851 to 1975) and a post-reference period over the following 125 years (1975 to 2099) (Figure 5.8). The reference period presents fluxes that are almost in equilibrium when averaged temporally (with a small total residual of 0.11 Sv psu in the subtropical region (STR) and 0.02 Sv psu in the subpolar region (SPR), Figure 5.9). These reference salinity transports at the three latitudes used (20° N, 48° and 60° N), therefore represent the fluxes prior to destabilisation by the anthropogenic forcing (Figure 5.8a).

All three latitudes have a positive, northwards flux of salt via both the overturning component and the horizontal gyre component, apart from $\mathcal{S}_{\text{az}}|_{20N}$ (southwards). This creates a divergence of salt by $\mathcal{S}_{\text{az}}$ in the STR of almost equal transport northwards and southwards (-8.12 Sv psu via $\mathcal{S}_{\text{az}}|_{20N}$ and 8.26 Sv psu via $\mathcal{S}_{\text{az}}|_{48N}$). $\mathcal{S}_{\text{ov}}|_{20N}$ induces the largest flux into the STR (15.58 Sv psu) and $\mathcal{S}_{\text{ov}}|_{60N}$ the smallest flux out of the SPR (0.60 Sv psu) (Figure 5.9). The generally northward fluxes are consistent with findings from Rahmstorf (1996) showing that freshwater transport from the overturning circulation is southwards everywhere in the North Atlantic (i.e., northwards salinity transport).

Upon examining the subtropical and subpolar regions' transports separately over the reference period, the combined positive and negative fluxes at different latitudes result in a net $\mathcal{S}_{\text{ov}}$ import of salt into both the STR and SPR and a net $\mathcal{S}_{\text{az}}$ export of salt out of both regions (Figure 5.8b and c). The highest salinity transport is via $\mathcal{S}_{\text{az}}|_{\text{ST}}$ export (16.38 Sv psu), due to the divergence mentioned above. The total oceanic transports $\mathcal{S}_{\text{ov}} + \mathcal{S}_{\text{az}}|_{\text{ST}}$ and $\mathcal{S}_{\text{ov}} + \mathcal{S}_{\text{az}}|_{\text{SP}}$ generate a transport of salt out of the STR (-7.38 Sv psu) and into the SPR (4.54 Sv psu) during the equilibrium. To retrieve the time-derivative of total salinity transport (that is minimal during this equilibrium phase of the forced component), the atmospheric forcing ($\mathcal{F}$) is computed as the residual component flux. Assuming the residual is primarily due to precipitation and evaporation (and also potentially river run-off), this implies that in equilibrium, there is freshwater outflux from evaporation in the STR (increasing salinity by 7.50 Sv psu), and freshwater influx from precipitation in the SPR (decreasing salinity by 4.52 Sv psu in Figure 5.8b and c and Figure 5.9).

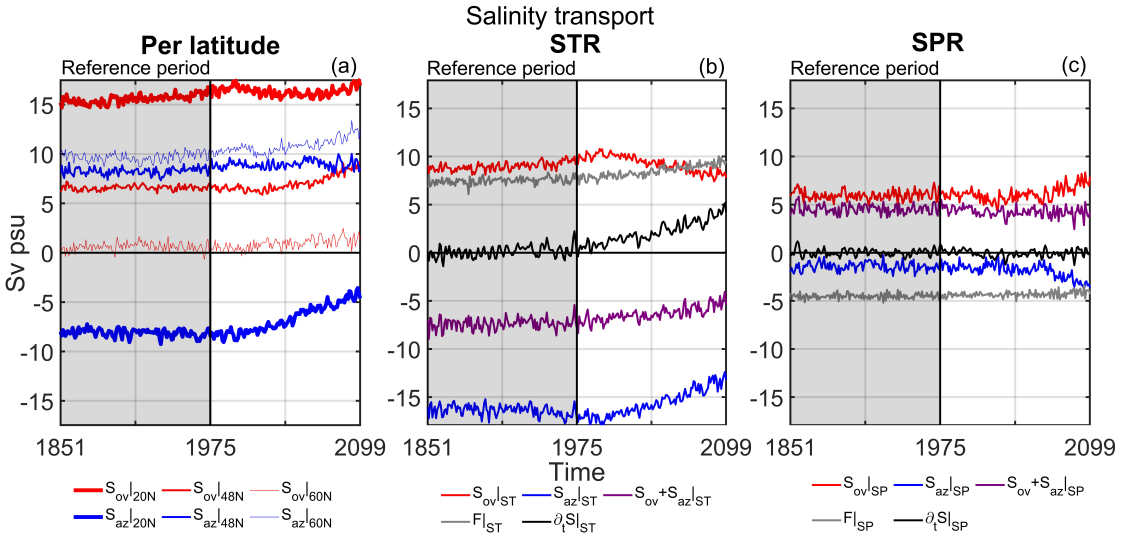

FIGURE 5.8: Annual mean salinity transport [Sv psu] derived from CMIP5 ensemble mean (i.e. forced component) historical and RCP8.5 output from 1851 to 2099. The reference period (1851 to 1975), representing the fluxes almost in equilibrium, is shaded in grey and summarised in the schematic below (Figure 5.9). (a) The two oceanic salinity transports: overturning, $\mathcal{S}_{\rm ov}$ (red lines) and horizontal gyre, $\mathcal{S}_{\rm az}$ (blue lines) at the three latitudes marking the meridional boundaries for the subtropical region (STR) and subpolar region (SPR), at 20° N (thick, solid lines), 48° N (weakly thick, solid lines) and 60° N (thin, solid lines). Positive (negative) values indicate northward (southward) fluxes. (b) The STR oceanic salinity transports via $\mathcal{S}_{\rm ov}|_{\rm ST}$ (red line), i.e.,$\mathcal{S}_{\rm ov}|_{20N} - \mathcal{S}_{\rm ov}|_{48N}$ from (a), and $\mathcal{S}_{\rm az}|_{\rm ST}$ (blue line), i.e.,$\mathcal{S}_{\rm az}|_{20N} - \mathcal{S}_{\rm az}|_{48N}$, the combined $\mathcal{S}_{\rm ov}+\mathcal{S}_{\rm az}|_{\rm ST}$ (purple line), the residual (grey line), $\mathcal{F}$, and the total net salinity transports (black line), $\partial_t {\rm S}|_{\rm ST}$, are displayed. (c) SPR transports as in (b), with the southern boundary being 48° N and northern boundary 60° N. Positive (negative) values in (b) and (c) indicate an addition (dilution) of salt in the region.

5.3.3.2 Multi-decadal temperature and salinity anomalies in the 21st century

Salinity anomalies of the ensemble mean referenced to 1975, as a function of latitude and averaged over different depth ranges, further support that during the reference period, the concentrations do not vary greatly (shown by the Hovmöller plots in Figures 5.10 and 5.11). This next subsection looks at the anomalies as 10-year running means, and the analysis focuses on the period from 1975 to 2095, where the subtropical and subpolar forced components of salinity show a dramatic change compared to the reference period.

Although temperature changes are not the focus of this study, a brief description is mentioned here, to acknowledge the shared thermal and haline contributions to changes in buoyancy under external forcings (Stommel, 1961; Marotzke, 1996; Thorpe et al., 2001; Sévellec and Fedorov, 2011). The forced-component of the temperature anomalies, post-1975 and throughout the 21st century, increase almost uniformly throughout the North Atlantic upper ocean (top 2,500 m), or when averaged over the full depth under both CMIP5 future scenarios (Figures 5.10a, b, and d, and 5.11a, b, and d for RCP4.5

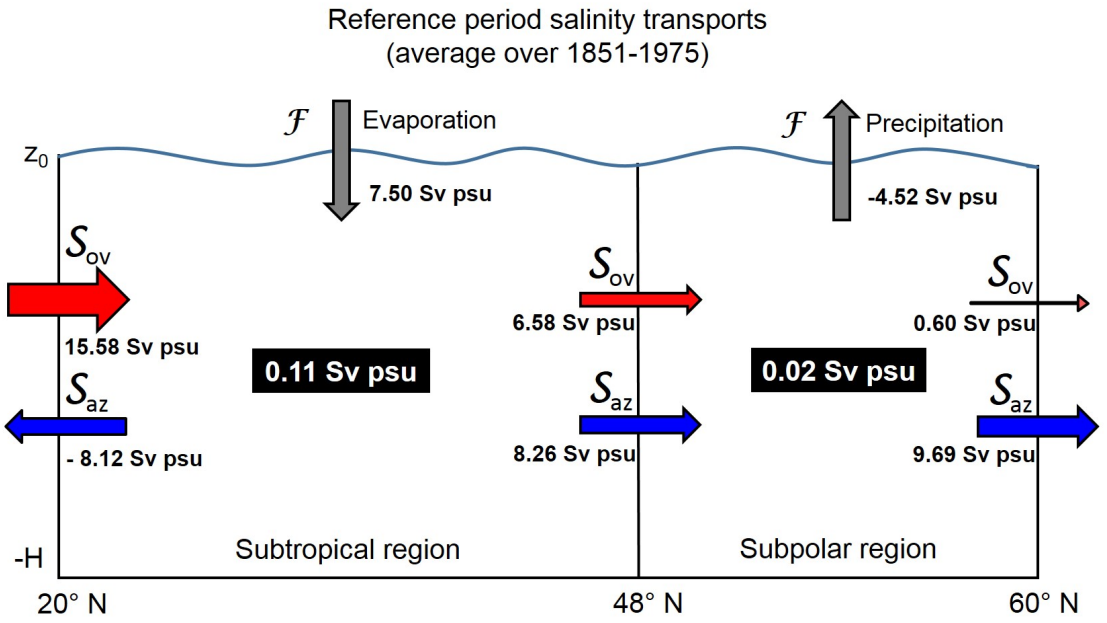

FIGURE 5.9: A schematic displaying the almost equilibrium of salinity influx and outflux [Sv psu], temporally averaged over the reference period (1851 to 1975) of the ensemble mean (i.e. forced component), into and out of the subtropical and subpolar regions. The zonally and vertically-integrated oceanic transports comprise of $\mathcal{S}_{ov}$, transport via the overturning component (red arrows), and $\mathcal{S}_{az}$, transport via the azonal, gyre transport (blue arrows). Positive (negative) values indicate northward (southward) fluxes across these latitudes (where all are positive apart from $\mathcal{S}_{az}|_{20N}$). The residual (grey arrows), assumed here to be atmospheric forcing, $\mathcal{F}$, is computed per region, with a positive value showing net evaporation (indicated by a downward arrow) and a negative value showing net precipitation (indicated by an upward arrow). The small total net salinity transport in each region is the black box (0.11 Sv psu in the STR, and 0.02 Sv psu in the SPR). The width of the arrows are scaled to their strength of transport but the size of the regions is not proportional to the actual size.

and RCP8.5, respectively). For the surface values, this is consistent with Delworth et al. (2007) showing that multi-decadal sea surface temperature patterns in the North Atlantic produce anomalies with the same sign on a basin scale between the equator and 60° N. This homogeneous warming coincides with the projections of anthropogenically-forced global atmospheric temperature rise, insinuating that the residual surface flux could play a dominant role in upper ocean temperature changes, as opposed to oceanic fluxes (although a temperature budget to verify this is outside the scope of this study). The negative temperature feedback mechanism indicates that an increase in the gradient between the STR and SPR would onset a stronger AMOC transport (Marotzke, 1996), therefore as per the results here, a weakening of the AMOC is induced. Although there are studies showing that from 50 to 60° N there is a subpolar 'Warming Hole' (Drijfhout et al., 2012), the CMIP5 zonally-integrated upper ocean ensemble mean does not exhibit this anomaly (Figures 5.10a and b, and Figures 5.11a and b), possibly since the global mean temperature signal must be removed in order to identify it. Averages from 2,500 m to the bottom, however, show a decrease in temperature in the SPR, but not in the

STR which still indicates a warming (Figures 5.10c and 5.11c for RCP4.5 and RCP8.5, respectively). With subpolar upper ocean waters becoming more positively buoyant as a result of an increase in temperature, a potential reduction in deep water convection could occur at the higher latitudes, causing a larger difference in temperature between the top 2,500 and bottom 2,500 m. Anomalous spatial patterns are consistent across results under the RCP4.5 and RCP8.5 scenarios, with the 'business-as-usual' scenario showing stronger anomalies (reaching a full depth average maximum of 1.19 K under RCP8.5 by 2095, versus 0.76 K under RCP4.5).

Salinity anomalies, on the other hand, show a bipole response to anthropogenic forcing in the 21st century, with a freshening in the SPR and a salinification in the STR. This potentially suggests that the positive salinity feedback mechanism is generated under a warming climate, and a weakened AMOC is linked to a stronger salinity gradient between the SPR and STR, which further weakens the AMOC transport (Marotzke, 1996). The other hypothesis would be an intensification of the atmospheric water cycle, with stronger evaporation in the STR and precipitation in the SPR, which is a hypothesis formulated as a consequence of anthropogenically-forced climate change (Stocker et al., 2013). This ensemble mean salinity anomaly is consistent across all depth ranges and under both future scenarios (Figures 5.10, and 5.11 for RCP4.5 and RCP8.5, respectively), although the average below 2,500 m does not show an increase in salinity in the STR (Figures 5.10g, and 5.11g). The integrated anomalies averaged over the full depth are used to define the latitude (48° N) that separates the two regions dynamically in this study (Figures 5.10h, and 5.11h). In the rest of this section the salinity budget, previously defined, is used to attribute the cause of the forced-component of the salinity change to either internal oceanic processes (i.e., positive salinity feedback through AMOC and gyre circulation change) or external atmospheric processes (i.e., intensification of the atmospheric water cycle).

By the end of the 21st century, the increase in the net STR salinity (+0.09 psu) and decrease in SPR salinity (−0.03 psu) relative to 1975 is seen, both as a function of latitude, averaged over the full water column (see the Hovmöller plot in Figure 5.11h), and computed from the salinity budgets (see the schematic in Figure 5.13). The accumulated anomalies since 1975 (Figure 5.12) of the oceanic salinity transports ($\mathbf{\Sigma}_{\text{ov}}$ and $\mathbf{\Sigma}_{\text{az}}$) and atmospheric salinity transport ($\mathbf{\Sigma}\mathcal{F}$) are used to address potential drivers of changes in long-term salinity transport over 125 years.

At the three latitudes (20° N, 48° N and 60° N), the transports generally tend towards an increase in salinity anomalies throughout the 21st century (Figure 5.12a). $\mathbf{\Sigma}_{\text{az}}|_{20N}$, $\mathbf{\Sigma}_{\text{ov}}|_{60N}$, and $\mathbf{\Sigma}_{\text{ov}}|_{48N}$ have slight negative anomalies for the first few decades before becoming positive by 2020, 2030 and 2060, respectively. The component with the largest total accumulated flux after 125 years is the $\mathbf{\Sigma}_{\text{az}}|_{20N}$ (5.02 Pm^3 psu), meaning it has reduced its originally southward transport drastically (compared to its reference fluxes

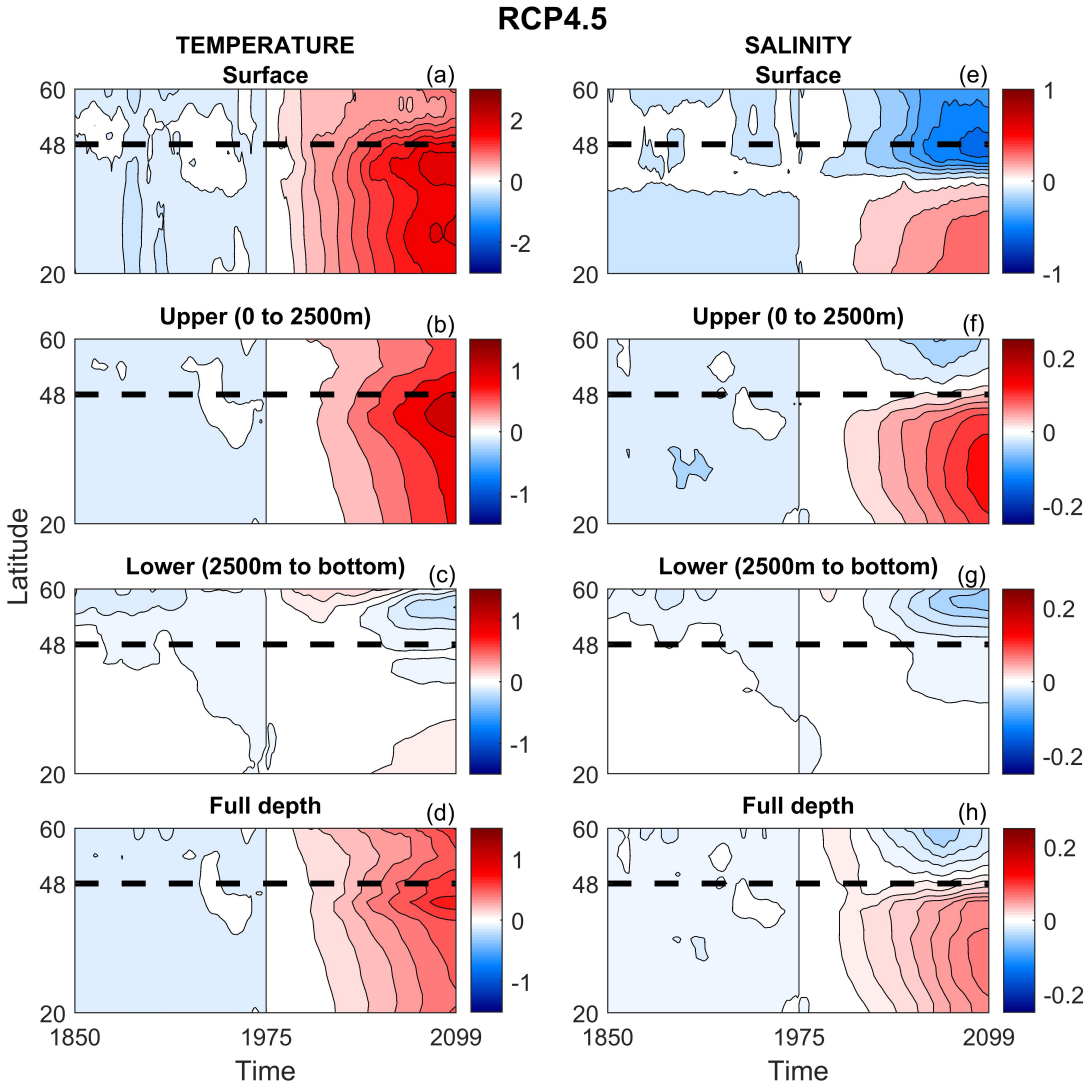

FIGURE 5.10: Hovmöller plots showing zonally-integrated and averaged temperature [K] and salinity [psu] anomalies referenced to 1975 (vertical, black line), from 1850 to 2099 and filtered using 10-year moving means under the RCP4.5 scenario. Displayed as a function of latitude, the boundary between the SPR and STR is shown at 48° N (dashed horizontal, black line). The anomalies are integrated vertically and presented at different depths; at the surface in (a) for temperature and (e) for salinity, averaged over the upper ocean (from 0 to 2,500 m) in (b) for temperature and (f) for salinity, averaged over the lower ocean (from 2,500 m to the bottom) in (c) for temperature and (g) for salinity, and averaged over the full depth in (d) for temperature and (h) for salinity.

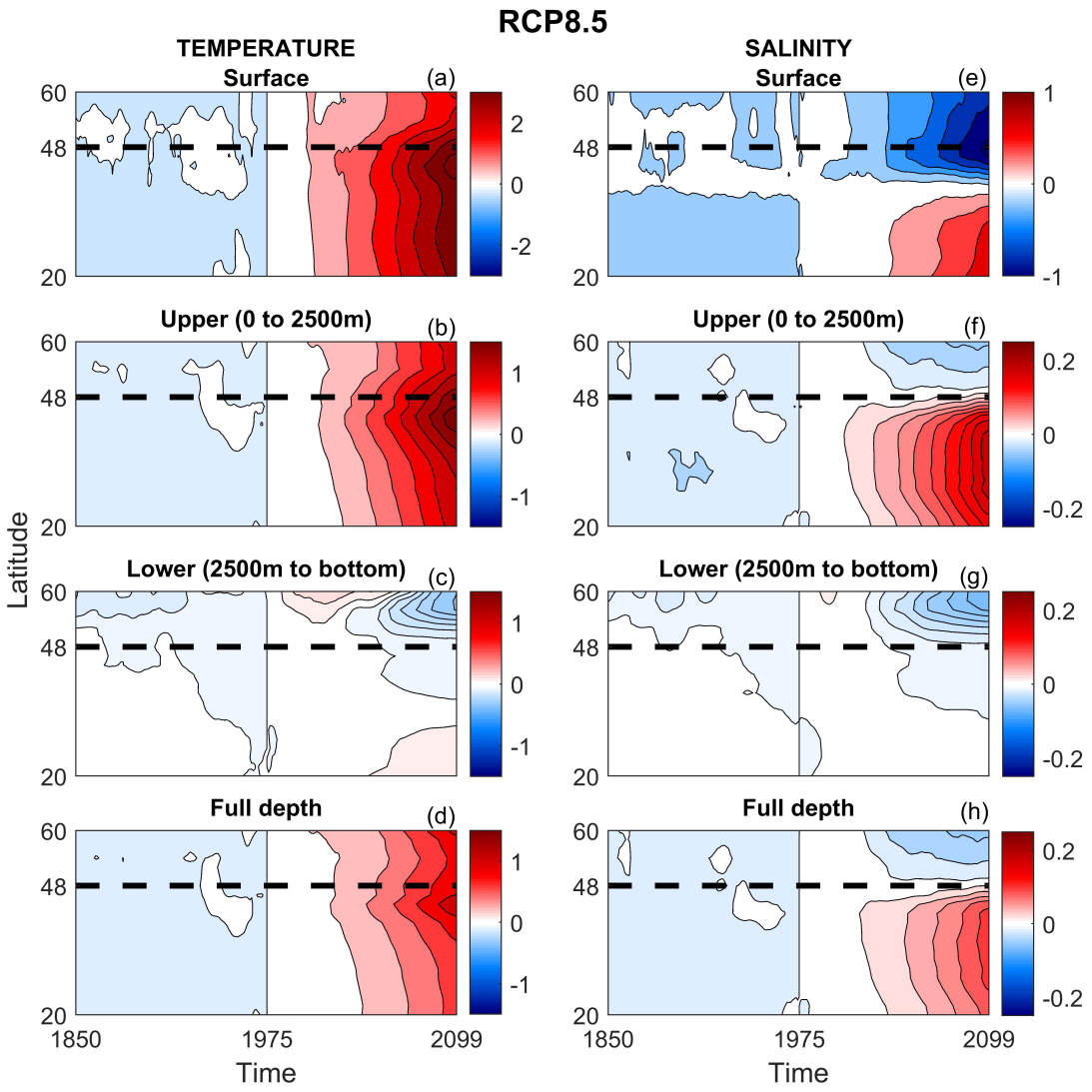

FIGURE 5.11: As Figure 5.10, but for CMIP5 historical data followed by RCP8.5 scenario.

in Figure 5.9), leading to retention of salt within the STR. $\mathbf{\Sigma}_{\text{az}}|_{60N}$ is also the dominant term for exporting salt in the SPR, reaching 4.01 Pm^3 psu by 2095 (Figure 5.13).

Combining the effects of the boundary fluxes provides an estimate of divergences and convergences of salinity within each region from 1975 to 2095. In the subtropics, the consistently positive exponential increase in accumulated salinity (Figure 5.12b) seems to be dominated by $\mathbf{\Sigma}_{\text{ov}}|_{\text{ST}}$ until approximately 2050 (where it reaches its maximum of 1.93 Pm^3 psu). $\mathbf{\Sigma}_{\text{az}}|_{\text{ST}}$ has an opposing effect, exporting salinity until 2060 (reaching its minimum in 2020 of -0.85 Pm^3 psu). Post-2060, joint efforts between the accumulated $\mathbf{\Sigma}_{\text{az}}|_{\text{ST}}$ and increased evaporation ($\mathbf{\Sigma}\mathcal{F}|_{\text{ST}}$) appear to dominate net accumulation of salinity ($\mathbf{\Sigma}\mathcal{S}$), while $\mathbf{\Sigma}_{\text{ov}}|_{\text{ST}}$ imports less salt until the end of the century (Figure 5.12b). Upon combining $\mathbf{\Sigma}_{\text{ov}}$ and $\mathbf{\Sigma}_{\text{az}}$, the oceanic transports ($\mathbf{\Sigma}_{\text{ov+az}}|_{\text{ST}}$) and atmospheric forcing ($\mathbf{\Sigma}\mathcal{F}|_{\text{ST}}$) have almost identical exponentially increasing impact. This suggests

that the forced salinity change in the subtropics comes evenly from oceanic internal feedbacks and atmospheric external forcing.

In the subpolar region, the scale of accumualted salt transport marks the largest difference between STR and SPR dynamics. The SPR's range of accumulated transports is a lot smaller than the STR's (between -1.45 and 0.69 Pm^3 psu in the SPR compared to -0.85 and 3.54 Pm^3 psu in the STR) (Figure 5.12b, and c). Note that the first couple of decades (1975 to 2020) see an intriguing relationship between the components that is further investigated in Section 5.3.3.3 below. The general tendency after 2020 is an opposing effect between the atmospheric forcing ($\mathbf{\Sigma}\mathcal{F}|_{\mathrm{SP}}$), that causes a constant increase in salinity retention from 1975 to 2095 (implying a decrease in precipitation), and the oceanic transports ($\mathbf{\Sigma}_{\mathrm{ov+az}}|_{\mathrm{SP}}$) that export more salinity. However, $\mathbf{\Sigma}_{\mathrm{ov+az}}|_{\mathrm{SP}}$ dominates over the atmospheric residual term and leads to the net decrease in salinity in the SPR, contrary to the STR, both $\mathbf{\Sigma}_{\mathrm{ov}}$ and $\mathbf{\Sigma}_{\mathrm{az}}$ generally produce negative accumulated anomalies. (It is worth noting that in the subpolar region both overturning and azonal transport contribute to the AMOC, since the AMOC becomes a lot more horizontal than in the suptropical region).

These results indicate that by 2095, salinity change in the subtropics is equally due to oceanic feedback ($\mathbf{\Sigma}_{\mathrm{ov+az}}|_{\mathrm{ST}}$) and atmospheric forcing ($\mathbf{\Sigma}\mathcal{F}|_{\mathrm{ST}}$), producing accumulated anomalies of 3.70 Pm^3 psu and 3.54 Pm^3 psu, respectively. In the subpolar region, however, $\mathbf{\Sigma}_{\mathrm{ov+az}}|_{\mathrm{SP}}$ dominates over $\mathbf{\Sigma}\mathcal{F}|_{\mathrm{SP}}$ ($-1.04\,\mathrm{Pm}^3$ psu versus $+0.69\,\mathrm{Pm}^3$ psu, respectively (Figure 5.13).

5.3.3.3 Rogue AMOC period and its relation to salinity changes

In Part I, a 'rogue period' is characterised upon identifying a 20-year period (from 1995 to 2015) in which the AMOC at 48° N shows two unique features: (1) a sudden shift in probability of a decline in transport (reaching a 95.4% probability of a 20-year declining trend, with a 55.7% probability of an intense AMOC decrease), and (2) revealing its strongest forced trend (-0.11 $\mathrm{Sv\,psu\,yr}^{-1}$) relative to the full 250-year timeseries. To explore the cause and consequences of the rogue period, this section investigates whether there is also a change in behaviour in the forced component of salinity transports over this period, for direct timing comparison to the AMOC (Figures 5.14 and 5.15). It is noteworthy to be reminded that a 20-year trend (here denoted as ($\Theta\mathcal{S}$) in 1995, for example, refers to a linear regression from 1985 to 2005 in this study.

The 20-year trends of the ensemble mean salinity transport in the SPR ($\Theta\mathcal{S}|_{\mathrm{SP}}$) are consistently negative over the rogue period (Figure 5.14b). This feature is not seen over any other 20-year period throughout the 250-year timeseries of historical and RCP8.5 data output. Almost simultaneously, both the ΘAMOC, and $\Theta\mathcal{S}|_{\mathrm{SP}}$ 20-year declines fall outside the variability found during their historical period. Furthermore, the 20-year

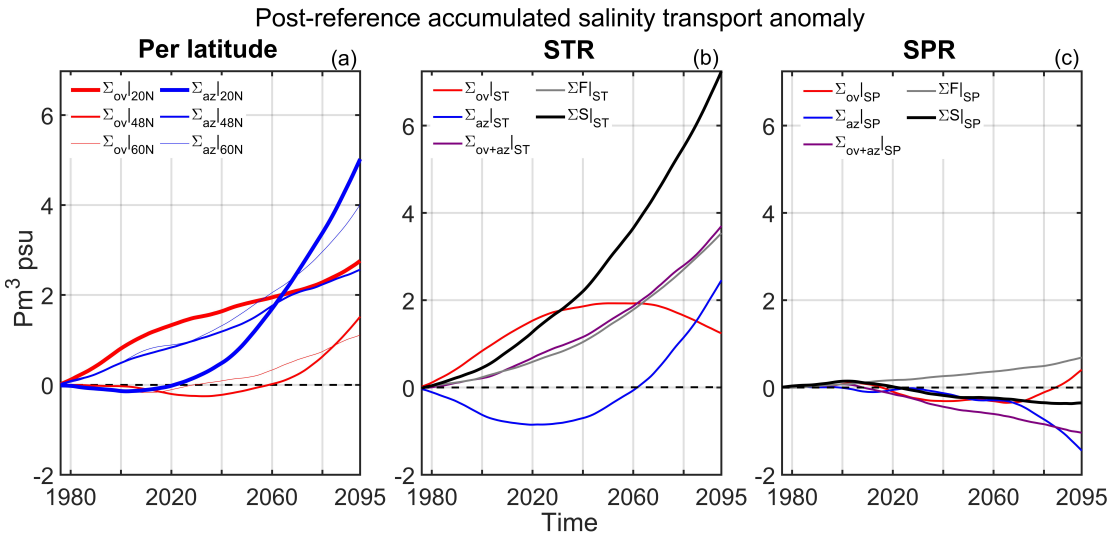

FIGURE 5.12: Accumulated anomalies of salinity transport ($\boldsymbol{\Sigma}$) from 1975 to 2095, derived from CMIP5 ensemble historical and RCP8.5 data, referenced to the t_{ref} (1975) values in Figure 5.8, filtered using a 10-year moving average. Accumulated transport units are in Pm^3 psu ($1\ Pm^3 = 10^{15}\ m^3$). See Figure 5.8 for a description of the legend colours; note that now they represent accumulated transports.

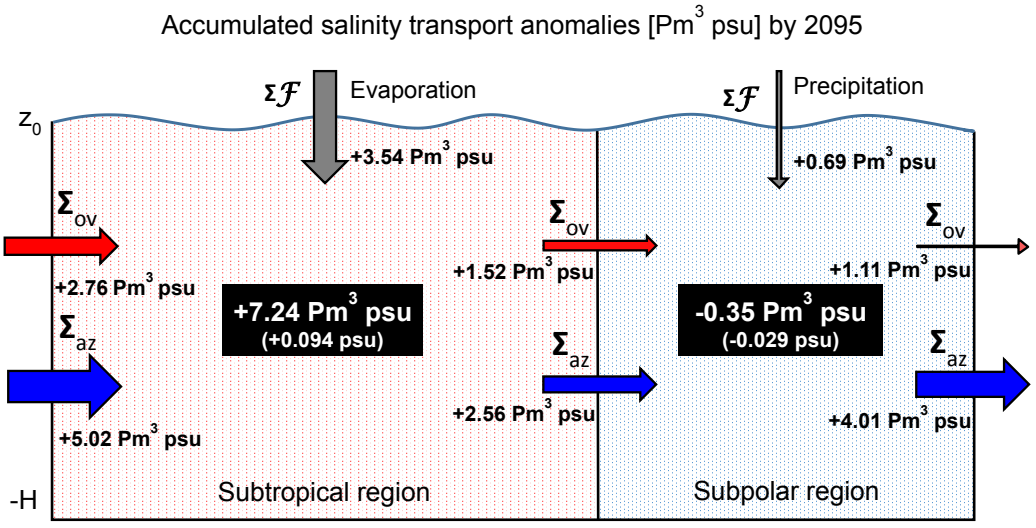

FIGURE 5.13: Schematic of the accumulated salinity anomaly transport ($\boldsymbol{\Sigma}\mathcal{S}$), in Pm^3 psu by 2095 referenced to 1975. The direction of the arrows shows whether the accumulated anomaly causes a flux of salinity into or out of the STR and SPR. The equivalent average change in salinity concentration is shown in brackets in the black box for each region (+0.09 psu in the STR and −0.03 psu in the SPR). All other arrows and colours represent the same fluxes as in Figure 5.9, but are now accumulated transports.

trend around 2001 (from 1991 to 2011) marks the maximum net salinity decline in the trend (of -0.051 $\mathrm{Sv\,psu\,yr^{-1}}$). Changes in STR transport trends do not seem exclusive to the rogue period and therefore the SPR remains the point of focus.

For a deeper analysis, to investigate whether this subpolar salinity rogue period is mostly linked to ocean or atmospheric fluxes, $\Theta_{ov}|_{SP}$, $\Theta_{az}|_{SP}$, and $\Theta\mathcal{F}|_{SP}$ are used. It becomes evident that the subpolar oceanic transport components of salinity demonstrate a behaviour that is unique to this period. In the first seven years (1995 to 2002), $\Theta_{az}|_{SP}$ 20-year trends are negative, and soon after in 1998, $\Theta_{ov}|_{SP}$ trends change to a negative sign (reaching the 250-year maximum in 2008, of -0.064 $\mathrm{Sv\,psu\,yr^{-1}}$), and then sustaining a decline until the end of the rogue period (Figure 5.14b). This is caused by an average divergence of salinity by $\Theta_{ov}|_{SP}$, with both $\Theta_{ov}|_{48N}$ and $\Theta_{ov}|_{60N}$ exporting salt out of the SPR (Figure 5.15). The maximum net salinity transport decline in 2001 (as mentioned above) coincides with an overlap of a 20-year negative trend shared by $\Theta_{ov}|_{SP}$ and $\Theta_{az}|_{SP}$ of -0.025 $\mathrm{Sv\,psu\,yr^{-1}}$. This is unprecedented and not repeated after the rogue period since Θ_{ov} and Θ_{az} normally complement each other, in that one transport component increases while the other decreases (both in the historical and future scenario).

The 20-year atmospheric salinity transport trends $\Theta\mathcal{F}|_{SP}$, on the other hand, do not show any anomalous feature during the rogue period, with positive and negative trend oscillations occurring consistently over the 250 years (Figure 5.14b). Its average trend over the rogue period is negligible (Figure 5.15). These results illustrate that on this short (decadal) period, the oceanic internal processes, such as the overturning and gyre circulation, largely dominate over the effects of atmospheric fluxes to set the forced component of the salinity changes consistent with an AMOC reduction.

5.3.4 Conclusion

Following the IPCC's findings that the AMOC is very likely to experience a decline in transport in the 21st century (Flato et al., 2013), this study starts with a probability analysis of the decline in past and future strength of the AMOC at 48° N over 250 years. Trends of different lengths, covering interannual to multi-decadal timescales, are analysed to reveal that under both future scenarios used (RCP4.5 and RCP8.5), the forcing is only detected outside the range of internal natural variability beyond 5 years of a consistent decline. This suggests that any interannual intense events, such as the 2009-2010 30% decline in transport recorded by RAPID (Bryden et al., 2014), are highly likely to come from natural variability. The results also imply that there was a high probability (up to 84.9% at the turn of the century, in RCP8.5) of seeing a weak decadal decline, such as that seen in RAPID (Smeed et al., 2014), due to anthropogenic forcing. This does not, however, rule out that a decadal trend could still be dominated by natural variability (characterised as a hiatus in Sévellec et al. (2016)) at certain periods, as suggested by

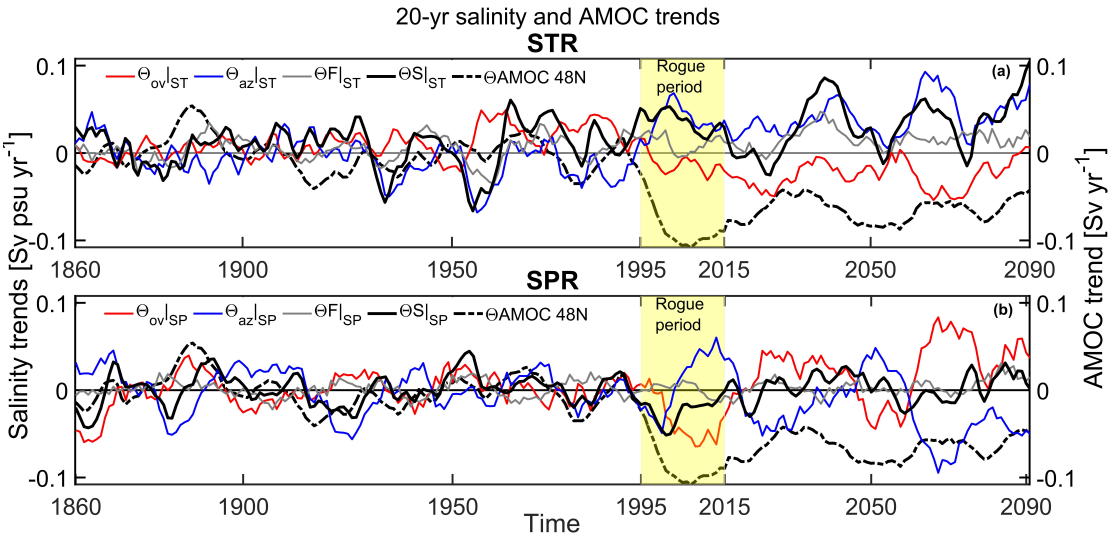

FIGURE 5.14: A comparison of salinity and AMOC transport trends ($\Theta\mathcal{S}$ and ΘAMOC, respectively) filtered using 20-year sliding windows from 1850 to 2099 in the (a) subtropical region (STR), and (b) subpolar region (SPR). Linear regression trends are fit to the raw salinity transport data (for the STR data in Figure 5.8b and for the SPR data in Figure 5.8c). Legend colours are the same as in Figure 5.8. The 20-year sliding window trend of the AMOC at 48° N (black, dash-dotted line) is the same timeseries plotted in Part I, Figure 5.5c. The 'rogue period' (highlighted in yellow) from 1995 to 2015 marks the period in which the forced component of the AMOC's 20-year trends rapidly fall out of the range of the historical data and overshoot the range found in the 21st century data.

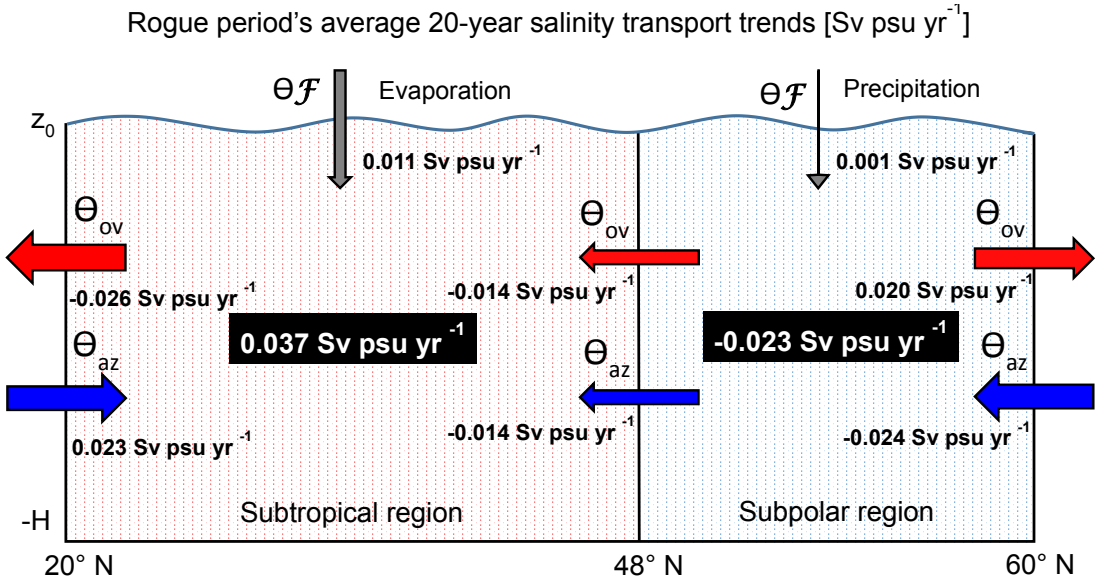

FIGURE 5.15: A schematic of the average 20-year salinity transport trends ($\Theta\mathcal{S}$) over the 'rogue period' (1995 to 2015, corresponding to the yellow highlighted patch in Figure 5.14). The arrows therefore now represent trend values [in $\mathrm{Sv\,psu\,yr^{-1}}$], averaged over the rogue period, and the colours represent the trends of the fluxes shown in Figure 5.9.

Roberts et al. (2014), for example. Upon increasing the time-duration of the forced trends, stronger intensities and probabilities of a decline are seen (86.2% time-average probability of an intense 40-year decline under RCP8.5). Using time-varying forced trends, the 'business-as-usual' scenario shows a sustained high probability of a decline in the AMOC, whereas the 'stabilisation' scenario returns to pre-industrial probabilities of an equal chance in increasing or decreasing (for all trend durations over 5 years).

From 1995 to 2015, a rogue period is identified by features of the timeseries that are unique to this timeframe: (1) a rapid increase in probability of a decline in transport (from the historical average probability of 50% to 95.4% for a 20-year RCP8.5 negative trend), and (2) the strongest forced-trend intensity of the full 250-year timeseries is detected (-0.11 $\mathrm{Sv\,yr^{-1}}$). These initial results from Part I, that show the fundamental role of forced-variation, tailored the aims of Part II to investigate whether these forced changes in the AMOC trends occur at the same time as forced changes in associated oceanic properties, namely temperature and salinity transport. The ocean and atmosphere maintain coupled feedback mechanisms with the intention to restore equilibrium in any destabilised state. The focus here is on the positive feedback of salinity transport; a decline in the AMOC decreases salt transport to higher latitudes, which reduces NADW formation and further slows down the AMOC (Marotzke, 1996). The stability of the AMOC is dependent on a complex salinity balance resulting from freshwater or salinity transport by the gyre circulation, the meridional overturning circulation and atmospheric fluxes (Rahmstorf, 1996), hence the reason for computing these three transports from ensemble mean salinity budgets in the subpolar and subtropical regions. After establishing the average salinity transports in equilibrium (from 1850 to 1975), two anomalous cases are analysed: (1) the long-term accumulated anomalies of salinity transports after 125 years (1975 to 2099), and (2) the 20-year salinity transport trends over the rogue period identified in Part I (1995 to 2015).

In the first case, a general dipole salinity gradient forms after 1975, which increases until the end of the 21st century; portrayed by a freshening of the SPR and a salinification of the STR. This results in an accumulated decrease in salinity of 0.03 psu and increase of 0.09 psu by 2095 in the SPR and STR, respectively. The sustained increase in salt in the STR is influenced by both oceanic components, where $\mathcal{S}_{\mathrm{ov}}|_{ST}$ dominates the import of salt from 1975 to 2050 and then $\mathcal{S}_{\mathrm{az}}|_{ST}$, over the last 50 years. The SPR's accumulated negative transport of salt from 2020 to 2099 is a result of the shared negative anomalies of $\mathcal{S}_{\mathrm{ov}}|_{SP}$ and $\mathcal{S}_{\mathrm{az}}|_{SP}$, exporting salt out of the SPR. When comparing the long-term effects of $\mathcal{S}_{\mathrm{ov}} + \mathcal{S}_{\mathrm{az}}|_{ST}$ compared to the $\mathcal{F}|_{ST}$, their accumulated transports are almost identical through time, hence the accumulation of salt is caused by both evaporation and ocean export. The SPR completely relies on the oceanic components to produce net negative salinity transport by 2099, since the atmospheric forcing causes positive transport (net decrease in precipitation) in the model ensemble. Controlling the salinity difference, hence the AMOC slowdown through the positive feedback, the $\mathcal{S}_{\mathrm{ov}} + \mathcal{S}_{\mathrm{az}}$

transports in the subpolar region are therefore the dominant drivers on multi-decadal to centennial timescales, overriding atmospheric effects, consistent with results from other studies (Manabe and Stouffer, 1988; Rahmstorf, 1996).

The 20-year rogue period of the AMOC decline from 1995 to 2015 coincides with changes in the 20-year subpolar trends of salinity transport that exclusively occur during this period. Yeager and Danabasoglu (2014) demonstrate that the AMOC's decadal variability mainly responds to high-latitude buoyancy forcing anomalies, and here results demonstrate a similar response over decadal abrupt periods. Robson et al. (2016) infer that the deep Labrador Sea density produced negative anomalies concurrently with an AMOC decline since the mid 1990s and that although deep ocean warming seems to dominate the density anomaly, waters are not yet warmer than in the 1970s, however the waters are fresher. This suggests that although the salinity changes are smaller than temperature changes, the accumulated effects of freshwater increase plays a significant role on surface buoyancy and therefore AMOC transport (Robson et al., 2016).

The results here extend beyond their study (since it makes use of a longer timeseries) and show that it is the only 20-year period, over 250 years, showing a net total SPR salinity transport forced trend that is continuously negative. Therefore this demonstrates that the period of high decline probability is due to the forced component. This is different from some previous studies that cannot separate forced and natural variations. The analysis goes further, by showing the components that drive the changes; being initiated by a $\Theta_{\text{az}}|_{SP}$ decline and sustained by a $\Theta_{\text{ov}}|_{SP}$ decline. $\Theta_{\text{ov}}|_{SP}$ also reaches its maximum declining trend (export of salt) relative to the full timeseries in 2008.

One specific year during the rogue period, 2001 (i.e., 20 year trends from 1991 to 2011), marks two unique features that happen simultaneously: (1) The net trend in salinity transport $\Theta_S|_{SP}$ reaches its 250-year maximum (-0.051 $\text{Sv}\,\text{psu}\,\text{yr}^{-1}$), (2) negative 20-year trends in both $\Theta_{\text{ov}}|_{SP}$ and $\Theta_{\text{az}}|_{SP}$ overlap at -0.02 $\text{Sv}\,\text{psu}\,\text{yr}^{-1}$, and (3) the difference between the SPR declining trend ($\Theta\mathcal{S}|_{SP}$) and STR ($\Theta\mathcal{S}|_{ST}$) increasing trend is largest. The latter point has been extensively studied previously, wherein alterations to the large-scale meridional density gradient between the North Atlantic gyres affects the AMOC (Zhang, 2010; Robson et al., 2014; McCarthy et al., 2015b; Yeager and Danabasoglu, 2014; Sévellec and Huck, 2016). It appears that the collective effect of these periods happening in parallel could be the explanation for a shift in probability of an AMOC decline due to forced variations. On this decadal timescale, the residual term seems to have a negligible effect on the salinity of the rogue period since there is no anomalous increase in evaporation in the STR, nor precipitation in the SPR and therefore the results suggest that the joint $\mathcal{S}_{\text{ov}} + \mathcal{S}_{\text{az}}$ dominates forced salinity transport over 20-year timescales.

It is commonly known that numerical model outputs exhibit uncertainty, which is addressed in this study by using the ensemble mean (both for the forced component and

the PDF of the natural variability) to dampen errors found in single models. Nevertheless, it is challenging to compare these results to observations due to sparsity of direct salinity or freshwater transport estimates (Talley, 2008; Liu et al., 2014; McDonagh et al., 2010). Several studies have therefore used numerical models, following the same computations as this study, to generate freshwater flux estimates (referred to as Mov and Maz) (de Vries and Weber, 2005; Bryden et al., 2011; Drijfhout et al., 2011; McDonagh et al., 2015; Mecking et al., 2016, 2017). Although the budget shows that net evaporation over the Atlantic basin is required for deep convection (Drijfhout et al., 2011), a thorough analysis to understand CMIP5 biases in Mecking et al. (2017) demonstrate that evaporation could be overestimated over the North Atlantic in the models, compared to available observations, reanalysis products, and other models. This could both affect our results over the equilibrium and potentially change the lack of intensification of the water cycle under anthropogenic climate change. An increase in CO_2 concentrations should increase absolute atmospheric humidity and increase poleward water vapour transport, therefore increasing precipitation (Manabe and Stouffer, 1994, 1999). A follow-up study could be performed to test whether correcting these estimated biases could affect the results.

Finally, the relevance and application of this study is the potential for skilful decadal to multi-decadal predictions, for example, if these rogue period unique features are a robust identification of a shift towards a sustained probability of an AMOC decline. A complete collapse of the AMOC is highly unlikely to occur in the 21st century, due to the order of magnitude of changes in salinity in CMIP5 being too small (Stocker et al., 2013). Nevertheless, a rapid shift to a long decadal transient decline in the AMOC can also have drastic effects on the localised and global climate system (Vellinga and Wood, 2002). There is therefore a need for a constant improved understanding of early warning signs of an AMOC decline (Boulton et al., 2014). Despite being focused on the forced component, this study proposes that with further analysis, such a proxy could be achieved from identifying concurrent changes in the 20-year AMOC and salinity transport trends.

Chapter 6

Summary and future work

6.1 Summary

The global climate system is at risk of being severely affected by the anthropogenically-driven increase in greenhouse gases throughout the 21st century (Stocker et al., 2013). Some risks could potentially arise from anticipated changes in large-scale ocean circulations, such as a decline in strength of the Atlantic Meridional Overturning Circulation. The coupled interdependence between the atmosphere and oceans is clearly demonstrated in the North Atlantic, where the ocean's heat is released at higher latitudes, after being transported from the southern hemisphere, and the atmosphere's carbon is carried and stored into the deep ocean (Sabine et al., 2004; Pérez et al., 2013). These roles are attributed to the pathway of the overturning circulation that is unique to the Atlantic, which transports warmer near-surface waters northwards, sinks, and carries cooler deeper waters southwards (Stommel, 1957).

A localised example of the effects of this distribution of heat is western Europe's surface air temperatures being milder than the global average at the same latitudes (Rhines et al., 2008). Upon artificially simulating an abrupt collapse of the AMOC, an average decrease in atmospheric temperatures could occur in the northern hemisphere, by 1-2°C within the first fifty years post-collapse (Vellinga and Wood, 2002). Paleoclimate records also suggest that the AMOC can affect the global climate system due to its potential bistability; previous switches from an 'on' to an 'off' state coincided with abrupt climate shifts (cooler periods lasting ∼1500 years) (Broecker et al., 1985). Although the United Nations' Intergovernmental Panel on Climate Change predict a total collapse to be highly unlikely by the end of the century, a decrease in strength, of 34% on average, is very likely (Flato et al., 2013).

Evidently, knowledge of the AMOC's importance has encouraged the scientific community to investigate its natural variability and trends, in order to consequently identify

anomalies that could indicate impacts from climate change. The RAPID array monitoring program at 26.5° N was launched in 2004, as an initiative to provide continuous data of a zonally and vertically accumulated estimation of the AMOC (McCarthy et al., 2015a). Some initial findings suggested that a decline of -0.54 Sv yr^{-1} occurred over the first 8.5 years of observations (Smeed et al., 2014). This raised the doubt concerning whether such a feature can be part of natural decadal oscillations, or a trend caused by anthropogenic forcing, with studies almost unanimously concluding that a decade is too short to distinguish the two (Weatherhead et al., 1998; Baehr et al., 2007; Roberts et al., 2014; Parker and Ollier, 2016; Smeed et al., 2018). This cultivated the motivation behind the first question explored in this thesis: how many years of observations are required in order to detect a statistically significant decline in the AMOC? The results agree that the RAPID data is currently not long enough to estimate a statistically significant trend, and an approximate 25-45 years of monitoring are needed.

With a confirmation of this temporal limitation in available observations, a follow-up question emerged that shaped the second analysis: is there a robust correlation between the AMOC and other multi-decadally available observations, that could be used as a proxy to produce an extended AMOC timeseries? Tide gauge sea level data seemed a suitable candidate due to its long record and expected dynamical relationship with the AMOC (Bingham and Hughes, 2009; Ezer, 2015; Frajka-Williams, 2015). Using both observations and numerical model output, the results show that AMOC reconstructions using SSH generally poorly represent both the interannual variability and the trend of the AMOC using 19 CMIP5 models. One of the underlying potential reasons for these results is the artefact of large differences in AMOC and SSH behaviour between individual models (Flato et al., 2013), which can consequently hinder their relationship.

Building on what was discovered from the second analysis, the third analysis was tailored to address these outcomes. Firstly, ensemble mean CMIP5 data were used in attempts to dampen error and bias of individual models. The AMOC's ensemble mean probability density function of natural variability plus RCP8.5 forcing, shifts towards a high probability of a decline throughout the 21st century for 5-year to multi-decadal trends, although RCP4.5 allows for the recovery of pre-industrial probability by 2100. Secondly, a detailed dissection of another dynamical relationship was used, namely the positive feedback loop generated between the AMOC and salinity transport (Drijfhout et al., 2011; Mecking et al., 2017). And lastly, targeted time periods of high-probability AMOC declines was investigated. Chapter 5 therefore investigates the question: under periods of a high probability of an AMOC decline, can changes in ocean and atmosphere salinity fluxes be indicators for internally and externally forced changes in the AMOC? Two periods with an increased chance of an AMOC decline are identified from the 250 years of simulations; one over the 21st century and another over 20 years (from 1995 to 2015), both of which show unique coinciding changes in salinity fluxes in the subpolar and subtropical regions. These results suggest that the numerical models' ensemble

mean finds simultaneous changes in the salinity budget and AMOC decline, which has the potential to be used to detect shifts in AMOC trends over decadal or quasi-centennial timescales. Further detailed summaries of each chapter's results is now outlined.

The first analysis identifies the sample size of observations required to detect a statistically significant long-term decline in the AMOC. Artificial simulations of a 100-year AMOC are generated using three parameters from the CMIP5 'business-as-usual' output and RAPID observations. The detection time for the CMIP5 ensemble mean (from 20 models) is 35.25 years (with a standard deviation of 9.7 years) and 28 years for RAPID. Previous AMOC detection studies focus on time of emergence (when a forced signal is distinguished from natural variability) (Santer et al., 1995; Keller et al., 2007a; Baehr et al., 2008), however this study looks solely at detection of a significant trend. Results from using a range of the three parameters used in this work show the fastest trend detections in AMOC data pertaining a strong trend, low white noise variability, and low autocorrelation. It is important to consider the latter parameter when dealing with the environmental data since it seemingly often exhibits short-term memory (Weatherhead et al., 1998). This justifies the use of the generalised least squares regression to generate the autoregressive simulations, so as to isolate the trend and not confound it with autocorrelated trend-like segments in the data (Beaulieu et al., 2013). Trend detection is a powerful tool, as is shown for this study, to determine how long a monitoring system needs to operate before providing the scientific community with significant information regarding the data's trend, and should be used prior to any attribution study. The conclusion that RAPID's data is not long enough to detect a robust trend steered the next analyses towards the exploration of identifying proxies using other observations or numerical model output, to further understand the AMOC's trend and variability.

The second analysis examines whether there is a robust relationship between the AMOC and SSH in the North Atlantic over different timescales and across observations and numerical models. Such a relationship would allow for observational data, such as tide gauge or satellite altimetry data to be used as a proxy and reconstruct a multi-decadal AMOC timeseries. SSH has been used in previous work as an indicator for AMOC changes via the geostrophic relationship; for example, Hirschi et al. (2009) use the zonal difference of SSH as a proxy of the top 1,000 m of the eastern and western branch of the AMOC, and McCarthy et al. (2015b) use the meridional difference, north and south of the intergyre transport along the east coast of the United States. Other studies use only the western basin SSH, where the Upper Mid-Ocean's variability is supposedly dominant (Bingham and Hughes, 2009; Willis, 2010; Frajka-Williams, 2015). The ongoing discussions surrounding the ideal location for determining a relationship between the SSH and AMOC, as well as the depth at which to extract the SSH or AMOC data, leads to this chapter testing numerous locations and components of the AMOC. All reconstructions, using a 13-year (RAPID length) training period, poorly represent the AMOC

data, and therefore a robust relationship in order to extend the observations into the past cannot be developed with this methodology. The results do show, however, that after 50-60 years the proxy does start to reproduce the interannual variability. A potential reason for the lack of decadal relationship could be that there is a wide spread in the behaviour of the AMOC and SSH temporally and spatially across the CMIP5 model output data (Schmittner et al., 2005; Manabe and Stouffer, 1999). This leads to large uncertainty in the response to forcing when using one model, refining our focus in the third chapter to the multi-model ensemble.

The final analysis first determines the probability of a negative and positive trend from 1850 to 2100 using trends of different lengths, over interannual to multi-decadal timescales. The probability analysis highlights that both past and future forced interannual trends are weak relative to the natural variability. The results therefore suggest that anthropogenic forcing cannot affect high-frequency changes in the AMOC variation probability, and a sustained 5-year decline is required to shift a trend probability outside its natural variability. Using 'business-as-usual' (RCP8.5) and a 'stabilisation' (RCP4.5) forcing, a sudden increase to a high probability of a decline is seen at the turn of the century and remains for RCP8.5, but returns to pre-industrial probability by 2100 in RCP4.5. Two prominent time periods are isolated from the RCP8.5 probability analysis; a long-term sustained period of a high probability of negative trends across the 21st century, and a rapid shift to the highest probability and trend magnitude covering a 20-year rogue period (from 1995 to 2015). The second part of the analysis harnesses the connection between the AMOC and salinity established by their coupled positive feedback mechanism. A weaker AMOC leads to further reduction in transport due to the lack of sufficient northward transport of salt required for deep convection preconditioning (Marotzke, 1996). Results show the generation of a dipole phenomenon north and south of 48° N in the 21st century, consistent with the expected freshening of the higher latitudes and accumulation of salt in the lower latitudes. After computing salinity budgets of the forced component for the subpolar region and subtropical region, the source of the anomalies is determined by splitting the salinity transport into ocean components; namely the overturning and gyre components, and atmospheric fluxes. When combined, these three transports estimate the changes of divergence or convergence of salt transport in each region through time (Drijfhout et al., 2011; Mecking et al., 2016, 2017). By 2100, the lower frequency trend of the forced AMOC is associated with the accumulated transport anomalies dominated by equal oceanic and atmospheric transport contributions in the subtropical region and solely the oceanic transport in the subpolar region. The rogue period (from 1995 to 2015) presents distinct features in the SPR that are unique to this period; there is a maximum 20-year decline in both the net salt transport and overturning trend transport, and it is the only period over which the overturning and the azonal trend transports have overlapping and sustained negative trends. During this rogue period, the atmospheric contribution is almost negligible (maintaining the same variability seen over the full 250 years), although a known bias

causing overestimation of evaporation in the models, and potentially impacting the accuracy of the analysis, should not be ignored (Mecking et al., 2017). These findings lay the foundation for potentially using such features to detect changes in past and future trends and variability of the AMOC, at least in a probabilistic sense.

In the interests of investigating the AMOC's trend over different timescales, this thesis provides results from three analyses to explore its natural and anthropologically-affected behaviour. The RAPID array decline could be a section of a decadal oscillation, maybe even natural, although discussions are still ongoing as to whether this could be the beginning of an expected 21st century decline of 34% on average according to CMIP5 models (Stocker et al., 2013). The main findings here suggest that 28-35 years are required to detect a statistically significant trend, and 5 years of a sustained decline in subpolar salinity transport can be indicative of a rapid shift into an anthropogenically-driven AMOC decline that is sustained over almost a century (even if natural variations in salinity might hide this forced indicator). However, these proxies using numerical model outputs, seem to be representative of the AMOC's variability or trend solely when using the ensemble mean (that captures the average effects of anthropogenic forcing), potentially due to individual models exhibiting large natural variability that hinder the forced signal. Ultimately, there is a general agreement that when certain thresholds are reached, AMOC changes can exceed the natural variability, and possibly affect climate phenomena worldwide. This thesis therefore affirms the potential for the RAPID array, after an additional 15 years of observations, or current numerical models, to capture such a trend through proxy indicators. Ultimately, timely detection of the AMOC trend and any rapid AMOC changes have the potential to be used for the design of climate risk management strategies and decision-making in the 21st century.

6.2 Targets for future work

Upon completion of this thesis, links between the three analyses come to light, and it is important to outline the next steps that could be taken in order to continue this research.

Being formulated as an introductory analysis, Chapter 3 identifies the number of years required to detect a declining trend of the full AMOC (i.e., the estimated transport streamfunction consisting of the Florida Straits, Ekman transport and Upper Mid-Ocean). From Chapter 4, the strong influence of higher frequency dynamics in the North Atlantic (for example, the influence of wind on annual AMOC variability) leads to the suggestion of exploring whether using the UMO instead of the AMOC in Chapter 3 could shorten the detection time. Furthermore, from the analysis in Chapter 5, if salinity transport trends can be used as an indicator of an AMOC decline, the trend

detection analysis could also be run using salinity transport in the subpolar North Atlantic instead of the AMOC. Another idea could be to delve into the non-linearity of the AMOC. Although of the 20 CMIP5 RCP8.5 models, only two showed significant autocorrelations beyond lag-1 (i.e., long-term memory which could be indicative of a periodic feature), further analysis to identify natural oscillations by fitting a higher polynomial regression to the timeseries could be of interest.

Extensive analyses are presented in Chapter 4 to show that RAPID observations cannot be extended into the past using surface measurements (SSH and SST). Therefore, using full-depth estimations from dynamic height, for example, could provide a more accurate relationship with the AMOC or the UMO. The issue here would be that verification of this methodology could only be done in models since RAPID provides the longest continuous records of dynamic height measurements in the North Atlantic (and the RAPID computations are based on those same dynamic height measurements). Another follow-up analysis could be to determine the n* (number of years to identify a relationship between the AMOC and SSH or SST that is robust through time) in the NEMO model, since the initial results using 13 years seem to reproduce the AMOC better than the CMIP5 reconstructions (potentially due to NEMO providing higher resolution data). The research question would have to change in order to ignore the validation of a robust relationship, however, since only one model would be used. The entire analysis could also be repeated using sea surface salinity (SSS) after the promising results from Chapter 5. Lastly, since Chapter 5 also suggests that an ensemble mean is required in order to capture the forced component, this could be tested (for SSH, SST, and SSS) instead of using each CMIP5 model separately.

Finally, for Chapter 5, verifying the robustness of the characterisations of the 20-year rogue period from 1995 to 2015 would be an intriguing next step. This could be done both by going back to the original data within the 16 models selected and identifying how many of them pertain this rogue period (and the salinity transport features). This goes against the initial reason for using the ensemble mean since Chapter 4 shows the issues that can occur when models are used separately to investigate dynamic relationships, however, it could be an interesting addition. The preferred proposed method for checking the robustness, however, would be to perform a hosing experiment, using the exact 20-year salinity transport decline trends in the subpolar gyre and identifying what occurs to the AMOC trend during this period, as well as a century beyond this period, to verify if the rogue period onsets a sustained decline scenario.

The suggestions outlined above should be considered as ideas for future work, and extensive evaluations of their feasibility should first be performed.

Bibliography

Abramowitz, M. and Stegun, I. A., editors (1972). *Handbook of Mathematical Functions with Formulas, Graphs, and Mathematical Tables*. Dover Publications, Inc., New York.

Aitken, A. C. (1934). On Least-squares and Linear Combinations of Observations. *Proceedings of the Royal Society of Edinburgh*, 55:42–48.

Alley, R. B., Marotzke, J., Nordhaus, W. D., Overpeck, J. T., Peteet, D. M., Pielke, R. A., Pierrehumbert, R. T., Rhines, P. B., Stocker, T. F., Talley, L. D., and Wallace, J. M. (2003). Abrupt Climate Change. *Science*, 299(5615):2005–2010.

Ansorge, I. J., Baringer, M. O., Campos, E. J. D., Dong, S., Fine, R. A., Garzoli, S. L., Goni, G., Meinen, C. S., Perez, R. C., Piola, A. R., Roberts, M. J., Speich, S., Sprintall, J., Terre, T., and Van Den Berg, M. A. (2014). Basin-wide oceanographic array bridges the South Atlantic. *Eos*, 95(6):53–54.

Arzel, O., Colin de Verdière, A., and England, M. H. (2010). The Role of Oceanic Heat Transport and Wind Stress Forcing in Abrupt Millennial-Scale Climate Transitions. *Journal of Climate*, 23(9):2233–2256.

Baehr, J., Cunnningham, S., Haak, H., Heimbach, P., Kanzow, T., and Marotzke, J. (2009). Observed and simulated estimates of the meridional overturning circulation at 26.5°N in the Atlantic. *Ocean Science*, 5:575–589.

Baehr, J., Haak, H., Alderson, S., Cunningham, S., Jungclaus, J., and Marotzke, J. (2007). Timely Detection of Changes in the Meridional Overturning Circulation at 26N in the Atlantic. *Journal of Climate*, 20(23):5827–5841.

Baehr, J., Keller, K., and Marotzke, J. (2008). Detecting potential changes in the meridional overturning circulation at 26N in the Atlantic. *Climatic Change*, 91(1-2):11–27.

Bakker, P., Schmittner, A., Lenaerts, J. T. M., Abe-Ouchi, A., Bi, D., van den Broeke, M. R., Chan, W. L., Hu, A., Beadling, R. L., Marsland, S. J., Mernild, S. H., Saenko, O. A., Swingedouw, D., Sullivan, A., and Yin, J. (2016). Fate of the Atlantic Meridional Overturning Circulation: Strong decline under continued warming and Greenland melting. *Geophysical Research Letters*, 43(23):12252–12260.

Barnier, B., Madec, G., Penduff, T., Molines, J., Treguier, A., Le Sommer, J., Beckmann, A., Biastoch, A., Boning, C., Dengg, J., Derval, C., Durand, E., Gulev, S., Remy, E., Talandier, C., Theetten, S., Maltrud, M., McClean, J., and de Cuevas, B. (2006). Impact of partial steps and momentum advection schemes in a global ocean circulation model at eddy-permitting resolution. *Ocean Dynamics*, 56(5-6):543–567.

Barron, E. J., Thompson, S. L., Hayt, W. W., Weaver, B. L., and Tarney, J. (1984). Continental distribution as a forcing factor for global-scale temperature. *Nature*, 310(5978):574–575.

Baumgartner, A. and Reichel, E. (1975). The World Water Balance: Mean Annual Global, Continental and Maritime Precipitation, Evaporation and Run-off. *Elsevier Scientific, New York*, page 179.

Beaulieu, C., Henson, S. A., Sarmiento, J. L., Dunne, J. P., Doney, S. C., Rykaczewski, R. R., and Bopp, L. (2013). Factors challenging our ability to detect long-term trends in ocean chlorophyll. *Biogeosciences*, 10(4):2711–2724.

Beaulieu, C. and Killick, R. (2018). Distinguishing trends and shifts from memory in climate data. *Journal of Climate*, 31(23):9519–9543.

Biastoch, A., Boning, C., and Lutjeharms, J. (2008a). Agulhas leakage dynamics affects decadal variability in Atlantic overturning circulation. *Nature*, 456:489–492.

Biastoch, A., Böning, C. W., Getzlaff, J., Molines, J.-M., and Madec, G. (2008b). Causes of Interannual-Decadal Variability in the Meridional Overturning Circulation of the Midlatitude North Atlantic Ocean. *Journal of Climate*, 21(24):6599–6615.

Bingham, R. J. and Hughes, C. W. (2009). Signature of the Atlantic meridional overturning circulation in sea level along the east coast of North America. *Geophysical Research Letters*, 36(December 2008):1–5.

Bond, G. C., Showers, W., Elliot, M., Evans, M., Lotti, R., Hajdas, I., Bonani, G., and Johnson, S. (1999). The North Atlantic's 1-2 kyr Climate Rhythm: Relation to Heinrich Events, Dansgaard/Oeschger Cycles and the Little Ice Age. *Geophysical Monograph Series*, 112:35–58.

Böning, C. W., Behrens, E., Biastoch, A., Getzlaff, K., and Bamber, J. L. (2016). Emerging impact of Greenland meltwater on deepwater formation in the North Atlantic Ocean. *Nature Geoscience*, 9(7):523–527.

Booth, B. B. B., Dunstone, N. J., Halloran, P. R., Andrews, T., , and Bellouin, N. (2012). Aerosols implicated as a prime driver of 20th century north atlantic climate variability. *Nature*, 484(7393):228–232.

Boulton, C. A., Allison, L. C., and Lenton, T. M. (2014). Early warning signals of Atlantic Meridional Overturning Circulation collapse in a fully coupled climate model. *Nature Communications*, 5(7):5752.

Brockwell, P. J. and Davis, R. A. (2002). *Introduction to time series and forecasting*. Springer, New York, 2 edition.

Broecker, W. S. (1987). The biggest chill. In *Global Climate Change Linkages; Acid Rain, Air Quality, and Stratospheric Ozone*, pages 13–22. Elsevier New York.

Broecker, W. S. (1991). The great ocean conveyor belt. *Oceanography*, 4:79–89.

Broecker, W. S. (1998). Paleocean circulation during the Last Deglaciation: A bipolar seesaw? *Paleoceanography*, 13(2):119–121.

Broecker, W. S., Peteet, D. M., and Rind, D. (1985). Does the ocean-atmosphere system have more than one stable mode of operation? *Nature*, 315(2):21–26.

Broecker, W. S. and Tsung, H. P. (1987). The role of $CaCO_3$ compensation in the glacial to interglacial atmospheric CO_2 change. *Global Biogeochemical Cycles*, 1(1):15–29.

Bryan, K. (1996). The steric component of sea level rise associated with enhanced greenhouse warming: a model study. *Climate Dynamics*, 12(8):545–555.

Bryden, H. L., King, B. A., and Mccarthy, G. D. (2011). South Atlantic overturning circulation at 24°S. *Journal of Marine Research*, 69(1):39–56.

Bryden, H. L., King, B. A., McCarthy, G. D., and McDonagh, E. L. (2014). Impact of a 302009-2010. *Ocean Science*, 10(4):683–691.

Bryden, H. L., Longworth, H. R., and Cunningham, S. A. (2005). Slowing of the Atlantic meridional overturning circulation at 25N. *Nature*, 438(7068):655–657.

Buckley, M. W. and Marshall, J. (2016). Observations, inferences, and mechanisms of the Atlantic Meridional Overturning Circulation: A review. *Reviews of Geophysics*, 54:5–63.

Caesar, L., Rahmstorf, S., Robinson, A., Feulner, G., and Saba, V. (2018). Observed fingerprint of a weakening Atlantic Ocean overturning circulation. *Nature*, 556(7700):191–196.

Cattiaux, J., Vautard, R., Cassou, C., Yiou, P., Masson-Delmotte, V., and Codron, F. (2010). Winter 2010 in Europe: A cold extreme in a warming climate. *Geophysical Research Letters*, 37(20):1–6.

Chambers, D. P., Merrifield, M. A., and Nerem, R. S. (2012). Is there a 60-year oscillation in global mean sea level? *Geophysical Research Letters*, 39(18):1–6.

Cheng, W., Chiang, J. C., and Zhang, D. (2013). Atlantic meridional overturning circulation (AMOC) in CMIP5 Models: RCP and historical simulations. *Journal of Climate*, 26(18):7187–7197.

Chidichimo, M. P., Kanzow, T., Cunningham, S. A., Johns, W. E., and Marotzke, J. (2010). The contribution of eastern-boundary density variations to the Atlantic meridional overturning circulation at 26.5°N. *Ocean Science*, 6:475–490.

Chylek, P., Folland, C. K., Dijkstra, H. A., Lesins, G., and Dubey, M. K. (2011). Ice-core data evidence for a prominent near 20 year time-scale of the Atlantic Multidecadal Oscillation. *Geophysical Research Letters*, 38(13):1–5.

Colin de Verdière, A., Ben Jelloul, M., and Sévellec, F. (2006). Bifurcation Structure of Thermohaline Millennial Oscillations. *Journal of Climate*, 19(22):5777–5795.

Collins, M., Knutti, R., Arblaster, J., Dufresne, J.-L., Fichefet, T., P.Friedlingstein, Gao, X., Gutowski, W., Johns, T., G.Krinner, Shongwe, M., Tebaldi, C., Weaver, A., and Wehner, M. (2013). IPCC 2013 AR5 - Chapter 12: Long-term Climate Change: Projections, Commitments and Irreversibility. In *Climate Change 2013: The Physical Science Basis. Contribution of Working Group I to the Fifth Assessment Report of the Intergovernmental Panel on Climate Change*, pages 1029–1136.

Collins, M. and Sinha, B. (2003). Predictability of decadal variations in the thermohaline circulation and climate. *Geophysical Research Letters*, 30(6):1–4.

Cromwell, D., Shaw, A. G. P., Challenor, P., Houseago-Stokes, R. E., and Tokmakian., R. (2007). Towards measuring the meridional overturning circulation from space. *Ocean Science*, 3(2):223–228.

Cunningham, S., Kanzow, T., Rayner, D., Baringer, M. O., Johns, W. E., Marotzke, J., Longworth, H. R., Grant, E. M., Hirschi, J. J.-M., Beal, L. M., Meinen, C. S., and Bryden, H. L. (2007). Temporal variability of the Atlantic meridional overturning circulation at 26.5N. *Science*, 317(5840):935–8.

Dansgaard, W., Johnsen, S. J., Clausen, H. B., Dahl-Jensen, D., Gundestrup, N. S., Hammer, C. U., Hvidberg, C. S., Steffensen, J. P., Sveinbjörnsdottir, A. E., Jouzel, J., and Bond, G. (1993). Evidence for general instability of past climate from a 250-kyr ice-core record. *Nature*, 364:218–220.

de Jong, S. (1993). SIMPLS : an alternative approach to partial least squares regression. *Chemometrics and Intelligent Laboratory Systems*, 18(3):251–263.

de Vries, P. and Weber, S. L. (2005). The Atlantic freshwater budget as a diagnostic for the existence of a stable shut down of the meridional overturning circulation. *Geophysical Research Letters*, 32(9):1–4.

Delworth, T. L. and Dixon., K. W. (2000). Implications of the Recent Trend in the Arctic / North Atlantic Oscillation for the North Atlantic Thermohaline Circulation. *Journal of Climate*, 13(21):3721–3727.

Delworth, T. L., Zhang, R., and Mann, M. E. (2007). Decadal to Centennial Variability of the Atlantic From Observations and Models. *Ocean Circulation: Mechanisms and Impacts*, 173:131–148.

Dickson, B., Yashayaev, I., Meincke, J., Turrell, B., Dye, S., and Holfort, J. (2002). Rapid freshening of the deep North Atlantic Ocean over the past four decades. *Nature*, 416(6883):832–837.

Dijkstra, H. A. (2007). Characterization of the multiple equilibria regime in a global ocean model. *Tellus A: Dynamic Meteorology and Oceanography*, 59(5).

Draper, N. R. and Smith, H. (1998). *Applied Regression Analysis*. John Wiley and Sons, 3 edition.

Drijfhout, S., Jan van Oldenborgh, G., and Cimatoribus, A. (2012). Is a Decline of AMOC Causing the Warming Hole above the North Atlantic in Observed and Modeled Warming Patterns? *Journal of Climate*, 25:8373–8379.

Drijfhout, S. S., Weber, S. L., and Swaluw, E. V. D. (2011). The stability of the MOC as diagnosed from model projections for pre-industrial, present and future climates. *Climate Dynamics*, 37(7-8):1575–1586.

Duchez, A., Hirschi, J. J., Cunningham, S. A., Blaker, A. T., Bryden, H. L., de Cuevas, B., Atkinson, C. P., McCarthy, G. D., Frajka-Williams, E., Rayner, D., Smeed, D., and Mizielinski, M. S. (2014). A new index for the Atlantic meridional overturning circulation at 26N. *Journal of Climate*, 27(17):6439–6455.

Durbin, B. Y. J. and Watson, G. S. (1950). Testing for serial correlation in least squares regression, I. *Biometrika*, 37(3-4):409–428.

Easterling, D. R. and Wehner, M. F. (2009). Is the climate warming or cooling? *Geophysical Research Letters*, 36(8):4–6.

Ekman, W. (1905). On the influence of the earth's rotation on ocean-currents.

Elipot, S., Frajka-Williams, E., Hughes, C., and Willis, J. (2014). The observed North Atlantic Meridional Overturning Circulation, its Meridional Coherence and Ocean Bottom Pressure. *Journal of Physical Oceanography*, 44(2):517–537.

Emile-Geay, J., Cane, M. A., Naik, N., Seager, R., Clement, A. C., and Geen, A. V. (2003). Warren revisited: Atmospheric freshwater fluxes and "Why is no deep water formed in the North Pacific ". *Journal of Geophysical Research*, 108(C6):1–12.

Engle, R. F. (1982). Autoregressive Conditional Heteroscedasticity with Estimates of the Variance of United Kingdom Inflation. *Econometrica*, 50(4):987–1007.

Ezer, T. (2015). Detecting changes in the transport of the Gulf Stream and the Atlantic overturning circulation from coastal sea level data: The extreme decline in 2009-2010 and estimated variations for 1935-2012. *Global and Planetary Change*, 129:23–36.

Ferreira, D., Cessi, P., Coxall, H. K., Boer, A. D., Dijkstra, H. A., Drijfhout, S. S., Eldevik, T., Harnik, N., Mcmanus, J. F., and Marshall, D. P. (2018). Atlantic-Pacific Asymmetry in Deep Water Formation. *Annual Review of Earth and Planetary Sciences*, 46:327–352.

Fischer, J., Visbeck, M., Zantopp, R., and Nunes, N. (2010). Interannual to decadal variability of outflow from the Labrador Sea. *Geophysical Research Letters*, 37(24):1–5.

Flato, G., Marotzke, J., Abiodun, B., Braconnot, P., Chou, S., Collins, W., Cox, P., Driouech, F., Emori, S., Eyring, V., Forest, C., Gleckler, P., Guilyardi, E., Jakob, C., Kattsov, V., Reason, C., and Rummukainen, M. (2013). IPCC 2013 AR5 - Chapter 9: Evaluation of Climate Models. In *Climate Change 2013: The Physical Science Basis. Contribution of Working Group I to the Fifth Assessment Report of the Intergovernmental Panel on Climate Change*, pages 741–866.

Fletcher, S. E. M., Gruber, N., Jacobson, A. R., Doney, S. C., Dutkiewicz, S., Gerber, M., Follows, M., Joos, F., Lindsay, K., Menemenlis, D., Mouchet, A., Mu, S. A., and Sarmiento, J. L. (2006). Inverse estimates of anthropogenic CO_2 uptake , transport, and storage by the ocean. *Global Biogeochemical Cycles*, 20:1–16.

Frajka-Williams, E. (2015). Estimating the Atlantic overturning at 26°N using satellite altimetry. *Geophysical Research Letters*, 42:3458–3464.

Frajka-Williams, E., Ansorge, I. J., Baehr, J., Bryden, H. L., Chidichimo, M. P., Cunningham, S. A., Danabasoglu, G., Dong, S., Donohue, K. A., Elipot, S., Heimbach, P., Holliday, N. P., Hummels, R., Jackson, L. C., Karstensen, J., Lankhorst, M., Le Bras, I. A., Lozier, M. S., McDonagh, E. L., Meinen, C. S., Mercier, H., Moat, B. I., Perez, R. C., Piecuch, C. G., Rhein, M., Srokosz, M. A., Trenberth, K. E., Bacon, S., Forget, G., Goni, G., Kieke, D., Koelling, J., Lamont, T., McCarthy, G. D., Mertens, C., Send, U., Smeed, D. A., Speich, S., van den Berg, M., Volkov, D., and Wilson, C. (2019). Atlantic Meridional Overturning Circulation: Observed Transport and Variability. *Frontiers in Marine Science*, 6(250):1–18.

Frajka-Williams, E., Lankhorst, M., Koelling, J., and Send, U. (2018). Coherent Circulation Changes in the Deep North Atlantic From 16°N and 26°N Transport Arrays. *Journal of Geophysical Research*, 123:3427–3443.

Frajka-Williams, E., Meinen, C. S., Johns, W. E., Smeed, D. A., Duchez, A., Lawrence, A. J., Cuthbertson, D. A., Mccarthy, G. D., Bryden, H. L., Baringer, M. O., Moat, B. I., and Rayner, D. (2016). Compensation between meridional flow components of the Atlantic MOC at 26°N. *Ocean Science*, 12:481–493.

Frankcombe, L. M., von der Heydt, A., and Dijkstra, H. A. (2010). North atlantic multidecadal climate variability: An investigation of dominant time scales and processes. *Journal of Climate*, 23(13):3626–3638.

Ganachaud, A. and Wunsch, C. (2000). Improved estimates of global ocean circulation, heat transport and mixing from hydrographic data. *Nature*, 408:453–458.

Ganachaud, A. and Wunsch, C. (2003). Large-Scale Ocean Heat and Freshwater Transports during the World Ocean Circulation Experiment. *Journal of Climate*, 16:696–705.

Garzoli, S. L. and Matano, R. (2011). The South Atlantic and the Atlantic meridional overturning circulation. *Deep Sea Research Part II: Topical Studies in Oceanography*, 58(17):1837–1847.

Geladi, P. and Kowalski, B. R. (1986). Partial least-squares regression: a tutorial. *Analytica Chimica Acta*, 185:1–17.

Goddard, P. B., Yin, J., Griffies, S. M., and Zhang, S. (2015). An extreme event of sea-level rise along the Northeast coast of North America in 2009–2010. *Nature Communications*, 6:1–9.

Gordon, A. L. (1986). Inter-ocean exchange of thermohaline water. *Journal of Geophysical Research*, 91(6):5037–5046.

Gregory, J. M., Dixon, K. W., Stouffer, R. J., Weaver, A. J., Driesschaert, E., Eby, M., Fichefet, T., Hasumi, H., Hu, A., Jungclaus, J. H., Kamenkovich, I. V., Levermann, A., Montoya, M., Murakami, S., Nawrath, S., Oka, A., Sokolov, A. P., and Thorpe, R. B. (2005). A model intercomparison of changes in the Atlantic thermohaline circulation in response to increasing atmospheric CO_2 concentration. *Geophysical Research Letters*, 32:1–5.

Gregory, J. M. and Lowe, J. A. (2000). Predictions of global and regional sea-level rise using AOGCMs with and without flux adjustment. *Geophysical Research Letters*, 27(19):3069–3072.

Häkkinen, S. (1999). Variability in sea surface height: a qualitative measure for the meridional overturning in the North Atlantic. *NASA Goddard Space Flight Centre*, pages 1–35.

Häkkinen, S. (2001). Variability in sea surface height: A qualitative measure for the meridional overturning in the North Atlantic. *Journal of Geophysical Research*, 106(C7):13,837–13,848.

Hall, M. M. and Bryden, H. L. (1982). Direct estimates and mechanisms of ocean heat transport. *Deep Sea Research Part A, Oceanographic Research Papers*, 29(3):339–359.

Haynes, K., Eckley, I. A., and Fearnhead, P. (2017). Computationally Efficient Change-point Detection for a Range of Penalties. *Journal of Computational and Graphical Statistics*, 26(1):134–143.

Henson, S., Sarmiento, J., Dunne, J., Bopp, L., Lima, I., Doney, S., John, J., and Beaulieu, C. (2010). Detection of anthropogenic climate change in satellite records of ocean chlorophyll and productivity. *Biogeosciences*, 7:621–640.

Hirschi, J., Killworth, P., Blundell, J., and Cromwell, D. (2009). Sea Surface Height Signals as Indicators for Oceanic Meridional Mass Transports. *Journal of Physical Oceanography*, 39:581–601.

Hirschi, J. and Marotzke, J. (2007). Reconstructing the Meridional Overturning Circulation from Boundary Densities and the Zonal Wind Stress. *Journal of Physical Oceanography*, 37:743–763.

Hodson, D. L. and Sutton, R. T. (2012). The impact of resolution on the adjustment and decadal variability of the Atlantic meridional overturning circulation in a coupled climate model. *Climate Dynamics*, 39(12):3057–3073.

Hofmann, M. and Rahmstorf, S. (2009). On the stability of the Atlantic meridional overturning circulation. *Proceedings of the National Academy of Sciences*, 106(49):20584–20589.

Holgate, S. J., Matthews, A., Woodworth, P. L., Rickards, L. J., Tamisiea, M. E., Bradshaw, E., Foden, P. R., Gordon, K. M., Jevrejeva, S., and Pugh, J. (2013). New Data Systems and Products at the Permanent Service for Mean Sea Level. *Journal of Coastal Research*, 29(3):493–504.

Hu, A., Meehl, G. a., Han, W., and Yin, J. (2009). Transient response of the MOC and climate to potential melting of the Greenland Ice Sheet in the 21st century. *Geophysical Research Letters*, 36(April):1–6.

Huang, B., Hu, Z.-Z., Schneider, E. K., Wu, Z., Xue, Y., and Klinger, B. (2012a). Influences of tropical-extratropical interaction on the multidecadal AMOC variability in the NCEP climate forecast system. *Climate Dynamics*, 39(3-4):531–555.

Huang, B., Xue, Y., Kumar, A., and Behringer, D. W. (2012b). AMOC variations in 1979 – 2008 simulated by NCEP operational ocean data assimilation system. *Climate Dynamics*, 38(3):513–525.

Ivchenko, V. O., Sidorenko, D., Danilov, S., Losch, M., and Schröter, J. (2011). Can sea surface height be used to estimate oceanic transport variability? *Geophysical Research Letters*, 38:1–5.

Jackson, L. C., Peterson, K. A., Roberts, C. D., and Wood, R. A. (2016). Recent slowing of Atlantic overturning circulation as a recovery from earlier strengthening. *Nature Geoscience*, 9(7):518–522.

Jacob, D., Goettel, H., Jungclaus, J., Muskulus, M., and Podzun, R. (2005). Slowdown of the thermohaline circulation causes enhanced maritime climate influence and snow cover over Europe. *Geophysical Research Letters*, 32:1–5.

Johns, W. E., Baringer, M. O., Beal, L. M., Cunningham, S. A., Kanzow, T., Bryden, H. L., Hirschi, J. J. M., Marotzke, J., Meinen, C. S., Shaw, B., and Curry, R. (2011). Continuous, Array-Based Estimates of Atlantic Ocean Heat Transport at 26.5N. *Journal of Climate*, 24(10):2429–2449.

Johns, W. E., Beal, L. M., Baringer, M. O., Molina, J. R., Cunningham, S. A., Kanzow, T., and Rayner, D. (2008). Variability of Shallow and Deep Western Boundary Currents off the Bahamas during 2004–05: Results from the 26N RAPID–MOC Array. *Journal of Physical Oceanography*, 38(3):605–623.

Johns, W. E., Kanzow, T., and Zantopp, R. (2005). Estimating ocean transports with dynamic height moorings: An application in the Atlantic Deep Western Boundary Current at 26°N. *Deep Sea Research Part I: Oceanographic Research Papers*, 52(8):1542–1567.

Josey, S. A. and Marsh, R. (2005). Surface freshwater flux variability and recent freshening of the North Atlantic in the eastern subpolar gyre. *Journal of Geophysical Research*, 110:1–17.

Kanzow, T., Cunningham, S. A., Johns, W. E., Hirschi, J. J., Marotzke, J., Baringer, M. O., Meinen, C. S., Chidichimo, M. P., Atkinson, C., Beal, L. M., Bryden, H. L., and Collins, J. (2010). Seasonal variability of the Atlantic meridional overturning circulation at 26.5°N. *Journal of Climate*, 23(21):5678–5698.

Kariya, T. and Kurata, H. (2004). *Generalized Least Squares*. John Wiley and Sons.

Keller, K., Deutsch, C., Hall, M. G., and Bradford, D. F. (2007a). Early detection of changes in the North Atlantic meridional overturning circulation: Implications for the design of ocean observation systems. *Journal of Climate*, 20(2):145–157.

Keller, K., Kim, S. R., Baehr, J., Bradford, D. F., and Oppenheimer, M. (2007b). What is the economic value of information about uncertain climate thresholds? In *Human-Induced Climate Change: an Interdisciplinary Assessment*, pages 343–354. Cambridge University Press.

Killick, R., Fearnhead, P., and Eckley, I. (2012). Optimal detection of changepoints with a linear computational cost. *Journal of the American Statistical Association*, 107(500):1590–1598.

Killworth, P. (1983). Deep convection in the world ocean. *Reviews of Geophysics and Space Physics*, 21(1):1–26.

Kim, W. M., Yeager, S., Chang, P., and Danabasoglu, G. (2018). Low-frequency North Atlantic climate variability in the community earth system model large ensemble. *Journal of Climate*, 31(2):787–813.

Knight, J. R., Allan, R. J., Folland, C. K., Vellinga, M., and Mann, M. E. (2005). A signature of persistent natural thermohaline circulation cycles in observed climate. *Geophysical Research Letters*, 32(20):1–4.

Knight, J. R., Folland, C. K., and Scaife, A. A. (2006). Climate impacts of the Atlantic Multidecadal Oscillation. *Geophysical Research Letters*, 33(17):1–4.

Kopp, R. E. (2013). Does the mid-Atlantic United States sea level acceleration hot spot reflect ocean dynamic variability? *Geophysical Research Letters*, 40(15):3981–3985.

Kostov, Y., Armour, K. C., and Marshall, J. (2014). Impact of the Atlantic meridional overturning circulation on ocean heat storage and transient climate change. *Journal of Geophysical Research*, 41:2108–2116.

Kuhlbrodt, T. and Gregory, J. M. (2012). Ocean heat uptake and its consequences for the magnitude of sea level rise and climate change. *Geophysical Research Letters*, 39(17):1–6.

Kvålseth, T. O. (1985). Cautionary note about R2. *The American Statistician*, 39(4):279–285.

Landerer, F. W., Jungclaus, J. H., and Marotzke, J. (2007). Regional Dynamic and Steric Sea Level Change in Response to the IPCC-A1B Scenario. *Journal of Physical Oceanography*, 37(2):296–312.

Landerer, F. W., Wiese, D. N., Bentel, K., Boening, C., and Watkins, M. M. (2015). North Atlantic meridional overturning circulation variations from GRACE ocean bottom pressure anomalies. *Geophysical Research Letters*, 42:8114–8121.

Larsen, J. C. and Sanford, T. (2014). Florida Current Volume Transports from Voltage Measurements. *Science*, 227(4684):302–304.

Latif, M., Roeckner, E., Mikolajewicz, U., and Voss, R. (2000). Tropical Stabilization of the Thermohaline Circulation in a Greenhouse Warming Simulation. *Journal of Climate*, 13(11):1809–1813.

Lavin, A., Bryden, H. L., and Parrilla, G. (1998). Meridional transport and heat flux variations in the subtropical North Atlantic. *The Global atmosphere and ocean system*, 6:269–293.

Ledwell, J. R., St. Laurent, L. C., Girton, J. B., and Toole, J. M. (2011). Diapycnal Mixing in the Antarctic Circumpolar Current. *Journal of Physical Oceanography*, 41(1):241–246.

Ledwell, J. R., Watson, A. J., and Law, C. S. (1998). Mixing of a tracer across the pycnocline. *J. Geophys.Res. Oceans*, 103:21499–21529.

Lennartz, S. and Bunde, A. (2011). Distribution of natural trends in long-term correlated records:A scaling approach. *Physical Review E*, 84(021129):1–9.

Levermann, A., Griesel, A., Hofmann, M., Montoya, M., and Rahmstorf, S. (2005). Dynamic sea level changes following changes in the thermohaline circulation. *Climate Dynamics*, 24(4):347–354.

Li, F., Lozier, S., and Johns, W. E. (2017). Calculating the Meridional Volume, Heat ,and Freshwater Transports from an Observing System in the Subpolar North Atlantic: Observing System Simulation Experiment. *Journal of Atmospheric and Oceanic Technology*, 34:1483–1500.

Little, C. M., Piecuch, C. G., and Ponte, R. M. (2017). On the relationship between the meridional overturning circulation, alongshore wind stress, and United States East Coast sea level in the Community Earth System Model Large Ensemble. *Journal of Geophysical Research*, 122:1–15.

Liu, W., Liu, Z., and Brady., E. C. (2014). Why is the AMOC Monostable in Coupled General Circulation Models? *Journal of Climate*, 27(6):2427–2443.

Liu, W., Xie, S. P., Liu, Z., and Zhu, J. (2017). Overlooked possibility of a collapsed atlantic meridional overturning circulation in warming climate. *Science Advances*, 3(1):1–8.

Livina, V. N. and Lenton, T. M. (2007). A modified method for detecting incipient bifurcations in a dynamical system. *Geophysical Research Letters*, 34(3):1–5.

Longworth, H. R., Bryden, H. L., and Baringer, M. O. (2011). Historical variability in Atlantic meridional baroclinic transport at 26.5 N from boundary dynamic height observations. *Deep-Sea Research Part II*, 58(17-18):1754–1767.

Lorbacher, K., Dengg, J., Boning, C., and Biastoch, A. (2010). Regional Patterns of Sea Level Change Related to Interannual Variability and Multidecadal Trends in the Atlantic Meridional Overturning Circulation. *Journal of Climate*, 23:4243–4254.

Lozier, M. S. (2010). Deconstructing the conveyor belt. *Science*, 328(5985):1507–1511.

Lozier, M. S., Bacon, S., Bower, A. S., Cunningham, S. A., De Jong, M. F., De Steur, L., De Young, B., Fischer, J., Gary, S. F., Greenan, B. J., Heimbmbach, P., Holliday, N. P., Houpert, L., Inall, M. E., Johns, W. E., Johnson, H. L., Karstensen, J., Li, F., Lin, X., Mackay, N., Marshall, D. P., Mercier, H., Myers, P. G., Pickart, R. S., Pillar, H. R., Straneo, F., Thierry, V., Weller, R. A., Williams, R. G., Wilson, C., Yang, J., Zhao, J., and Zika, J. D. (2017). Overturning in the Subpolar north Atlantic program:

A new international ocean observing system. *Bulletin of the American Meteorological Society*, 98(4):737–752.

Ludescher, J., Bunde, A., and Schellnhuber, H. J. (2017). Statistical significance of seasonal warming/cooling trends. *Proceedings of the National Academy of Sciences*, 114(15):1–6.

Madec and the NEMO Team, G. (2016). *NEMO ocean engine*. Number 27. Institut Pierre-Simon Laplace (IPSL).

Mahajan, S., Zhang, R., Delworth, T. L., Zhang, S., Rosati, A. J., and Chang, Y. S. (2011). Predicting Atlantic meridional overturning circulation (AMOC) variations using subsurface and surface fingerprints. *Deep-Sea Research Part II: Topical Studies in Oceanography*, 58(17-18):1895–1903.

Manabe, S. and Stouffer, R. J. (1988). Two Stable Equilibria of a Coupled Ocean-Atmosphere Model. *Journal of Climate*, 1:841–866.

Manabe, S. and Stouffer, R. J. (1994). Multiple-century response of a coupled ocean-atmosphere model to an increase of atmospheric carbon dioxide. *Journal of climate*, 7(1):5–23.

Manabe, S. and Stouffer, R. J. (1999). The role of thermohaline circulation in climate. *Tellus B : Chemical and Physical Meteorology*, 51(1):91–109.

Marotzke, J. (1996). Analysis of thermohaline feedbacks. In *Decadal Climate Variability*, pages 333–378. Springer, Berlin, Heidelberg.

Marshall, J., Donohoe, A., Ferreira, D., and McGee, D. (2014). The ocean's role in setting the mean position of the Inter-Tropical Convergence Zone. *Climate Dynamics*, 42(7-8):1967–1979.

Marshall, J. and Schott, F. (1999). Open-Ocean Convection: Observations, Theory and Models. *Reviews of Geophysics*, 37(1):1–64.

Marshall, J. and Speer, K. (2012). Closure of the meridional overturning circulation through Southern Ocean upwelling. *Nature Geoscience*, 5(3):171–180.

Matei, D., Baehr, J., Jungclaus, J. H., Haak, H., Müller, W. A., and Marotzke, J. (2012). Multiyear predication of monthly mean Atlantic Meridional Overturning Circulation at 26.5°N. *Science*, 335(6064):76–79.

McCarthy, G., Frajka-Williams, E., Johns, W. E., Baringer, M. O., Meinen, C. S., Bryden, H. L., Rayner, D., Duchez, A., Roberts, C., and Cunningham, S. A. (2012). Observed interannual variability of the Atlantic meridional overturning circulation at 26.5°N. *Geophysical Research Letters*, 39(19):1–5.

McCarthy, G., Smeed, D., Johns, W., Frajka-Williams, E., Moat, B., Rayner, D., Baringer, M., Meinen, C., Collins, J., and Bryden, H. (2015a). Measuring the Atlantic Meridional Overturning Circulation at 26N. *Progress in Oceanography*, 130:91–111.

McCarthy, G. D., Haigh, I. D., Hirschi, J. J.-M., Grist, J. P., and Smeed, D. A. (2015b). Ocean impact on decadal Atlantic climate variability revealed by sea-level observations. *Nature*, 521:508–523.

McCarthy, G. D., Menary, M. B., Mecking, J., Moat, B. I., Johns, W., Andrews, M., Rayner, D., Smeed, D., and 1National (2017a). The importance of deep, basinwide measurements in optimized Atlantic Meridional Overturning Circulation observing arrays. *Journal of Geophysical Research: Oceans*, 112:1–19.

McCarthy, G. D., Smeed, D. A., Cunningham, S. A., and Roberts, C. D. (2017b). Atlantic Meridonal Overturning Circulation. *Marine Climate Change Impacts Partnership: Science Review*, pages 1–7.

McDonagh, E. L., King, B. A., Bryden, H. L., Courtois, P., Szuts, Z., Baringer, M., Cunningham, S. A., Atkinson, C., and McCarthy, G. (2015). Continuous Estimate of Atlantic Oceanic Freshwater Flux at 26.5N. *Journal of Climate*, 28(22):8888–8906.

McDonagh, E. L., McLeod, P., King, B. A., Bryden, H. L., and Torres Valdes, S. (2010). Circulation, Heat, and Freshwater Transport at 36N in the Atlantic. *Journal of Physical Oceanography*, 40:2661–2678.

McManus, J. F., Francois, R., Gherardi, J.-M., Keigwin, L. D., and Brown-Leger, S. (2004). Collapse and rapid resumption of Atlantic meridional circulation linked to deglacial climate changes. *Nature*, 428(6985):834–837.

Mecking, J., Drijfhout, S. S., Jackson, L. C., and The, M. B. A. (2017). The effect of model bias on Atlantic freshwater transport and implications for AMOC bi-stability. *Tellus A: Dynamic Meteorology and Oceanography*, 69:1–15.

Mecking, J. V., Drijfhout, S. S., Jackson, L. C., and Graham, T. (2016). Stable AMOC off state in an eddy-permitting coupled climate model. *Climate Dynamics*, 47(7-8):2455–2470.

Medhaug, I. and Furevik, T. (2011). North Atlantic 20th century multidecadal variability in coupled climate models: sea surface temperature and ocean overturning circulation. *Ocean Science*, 7:389–404.

Meinen, C. S., Baringer, M. O., and Garcia, R. F. (2010). Florida Current transport variability : An analysis of annual and longer-period signals. *Deep-Sea Research Part I*, 57(7):835–846.

Meinen, C. S., Speich, S., Perez, R. C., Dong, S., Piola, A. R., Garzoli, S. L., Baringer, M. O., Gladyshev, S., and Campos, E. J. (2013). Temporal variability of the meridional overturning circulation at 34.5S: Results from two pilot boundary arrays in the South Atlantic. *Journal of Geophysical Research: Oceans*, 118(12):6461–6478.

Morris, T., Hermes, J., Beal, L., Du Plessis, M., Rae, C. D., Gulekana, M., Lamont, T., Speich, S., Roberts, M., and Ansorge, I. J. (2017). The importance of monitoring the Greater Agulhas Current and its inter-ocean exchanges using large mooring arrays. *South African Journal of Science*, 113(7-8):1–7.

Msadek, R., Dixon, K. W., Delworth, T. L., and Hurlin, W. (2010). Assessing the predictability of the Atlantic meridional overturning circulation and associated fingerprints. *Geophysical Research Letters*, 37(19):1–5.

Msadek, R., Johns, W. E., Yeager, S. G., Danabasoglu, G., Delworth, T. L., and Rosati, A. (2013). The Atlantic Meridional Heat Transport at 26.5 N and Its Relationship with the MOC in the RAPID Array and the GFDL and NCAR Coupled Models. *Journal of Climate*, 26(12):4335–4356.

Muir, L. C. and Fedorov, A. V. (2017). Evidence of the AMOC interdecadal mode related to westward propagation of temperature anomalies in CMIP5 models. *Climate Dynamics*, 48(5-6):1517–1535.

Munk, W. and Wunsch, C. (1998). Abyssal recipes II: energetics of tidal and wind mixing. *Deep Sea Research*, 45(12):1977–2010.

Nikurashin, M. and Vallis, G. (2012). A Theory of the Interhemispheric Meridional Overturning Circulation and Associated Stratification. *Journal of Physical Oceanography*, 42:1652–1667.

Orsini, N., Bellocco, R., and Greenland, S. (2006). Generalized least squares for trend estimation of summarized dose – response data. *The Stata Journal*, 6(1):40–57.

Park, T., Park, W., and Latif, M. (2016). Correcting North Atlantic sea surface salinity biases in the Kiel Climate Model: influences on ocean circulation and Atlantic Multidecadal Variability. *Climate Dynamics*, 47(7-8):2543–2560.

Parker, A. and Ollier, C. D. (2016). There is no real evidence for a diminishing trend of the Atlantic meridional overturning circulation. *Journal of Ocean Engineering and Science*, 1(1):30–35.

Patricola, C. M., Chang, P., and Saravanan, R. (2013). Impact of Atlantic SST and high frequency atmospheric variability on the 1993 and 2008 Midwest floods: Regional climate model simulations of extreme climate events. *Climatic Change*, 129(3-4):397–411.

Pérez, F. F., Mercier, H., Vázquez-Rodríguez, M., Lherminier, P., Velo, A., Pardo, P. C., Rosón, G., and Ríos, A. F. (2013). Atlantic Ocean CO_2 uptake reduced by weakening of the Meridional Overturning Circulation. *Nature Geoscience*, 6(2):146–152.

Piecuch, C. G. and Ponte, R. M. (2011). Mechanisms of interannual steric sea level variability. *Geophysical Research Letters*, 38:1–6.

Pillar, H. R., Heimbach, P., Johnson, H. L., and Marshall, D. P. (2016). Dynamical attribution of recent variability in Atlantic overturning. *Journal of Climate*, 29(9):3339–3352.

Pinheiro, J. C. and Bates, D. M. (2000). *Mixed-effects models in S and S-Plus*. Springer-Verlag, New York.

Pohlmann, H., Sienz, F., and Latif, M. (2006). Influence of the Multidecadal Atlantic Meridional Overturning Circulation Variability on European Climate. *Journal of Climate-Special Section*, 19:6062–6067.

(PSMSL), P. S. f. M. S. L. (2019). Tide Gauge Data. (Retrieved 15 Apr 2019 from http://www.psmsl.org/da).

Rahmstorf, S. (1995). Bifurcations of the Atlantic thermohaline circulation in response to changes in the hydrological cycle. *Nature*, 378(6553):145–149.

Rahmstorf, S. (1996). On the freshwater forcing and transport of the Atlantic thermohaline circulation. *Climate Dynamics*, 12(12):799–811.

Rahmstorf, S. (2000). The thermohaline ocean circulation: A system with dangerous thresholds? *Climatic Change*, 46(3):247–256.

Rahmstorf, S., Box, J. E., Feulner, G., Mann, M. E., Robinson, A., Rutherford, S., and Schaffernicht, E. J. (2015). Exceptional twentieth-century slowdown in Atlantic Ocean overturning circulation. *Nature Climate Change*, 5(5):475–480.

Rahmstorf, S. and Ganopolski, A. (1999). Long-term global warming scenarios computed with an efficient coupled climate model. *Climatic Change*, 43:353–367.

Rao, C. R. (1973). Representations of Best Linear Unbiased Estimators in the Model with a Singular Dispersion Matrix. *Journal of Multivariate Analysis*, 3:276–292.

Rayner, D. and Kanzow, T. (2011). The design strategy and methodology of the RAPID-MOC project moorings. *Underwater Technology*, 29(4):159–171.

Reintges, A., Martin, T., and Latif, M. (2017). Uncertainty in 21st Century Projections of the Atlantic Meridional Overturning Circulation in CMIP3 and CMIP5 models. *Climate Dynamics*, 49(5-6):1495–1511.

Rhines, P., Häkkinen, S., and Josey, S. A. (2008). Is oceanic heat transport significant in the climate system? In Dickson, R., Meincke, J., and Rhines, P., editors, *Arctic-Subarctic Ocean Fluxes*, pages 87–109. Springer, Dordrecht.

Roberts, C. D., Jackson, L., and McNeall, D. (2014). Is the 2004-2012 reduction of the Atlantic meridional overturning circulation significant? *Geophysical Research Letters*, 41(9):3204–3210.

Roberts, C. D. and Palmer, M. D. (2012). Detectability of changes to the Atlantic meridional overturning circulation in the Hadley Centre Climate Models. *Climate Dynamics*, 39(9-10):2533–2546.

Roberts, C. D., Waters, J., Peterson, K. A., Palmer, M. D., McCarthy, G. D., Frajka-Williams, E., Haines, K., Lea, D. J., Martin, M. J., Storkey, D., Blockley, E. W., and Zuo, H. (2013). Atmosphere drives recent interannual variability of the Atlantic meridional overturning circulation at 26.5°N. *Geophysical Research Letters*, 40(19):5164–5170.

Robson, J., Hodson, D., Hawkins, E., and Sutton, R. (2014). Atlantic Overturning in decline? *Nature*, 7(1):2–3.

Robson, J., Ortega, P., and Sutton, R. (2016). A reversal of climatic trends in the North Atlantic since 2005. *Nature Geoscience*, 9(7):513–517.

Rosipal, R. and Krämer, N. (2006). Overview and Recent Advances in Partial Least Squares. In Saunders, C., Grobelnik, M., Gunn, S., and Shawe-Taylor, J., editors, *Subspace, Latent Structure and Feature Selection*, pages 34–51. Springer, Berlin, Heidelberg.

Sabine, C. L., Feely, R. A., Gruber, N., Key, R. M., Bullister, J. L., Wanninkhof, R., Wong, C. S., Wallace, D. W. R., Millero, F. J., Peng, T.-h., Kozyr, A., and Ono, T. (2004). The ocean sink for anthropogenic CO_2. *Science*, 305(5682):367–371.

Sandström, J. W. (1908). Dynamische versuche mit meerwasser. *Ann. Hydrogr. Mar. Meteorol.*, 36:6–23.

Santer, B. D., Mikolajewicz, U., Br, W., Cubasch, U., Hasselmann, K., Hck, H., Maier-reimer, E., and Wigley, T. M. L. (1995). Ocean variability and its influence on the detectability of greenhouse warming signals. *Journal of Geophysical Research: Oceans*, 100(C6):10693–10725.

Schleussner, C.-F., Levermann, A., and Meinschausen, M. (2014). Probabilistic projections of the Atlantic overturning. *Climatic Change*, 127(3-4):579–586.

Schmittner, A., Latif, M., and Schneider, B. (2005). Model projections of the North Atlantic thermohaline circulation for the 21st century assessed by observations. *Geophysical Research Letters*, 32(23):1–4.

Sen, A. and Srivastava, M. (2012). *Regression analysis: theory, methods, and applications.* Springer Science and Business Media.

Send, U., Lankhorst, M., and Kanzow, T. (2011). Observation of decadal change in the Atlantic meridional overturning circulation using 10 years of continuous transport data. *Geophysical Research Letters*, 38(24):1–5.

Sévellec, F., Federov, A. V., and Liu, W. (2017). Arctic sea ice decline weakens the Atlantic Meridional Overturning Circulation. *Nature Climate Change*, 7:604–610.

Sévellec, F. and Fedorov, A. V. (2011). Stability of the Atlantic meridional overturning circulation and stratification in a zonally averaged ocean model: Effects of freshwater flux, Southern Ocean winds, and diapycnal diffusion. *Deep-Sea Research Part II: Topical Studies in Oceanography*, 58(17-18):1927–1943.

Sévellec, F. and Fedorov, A. V. (2014). Millennial Variability in an Idealized Ocean Model : Predicting the AMOC Regime Shifts. *Journal of Climate*, 27:3551–3564.

Sévellec, F. and Huck, T. (2016). Geostrophic Closure of the Zonally Averaged Atlantic Meridional Overturning Circulation. *Journal of Physical Oceanography*, 46(3):895–917.

Sévellec, F., Huck, T., and Verdière, A. C. D. (2010). From centennial to millennial oscillation of the thermohaline circulation. *Journal of Marine Research*, 68(5):723–742.

Sévellec, F., Sinha, B., and Skliris, N. (2016). The rogue nature of hiatuses in a global warming climate. *Geophysical Research Letters*, 43(15):8169–8177.

Shoosmith, D. R., Baringer, M. O., and Johns, W. E. (2005). A continuous record of Florida Current temperature transport at 27 ° N. *Geophysical Research Letters*, 32:1–5.

Sime, L. C., Stevens, D. P., Heywood, K. J., and Oliver, K. I. (2006). A decomposition of the atlantic meridional overturning. *Journal of Physical Oceanography*, 36(12):2253–2270.

Sinha, B., Smeed, D., McCarthy, G., Moat, B., Josey, S., Hirschi, J.-M., Frajka-Williams, E., Blaker, A., Rayner, D., and Madec, G. (2018). The accuracy of estimates of the overturning circulation from basin-wide mooring arrays. *Progress in Oceanography*, 160(December 2017):101–123.

Smeed, D., McCarthy, G., Cunningham, S., Frajka-Williams, E., Rayner, D., Johns, W., Meinen, C., Baringer, M., Moat, B., Duchez, A., and Bryden, H. (2013). Observed decline of the Atlantic Meridional Overturning Circulation 2004 to 2012. *Ocean Science Discussions*, 10(5):1619–1645.

Smeed, D. A., Josey, S. A., Beaulieu, C., Johns, W. E., Moat, B. I., Frajka-Williams, E., Rayner, D., Meinen, C. S., Baringer, M. O., Bryden, H. L., and McCarthy, G. D. (2018). The North Atlantic Ocean is in a state of reduced overturning. *Geophysical Research Letters*, 45(3):1527–1533.

Smeed, D. A., McCarthy, G. D., Cunningham, S. A., Frajka-Williams, E., Rayner, D., Johns, W. E., Meinen, C. S., Baringer, M. O., Moat, B. I., Duchez, A., and Bryden, H. L. (2014). Observed decline of the Atlantic meridional overturning circulation 2004 - 2012. *Ocean Science*, 10:29–38.

Srokosz, M., Baringer, M., Bryden, H., Cunningham, S., Delworth, T., Lozier, S., Marotzke, J., and Sutton, R. (2012). Past, Present, and Future Changes in the Atlantic Meridional Overturning Circulation. *Bulletin of the American Meteorological Society*, 93(11):1663–1676.

Stigler, S. M. (1981). Gaus and the invention of least squares. *The Annals of Statistics*, 9(3):465–474.

Stocker, T., Qin, D., Plattner, G., Tignor, M., Allen, S., Boschung, J., Nauels, A., Xia, Y., Bex, V., and Midgley, P. (2013). Summary for Policymakers. In *Climate Change 2013: The Physical Science Basis.Contribution of Working Group I to the Fifth Assessment Report of the Intergovernmental Panel on Climate Change*, pages 3–29. Cambridge University Press, Cambridge, UK, and New York, USA.

Stommel, H. (1957). A survey of ocean current theory. *Deep Sea Research (1953)*, 4(January):149–184.

Stommel, H. (1958). The abyssal circulation. *Deep Sea Research*, 5(1):80–82.

Stommel, H. (1961). Thermohaline convection with two stable regimes. *Tellus*, 13(2):224–230.

Stouffer, R., Yin, J., Gregory, J., Dixon, K., Spelman, M., Hurlin, W., Weaver, A., Eby, M., Flato, G., Hasumi, H., Hu, A., Jungclaus, J., Kamenkovich, I. V., Levermann, A., Montoya, M., Mukarami, S., Nawrath, S., Oka, A., Peltier, W. R., Robitaille, D. Y., Sokolov, A., Vettoretti, G., and Weber, S. L. (2006). Investigating the Causes of the Response of the Thermohaline Circulation to Past and Future Climate Change. *Journal of Climate*, 19(8):1365–1387.

Sutton, R. T. and Hodson, D. L. (2005). Atlantic Ocean Forcing of North American and European Summer Climate. *Science*, 309(5731):115–118.

Sverdrup, H. U. (1933). On vertical circulation in the ocean due to the action of the wind with application to conditions within the Antarctic Circumpolar Current. *University Press*.

Szuts, Z. B., Blundell, J. R., Chidichimo, M. P., and Marotzke, J. (2012). A vertical-mode decomposition to investigate low-frequency internal motion across the Atlantic at 26 N. *Ocean Science*, 8(3):345–367.

Takahashi, T., Sutherland, S. C., Sweeney, C., Poisson, A., Metzl, N., Tilbrook, B., Bates, N., Wanninkhof, R., Feely, R. A., Sabine, C., Olafsson, J., and Nojiri, Y.

(2002). Global sea-air CO_2 flux based on climatological surface ocean pCO_2, and seasonal biological and temperature effects. *Deep-Sea Research Part II: Topical Studies in Oceanography*, 49(9-10):1601–1622.

Talley, L. D. (2008). Freshwater transport estimates and the global overturning circulation: Shallow, deep and throughflow components. *Progress in Oceanography*, 78:257–303.

Talley, L. D., Reid, J. L., and Robbins, P. E. (2003). Data-based meridional overturning streamfunctions for the global ocean. *Journal of Climate*, 16(19):3213–3226.

Taylor, K. E., Stouffer, R. J., and Meehl, G. A. (2012). An overview of CMIP5 and the experiment design. *Bulletin of the American Meteorological Society*, 93(4):485–498.

Thornalley, D. J., Oppo, D. W., Ortega, P., Robson, J. I., Brierley, C. M., Davis, R., Hall, I., Moffa-Sanchez, P., Rose, N., Spooner, P., and Yashayaev, I. (2018). Anomalously weak Labrador Sea convection and Atlantic overturning during the past 150 years. *Nature*, 556(7700):227–230.

Thorpe, R. B., Gregory, J. M., Johns, T. C., Wood, R. A., and Mitchell, J. F. B. (2001). Mechanisms Determining the Atlantic Thermohaline Circulation Response to Greenhouse Gas Forcing in a Non-Flux-Adjusted Coupled Climate Model. *Journal of Climate*, 14(14):3102–3116.

Tiao, G., Reinsel, G., Xu, D., Pedrick, J., Zhu, X., Miller, A., DeLuisi, J., Mateer, C., and Wuebbles, D. (1990). Effects of autocorrelation and temporal sampling schemes on estimates of trend and spatial correlation. *Journal of Geophysical Research*, 95(D12):20,507–20,517.

Trenberth, K. E. and Karon, J. M. (2001). Estimates of meridional atmosphere and ocean heat transports. *Journal of Climate*, 14(16):3433–3443.

Urban, N. M. and Keller, K. (2010). Probabilistic hindcasts and projections of the coupled climate, carbon cycle and Atlantic meridional overturning circulation system: A Bayesian fusion of century-scale observations with a simple model. *Tellus, Series A: Dynamic Meteorology and Oceanography*, 62(5):737–750.

Valdes, P. (2011). Built for stability. *Nature Geoscience*, 4(7):414–416.

Vallis, G. K. (2005). *Atmospheric and Oceanic Fluid Dynamics*. Cambridge University Press, 1 edition.

van Sebille, E., Baringer, M. O., Johns, W. E., Meinen, C. S., Beal, L. M., De Jong, M. F., and Van Aken, H. M. (2011). Propagation pathways of classical Labrador Sea water from its source region to 26°N. *Journal of Geophysical Research: Oceans*, 116(12):1–18.

van Sebille, E., Gri, S. M., Abernathey, R., Adams, T. P., Berlo, P., Biastoch, A., Blanke, B., Chassignet, E. P., Cheng, Y., Cotter, C. J., Deleersnijder, E., Döös, K., Drake, H. F., Drijfhout, S., Gary, S. F., Heemink, A. W., Kjellsson, J., Monika, I., Lange, M., Lique, C., Macgilchrist, G. A., Marsh, R., Mayorga, C. G., Mcadam, R., Nencioli, F., Paris, C. B., Piggott, M. D., Polton, A., Rühs, S., Shah, S. H. A. M., Thomas, M. D., Wang, J., Wolfram, P. J., Zanna, L., and Zika, J. D. (2018). Lagrangian ocean analysis : Fundamentals and practices. *Ocean Modelling*, 121:49–75.

Vellinga, M. and Wood, R. A. (2002). Global Climatic Impacts of a Collapse of the Atlantic Thermohaline Circulation. *Climatic Change*, 54:251–267.

Vellinga, M. and Wood, R. A. (2004). Timely detection of anthropogenic change in the Atlantic meridional overturning circulation. *Geophysical Research Letters*, 31(14):2–5.

Vinogradova, N. T., Ponte, R. M., and Stammer, D. (2007). Relation between sea level and bottom pressure and the vertical dependence of oceanic variability. *Geophysical Research Letters*, 34(December 2006):1–5.

Visbeck, M. (2007). Oceanography: Power of pull. *Nature*, 447(7143):383.

Visbeck, M., Chassignet, E. P., Curry, R. G., Delworth, T. L., Dickson, R. R., and Krahmann, G. (2003). The Ocean's Response to North Atlantic Oscillation Variability. In *The North Atlantic Oscillation: climatic significance and environmental impact*, pages 113–145. 134 edition.

Von Storch, H. (1999). Misuses of statistical analysis in climate research. In *Analysis of climate variability*, pages 11–26. Springer.

Vyushin, D., Kushner, P., and Zwiers, F. (2012). Modeling and understanding persistence of climate variability. *Journal of Geophysical Research: Atmospheres*, 117(D21).

Wang, Z., Lu, Y., Dupont, F., Loder, J. W., Hannah, C., and Wright, D. G. (2015). Variability of sea surface height and circulation in the North Atlantic : Forcing mechanisms and linkages. *Progress in Oceanography*, 132:273–286.

Warren, B. A. (1983). Why is no deep water formed in the North Pacific? *Journal of Marine Research*, 41:327–347.

Weatherhead, E. C., Reinsel, G. C., Tiao, G. C., Meng, X.-L., Choi, D., Cheang, W.-K., Keller, T., DeLuisi, J., Wuebbles, D. J., Kerr, J. B., Miller, A. J., Oltmans, S. J., and Frederick, J. E. (1998). Factors affecting the detection of trends: Statistical considerations and applications to environmental data. *Journal of Geophysical Research*, 103(D14):17149–17161.

Weaver, A. J., Sedláček, J., Eby, M., Alexander, K., Crespin, E., Fichefet, T., Philippon-Berthier, G., Joos, F., Kawamiy, M., Matsumoto, K., Steinacher, M., Tachiiri, K.,

Tokos, K., Yoshimori, M., and Zickfeld, K. (2012). Stability of the Atlantic meridional overturning circulation: A model intercomparison. *Geophysical Research Letters*, 39(20):1–8.

Williams, D. N., Taylor, K. E., Cinquini, L., Evans, B., Kawamiya, M., Lawrence, B. N., and Middleton, D. E. (2011). The Earth System Grid Federation: Software Framework Supporting CMIP5 Data Analysis and Dissemination. *CLIVAR Exchanges*, 16(56):40–42.

Williams, J., Hughes, C. W., and Tamisiea, M. E. (2015). Detecting trends in bottom pressure measured using a tall mooring and altimetry. *Journal of Geophysical Research:Oceans*, 120:5216–5232.

Willis, J. K. (2010). Can in situ floats and satellite altimeters detect long-term changes in Atlantic Ocean overturning? *Geophysical Research Letters*, 37(6).

Wold, H. (1982). Soft modelling: The basic design and some extensions. In Joreskog, K.-G. and Wold, H., editors, *Systems Under Indirect Observation*, page 343. Amsterdam.

Wold, S., Sjostrom, M., and Eriksson, L. (2001). PLS-regression: a basic tool of chemometrics. *Chemometrics and Intelligent Laboratory Systems*, 58:109–130.

Wood, R. A., Keen, A. B., Mitchell, J. F. B., Gregory, J. M., Wood, R. A., Keen, A. B., Mitchell, J. F. B., and Gregory, J. M. (1999). Changing spatial structure of the thermohaline circulation in response to atmospheric CO_2 forcing in a climate model. *Nature*, 399:572–575.

Woodworth, P. L., Maqueda, M., Roussenov, V. M., Williams, R. G., and Hughes, C. W. (2014). Mean sea-level variability along the northeast American Atlantic coast and the roles of the wind and the overturning circulation. *Journal of Geophysical Research: Oceans*, 119:8916–8935.

Wunsch, C. (2005). The total meridional heat flux and its oceanic and atmospheric partition. *Journal of Climate*, 18:4374–4380.

Yan, X., Zhang, R., and Knutson, T. R. (2018). Underestimated AMOC Variability and Implications for AMV and Predictability in CMIP Models. *Geophysical Research Letters*, 45(9):4319–4328.

Yang, J. (1999). A linkage between decadal climate variations in the Labrador Sea and the tropical Atlantic Ocean. *Geophysical Research Letters*, 26(8):1023–1026.

Yeager, S. and Danabasoglu, G. (2014). The origins of late-twentieth-century variations in the large-scale North Atlantic circulation. *Journal of Climate*, 27:3222–3247.

Yin, J. and Goddard, P. B. (2013). Oceanic control of sea level rise patterns along the East Coast of the United States. *Geophysical Research Letters*, 40(20):5514–5520.

Zantopp, R., Fischer, J., Visbeck, M., and Karstensen, J. (2017). From interannual to decadal: 17 years of boundary current transports at the exit of the Labrador Sea. *Journal of Geophysical Research: Oceans*, 122:1724–1748.

Zhang, R. (2008). Coherent surface-subsurface fingerprint of the Atlantic meridional overturning circulation. *Geophysical Research Letters*, 35(20):1–6.

Zhang, R. (2010). Latitudinal dependence of Atlantic meridional overturning circulation (AMOC) variations. *Geophysical Research Letters*, 37:1–6.

Zhang, R. and Delworth, T. (2005). Simulated Tropical Response to a Substantial Weakening of the Atlantic Thermohaline Circulation. *Journal of Climate*, 18:1853–1860.

Zhang, R. and Delworth, T. L. (2006). Impact of Atlantic multidecadal oscillations on India/Sahel rainfall and Atlantic hurricanes. *Geophysical Research Letters*, 33:1–5.

Zhang, R., Delworth, T. L., and Held, I. M. (2007). Can the Atlantic Ocean drive the observed multidecadal variability in Northern Hemisphere mean temperature? *Geophysical Research Letters*, 34(2):1–6.